

# Design, Fabrication, and Control Methods for Exploiting the Multifunctional Sensing and Actuation Capabilities of Shape Memory Alloy Wires

Dissertation  
zur Erlangung des Grades  
des Doktors der Ingenieurwissenschaften  
der Naturwissenschaftlich-Technischen Fakultät II  
- Physik und Mechatronik -  
der Universität des Saarlandes

von

Stephen Furst

Saarbrücken

2012

Tag des Kolloquiums: 16.10.2012  
Dekanin/Dekan: Herr Univ.-Prof. Dr. rer. nat. Helmut Seidel  
Mitglieder des  
Prüfungsausschusses: Herr Univ.-Prof. Dr. rer. nat. Helmut Seidel  
Herr Univ.-Prof. Dr.-Ing. habil. Stefan Seelecke  
Herr PD Dr. Manfred Kohl  
Herr Prof. Dr. Etienne Patoor  
Herr Dr. rer. nat. Frank Müller

# Abstract

FURST, STEPHEN JOSEPH. Design, Fabrication, and Control Methods for Exploiting the Multifunctional Sensing and Actuating Capabilities of Shape Memory Alloy Wires. (Under the direction of Prof. Dr.-Ing. Stefan Seelecke)

The benefits of replacing space and energy consuming actuators and sensors with so-called “active” materials have been well known for decades. One such material, shape memory alloys (SMAs), inspire particularly novel applications because of their unmatched power density, high force output, and ability to be multifunctional – acting simultaneously as both actuator and sensor. Recently, improved material processing techniques by companies such as Dynalloy have enabled repeatable, low-cost production of small-diameter (<100  $\mu\text{m}$ ) SMA wires capable of being actuated with minimal power at rates faster than 1 Hz. Additionally, a multifunctional power controller has been developed at North Carolina State University to simultaneously control the heating power input to SMA wires while measuring their changing electrical resistance. Advances such as these have enabled new applications to be considered in academia, such as steerable catheters and guidewires for use inside the human body, light-weight actuator systems for micro-air-vehicles, energy-efficient linear actuators to replace traditional solenoid or coil driven motors, and a multifunctional sensor-actuator system to control an adaptive Smart Inhaler nozzle without disrupting a delicate laminar air flow.

Despite the obvious advantages and an abundance of novel application concepts, very few SMA-wire-based applications are commercially available. This development gap is caused by a number of significant practical challenges. First, the SMA material itself is non-linear and hysteretic, so design requires in-depth understanding of a complex kinematics problem. The design challenge is complicated further by a coupled thermo-mechanical interaction between a tiny SMA wire and surrounding structure that typically has a much larger thermal mass. Next, making reliable electrical and mechanical connections between the tiny SMA wires and the structure is non-trivial, and it is necessary to track the treatment history of the SMA materials during the fabrication process so that the behavior will be predictable. Finally, controlling the actuation or interpreting the sensor information of the electro-thermo-mechanically coupled SMA-structure system requires a ground-up understanding of the material’s characteristics and the physics of the coupled interactions.

This dissertation provides a path for bringing miniature embedded SMA-wire applications from concept to functionality. Part 1 gives an overview of design with SMA wires, fabrication methods, and the implications of thermo-mechanical coupling. Throughout Part 1, design optimization and fabrication methods are presented in the context of an adaptive nozzle and a bio-inspired wing joint.

Part 2 uses side-by-side physics-based modeling and experimental results to build an understanding of the stress, strain, and resistance characteristics of SMA wire within SMA-spring systems that provide simplified analogs for many embedded SMA applications. Then, methods for multifunctional sensing and control are outlined, implemented, and tested on the analog systems before finally being applied to the adaptive nozzle joint developed in Part 1, where SMA wires are used simultaneously to deform

the joint and to measure the deformation for a closed-loop control scheme. The framework and case studies presented provide engineers with a design and control method that can be applied to a wide array of embedded SMA-wire applications in a multitude of industries.

# Zusammenfassung

FURST, STEPHEN JOSEPH. Design, Fabrication, and Control Methods for Exploiting the Multifunctional Sensing and Actuating Capabilities of Shape Memory Alloy Wires. (Under the direction of Prof. Dr.-Ing. Stefan Seelecke)

Die Vorteile sogenannter „aktiver“ Materialien beim Einsatz in platz- und energiesparenden Anwendungen sind seit langem bekannt. Formgedächtnislegierungen (FGL) sind Beispiele für solche Materialien, die neue Anwendungen durch ihre einzigartige Leistungsdichte, hohe Kraftwirkung und Multifunktionalität als Sensor und Aktor inspirieren. Seit kurzer Zeit ist, durch verbesserte Herstellungstechniken von Unternehmen wie Dynalloy, Inc., USA, die kostengünstige Produktion von FGL-Drähten mit geringem Durchmesser ( $<100 \mu\text{m}$ ) möglich, die zudem bei minimalem Energieeinsatz mit Raten größer 1 Hz aktuiert werden können. An der North Carolina State University wurde darüber hinaus ein multifunktionaler Leistungsregler entwickelt, mit dem sich gleichzeitig die Heizleistung der FGL-Drähte steuern, und die Veränderung ihrer elektrischen Widerstände messen lassen. Entwicklungen wie diese haben im akademischen Bereich bereits zu neuen Anwendungen geführt, wie beispielsweise steuerbare Katheter und Steuerdrähte für die Verwendung im menschlichen Körper, leichte Aktuatorssysteme für Mikro-Luftfahrzeuge, energieeffiziente Linearaktoren, welche klassische, elektromagnetisch angesteuerte Motoren ersetzen können, und ein nicht-intrusives Sensor-Aktor-System zur Steuerung der adaptiven Düse eines Inhalatorsystems („Smart Inhaler“) ohne Störung der empfindlichen laminaren Luftströmung.

Trotz der offensichtlichen Vorteile und einer Fülle an neuen Anwendungskonzepten finden bis heute nur sehr wenige FGL-Draht-Anwendungen Verwendung in kommerziellen Produkten. Diese Entwicklungslücke ist durch eine Reihe von Komplexitäten in der Handhabung von FGL-Aktorsystemen bedingt. Zunächst einmal verhält sich das Material der FGL nichtlinear hysteretisch, so dass die Konzeption ein tiefgreifendes Verständnis eines komplexen kinematischen Problems voraussetzt. Eine weitere Herausforderung besteht in der gekoppelt thermo-mechanischen Interaktion zwischen dem dünnen FGL-Draht und der umgebenden Struktur mit üblicherweise viel größerer Wärmekapazität.

Die nächste Schwierigkeit ist das Anbringen der elektrischen und mechanischen Verbindungen zwischen dem FGL-Draht und der Struktur. Zudem ist es notwendig, die Bearbeitungsgeschichte des Drahtes während der Herstellung nachzuvollziehen, damit das Verhalten vorhersagbar wird. Letztendlich wird für die Steuerung der Aktuierung und die Interpretation der Sensorsignale des elektro-thermo-mechanisch gekoppelten FGL-Systems ein grundlegendes Verständnis der Materialcharakteristik und der zugrundeliegenden physikalischen Vorgänge benötigt.

Diese Dissertation stellt das Vorgehen für die Entwicklung von FGL-Drahtanwendungen vom Konzept hin zur Funktionalität dar. Teil 1 liefert einen Überblick über die Konstruktion mit FGL-Drähten, Herstellungsmethoden und die Konsequenzen der thermo-mechanischen Kopplung. In Teil 1

werden Designoptimierung und Herstellungsverfahren im Rahmen einer adaptiven Düse und eines bioinspirierten Flügelgelenkes dargestellt.

Teil 2 vergleicht physikalische Modellierung und experimentelle Ergebnisse, um ein Verständnis für den Verlauf von Spannung, Dehnung und elektrischem Widerstand von FGL-Drähten in Feder-FGL-Draht-Systemen zu entwickeln. Diese Systeme liefern vereinfachte Referenzsysteme für viele FGL-Anwendungen. Danach werden Verfahren für multifunktionales Messen und Regeln beschrieben, auf den Referenzsystemen implementiert und getestet, bevor sie auf das in Teil 1 entwickelte System, das adaptive Gelenk einer Inhalatordüse, angewandt werden. Die FGL-Drähte werden in dieser Anwendung gleichzeitig dazu verwendet, die Düse zu verformen und die Verformung zu messen, wodurch eine Regelung realisiert werden kann. Das dargestellte Vorgehen und die Fallstudien bieten Ingenieuren grundlegende Design- und Regelungsmethoden, die für eine Vielzahl an FGL-Drahtaktor/sensor Anwendungen verwendet werden können.

# **Dedication**

*To Dr. Seelecke, Dr. Dow, and Coach Geiger—for valuing results.*

# Biography

Stephen Furst was born and raised in bucolic Goshen, NY, about an hour from the big city. Stephen's mother Diane is a social worker, having worked with geriatrics through Hospice, children through the school district, and everyone else through private practice. His father, Richard, is an Earth Science teacher with an uncanny supply of trivial knowledge and a curiosity for the natural world. Richard Furst was also collegiate distance runner and currently coaches one of the most successful high school Track and Cross Country teams in America. Stephen was raised alongside his older brother, Eric, a dedicated role model with a BS in Physics from Bucknell, MS in Computational Math from John Hopkins, and a mangled Achilles tendon from a decade of running too hard for his high school and college track teams.

Stephen graduated from Goshen HS in 2003 and went to North Carolina State University to run. He graduated with a BS in Aerospace Engineering in 2007, and while pursuing a MS in Mechanical Engineering, Stephen won the 2008 ACC Championship in the 5k and 10k and was 10<sup>th</sup> in the NCAA 5k, earning All-American honors. In the Fall of 2008, Stephen defended his thesis titled "Automated Handling Technology for Precision Machining of Two-Sided Parts" to Dr. Thomas Dow at the NCSU Precision Engineering Center.

Stephen began PhD work with Dr. -Ing. Stefan Seelecke at NC State with emphasis on Smart Materials research. In January 2011, Dr. Seelecke left NC State for Saarland University, affording Stephen the opportunity to continue his research in Saarbrücken, Germany in the Winter and Summer, while returning to the US for his Fall and Spring racing schedule. In the Spring of 2012, Stephen will defend his thesis and return to Raleigh to prepare to compete in the 5000 m at the US Olympic Team Trials.

# Acknowledgements

I would first like to acknowledge my family and friends from Goshen, NY for placing such a high value on education. In Raleigh, I owe thanks to Coach Geiger for giving me the opportunity to come to NC State and for leading me in my running, without which there would have been no PhD (or Dr. – Ing., as its called in Germany). Also, thanks to Dr. Dow for instilling in me a sense of practicality, forcing me to consider the inconvenient question “who cares?” every time I started doing something pointless, and for giving me a place to work while home from Germany. I credit my teammate, friend, and colleague John Crews for teaching me good MATLAB practices, helping me debug code, and programming most of the simulations in our co-authored papers, all over the course of our Wednesday pre-dawn 15-milers through downtown Raleigh.

At the MMSL, I must give thanks to Alex York for keeping the lab functional, for helping me program LabVIEW, and for leading our group of intrepid Americans across the Atlantic. I would also like to acknowledge Rohan Hangekar for creating the robust version of the multifunctional power controller that is the backbone of most of my experimental data. And thanks to Prof. Dr. –Ing. Joachim Rudolph, PD Dr. rer. nat. Manfred Kohl and Prof. Dr. -Ing. Stefan Seelecke for agreeing to oversee my defense and review this dissertation.

Finally I would like to thank Dr. Seelecke for having patience and empathy, and for giving me the flexibility to pursue my non-academic dreams alongside my PhD. Most other advisers would not have been able to acknowledge the importance that I place on such an irrational pursuit, or to recognize the synergetic coupling between my athletics and my academics.

# Table of Contents

Introduction.....	1
I. Motivation.....	3
i. Shape Memory Alloys.....	3
ii. Challenges of Working with SMAs.....	4
iii. Current SMA Applications.....	5
iv. Adaptive Smart Inhaler Nozzle.....	5
v. Bio-Inspired Application.....	7
II. Objectives.....	8
Part 1: Design and Fabrication Methods for Embedded SMA Systems.....	9
1.1 Design of Embedded SMA Systems.....	11
1.1.1 SMA-Structure Interaction.....	11
1.1.2 Steps in the Design Process.....	16
1.1.3 Formulation of a Design Optimization Problem.....	16
1.2 Case Studies of SMA-Based Design and Optimization Process: Adaptive Nozzle and Bio-Inspired Joint Applications.....	19
1.2.1 Adaptive Inhaler Nozzle Application Overview and Design Objectives.....	19
1.2.2 Bio-Inspired Wing Application Overview and Design Objectives.....	20
1.2.3 Joint Bending Kinematics.....	21
1.2.4 Force and Moment Balance of Bio-Inspired Joint.....	27
1.2.5 Design Optimization of Bio-Inspired Joint.....	29
1.3 Fabrication Methods for Embedded SMA Wires.....	33
1.3.1 Challenges.....	33
1.3.2 Case Studies of Fabrication Process: Adaptive Nozzle and Bio-Inspired Flapping Bat.....	33
1.4 Summary of Design and Fabrication for Embedded SMA Actuator Wire Applications.....	53
1.4.1 Summary of Adaptive Nozzle Design and Fabrication.....	53
1.4.2 Summary of Bio-Inspired Wing Design and Fabrication.....	54
1.5 Future Work for Part 1.....	55
Part 2: SMA Wire Modeling, Characterization, and Multifunctional Sensing and Control.....	57
2.1 Modeling and Characterization of SMA Actuator Systems.....	59

2.1.1	SMA Single-Crystal Model .....	59
2.1.2	Single SMA-Spring System.....	64
2.1.3	Opposing SMA System .....	81
2.1.4	Smart Inhaler Nozzle Joint .....	99
2.2	Sensing and Controls with Multifunctional SMA Wires.....	109
2.2.1	Sensor Mapping and Control of Single SMA-Spring System .....	109
2.2.2	Sensor Mapping and Control of Opposing SMA System.....	115
2.2.3	Sensor Mapping and Control of Smart Inhaler Nozzle Joint.....	131
2.3	Summary of Part 2.....	145
2.4	Future Work for Part 2.....	146
	References.....	147
	Appendices .....	151
	Appendix A: Adhesive Strength Experiments.....	152
A.1	Using Adhesives for Mechanical Attachments.....	153
A.2	Adhesive Experiment Setup.....	153
A.3	Adhesive Testing Procedure and Matrix.....	154
A.4	Results and Discussion .....	159
A.5	Adhesive Test Conclusions.....	163
	Appendix B: The Effects of Thermal Boundary Conditions on SMA Actuator Wires .....	164
B.1	Introduction.....	165
B.2	Numerical Simulation .....	166
B.3	Experimental Tensile Test Setup and Procedure .....	173
B.4	Results.....	177
B.5	Conclusions on the Effects of Thermal BCs on SMA Actuator Wires.....	189

## List of Tables

Table 1: Adaptive Smart Inhaler Geometric Parameters.....	25
Table 2: Design Variables for Bio-Inspired Joint Optimization .....	29
Table 3: Optimal and Actual Design Variables and Objectives for Bio-Inspired Joint .....	31
Table 4: Numerical Model – Coupled Temperature and Phase Fraction Evolution Equations .....	60
Table 5: List of Variables Used in Transition Probability Calculations .....	61
Table 6: SMA Wire and Heat Transfer Model Parameters .....	68
Table 7: SMA Wire Resistance Model Parameters.....	68
Table 8: SMA Wire and Heat Transfer Model Parameters .....	85
Table 9: SMA Resistance Model Parameters.....	85
Table 10: Pre-Strain, Pre-Stress and Actuation Frequency/Amplitudes for Alternating Actuation Experiments.....	88
Table 11: RMS Tracking and Measurement Error for Single SMA-Spring System Pre-stressed to 150 MPa.....	114
Table 12: RMS of Tracking and Measurement Errors Using Resistance-Based and Laser Feedback Sensor.....	129
Table 13: Resistance to Deflection Mapping Coefficients for SMA-Actuated Joint.....	139
Table 15: Adhesives tested.....	156
Table 16: Experiment Parameter Matrix.....	157
Table 17: SMA Wire Resistance Model Parameters.....	170
Table 18: SMA Model Material Parameters .....	171
Table 19: Interrelated SMA Model Parameters .....	172
Table 20: Boundary Conditions Used to Simulate Steps of a Tensile Test Experiment.....	181

# List of Figures

Figure 1: Diagram of Shape Memory Alloy Phase Change in Response to Heating, Cooling, and Stressing.....	4
Figure 2: Diagram of Smart Inhaler (left) and Flexible Top Joint (middle) and Picture of Flexible Top Joint (right) .....	6
Figure 3: Dual-Joint Smart Inhaler Nozzle.....	7
Figure 4: Biologically Inspired SMA-Actuated Bat .....	8
Figure 5: Generalization of an Embedded SMA Actuator - Structure System with a Pre-stretched Spring at Equilibrium .....	12
Figure 6: Load-Displacement Characteristics of Martensitic SMA Wire and Linear Spring on the Same Set of Axes.....	12
Figure 7: Stress-Strain Equilibrium between Perfect Single Crystal SMA and Spring during Thermal Loading and Unloading Cycle.....	13
Figure 8: Temperature-Strain Characteristic of SMA-Spring Actuator System.....	14
Figure 9: Effect of Spring (Structure) Stiffness on Stress-Strain Behavior of SMA Actuator System	14
Figure 10: Stress vs. Strain Plot for 100 $\mu\text{m}$ Diameter Flexinol SMA Wire at Low and High Temperature.....	15
Figure 11: Diagram of Adaptive Smart Inhaler Nozzle Joint.....	19
Figure 12: Museum Bat Prototype with Four Independent Joints .....	20
Figure 13: Picture of Deflected Nozzle and Bat Shoulder Joint with Simplified Kinematic Diagram	21
Figure 14: Sketch of Flexible Joint Simplified as a Uniform Arc .....	21
Figure 15: Effect of Changing SMA Strain on Bending Angle and Radius of Curvature.....	23
Figure 16: Effect of Changing Attachment Point ‘b’ on Bending Angle and Radius of Curvature ....	24
Figure 17: Effect of Changing Joint Length ‘c’ on Bending Angle and Radius of Curvature .....	24
Figure 18: Effect of Changing Radial Attachment Point ‘ $r_H$ ’ on Bending Angle and Radius of Curvature .....	25
Figure 19: Predicted Bending of Adaptive Smart Inhaler Nozzle Joint Due to SMA Wire Contraction .....	26
Figure 20: Measured Adaptive Nozzle Joint Bending and Kinematic Model.....	26
Figure 21: Free-Body Diagram for Bio-Inspired Joint .....	27
Figure 22: Uniform Bending of Super-Elastic SMA Joint .....	29
Figure 23: Model of Layer Smart Inhaler Adaptive Nozzle .....	34
Figure 24: Exploded View of Adaptive Nozzle Joint Assembly.....	34
Figure 25: 3D Model of Bio-Inspired Flapping Bat .....	35
Figure 26: Components of Bio-Inspired Flapping Bat Design .....	36
Figure 27: Shear Stress at Bond Failure between Different Adhesives and a 100 $\mu\text{m}$ Diameter SMA Wire Under Electric Current.....	38
Figure 28: Diagram of an SMA Wire attached to a Pre-Compressed Compliant Joint.....	39
Figure 29: Three Rigid and Two Flexible Elements Used in Adaptive Nozzle Assembly.....	39

Figure 30: Setup for Pre-compressing Compliant Viton Rubber Joint .....	39
Figure 31: Photo of Setup for Pre-compressing Compliant Silicon Joint .....	40
Figure 32: Setup for Pre-stressing and Attaching SMA Wires .....	40
Figure 33: Photo of Setup for Pre-stressing and Attaching SMA Wires.....	40
Figure 34: Stress-Strain Equilibrium after Stressing (Step1), Heating (Step 2) and Cooling (Step3) .41	
Figure 35: SMA Wire Wrapped Around Turn-Around Anchor with SuperGlue .....	42
Figure 36: Stress-Strain Equilibrium after Pre-Stressing.....	42
Figure 37: Stressed SMA Wire Tacked with SuperGlue .....	43
Figure 38: Close-up Photo of SMA Wire Under Tension with SuperGlue Tack.....	43
Figure 39: SMA Wires Secured with Loctite E40-HT High Temperature Epoxy .....	43
Figure 40: Photo of Guitar String Winders [77] .....	44
Figure 41: Diagram of Adjustable Screw Method for SMA Attachment and Tensioning.....	44
Figure 42: Structural Element with Screw for Mechanical Attachment of SMA Wire .....	44
Figure 43: Demonstration of SMA Wire Attached to Bio-Inspired Bone Structure with Adjustable Screw Method .....	45
Figure 44: Adjustable Screw Method Applied to Bat Elbow and Shoulder SMA Muscles.....	45
Figure 45: Diagram Showing the Contributions to SMA Resistance Measurements .....	46
Figure 46: Diagram of Electrical Connection Behind Mechanical Connection.....	46
Figure 47: Demonstration Lead Wire Loop Electrical Connection Process .....	47
Figure 48: Lead Wire Loop Electrical Connection Process Applied to Adaptive Nozzle .....	48
Figure 49: Adaptive Nozzle Electrical and Mechanical Connections.....	48
Figure 50: Adaptive Nozzle Electrical Connection Encased with Teflon Heat Shrink Tubing.....	48
Figure 51: Socket Block with Slack End of an SMA Wire.....	49
Figure 52: Socket Block with Copper Pin Holding SMA Wire.....	49
Figure 53: Wire Guide Loops from Bunget BATMAV Prototype [20].....	50
Figure 54: Teflon Tube Used for Guiding SMA Wires .....	50
Figure 55: Teflon Tube Wire Guides in Bio-Inspired Application .....	51
Figure 56: SMA Wire Guided Along Bat Wing with Teflon Tubes .....	51
Figure 57: Top Joint.....	54
Figure 58: SMA-Actuated Dual Joint Smart Inhaler Nozzle .....	54
Figure 59: Bottom Joint .....	54
Figure 60: Bio-Inspired Bat with Two SMA-Actuated Shoulder and Elbow .....	55
Figure 61: Diagram of Model Parameters on Stress-Strain Hysteresis Loop .....	62
Figure 62: Typical SMA Stress-Stain Curve with Austenitic and Martensitic Elastic Moduli.....	63
Figure 63: Diagram of SMA and Spring in Series .....	64
Figure 64: Stress-Strain Equilibrium Diagrams for an SMA Wire and Spring at Different Temperatures.....	65
Figure 65: Sketch of Coordinate System for Single SMA Wire and Spring System.....	66
Figure 66: Depiction of Single Crystal (black) and Polycrystalline (gray) Stress-Strain Characteristics and Expected Stroke.....	69

Figure 67: Equilibriums Attainable during Pre-stressing in a Single Crystal (left) and Polycrystalline (right) Material.....	70
Figure 68: Diagram of SMA-Flexure Test Setup .....	71
Figure 69: Photograph of SMA-Flexure Testing Setup.....	71
Figure 70: Input Power Signals Shown over 10 s at 0.1 Hz (left), 0.5 Hz (middle), and 1.0 Hz (right) .....	72
Figure 71: Power vs. Strain for Different Pre-stresses with 0.1 Hz Heating Frequency .....	73
Figure 72: Power vs. Stress for Different Pre-stresses with 0.1 Hz Heating Frequency .....	74
Figure 73: Power vs. Resistance for Different Pre-stresses with 0.1 Hz Heating Frequency.....	74
Figure 74: Stress vs. Strain for Different Pre-stresses with 0.1 Hz Heating Frequency .....	75
Figure 75: Resistance vs. Strain for Different Pre-stresses with 0.1 Hz Heating Frequency .....	75
Figure 76: Power vs. Strain for Different Heating Frequencies with 150 MPa Pre-stress .....	76
Figure 77: Power vs. Stress for Different Heating Frequencies with 150 MPa Pre-stress .....	77
Figure 78: Power vs. Resistance for Different Heating Frequencies with 150 MPa Pre-stress.....	77
Figure 79: Stress vs. Strain for Different Heating Frequencies with 150 MPa Pre-stress.....	78
Figure 80: Resistance vs. Strain for Different Heating Frequencies with 150 MPa Pre-stress .....	78
Figure 81: Resistance vs. Strain for Different Pre-stresses with 0.5 Hz Heating Frequency .....	79
Figure 82: Resistance vs. Strain for Different Pre-stresses with 1.0 Hz Heating Frequency .....	79
Figure 83: Diagram of Embedded SMA Application with Single-SMA (left) and Dual-SMA Actuation (right) .....	81
Figure 84: Opposing SMA-Spring System.....	81
Figure 85: Sketch of Coordinate System for Coupled SMA Wire and Spring System .....	82
Figure 86: Stress-Strain Characteristics of SMA Wires and Spring.....	82
Figure 87: Diagram of SMA-Flexure Test Setup .....	86
Figure 88: Photograph of SMA-Flexure Testing Setup.....	86
Figure 89: Stress-Strain Diagram of Pre-Straining (left) and Pre-Stressing (right) Procedure.....	87
Figure 90: Power input to SMA Wires during Constant Opposing Power (left) and Alternating Actuation (right) Experiments .....	88
Figure 91: Single-Crystal Approximation of the Stress-Strain Behavior during Constant Opposing Power Experiment .....	89
Figure 92: Simulated (left) and Experimental (right) Resistance and Stress vs. Strain for Various Wire 2 Power Inputs .....	91
Figure 93: Single-Crystal Approximation the Stress-Strain Behavior during Alternating Cycles Experiment.....	92
Figure 94: Simulated (left) and Experimental (right) Resistance and Stress vs. Strain for Various Pre-Strain Values.....	93
Figure 95: Simulated (left) and Experimental (right) Resistance and Stress vs. Strain for Various Pre-Stress Values.....	95
Figure 96: Resistance and Stress vs. Strain for Alternating Actuation Tests at Different Frequencies for a Pre-strain of 3.33%.....	96

Figure 97: Adaptive Smart Inhaler Nozzle Joint.....	99
Figure 98: Diagram of Test Setup Used to Measure SMA Strain and Nozzle Tip Displacement Showing Un-deformed (left) and Deformed (middle) Nozzle Tip. Photographed on Right.....	100
Figure 99: Time History of Power Input, SMA Resistance and Strain, and Nozzle Tip Displacement for Actuator 1 at 0.1 Hz.....	101
Figure 100: Hysteresis Plots for Top Joint Actuator 1 at 0.1 Hz .....	102
Figure 101: Hysteresis Plots for Top Joint Actuator 2 at 0.1 Hz .....	102
Figure 102: Hysteresis Plots for Top Joint Actuator 3 at 0.1 Hz .....	102
Figure 103: Top Joint Sensor Diagrams: Resistance vs. Tip Displacement in Actuator Direction 1, 2, or 3 at 0.1 Hz.....	103
Figure 104: Top Joint Sensor Diagrams: Resistance vs. Tip Displacement in Actuator Direction 1, 2, or 3 at 0.5 Hz.....	103
Figure 105: Hysteresis Plots for Bottom Joint Actuator 4 at 0.04 Hz.....	104
Figure 106: Hysteresis Plots for Bottom Joint Actuator 5 at 0.04 Hz.....	104
Figure 107: Hysteresis Plots for Bottom Joint Actuator 6 at 0.04 Hz.....	104
Figure 108: Bottom Joint Sensor Diagrams: Resistance vs. Tip Displacement in Actuator Direction 4, 5, or 6 at 0.04 Hz.....	105
Figure 109: Bottom Joint Sensor Diagrams: Resistance vs. Tip Displacement in Actuator Direction 4, 5, or 6 at 0.5 Hz.....	105
Figure 110: Time Histories for Top Joint Actuator 1 (red), 2 (green) and 3 (blue) for Mercedes Star Input at 0.05 Hz.....	106
Figure 111: Tip Displacement of Top Joint Mercedes Star Input.....	106
Figure 112: Single SMA-Spring System.....	109
Figure 113: Example of Using Characteristics of a SMA-Spring System to Generate a Displacement Sensor Mapping .....	110
Figure 114: Controller and Mapping Block Diagram .....	111
Figure 115: Position Tracking of 0.2 Hz Sinusoid (left) and Sensor Diagram Showing Displacement as measured by the Laser and the R- $\delta$ Mapping (right) .....	112
Figure 116: Position Tracking of 1.0 Hz Sinusoid (left) and Sensor Diagram Showing Displacement as measured by the Laser and the R- $\delta$ Mapping (right) .....	113
Figure 117: Position Tracking of 2.0 Hz Sinusoid (left) and Sensor Diagram Showing Displacement as measured by the Laser and the R- $\delta$ Mapping (right) .....	113
Figure 118: Position Tracking of Variable Step Input (left) and Sensor Diagram Showing Displacement as measured by the Laser and the R- $\delta$ Mapping (right) .....	114
Figure 119: Opposing SMA-Spring System .....	115
Figure 120: Block Diagram of Opposing SMA System Sensor Mapping and Control Scheme.....	115
Figure 121: Sensor Diagram for Coupled SMA System.....	116
Figure 122: Tracking (left) and Sensor Diagram (right) of a 0.2 Hz Sinusoid using Resistance Mapping as Feedback Measurement for 3.47% Pre-Strained SMA Wires .....	121

Figure 123: Tracking (left) and Sensor Diagram (right) of a 0.2 Hz Sinusoid using Laser Sensor as Feedback Measurement for 3.47% Pre-Strained SMA Wires .....	121
Figure 124: Tracking (left) and Sensor Diagram (right) of a 1.0 Hz Sinusoid using Resistance Mapping as Feedback Measurement for 3.47% Pre-Strained SMA Wires.....	122
Figure 125: Tracking (left) and Sensor Diagram (right) of a 1.0 Hz Sinusoid using Laser Sensor as Feedback Measurement for 3.47% Pre-Strained SMA Wires .....	122
Figure 126: Tracking (left) and Sensor Diagram (right) of a 2.0 Hz Sinusoid using Resistance Mapping as Feedback Measurement for 3.47% Pre-Strained SMA Wires.....	123
Figure 127: Tracking (left) and Sensor Diagram (right) of a 2.0 Hz Sinusoid using Laser Sensor as Feedback Measurement for 3.47% Pre-Strained SMA Wires .....	123
Figure 128: Tracking (left) and Sensor Diagram (right) of a Step Function using Resistance Mapping as Feedback Measurement for 3.47% Pre-Strained SMA Wires.....	124
Figure 129: Tracking (left) and Sensor Diagram (right) of a Step Function using Laser Sensor as Feedback Measurement for 3.47% Pre-Strained SMA Wires .....	124
Figure 130: Tracking (left) and Sensor Diagram (right) of a 0.2 Hz Sinusoid using Resistance Mapping as Feedback Measurement for 100 MPa Pre-Stressed SMA Wires .....	125
Figure 131: Tracking (left) and Sensor Diagram (right) of a 0.2 Hz Sinusoid using Laser Sensor as Feedback Measurement for 100 MPa Pre-Stressed SMA Wires .....	126
Figure 132: Tracking (left) and Sensor Diagram (right) of a 1.0 Hz Sinusoid using Resistance Mapping as Feedback Measurement for 100 MPa Pre-Stressed SMA Wires .....	126
Figure 133: Tracking (left) and Sensor Diagram (right) of a 1.0 Hz Sinusoid using Laser Sensor as Feedback Measurement for 100 MPa Pre-Stressed SMA Wires .....	127
Figure 134: Tracking (left) and Sensor Diagram (right) of a 2.0 Hz Sinusoid using Resistance Mapping as Feedback Measurement for 100 MPa Pre-Stressed SMA Wires .....	127
Figure 135: Tracking (left) and Sensor Diagram (right) of a 2.0 Hz Sinusoid using Laser Sensor as Feedback Measurement for 100 MPa Pre-Stressed SMA Wires .....	128
Figure 136: Tracking (left) and Sensor Diagram (right) of a Step Function using Resistance Mapping as Feedback Measurement for 100 MPa Pre-Stressed SMA Wires.....	128
Figure 137: Tracking (left) and Sensor Diagram (right) of a Step Function using Laser Sensor as Feedback Measurement for 100 MPa Pre-Stressed SMA Wires .....	129
Figure 138: Adaptive Nozzle Joint as an Opposing Actuator System.....	131
Figure 139: Alignment of Nozzle [ $\delta_1, \delta_2, \delta_3$ ] Coordinate System with Camera [ $x, y$ ] Coordinate System .....	132
Figure 140: Alignment of Camera and Nozzle Coordinate Frame Pre-Alignment (left), Aligned (middle) and Tested (right).....	133
Figure 141: Superposition of Nozzle Deflections in $\delta_1$ and $\delta_2$ Directions.....	133
Figure 142: Calibration (left) and Characterization (right) Resistance vs. Nozzle Deflection Plot for Power Cycled between 0-0.25 W .....	136
Figure 143: Stress, Strain, and Resistance Behavior for Idealized Single-Crystal (left) and Poly-Crystal (right) SMA Wire.....	137

Figure 144: Typical Resistance-Deformation Plot with Minimum Power Limit of 0.05 W.....	138
Figure 145: Coupled SMA-Spring Diagram .....	139
Figure 146: Diagram of Shifting R- $\delta$ Characteristics as a Result of Increasing Force .....	140
Figure 147: Plot Showing How Sensitivity Matrix Coefficients are Determined Based on Coupled Mapping Coefficients.....	141
Figure 148: Mapping and Controller Performance to Mercedes Star (top) and Circle (bottom) Command Trajectories using Uncoupled R- $\delta$ Mapping.....	142
Figure 149: Mapping and Controller Performance to Mercedes Star (left) and Circle (right) Command Trajectories using Coupled R- $\delta$ Mapping Concept .....	143
Figure 150: Tensile Test Setup Diagram.....	153
Figure 151: Tensile Test Setup Photo .....	154
Figure 152: Close-up of Clamps and Adhesive .....	154
Figure 153: Microscopic view of adhesive drop and SMA Wire in trough .....	154
Figure 154: Model of removable insert.....	154
Figure 155: Materials used when cleaning residue from a SMA wire .....	155
Figure 156: Photo of Removable Insert Prepared with SuperGlue Sample .....	157
Figure 157: Constant Current Pre-straining Inputs and Wire Stress .....	158
Figure 158: Constant Current Experiment Inputs and Measured Wire Stress .....	158
Figure 159: Test 2 pre-straining inputs and wire stress.....	159
Figure 160: Test 2 inputs and measured wire stress.....	159
Figure 161: Transient Behavior of Constant Displacement Test .....	160
Figure 162: Close-up of Transient Behavior.....	160
Figure 163: Nanotool UV-Cured Ceramic Resin .....	161
Figure 164: JB Weld Epoxy .....	161
Figure 165: Loctite Superglue.....	161
Figure 166: Loctite E40-HT High Temperature Epoxy.....	161
Figure 167: Loctite 1-Min Epoxy.....	162
Figure 168: SEC-1233 Conductive Epoxy.....	162
Figure 169: Comparison of Average Shear Stress at Failure of Unwashed, Test 2 Adhesive Samples .....	162

# Introduction



# I. Motivation

With space and resources becoming more coveted, engineers in many fields have been pushed to develop novel, space and energy conserving solutions. For example, automotive and aerospace engineers are looking for lightweight replacements to the motor and gear driven mechanisms currently used in automobiles, airplanes, and space craft. Meanwhile, biomedical device companies want to improve surgical success and recovery outlooks by taking highly-maneuverable, non-invasive surgical tools inside the human body through small openings in the skin.

At the same time as demand for miniaturization is increasing, the evolution of computers, electronics, and embedded systems have led to mounting expectations of customizability, adaptability, and precise automated control. These challenges have motivated the discovery and development of “active” or “smart” materials, such as piezo-ceramics (i.e. PZT), magneto-rheological fluids (MRFs), electro-active polymers (EAPs), and shape memory alloys (SMAs). Active materials can change their properties in response to stimuli such as a remotely applied magnetic or electric field, or a change in temperature. Engineers can exploit these changes in properties to produce a useable force or measurement quantity. In this way, an active material can be used as an actuator or a sensor, or in some cases both at the same time. Streamlined smart sensors and actuators can replace the bulky gears, ligatures, and coils that are required to convert the work done by conventional electric rotary or linear motors into a useable mechanical action. The elimination of these components results in a significant weight and space savings, and it reduces the number of moving parts that are prone to failure.

Moreover, many smart materials have very high energy and power densities, enabling them to efficiently convert electrical energy or power into mechanical work. Electromechanical actuators such as solenoids and motors waste energy due to effects such as fringe and resistive losses. Therefore active materials can offer significant cost savings, not only in terms of space and weight reduction, but also in terms of maximum attainable efficiency as defined by the power density.

## i. Shape Memory Alloys

Thermally-activated SMAs have the highest known power density of any known actuator system. This means they produce the most mechanical work output for every Watt of heating power put in. SMA material undergoes a strain change of up to 8% in response to a temperature-induced phase change. Figure 1 shows a conceptualization of how the crystal lattice structure of SMA changes in response to heating, cooling, and stressing. The phase change between the high-temperature austenite (A) phase, the low-temperature martensite twin ( $M^+$ /  $M^-$ ) phase, and the tensile-stress-induced martensite plus ( $M^+$ ) phase is responsible for the unique shape memory behavior of SMAs. SMA can also exist in the compressive-stress-induced martensite minus ( $M^-$ ) phase, but it is omitted from the diagram in Figure 1.

The most common thermally-activated SMA is the Nickel-Titanium alloy Nitinol. Nitinol can be molded into any shape and processed to change phase at below ambient temperature, in the case of a

super-elastic SMA, or above ambient temperature, in the case of an SMA actuator. SMA actuators can also be drawn into a thin wire (i.e.  $< 100 \mu\text{m}$  diameter) that can be heated by a controlled electric current or power input while its electrical resistance is simultaneously monitored for sensing purposes. Thanks to work by companies such as Dynalloy, Inc. [1], manufacturing processes have improved so that Nitinol actuator wires can be produced with consistent physical properties, including phase transition temperature and maximum transformation strain. It is because of these advances and the untapped potential for novel application that thermally-actuated Nitinol shape memory alloy actuator wires are the focus of this work.

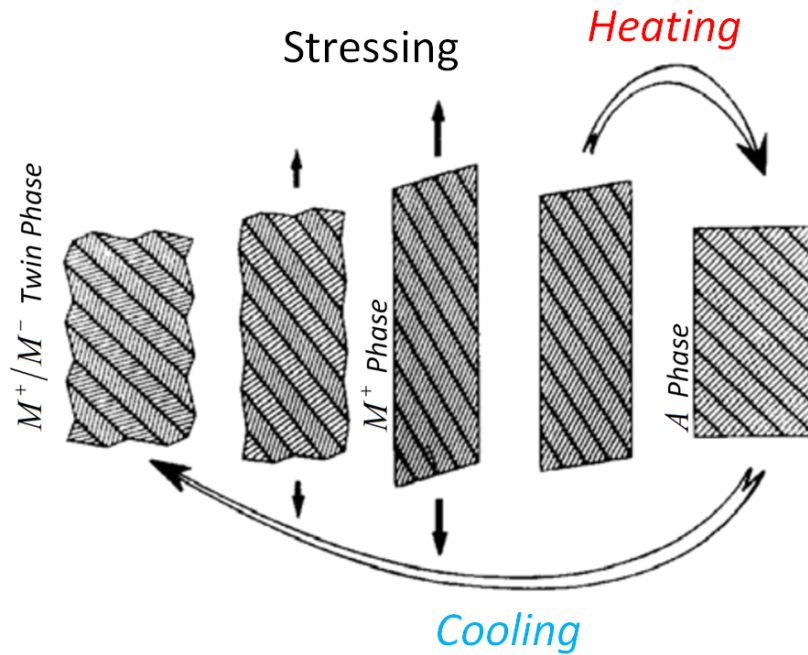


Figure 1: Diagram of Shape Memory Alloy Phase Change in Response to Heating, Cooling, and Stressing

## ii. Challenges of Working with SMAs

Though there are many potential benefits to SMA actuator wires, a number of practical challenges have delayed widespread implementation of SMA actuator wires in applications. First, the strain change (actuation) of the SMA material involves a phase change with intrinsic energy loss due to latent heat. As a result, repeated actuation is not conservative and the material characteristics are non-linear and hysteretic. Also, small wires have little thermal mass and are susceptible to coupled thermo-mechanical interaction with any part of the surrounding structure that they touch. In most cases, the structure acts as a heat sink, causing inhomogeneity in the temperature and thus phase fraction distribution within the wire. Both of these issues complicate the kinematics of an embedded SMA actuator design problem.

The next challenge arises from the practicality of fabrication. It is difficult to make reliable electrical and mechanical junctions between a hair-thin SMA wire and a structure. Large clamp or crimp mechanisms add bulk and defeat the purpose of using the wire in the first place. Also, it is difficult to make a bond with Nitinol by welding or soldering, and exposing the wire to such high temperatures can alter the properties of the material by effectively applying another heat treatment. Many common

adhesives soften or dissociate when exposed to elevated temperatures during actuation. Furthermore, creating a secure electrical bond is especially difficult because the local stress and strain at each point in the wire changes during actuation. A reliable electrical connection with constant contact pressure and contact resistance is critical so that the sensor measurements and heating power are consistent.

### **iii. Current SMA Applications**

Although the practical challenges of working with these complex hysteretic materials have delayed widespread application, shape memory alloy actuators have managed to find their way into a number of applications. Currently, SMA actuators have been particularly successful in biomedical, MEMS, and aerospace fields [2]-[27]. Nitinol SMA actuators are of interest in the biomedical field because the constitutive elements of Nitinol, Nickel and Titanium, are both biocompatible and corrosive resistant. However, passive super-elastic SMAs are used more commonly than SMA actuators, particularly in stents [2], because the passive elements do not require Joule heating. The small, streamlined profile of SMA actuator wires has made them attractive for non-intrusive surgical techniques, such as cardiac ablation [3], where the SMA actuator wires can be used to steer a robotic catheter in-vivo [4]. Active SMA materials have also been proposed for use in heart valves [5] or microvalves [7].

The aerospace industry and MEMS field have found use for SMA actuator systems as well, in large part because of their high force-output to mass ratio and miniaturizability. For example, SMA material is employed to actuate a variable area chevron to improve the efficiency of jet outlets [6],[8] or for in-flight tracking of helicopter rotor blades that require light-weight but high force actuator [9]. In the case of the variable geometry chevron, the actuators are actuated by the change in flow temperature of the exhaust effectively serving as temperature sensor and compensation actuator simultaneously. The MEMS field has many applications using SMA thin films [10],[11], but some researchers have also proposed integrating SMA wires to silicon wafers [12]. Similarly, the small profile of SMA makes them ideal for microactuators [13],[14].

Also, SMA actuator wires are enticing analogs for biological muscle fibers. As a result, SMA wires are proposed as “metal muscles” for a replica finger mechanism [15], hand [16], fish [17], or earthworm [18]. Further, natural interaction of the biological joint muscle inspires configurations of SMA actuators wires and structural joint material, and the associated kinematics.

The two applications used as case studies for embedded SMA actuator wire design, fabrication, and control in this work are an adaptive Smart Inhaler nozzle with SMA-actuated joints and a biologically-inspired micro air vehicle that is based on the flapping flight of a bat and uses SMA wires as metal muscles to rotate joints [22]. These applications are introduced in more detail the following sections.

### **iv. Adaptive Smart Inhaler Nozzle**

The “Smart Inhaler” concept was first developed at NC State University in 2004 by Seelecke and Klienstruer [19],[20]. The adaptive nozzle required for the Smart Inhaler is used throughout this work

as a case study of design, fabrication, and multifunctional sensing and controls methods. A Smart Inhaler, shown in Figure 2, is designed to provide targeted drug delivery to a certain location within the pulmonary system. Some ailments such as a cancerous tumor may affect only a small portion of the lungs and require toxic medications to be treated, so it is desirable to medicate the affected regions only. Unfortunately, medication in aerosol form that is delivered via a traditional inhaler is deposited all throughout the mouth, voice box, trachea, and both lungs. The Smart Inhaler is designed to reduce the unwanted deposition by positioning the medication stream at a controlled location within a benign bulk flow. Computational fluid dynamics (CFD) analysis suggests that the particles deposited on a certain location in the pulmonary system emanate from a predictable location in the flow inhaled at the mouth, and experimental tests verify that the deposition can indeed be controlled through the mouth, trachea, and several bifurcations of the lungs [21].

The Smart Inhaler requires an integrated design, with actuator and sensor embedded into the structure. In order for the medication deposition location to be predictable and repeatable, the inhaled stream must remain laminar. The model on the left of Figure 2 depicts a carrier airstream (yellow) and the medication stream (red) in aerosol form dispensed through an adaptive nozzle. The nozzle component used to position the medication within the bulk flow cannot be so obstructive as to induce turbulence. It also must be adaptable enough to control the location and trajectory of the medication stream. Such adaptability requires two flexible joints in series that can be deflected in any direction, each using at least three SMA actuators [19]. The center and right panels of Figure 2 show the top joint of an adaptive nozzle actuated by three SMA actuator wires. The 6 total SMA wires are designed to be used simultaneously as actuators through exploitation of the shape memory effect and position feedback sensors through measurement of the resistance across the SMA wire that varies with strain. They could also provide information on flow rate by carefully tracking the control input power required to hold the nozzle in a certain position during convective cooling.

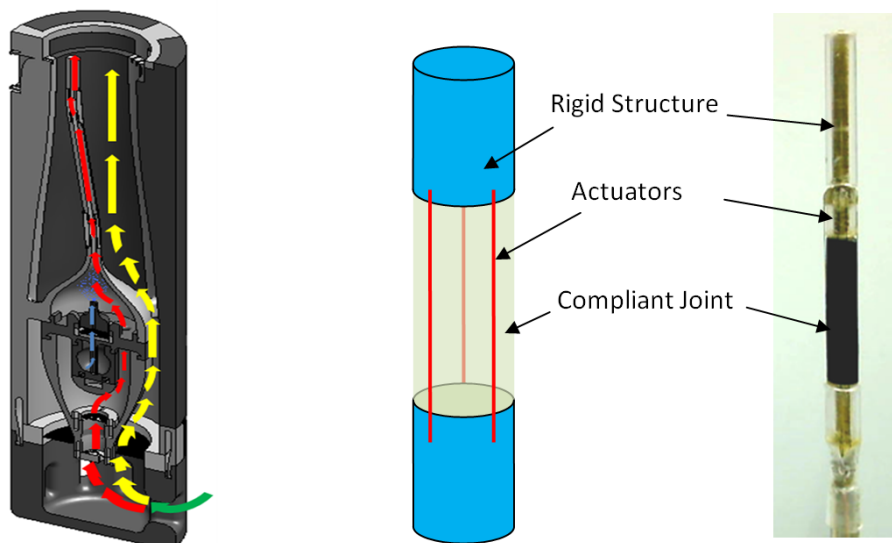


Figure 2: Diagram of Smart Inhaler (left) and Flexible Top Joint (middle) and Picture of Flexible Top Joint (right)

Figure 3 shows both joints of the adaptive nozzle deflected into various configurations. The process used for assembly of a two-joint Smart Inhaler nozzle with 6 actuators is summarized in later sections. The assembly process is carefully controlled to ensure that all 6 actuators have identical pre-stress and treatment history so that they will behave similarly. In addition, a method is presented for controlling the nozzle tip position with a closed-loop algorithm using the SMA wire for both actuation and measurement of tip displacement [28]-[30].



Figure 3: Dual-Joint Smart Inhaler Nozzle

## v. Bio-Inspired Application

SMA wires also lend themselves naturally to bio-inspired applications because their behavior is, in many ways, similar to that of biological muscles. One such application concept is a bio-inspired micro-air-vehicle (MAV) that is based on the biology and flapping flight of a bat [22],[23]. Although many different platforms for MAVs have been explored, natural flyers such as the bat are ideally suited because of their compact size and excellent maneuverability stemming from the fact that their wings are essentially reconfigurable wing structures, with multiple-DOF joints at the shoulder, elbow and wrist. The natural flyers also inspire a light-weight, energy efficient means of generating flapping power. Natural flyers generate their power and adjust their aerodynamic control surfaces using muscles. Most mechanical flyers rely on a large rotary motor that turns a propeller or turbine to deliver thrust to a fixed wing. The aerodynamic surfaces are then controlled separately by additional motors coupled with a large gear or ligature to distribute the control power. Along the same lines, a natural flyer's flexible joints are comprised of rigid bone structures connected by flexible ligaments and separated by low-friction cartilage that is constantly lubricated. In traditional mechanical ligatures, connections are made by hinges or ball screw joints that are often heavy and require constant maintenance. Bats in particular are chosen as a flapping flight platform because of their exceptionally large wingspan to body weight ratio and the resulting low wing-beat frequency that falls within the actuation frequency range of small SMA wires [23].

Instead of using traditional mechanical joints and motors, it is possible to mimic a biological joint by using flexures made from super-elastic SMA ribbons fixed to a rigid “bone” structure. These super-elastic joints are essentially frictionless, and it is not necessary to keep them clean or lubricated. Also, motors can be replaced by SMA actuator wires that can be stretched across the joints like muscles and tendons, only they contract in response to a heating current.

These biologically inspired solutions are implemented in the bat exhibit at the Nature Research Center at the North Carolina Museum of Science in Raleigh, NC. The bats in the exhibit each have independently controlled shoulder and elbow joints made from super-elastic SMAs and muscles made from SMA actuator wires, as shown in Figure 4. The design, assembly, and control methods are presented as a case study in this dissertation.

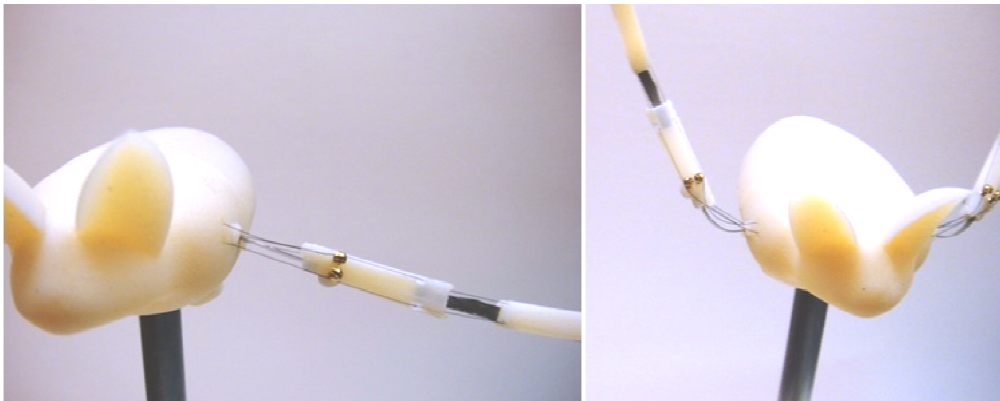


Figure 4: Biologically Inspired SMA-Actuated Bat

## II. Objectives

While the motivations for and applications of SMA actuators are nearly endless, the practical design, fabrication, and control challenges still stand in the way of widespread commercial use. The objectives of this dissertation are to facilitate proliferation by providing a roadmap of design and fabrication, and to outline multifunctional sensing and control techniques for one type of SMA actuator—small, thermally actuated Nitinol wires. These techniques are presented in two parts.

Part 1 details the process that can be used to design with non-linear hysteretic SMA wires. Part 1 also discusses some of the different fabrication processes used for small SMA wires, including adhesives and Teflon tube wire guides, and presents two design and fabrication case studies – the adaptive nozzle and robotic bat.

Part 2 focuses on developing the understanding necessary to use SMA wires simultaneously as a controllable actuator and a viable sensor. Simplified analog SMA-spring systems are studied in-depth alongside the physics-based Seelecke-Mueller-Achenbach model [30],[32] so that the physical mechanisms behind different performance characteristics can be identified. Then sensor mapping and control schemes are developed and applied first to simplified SMA-spring setups and finally to the more complex geometry of the adaptive Smart Inhaler nozzle.

# Part 1: Design and Fabrication Methods for Embedded SMA Systems



## 1.1 Design of Embedded SMA Systems

Embedded SMA actuator wires can offer the solution to many novel applications that are otherwise impractical or unrealizable. Further, SMA wires enable new engineering solutions to traditional design problems, and in the long run they can reduce costs by saving space and offering excellent energy efficiency. It is worth the extra up-front effort to learn the design process and fabrication considerations required for SMA-based solutions so that these benefits can be exploited. Passive SMA actuator springs and flexures have a niche in compensating for environmental temperature change, where the change in ambient temperature triggers some actuation. However, the focus of this work is on SMA wires that are actively heated by a controlled Joule heating power and passively cooled by a thermal environment that may or may not be stable.

The ultimate goal of any design problem is to meet a set of performance objectives subject to constraints defined by the application and the available materials, and the same is true for design of micro-SMA systems. For example, in the case of an SMA actuator embedded within a structure, it might be desirable to instigate a certain structural deformation angle without exposing the SMA wire to stresses greater than its yield stress. The relationship between the objectives and constraints is defined by the kinematics and force balance of the coupled SMA-structure system. The kinematics are dependent on variables such as the SMA wire attachment points and the bending modes of the structure, while the force balance also includes variables such as the diameter of the SMA wire and the stiffness of the structure. In the case of thermally-actuated SMA wires, both the kinematics and force balance problems are subject to coupling with the thermal field.

Given enough design and engineering work, SMA wire actuators could be used in almost any application. However, the low bandwidth of the heating and cooling processes makes SMA wires less suitable for some applications than others. In order for an actuation cycle to be repeated, the SMA wire must be heated and then cooled. This can be done arbitrarily quickly as long as heating power is high enough and the cooling can be achieved quickly enough. However, knowledge of the interaction between an embedded SMA and a structure is needed to determine the feasibility of an SMA based solution, then begin the process of design.

### 1.1.1 SMA-Structure Interaction

For applications with SMA actuator wires, a special understanding of the hysteretic characteristics of SMA is required because the hysteresis affects both the kinematics and the force balance problem. For an SMA wire to be implemented as an actuator, a restoring force is needed to enable repeated actuation. This restoring force may, for example, be provided by structural elements that flex when the wire is actuated (contracted) but then act as a spring to lengthen the SMA wire as it cools. For this analysis, the structural element is approximated as a pre-stretched linear bias spring. The analog actuator system showing such a spring in series with an SMA wire is shown in Figure 5.

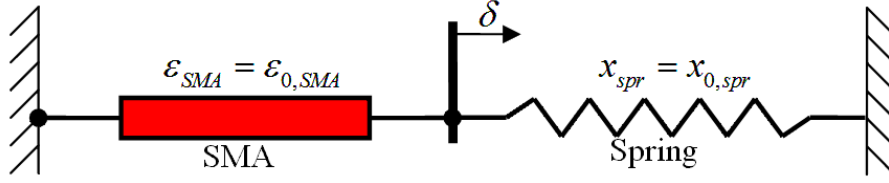


Figure 5: Generalization of an Embedded SMA Actuator - Structure System with a Pre-stretched Spring at Equilibrium

The position of the connection point between the SMA wire and the spring can move by  $\delta$ , as labeled in Figure 5, depending on the state of contraction of the SMA. However, a contraction of the SMA necessitates an elongation of the spring, and vice-versa. For the system in Figure 5 at static equilibrium, equation (1.1) shows how the strain of the SMA wire,  $\epsilon_{SMA}$  as referenced from its shortest possible austenitic free length, relates to  $\delta$  and to the initial equilibrium strain in the SMA,  $\epsilon_{0\_SMA}$ . Equation (1.2) shows how the stretch in the spring,  $x_{spr}$ , relates to  $\delta$  and the initial stretch of the spring at the equilibrium shown in Figure 5,  $x_{0\_spr}$ .

$$\epsilon_{SMA} = \frac{\delta}{L_{SMA}} + \epsilon_{0\_SMA} \quad (1.1)$$

$$x_{spr} = -\delta + x_{0\_spr} \quad (1.2)$$

The equilibrium force and position of the junction can be easily seen if the spring and SMA characteristics are plotted on the same set of axes. To do this, the common variable between equations (1.1) and (1.2),  $\delta$ , is used to find  $x_{spr}$  as a function of  $\epsilon_{SMA}$ :

$$x_{spr} = L_{SMA} (\epsilon_{0\_SMA} - \epsilon_{SMA}) + x_{0\_spr} \quad (1.3)$$

Figure 6 shows a simplification of the stress-strain diagram for a single-crystal SMA and a spring characteristic plotted on the same set of axes. Based on equation (1.3), the spring characteristic must be inverted, scaled and undergo a translation, as shown in the right panel.

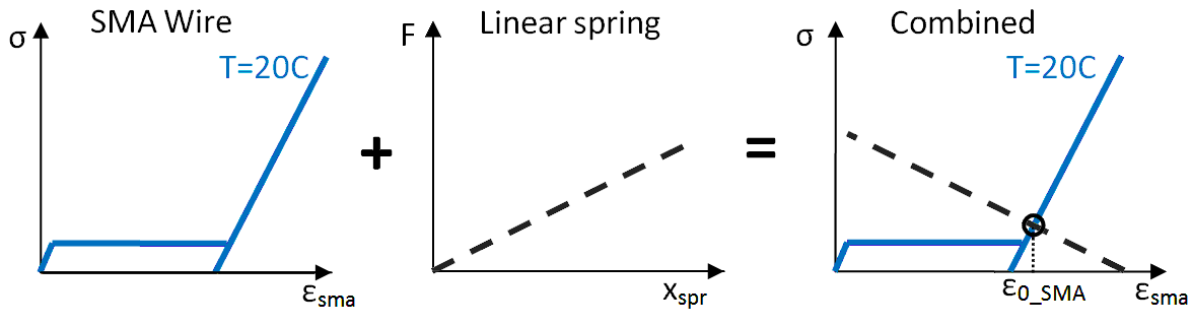


Figure 6: Load-Displacement Characteristics of Martensitic SMA Wire and Linear Spring on the Same Set of Axes

When an SMA wire is heated, its stress-strain characteristic changes due to the change in phase of the constitutive grains of the alloy. The hysteresis loop rises, causing a change in the equilibrium position as shown in Figure 7. Initially, in panel A, the cool wire is stressed to the tensile-preferred martensite

( $M^+$ ) line where it reaches an equilibrium that is indicated by the circle. Note that the  $M^+$  line intersects the strain axis at the maximum transformation strain labeled  $\varepsilon_T$  in panel A. As the temperature is increased in panel B, the equilibrium will be satisfied on the  $M^+$  line until it is forced to follow the bottom branch of the hysteresis loop as phase transformation begins. The equilibrium point will follow this bottom plateau through T2 in panel C until the wire is totally transformed to austenite ( $A$ ) in panel D. From this point, additional heating does not lead to additional phase or strain change.

On thermal unloading, the equilibrium is maintained on the austenite line until the top branch of the hysteresis loop sweeps through, forcing the wire to begin its transformation back to the  $M^+$  phase. Once the wire cools to  $T_0$  again, there is only 1 possible equilibrium on the  $M^+$  line, and additional cooling will not cause any additional elongation.

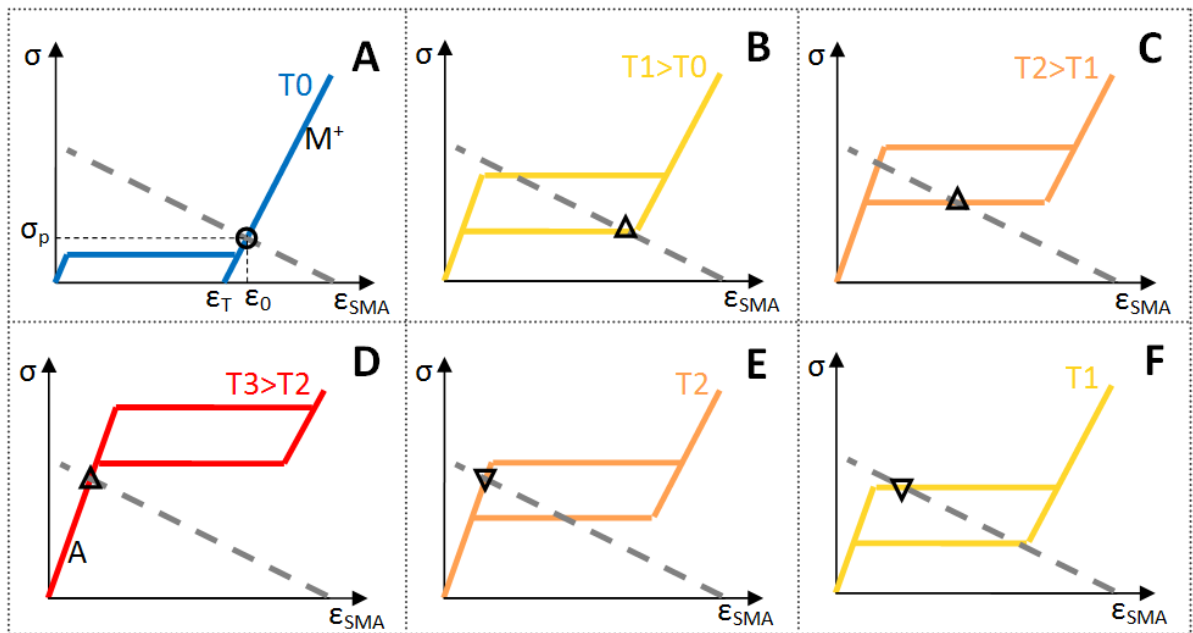


Figure 7: Stress-Strain Equilibrium between Perfect Single Crystal SMA and Spring during Thermal Loading and Unloading Cycle

In this case, the stress-strain (load-displacement) behavior is linear and non-hysteretic because it is constrained by the linear spring. However, the temperature-strain plot in Figure 8 reveals the hysteretic influence of the SMA material. The equilibrium points in Figure 7 are reproduced in Figure 8, where the total stroke of the actuator is indicated by the line labeled  $\Delta\varepsilon$ . The existence of this hysteresis loop leads to a significant difference in the strain (and stress) between panels C and E, and analogously between panels B and F.

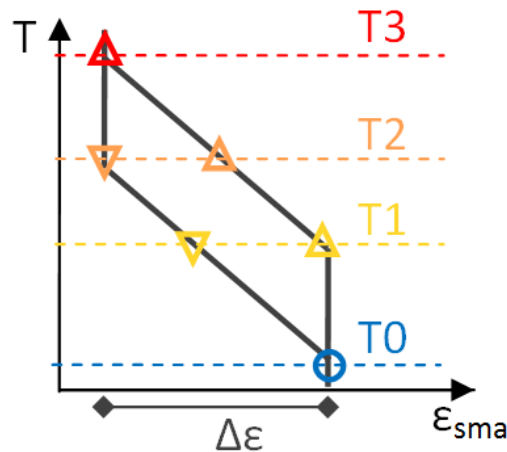


Figure 8: Temperature-Strain Characteristic of SMA-Spring Actuator System

Figure 9 shows how changing the stiffness of the structure (i.e. spring) changes the stroke and stress in the actuator system. For a stiff spring, shown in panel k1, a large stress is generated by the heating process from temperatures T1 to T3. The softer spring, depicted in panel k2, does not generate as high of a stress in the SMA wire. As a result the softer spring, k2, generates slightly more strain change because the stress at the high temperature equilibrium,  $\sigma_2$ , does not induce as much elastic strain up the austenite line as  $\sigma_1$  in panel k1. Also note that with the soft spring complete actuation could have been achieved at a much lower temperature, and that the pre-stretch in the spring would have to be much greater to generate the same pre-stress,  $\sigma_0$ . The limit of a soft spring is a hanging mass, depicted in the  $k=0$  panel. With a mass hanging from an SMA wire, the stress in the SMA is always constant, constrained by the weight of the mass. This case represents the limit of strain change for a given constant stress.

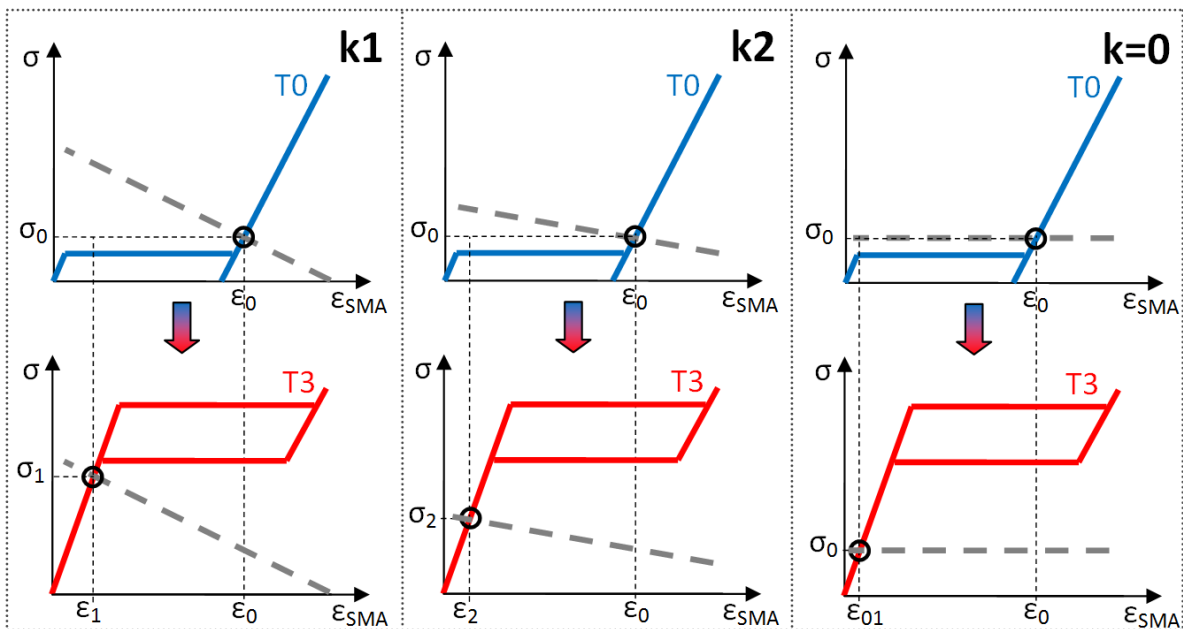


Figure 9: Effect of Spring (Structure) Stiffness on Stress-Strain Behavior of SMA Actuator System

Figure 9 shows that having a stiff structure requires more heating power and more force that induces more stress in the SMA wire. While this increases energy consumption and may reduce fatigue life,

some applications require more stiffness and the tradeoff is worthwhile. Also, this simplification represents a trivial, conservative system. In reality, it is impossible for any functional work to be done without some change in force from the “structure” and a resulting hysteresis in its load displacement characteristic, and higher forces do more work given a fixed stroke. Fortunately, SMA wires generally have higher force output than conventional actuator systems, and the force of the SMAs can easily be scaled up by either using bigger wires or multiple small wires in parallel.

It should also be noted that the SMA stress-strain curves in Figure 7 through Figure 9 depict the behavior of a perfect single crystal of SMA material. In reality, an SMA wire is composed of many crystals with slightly different properties and orientations, so the behavior observed at the attachment points between the SMA wire and the structure will represent the average behavior over the entire length of the wire. This averaging tends to smooth the stress-strain curve, as shown in the sample SMA characteristic in Figure 10 taken from experimental data of a real wire. The experimental plot also shows that the wire exhibits a “two-way” effect at low temperature that causes the wire to favor the  $M^+$  phase over the  $M^-$  phase when cooled under 0 stress. As a result, the cool wire remains slack until about 3% of strain.

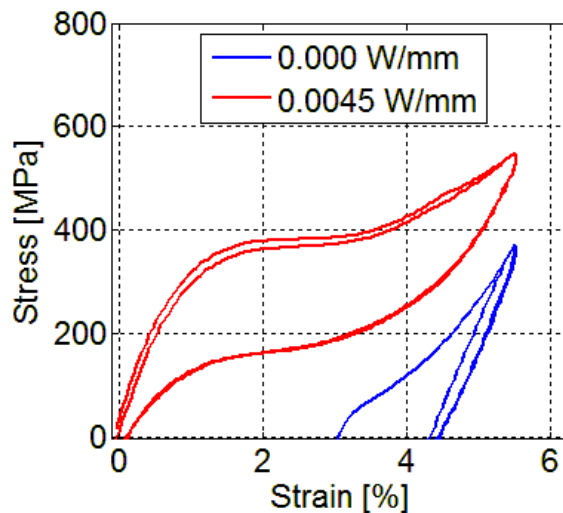


Figure 10: Stress vs. Strain Plot for 100  $\mu\text{m}$  Diameter Flexinol SMA Wire at Low and High Temperature

Other features of the experimental data are presented and discussed in detail in Appendix B and in Part 2. For example, the stress and temperature fields are not homogenous over the length of the wire, in large part because of the conductive cooling that occurs where the massive structure draws heat away from the tiny wires at the attachment points. The significant effect of this thermal inhomogeneity can be observed in Figure 10 but is fully documented with coupled thermo-mechanical FEA modeling and side-by-side experimental data in Appendix B. One of the results indicated by the simulations and experiments in Appendix B is that the actuator stroke is reduced because of incomplete phase transformation near the attachment points. In particular, for short SMA wires the stroke is reduced by up to 50% from heat loss near the wire ends.

Regardless of the behavioral complexities mentioned that are studied in greater detail in Appendix B as well as others discussed in Part 2, the basic understanding of kinematics garnered from the simplified pictures in Figure 7 through Figure 9 allow many of the design tradeoffs to be recognized and help motivate the steps required for a design process.

### 1.1.2 Steps in the Design Process

A systematic approach to the design process allows an engineer to not only check the feasibility of an SMA-based design but also to iterate through the process for the sake of design optimization. The basic steps of embedded SMA actuator design are to:

- 1) Define the **design objectives**, such as structural or actuator deformation.
- 2) Determine the **geometric constraints** based on the application. For example, answer the questions: “what should my final design look like, how big or small can it be, what does its profile look like, and what design variables can be changed?”
- 3) Develop a **kinematic relationship** between the SMA actuator wire length change and the structural deformations that are defined in the design objectives.
- 4) Establish the **force and moment balance** between the SMA and the structure by drawing a free body diagram of the attachment points and determining how much force will be needed to induce the required structural deformation or bending.
- 5) Identify the **material constraints**, such as limiting the maximum allowable SMA stress.
- 6) **Iterate** through the process, changing the design variables such as structural stiffness, SMA wire diameter and attachment points to meet objectives without violating constraints.

Concurrent to this whole process, it is also important to ask “can I build this?” Section 1.3 discusses many of the fabrication challenges that should be considered. As long as the design variables are limited such that they can be controlled during fabrication, the objectives and constraints can be used to formulate a design optimization problem and determine the best possible design for a given application.

### 1.1.3 Formulation of a Design Optimization Problem

A typical design constrained optimization problem consists of a set of design variables,  $\vec{x}$ , an objective function that dependent on those design variables,  $F(\vec{x})$ , and inequality,  $g_i(\vec{x})$ , or equality,  $h_j(\vec{x})$ , constraints that must be maintained while the objective function is minimized. An optimization algorithm is responsible for changing the design variables such that the objective function is minimized without the constraints being violated. In general, a single-objective constrained optimization problem is formed as

$$\begin{aligned}
 \min \quad & F(\vec{x}) \\
 \text{subject to} \quad & g_i(\vec{x}) \leq 0 \quad i = 1..n \\
 & h_j(\vec{x}) = 0 \quad j = 1..m
 \end{aligned} \tag{1.4}$$

This formulation of an optimization problem can be solved by many different types of optimization algorithms, such as a grid search, steepest decent method, or genetic algorithm [34]. Also, the objective function (or functions, in the case of a multi-objective problem) can be evaluated using a variety of different tools ranging from simple analytic expressions to fully-coupled multi-physics finite element simulations. A detailed example of design optimization of a SMA-actuated robotic catheter including comparison of different algorithms and multi-objective studies is presented by Crews [4], where the objective functions are solved using COMSOL Multiphysics simulation software (COMSOL, Inc., Burlington, MA) with a coupled physics-based SMA material model [31]. Similarly, work presented by Kohl uses computer aided optimization coupled with FEM simulations to optimize stress profiles in SMA microactuators [13],[14]. However, the goal of the embedded SMA-based design and optimization problem to be discussed in this dissertation is to demonstrate the process. Therefore, the single objective will be to maximize structural deformation, the objective function will be derived from a simplified kinematic model, and first-order errors are accepted. Meanwhile, the geometric and material limits will be presented as constraints, and other potential objectives such as structural stiffness or heating power costs will be ignored.



## 1.2 Case Studies of SMA-Based Design and Optimization Process: Adaptive Nozzle and Bio-Inspired Joint Applications

The sections below present an overview of two applications – an adaptive Smart Inhaler nozzle and a bio-inspired bat wing – and the design objectives and process used for each. A kinematic model of joint bending that applies to both applications is presented along with a parametric study showing how different geometric parameters affect joint bending. Then a force model is developed for the bio-inspired wing joint and used along with the kinematics model in a sample constrained optimization problem.

### 1.2.1 Adaptive Inhaler Nozzle Application Overview and Design Objectives

The Smart Inhaler nozzle introduced in section I.iv needs to be able to control the release position and trajectory of the medication that flows out from the tip of the nozzle. The adaptive nozzle utilizes two compliant joints, each actuated by three SMA wires oriented in a Mercedes star that enable both joints to be rotated in an arbitrary direction independently, as shown in Figure 3. Since the geometry of both joints is the same, only one is considered for the design problem. Figure 11 shows a diagram of a joint with 3 SMA actuators wires on the left and the effect of actuating one wire on the right. The joint on the left can be rotated to any  $(x,z)$  position by inducing different levels of contraction in one or two actuators at a time. The motion of the tip based on super-position of displacement in two of the actuation directions is discussed in detail in section 2.2.3. However, for this initial design process the effect of one actuator wire is isolated as shown in the right of Figure 11. Also, for this discussion the effects of the force from opposing SMA wires are ignored.

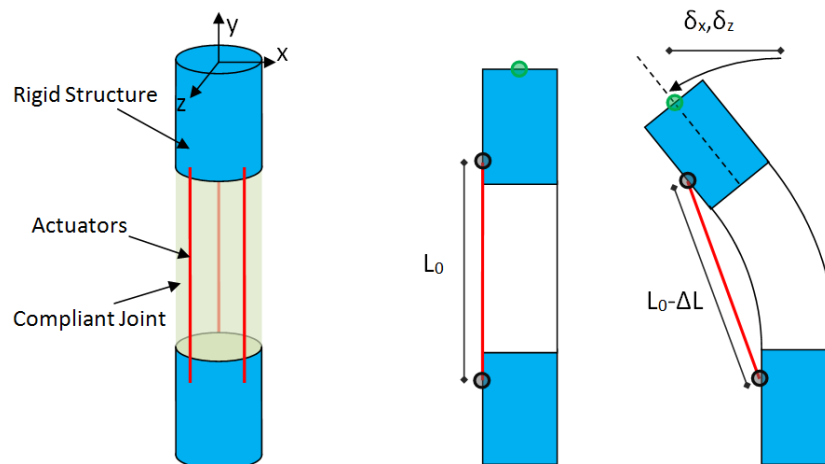


Figure 11: Diagram of Adaptive Smart Inhaler Nozzle Joint

The biggest design challenge with the adaptive nozzle is to keep everything streamlined. The objective of the Smart Inhaler is to position medication within an inhaled air stream. In principle, the location of that release position dictates where in the lung system the medication is deposited, so long as the inhaled air flow remains laminar [20]. Therefore, the adaptive nozzle must be streamlined such

that is does not include any protrusions that will disrupt the airflow. This design objective constrains the geometry significantly. The compliant joint material is a Viton rubber tube with the same outer diameter (1/8") as the rigid structure, that is composed of layered brass and nylon tubing, as will be described in section 1.3.2.1. Because of the necessity for a streamlined geometry, the SMA wire attachment points are constrained to locations directly on the surface of the tubing, and SMA to structure and to lead-wire attachment features cannot extend out into the airflow. However, there is some flexibility in the length of the rubber joint and the total length of the SMA wire. Since a bending angle of about 15 degrees is needed to induce the desired tip displacement, a kinematic model is needed to estimate how much bending can be expected based on the SMA length and attachment position. Since the form of the joint bending kinematic model is identical to the model needed to describe the bio-inspired wing joint, it is derive in a general sense in section 1.2.3.

### 1.2.2 Bio-Inspired Wing Application Overview and Design Objectives

A second embedded SMA application is an SMA-actuated bat for an exhibit at the Nature Research Center at the North Carolina Museum of Natural Science. The biologically-inspired concept, described in section I.v, is based on the BATMAV project started by Bunget and Seelecke [22],[23]. The main goal is to generate a platform that replicates the kinematics of a bat's natural flapping motion. While the bat's wing has many degrees of freedom, Bunget showed that most of the flap motion features can be captured by a simplified 2-degree-of-freedom wing with a flexible shoulder and elbow joint [22]. These joints must each be capable of a rotation of 80 degrees. For the case of an actual flying bat, wing-beat frequencies of up to 10 Hz are required; however, for the museum exhibit a flapping frequency of 0.3 Hz was ideal to demonstrate the motion in the still-air conditions of the exhibit. Figure 12 shows a museum exhibit bat with two functional elbow and two functional shoulder joints.

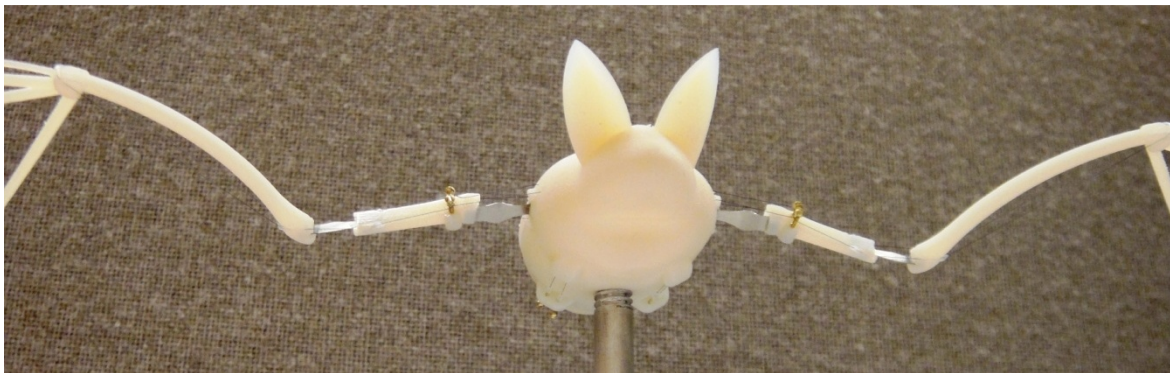


Figure 12: Museum Bat Prototype with Four Independent Joints

The design objectives for the bat were to develop a bone structure on the same scale as a *Plecotus auritus* species bat and include SMA actuator wires as effective “metal muscles” to induce rotation in the joints [23]. For the museum exhibit, the joints had to be small to match the scale of the bat without throwing off the aesthetics of the exhibit. Also, all 4 joints needed to be actuated independently for 100,000 cycles over the largest angular displacement range possible.

The bat bones are only  $\sim 3$  mm in diameter, so the joints needed to be very small. Also the desired actuation frequency required a SMA diameter of at most  $75 \mu\text{m}$ . Traditional joints with a hinge or ball screw mechanism inevitably introduce friction that is very significant on this small scale. Furthermore, an additional spring mechanism would be needed to provide a restoring force if a normal hinge were used. As a result of these limitations, a flexure joint was chosen. A flexure ribbon constrains the joint to rotation in 1 DOF, and has essentially no friction. A super-elastic SMA material is used to enable the large rotation angles needed without plastically deforming the joints. Super-elastic SMA can undergo a 5-7% strain without developing much stress because the material changes from the austenite to martensite phase. However, once sections of the joint are in the martensite phase, additional strain induces significant stress that will lead to failure over repeated cycles. In the case of a bending ribbon, strain, and thus stress, is highest on the top and bottom surfaces of the ribbon, so a super-elastic SMA ribbon  $75 \mu\text{m}$  thick was used for the joint. A rough estimate of the peak stress in the joint material is used as a design constraint.

### 1.2.3 Joint Bending Kinematics

The bat and nozzle joint structures are pictured in the left of Figure 13 and a simplification of the rigid structure, compliant joint, and SMA wire are shown to the right. This simplified diagram is used to constrain the geometry of the joint and formulate the kinematics of the joint rotation.

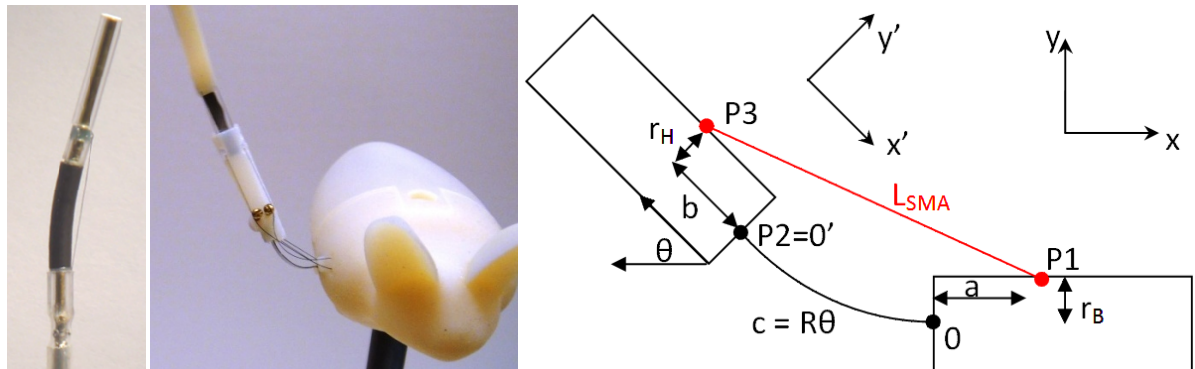


Figure 13: Picture of Deflected Nozzle and Bat Shoulder Joint with Simplified Kinematic Diagram

To solve the coupled geometry problem, two coordinate systems are defined. The fixed structure, namely the base of the nozzle or body of the bat, is located in the fixed  $(x, y)$  coordinate system (CS) with an origin at point  $O$  while the moving structure—nozzle tip or humerus of the bat—is on a moving CS  $(x', y')$  and has an origin at point  $P_2 = O'$ .

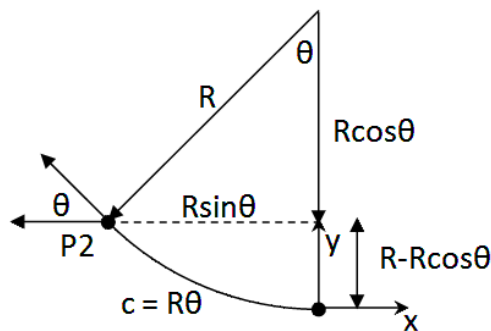


Figure 14: Sketch of Flexible Joint Simplified as a Uniform Arc

The joint, made from Viton rubber in the nozzle and super-elastic SMA in the bat, is assumed to be a uniform arc labeled  $c$  that is defined in Figure 14. This is a liberal assumption that neglects the variable moment induced by the SMA force, but the goal is to make a rough estimate of bending for the sake of explaining the design process. The location of the fixed structure attachment point of the SMA wire,  $P_1$  and the origin of the local CS,  $P_2$  are first in the global CS in equation (1.5) and (1.6).

$$P_1 = \langle a, r_B \rangle \quad (1.5)$$

$$P_2 = \langle -R \sin \theta, R(1 - \cos \theta) \rangle \quad (1.6)$$

Then the location of the attachment point of the SMA wire to the moving structure,  $P_3$  is written in the local CS in equation (1.7) before being transformed into the global CS via rotation transformation matrix  $T$  and translation  $P_2$  in equation (1.9).

$$P_3' = \langle -b, r_H \rangle \quad (1.7)$$

$$T = \begin{bmatrix} \cos \theta & -\sin \theta \\ \sin \theta & \cos \theta \end{bmatrix} \quad (1.8)$$

$$P_3 = P_2 + TP_3' \quad (1.9)$$

The contraction of the SMA wire stretching from  $P_1$  to  $P_3$  reduces the length of the SMA,  $L_{SMA}$ , to

$$L_{SMA} = L_{0A} (1 + \varepsilon_{SMA}) \quad (1.10)$$

where  $\varepsilon_{SMA}$  is the strain in the SMA, referenced from  $\varepsilon_{SMA} = 0$  when the wire is at its austenitic reference length,  $L_{0A}$ .

Once the points are located in the global CS and the length of the SMA is established, equations (1.11) and (1.12) are used to fully constrain the problem.  $R$  is the radius of curvature of the joint,  $\theta$  is the maximum bending angle, and  $L_{SMA}$  is the length of the SMA wire. The MATLAB 'solve' function is used to solve equation (1.12) for  $\theta$  then equation (1.11) for  $R$  given a set of input parameters,  $a$ ,  $b$ ,  $c$ ,  $r_B$ ,  $r_H$ ,  $\varepsilon_{SMA}$  and  $L_{0A}$ .

$$c = R\theta \quad (1.11)$$

$$L_{SMA} = |P_1 - P_3| \quad (1.12)$$

For this problem, it is assumed that there is no bending in the joint when the SMA is pre-strained to  $\varepsilon_{pre}$ , therefore

$$L_{0,A}(1 + \varepsilon_{pre}) = |P_1 - P_3|_{\theta=0}. \quad (1.13)$$

### 1.2.3.1 Parameter Study of SMA-Actuated Joint Kinematic Model

The kinematic bending model is used to determine the effect that several of the parameters have on max bending angle,  $\theta$ , and joint radius of curvature. The radius of curvature gives some indication of how much stress will be generated in the joint and accordingly how much force will be needed from the SMA wire, with more stress resulting from a tighter radius. The geometry in the parameter study is the same as defined in Figure 13. In all plots the austenitic free length of the SMA wire is set to  $L_{0,A} = 50$  mm, and the pre-strain is  $\varepsilon_{pre} = 0.04$  (4%). Figure 15 through Figure 18 show the effects of different parameter sweeps. In these figures, the rigid structure and joints are shown in shades of gray, while the SMA wire is plotted in red, with its attachment points on the fixed and moving structures plotted in red and green, respectively. Note that the SMA wire is assumed to be guided through the attachment points at the ends of the red wire line; its total length remains 50 mm for all cases shown.

Figure 15 shows the effect of simply contracting the SMA wire. Initially, the SMA is pre-strained to 4%, then reductions of strain cause the wire to contract inducing bending. Figure 15 shows that for 4% strain, there is no bending angle and an infinite radius of curvature, and that bending angle increases as SMA strain decreases, as expected.

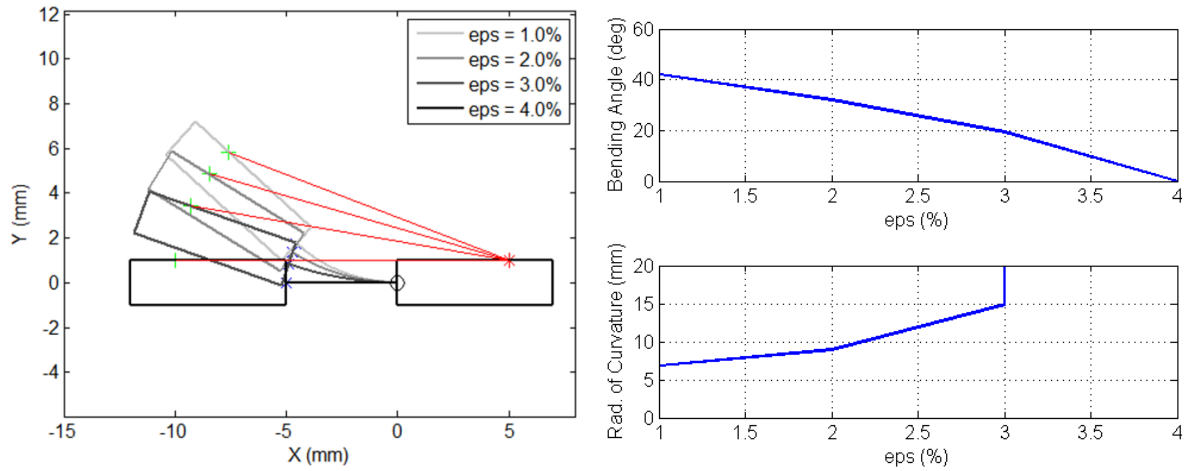


Figure 15: Effect of Changing SMA Strain on Bending Angle and Radius of Curvature

The effect of changing the location of the SMA attachment point is less intuitive. Figure 16 shows the joint with the axial attachment point on the rigid structure  $a$  set to 0, while the axial attachment point on the moving structure  $b$  changes. The highest bending is observed when the SMA wire is attached at  $b = 0$ , as close to the flexible joint as possible. Note that the total length of the SMA wire is maintained at 50 mm even as the attachment point is changed.

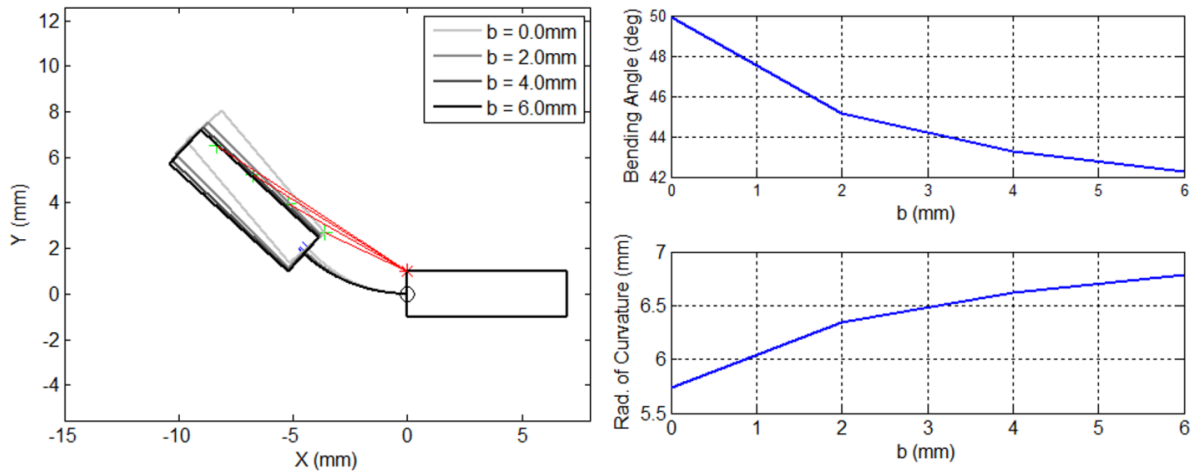


Figure 16: Effect of Changing Attachment Point 'b' on Bending Angle and Radius of Curvature

Figure 17 shows the effect of changing the length of the compliant joint  $c$ . The bending angle gets slightly higher when the joint is shortened; however, the small increase in bending angle is accompanied by a significant (~300%) reduction of the radius of curvature. This means that using a shorter joint will cause significantly higher SMA wire and joint stress with only a slight increase in bending angle.

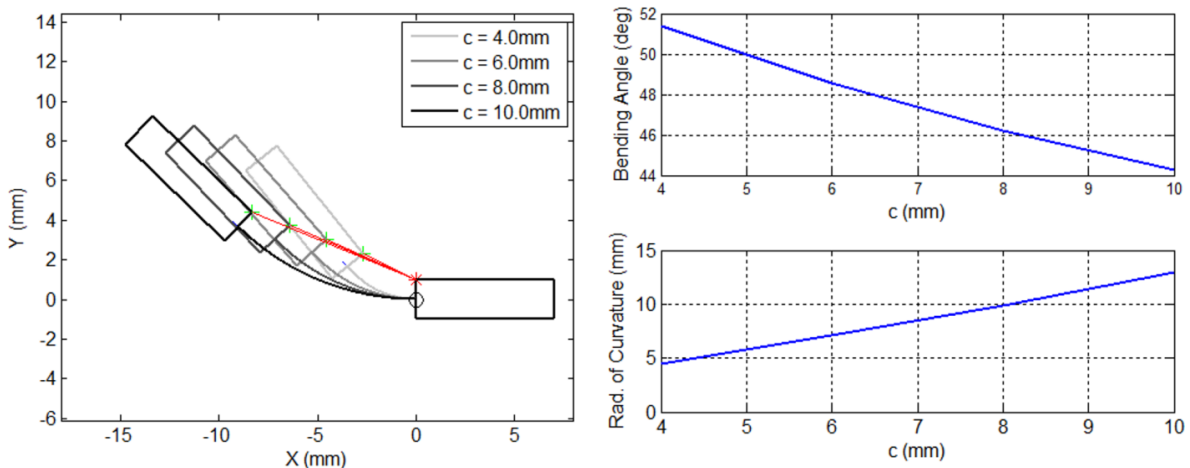


Figure 17: Effect of Changing Joint Length 'c' on Bending Angle and Radius of Curvature

The radial attachment point also has a very significant effect on bending, as shown in Figure 18. Reducing the radial attachment point on the moving structure from 1 to 0 mm causes bending angle to increase from 50 to 77 degrees.

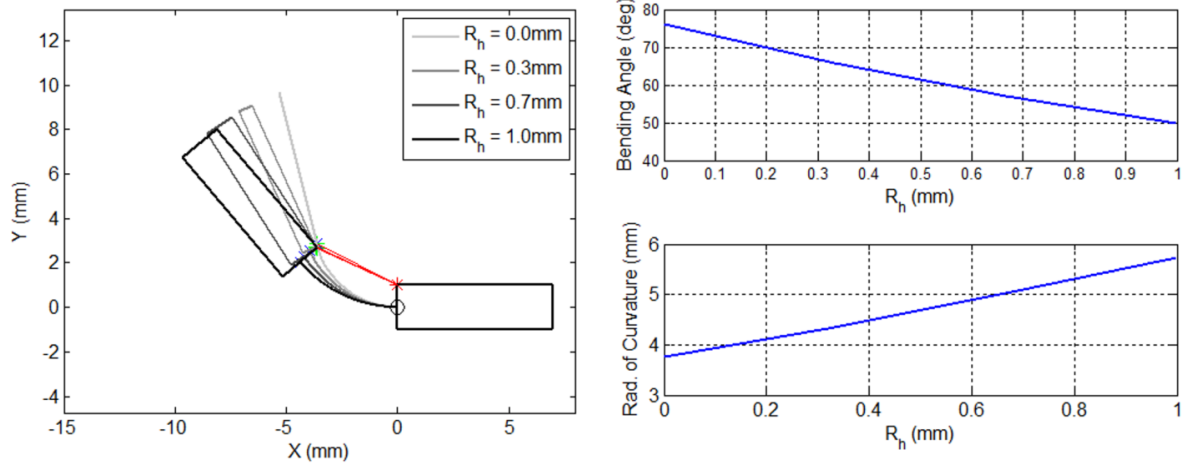


Figure 18: Effect of Changing Radial Attachment Point ' $r_H$ ' on Bending Angle and Radius of Curvature

The parametric study alone cannot be used to determine a fully optimal solution. However, the study does indicate that the highest bending comes from attaching the SMA wire as close to the flexible joint as possible, and maximizing the length change of the SMA wire during actuation. Also, Figure 17 indicates that reducing joint length also reduces the bending angle slightly, but a more detailed understanding of the force and moment balance discussed in section 1.2.4 is needed to determine whether the cost of added material stress is worthwhile.

### Smart Inhaler Nozzle Design Parameters

The lessons learned from this parameter study were employed in the assembly of the adaptive nozzle for the Smart Inhaler concept. The outer diameter of the nozzle is 3.2 mm, and the need to keep the nozzle streamlined constrained the radial attachment points to the surface of this outer tube, so  $r_B = r_H = 1.6$  mm. The other parameters are shown in Table 1, and the predicted bending response to an SMA wire contraction from 4% to 1% strain is plotted in Figure 19.

Table 1: Adaptive Smart Inhaler Geometric Parameters

Variable	Value	Description
$a$	0.5 mm	Body attachment point axial coordinate
$r_B$	1.6 mm	Body attachment point radial coordinate
$b$	4.0 mm	Humerus attachment point axial coordinate
$r_H$	1.6 mm	Humerus attachment point radial coordinate
$c$	15 mm	Length of super-elastic joint
$L_{0A}$	26 mm	Austenitic free length of SMA wire
$\varepsilon_{pre}$	0.04	Pre-strain of SMA wire

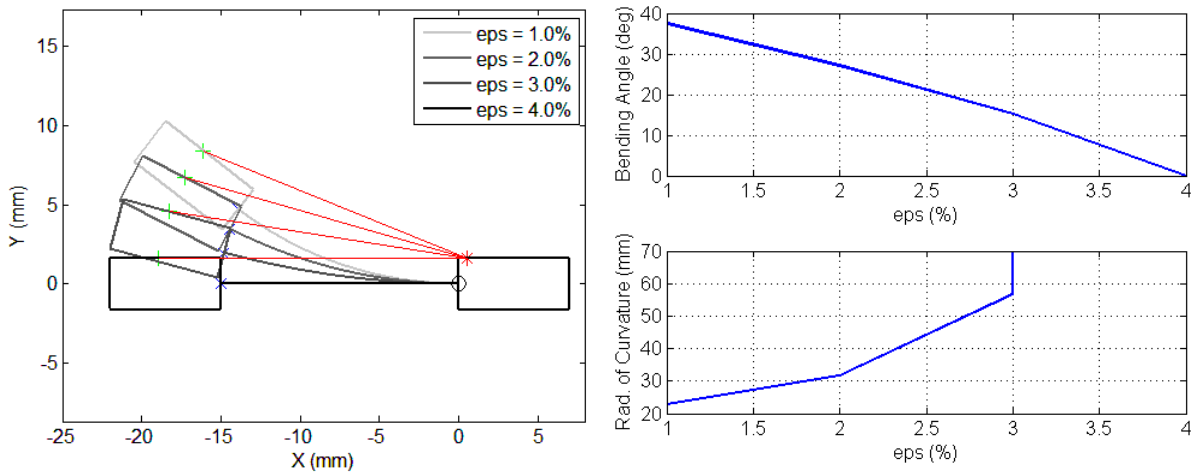


Figure 19: Predicted Bending of Adaptive Smart Inhaler Nozzle Joint Due to SMA Wire Contraction

While this prediction ignores the influence of the force balance, the joint material is chosen to be very soft so that it can easily be deformed by the pairs of 50  $\mu\text{m}$  diameter SMA wire. The functional nozzle was tested with the setup described in section 2.1.4.2 that uses a camera tracking system to measure the change in strain in the SMA wire and the deflection of the nozzle tip. In Figure 20, the measured strain in the three directions of a Smart Inhaler joint is plotted vs. the measured bending angle. Also, the kinematic model is applied to each value of measured SMA strain and the predicted bending angle is plotted in black.

Figure 20 shows that the measured strain vs. bending behavior is qualitatively similar to the prediction. However, the kinematic model predicts more bending than is measured. This is not surprising, considering the simplifications and assumptions made in modeling the compliant joint. The joint is modeled as a uniform arc with no axial compression, and the influence of the opposing SMA actuator wires are ignored. The opposing SMA wires increase the axial stress and thus axial compression of the joint. Therefore, some of the SMA contraction goes into shortening the joint, and less of the contraction is left to induce bending. In the future, the force and moment balance that follow could be used to develop a coupled linear bending model that includes the axial compression and the variation of bending moment along the length of the joint.

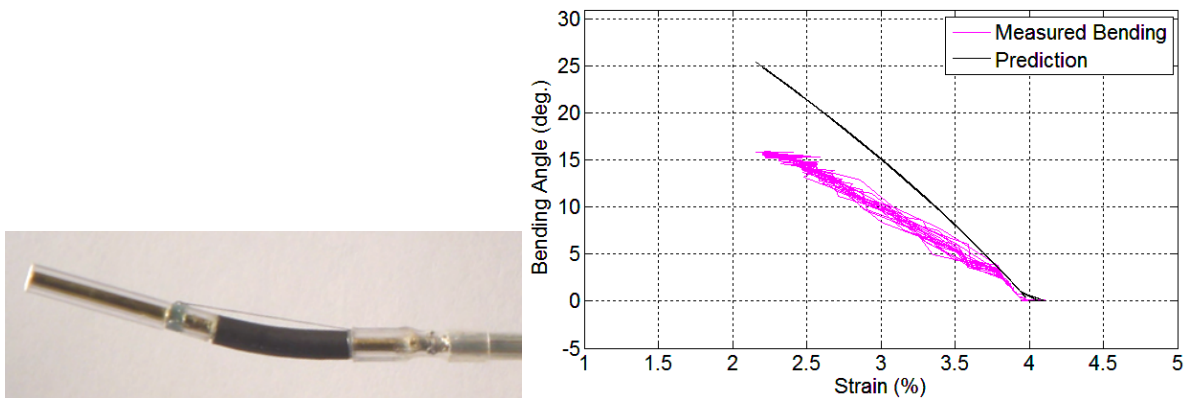


Figure 20: Measured Adaptive Nozzle Joint Bending and Kinematic Model

### 1.2.4 Force and Moment Balance of Bio-Inspired Joint

The force balance is also simplified under the assumption that the joint bends along a constant radius. This assumption requires the moment throughout the joint to be constant, therefore neglecting the variable moment that the axial component of the SMA force has at different points on the joint once significant bending begins. This simplifies the kinematics and force problems by decoupling them. The free-body diagram in Figure 21 shows the tensile force from the SMA wire,  $F_{SMA}$ , acting between  $P_1$  and  $P_3$  as well as the moment generated by the cumulative bending of the joint,  $M_J$ , that acts at joint attachment points  $P_0$  and  $P_2$ . Also, for the bio-inspired wing problem, the force of gravity,  $F_{grav}$ , acting on the center of mass of the wing contributes to the bending moment.

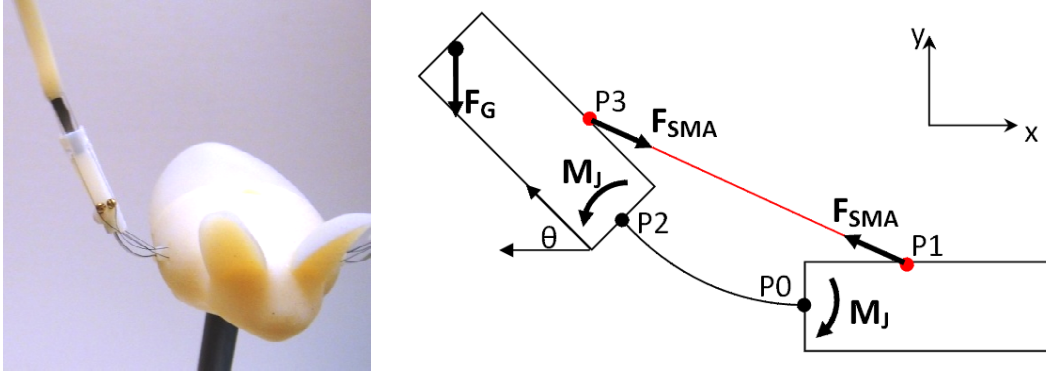


Figure 21: Free-Body Diagram for Bio-Inspired Joint

The moment generated by the super-elastic joint is approximated based on Euler-Bernoulli beam theory as shown in equation (1.15), where  $E$  is the Young's modulus and  $I_z$  is the area moment of inertia of the rectangular beam, defined as

$$I_z = \frac{1}{12} B_J H_J^3, \quad (1.14)$$

where  $B_J$  and  $H_J$  are the width and height of the joint cross-section, respectively. The use of a single constant value for  $E$  is a very rough approximation of the stiffness of the super-elastic SMA joint that is actually highly non-linear. However, once again the main point in this section is to demonstrate the kinematic and force balance process for a bending joint to get an estimate of the extreme bending limits, not to model the SMA materials and observe the non-linear, history-dependent behavior.

$$M_J = \frac{EI_z \theta}{c} \quad (1.15)$$

The moment generated by the force of gravity is approximated as

$$M_G = F_G x_{cg} \cos(\theta), \quad (1.16)$$

where  $F_G = m_{wing} g$  with  $m_{wing}$  the mass of the wing and  $g$  is the gravitational constant, and  $x_{cg}$  is the location of the center of mass of the wing in the global CS. Note that it is assumed that  $x_{cg} \gg c$ .

Since the only relevant forces in the  $x$  and  $y$  directions are from the SMA in tension, the force balance equations will be trivial. However, the moment balance offers insight to the impact that the bending joint will have on the SMA wire. The moments are summed about point  $P_0$  in equation (1.17)

$$\sum_{P_0} M \Rightarrow M_J + M_G - F_{SMA,x} p_{3,y} + F_{SMA,y} p_{3,x} = 0 \quad (1.17)$$

where the components of the SMA force vector are defined in equations (1.18) and (1.19)

$$F_{SMA,x} = F_{SMA} \frac{p_{1,x} - p_{3,x}}{|P_1 - P_3|} \quad (1.18)$$

$$F_{SMA,y} = F_{SMA} \frac{p_{1,y} - p_{3,y}}{|P_1 - P_3|} \quad (1.19)$$

Since the goal is to determine the force in the SMA required to bend the joint through an angle  $\theta$  as defined by the evaluation of the kinematic relationship, equations (1.15) (1.17), (1.18), and (1.19) are solved for  $F_{SMA}$  in equation (1.20).

$$F_{SMA} = \left( \frac{EI_z \theta}{c} + F_G \cos(\theta) \right) \left( \frac{p_{1,x} - p_{3,x}}{|P_1 - P_3|} p_{3,y} - \frac{p_{1,y} - p_{3,y}}{|P_1 - P_3|} p_{3,x} \right)^{-1} \quad (1.20)$$

This force can then be used to determine the stress in the SMA wire via

$$\sigma_{SMA} = \frac{4F_{SMA}}{\pi d_{SMA}^2}, \quad (1.21)$$

where  $d_{SMA}$  is the diameter of the SMA wire. Also, it is assumed that the maximum stress in the super-elastic joint under uniform bending is seen on the part of the joint furthest from the neutral axis, with compressive stresses on the inside radius and tensile stresses on the outside as shown in Figure 22.

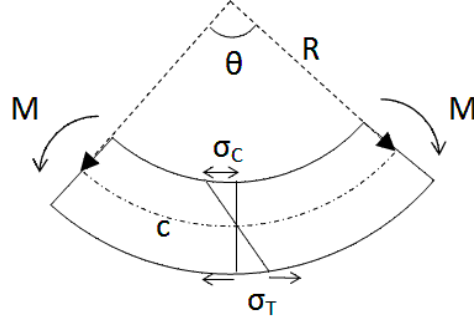


Figure 22: Uniform Bending of Super-Elastic SMA Joint

The maximum stress in the joint can be calculated based on the curvature and the distance from the neutral axis, assumed to be one half the height of the joint,  $H_J$ , via equation (1.22). This peak joint stress is one of the parameters that must be limited, particularly during repeated actuation. Since the stress term in equation (1.22) is coupled with the geometry and objective bending angle, it is needed as a constraint in an optimal design problem.

$$\sigma_{\max,j} = \frac{H_J E \theta}{2c} \quad (1.22)$$

### 1.2.5 Design Optimization of Bio-Inspired Joint

Design optimization requires definition of design variables  $\vec{x}$ , objective function  $F(\vec{x})$  and constraint functions  $g_i(\vec{x})$  and  $h_j(\vec{x})$  as listed in equation (1.4). The design variables for the bio-inspired joint bending problem are defined in Table 2, along with upper and lower bounds based on geometric restrictions.

Table 2: Design Variables for Bio-Inspired Joint Optimization

Variable	Unit	Lower Bound	Upper Bound	Description
$a$	mm	0	5	Body attachment point axial coordinate
$r_B$	mm	0	3	Body attachment point radial coordinate
$b$	mm	0	5	Humerus attachment point axial coordinate
$r_H$	mm	0	3	Humerus attachment point radial coordinate
$c$	mm	.5	10	Length of super-elastic joint
$L_{0A}$	mm	0	60	Austenitic free length of SMA wire
$d_{SMA}$	mm	0	0.1	Diameter of SMA wire
$\epsilon_{SMA}$		.02	0.04	Strain in SMA wire
$\epsilon_{pre}$		0	0.05	Pre-strain of SMA wire
$E$	MPa	0	inf	Modulus of super-elastic joint
$B_J$	mm	0	3	Width of super-elastic joint
$H_J$	mm	0	1	Thickness of super-elastic joint

The objective function that is minimized is

$$F(\vec{x}) = \frac{1}{\theta(\vec{x})} \quad (1.23)$$

where the bending angle  $\theta(\vec{x})$  is calculated using the kinematics derived in section 1.2.1 and an iterative equation solver. Minimizing the objective function in equation (1.23) effectively accomplishes the goal of maximizing the bending angle for  $\theta > 0$ .

The inequality constraint functions are defined in equation (1.24). The peak stresses are determined for a given set of geometry variables over the entire range of SMA strain between the current strain value,  $\varepsilon_{SMA}$ , and the initial strain value,  $\varepsilon_{pre}$ . This is done because during an actuation the SMA contracts from the pre-strain value to the minimum strain that occurs after thermal and static equilibrium are attained, defined at  $\varepsilon_{eq,SMA}$ . However, the force balance may find the peak force to be at a strain that is different  $\varepsilon_{eq,SMA}$ .

$$\begin{aligned} g_1(\vec{x}) &= \max\left(\sigma_{SMA}\left(\varepsilon_{SMA} = \varepsilon_{eq,SMA} \cdot \varepsilon_{pre}\right)\right) - \sigma_{Y,SMA} \\ g_2(\vec{x}) &= \max\left(\sigma_{\max,J}\left(\varepsilon_{SMA} = \varepsilon_{eq,SMA} \cdot \varepsilon_{pre}\right)\right) - \sigma_{Y,Joint} \end{aligned} \quad (1.24)$$

For example, constraint  $g_1(\vec{x})$  in equation (1.24) can be interpreted as: ‘the maximum stress seen by the SMA wire during contraction from its initial pre-strain  $\varepsilon_{pre}$  to its actuated equilibrium strain value  $\varepsilon_{eq,SMA}$  must be less than the yield stress of the SMA wire,  $\sigma_{Y,SMA}$ . For this problem,  $\sigma_{Y,SMA}$  is limited to 150 MPa to allow for many cycles [1], and the maximum stress allowed in the joint material during the contraction,  $\sigma_{Y,Joint}$  is limited to 300 MPa. The constrained optimization is solved using the MATLAB ‘fmincon’ function, and the upper and lower bounds that are defined in the function are also effectively inequality constraints. Some of the design variables are limited by availability of materials and feasibility of fabrication. Those design variables that are not subject to optimization are in this case simply set as equality constraints,

$$\begin{aligned} h_1(\vec{x}) &= B_j - 3 \\ h_2(\vec{x}) &= H_j - 0.075 \\ h_3(\vec{x}) &= E - 30000 \\ h_4(\vec{x}) &= d_{SMA} - 0.075 \\ h_5(\vec{x}) &= \varepsilon_{pre} - 0.04 \end{aligned} \quad (1.25)$$

The optimum values of the design variables,  $\tilde{x}$ , are listed in Table 3. The predicted bending angle for the optimum design variables is  $\theta = 114.9^\circ$ , and at the optimum the second inequality constraint,  $g_2(\vec{x})$  is active, meaning that the predicted peak stress in the joint is 300 MPa. Table 3 also lists the value of each design variable as measured after assembly. In some cases these differ from the

optimum due to inaccuracies during fabrication. The actual values resulted in a measured joint rotation of 80 degrees. A summary of additional performance results is given in section 1.4.2.

Table 3: Optimal and Actual Design Variables and Objectives for Bio-Inspired Joint

Variable	Unit	Lower Bound	Upper Bound	Optimum	Actual Values Used
$a$	mm	0	5	0	0
$r_B$	mm	0	3	0	0.2
$b$	mm	0	5	0	0
$r_H$	mm	0	3	0	1.2
$c$	mm	.5	10	7.5	8.5
$B_J$	mm	0	3	3*	3.5
$H_J$	mm	0	1	0.075*	0.075
$L_{OA}$	mm	0	60	50	60
$d_{SMA}$	mm	0	0.10	0.075*	0.075
$\varepsilon_{SMA}$		.02	0.04	0.02	
$\varepsilon_{pre}$		0	0.04	0.04*	~0.04
$E$	MPa	0	Inf	30000*	
$\theta$	deg			114.9	80
$R$	mm			3.8	6.1

\* - value defined by equality constraint



## 1.3 Fabrication Methods for Embedded SMA Wires

The process described in the previous sections can help engineers exploit the temperature-dependent non-linear behavior of SMA wires and produce a functional or optimal design. However, even the best performing design is useless if it cannot be brought to life via a controlled, repeatable fabrication process. This section addresses some of the biggest challenges of fabrication with small SMA actuator wires and presents solutions in the context of two case-studies.

### 1.3.1 Challenges

Fabrication with small (<100  $\mu\text{m}$  diameter) SMA actuator wires involves many unique challenges, such as:

- Making a firm mechanical connection between SMA wire and structure.
- Making a reliable electrical connection between SMA wire and lead wires.
- Guiding SMA actuator wires through a structure.
- Tracking the SMA wire treatment history during fabrication.

The successful mechanical and electrical attachment and wire guiding methods used in the development of the adaptive nozzle and bio-inspired applications are discussed in section 1.3.2. An example of a controlled assembly procedure with tracking of the SMA actuator wire's treatment history is documented for the adaptive inhaler in section 1.3.2.1.

### 1.3.2 Case Studies of Fabrication Process: Adaptive Nozzle and Bio-Inspired Flapping Bat

Fabrication methods and procedures are presented in this section for the adaptive nozzle and bio-inspired bat applications based on the design parameters established in section 1.2.5. First both of the applications are introduced with a description of the layout of the design. Then the challenges above are addressed one at a time along with the solutions developed for both of the applications.

#### 1.3.2.1 Adaptive Inhaler Nozzle – Overview of Design for Fabrication

Several generations of the Smart Inhaler have been designed and built to validate the concept [20]. The main challenges associated with the adaptive nozzle fabrication involve making the most streamlined mechanical and electrical connections possible to avoid disturbing the air flow around the nozzle. Additionally, a straight section is needed to facilitate attachment of the SMA wires under a controlled pre-stress. A model of the adaptive nozzle design is shown in Figure 23.

The nozzle consists of 3 rigid sections separated by 2 compliant joints (black). The rigid sections are built up of layers of concentric tubes. The rigid tip section has a length of  $13/16''$  (20.6 mm) and the rigid section between the top and bottom joints has a length of  $1\ 5/8''$  (41.3 mm). The inside layer of the rigid sections is made from brass with an inner diameter (ID) of  $1/32''$  (0.79 mm) and outer diameter (OD) of  $1/16''$  (1.59 mm). The next layer consists mostly of open space, but also of small rings, shown in blue in Figure 23, that have grooves that are used to guide coated copper lead wires. These rings also join the inner layer to the outer layer, a  $0.093''$  (2.36 mm) ID,  $1/8''$  (3.18 mm) OD

clear nylon tube. The compliant joints are made from Viton, a heat-resistant fluoro-elastomer (shore hardness 60A) with 1/16" ID and 1/8" OD, and a length of 5/8" (15.9 mm).

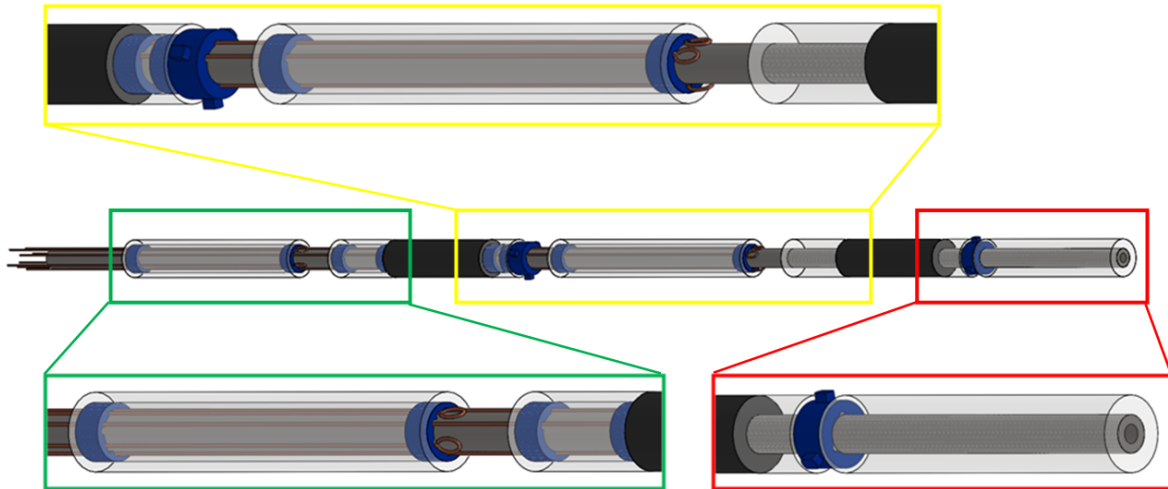


Figure 23: Model of Layer Smart Inhaler Adaptive Nozzle

The sets of 3 SMA wires are distributed around each joint, as diagrammed in Figure 3 and Figure 11. In concept, the inside of the brass section may be coated with a thin-walled Teflon tube that extends the length of the 2-joint nozzle to provide a smooth, continuous corridor for medication to flow. Also, the nozzle tip could be tapered to reduce turbulent flow right at the medication release point, and the entire length of the nozzle could be coated with a thin-walled Teflon or silicone tube.



Figure 24: Exploded View of Adaptive Nozzle Joint Assembly

The 6 SMA actuators used in this design need 6 channels of controlled power that can be individually adjusted based on the resistance measurement of respective channels. The power input is controlled through a custom-built power device presented previously by Hangekar and Seelecke [46],[69]. This power controller insures that the heating power remains constant even while the resistance of the SMA wire changes due to phase transformation. Since Joule heating is proportional to power input, controlling the power effectively controls the heating and by extension the temperature of the SMA wire. This is desirable because the material only responds directly to temperature, which scales with heating power as derived in Appendix B and section 2.1.1.

### 1.3.2.2 Bio-Inspired Wing – Overview of Design for Fabrication

Work on the bio-inspired flapping bat project was started by Bunget [22],[23] with the short-term goal of making a flapping platform capable of replicating the wing-beat frequencies and wing-tip trajectories needed for flight. However, for the design presented in this section, the goals have been amended to creating a flapping platform capable of demonstrating a natural flapping motion at slow frequency for museum viewing. Also, a second design goal was added to increase the number of flapping cycles that the bat could make before either joint or actuator fatigue failure. Finally, the

assembly needed to be simple and repeatable so that the design could be replicated in the future by other assemblers. Figure 25 shows a 3D model of the flapping bat with two flexible shoulder and two flexible elbow joints designed for demonstration in the North Carolina Museum of Science Nature Research Center.

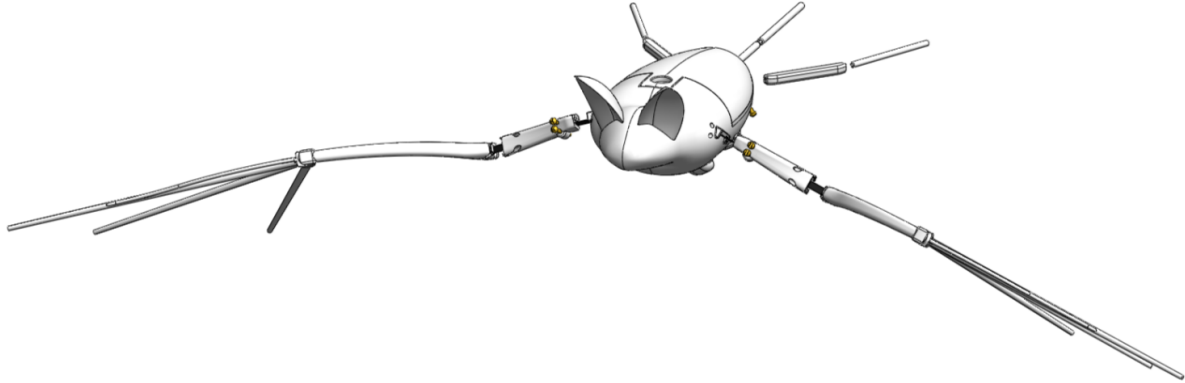


Figure 25: 3D Model of Bio-Inspired Flapping Bat

The rigid bone elements of the bat shown in Figure 25 are first modeled in SolidWorks and then created using a 3D printer. The flexible joints are made from ribbons of super-elastic SMA, highlighted in Figure 26, that can bend through large strains and constrain rotation to a single degree of freedom. The SMA actuator wires stretch across the flexible joints just like muscles. The mechanical attachments are made using small, 000-120 bolts, as will be described in section 1.3.2.3. Electrical connections are made by plugging both the SMA wire and the lead wire into a socket, as shown in section 1.3.2.4. The SMA wires are guided along the arms and body of the bat with small Teflon tube wire guides, as shown in section 1.3.2.5.

Repeatability is ensured by the computer modeling and 3D printing with 0.003" resolution that enables small features to be placed throughout the structure where guide tubes and attachment bolts are inserted. Some of these features are also labeled in Figure 26, where the components associated with the elbow and shoulder joints are labeled in blue and green, respectively. In the case of the shoulder joint, the SMA actuator wire (red) makes a turn-around right at the shoulder and then passes through a corridor into the body, where it is guided to the belly on the opposite side of the bat before being attached to bolts near the tail end. The elbow SMA actuator wire (yellow) makes a turnaround at the wrist and is guided along the arm bones before being attached to the bolts near the shoulder.

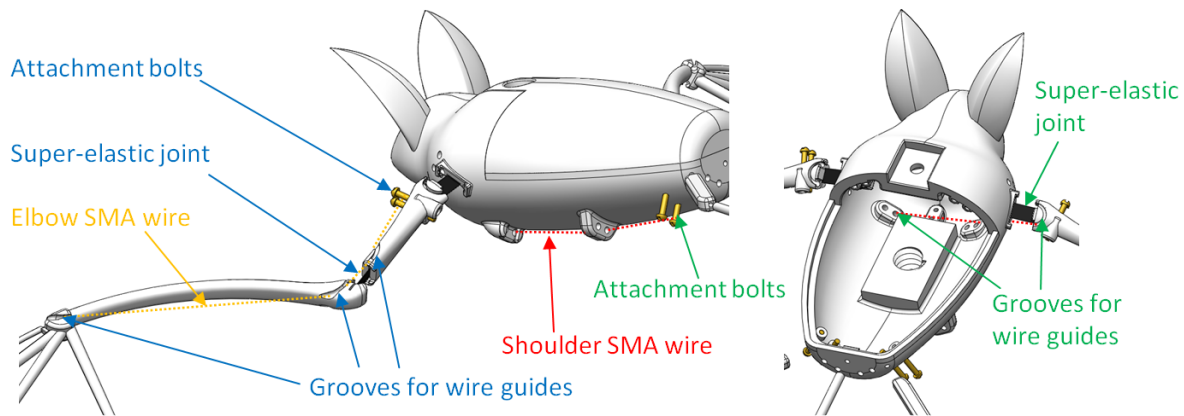


Figure 26: Components of Bio-Inspired Flapping Bat Design

When the bat is fabricated, the first step is to cut the profile of the super-elastic joints using a high-speed CNC mill and carbide tool, and glue the joints into pre-printed slots in the bones. Then the guide tubes are cut and inserted into the pre-printed groove before the SMA wires are threaded through and attached to the bolts. Finally the electrical connections are made and the bat can be tested.

### 1.3.2.3 Mechanical Attachments between SMA Wire and Structure

The mechanical connection between the SMA actuator wire and structure needs to be strong and stable. It must be robust to high temperatures and the changing stress and strain of the transforming wire, and it must be small so as not to negate the benefits of using an embedded actuator in the first place. If the wire slips at the attachment point it will develop slack resulting in a reduction in structural deformation during actuation. Standard welding or soldering is very difficult for SMA wires because exposing the wire to very high temperatures alters its properties. Also, crimps and clamps by nature cause a stress concentration between the clamps that is likely to become a failure point, particularly after repeated cycling.

### Temperature-Resistant Adhesives

One way to embed an SMA wire within a structure is to use adhesives. Adhesives are especially feasible for small diameter SMA wires that have a large surface to cross-sectional area ratio. Adhesives bond to the surface, so holding force is comparatively high, while actuation force is scaled by the cross-section and is therefore comparatively low. However, maintaining a bond to a wire that is contracting and expanding while being heated and cooled is not necessarily straightforward, and the operational envelope of the bond between adhesives and SMA wires is not well understood. Some researchers have endeavored to test adhesive bond strength for SMA-composite applications [74]-[77], and others have searched for a way to improve adhesion using techniques such as oxide coatings, etching, or sand-blasting [77]-[79], but none have run a comprehensive spectrum of repeated pull-out tests on SMA actuator wires at different temperatures bonded with different types of adhesives. Since adhesives can be as structurally streamlined as the SMA wires themselves, they could provide a simple, elegant means of wire attachment. Some adhesives even boast electrical conductivity and could thus be considered for both the electrical and mechanical coupling.

A complete set of experiments was run in this work to quantify the effectiveness of various adhesives at holding an SMA wire during actuation. These experiments are presented in detail in Appendix A at the end of Part 1. The adhesive experiments found that the bonding strength of some adhesives, particularly Loctite E40-HT high temperature epoxy and SuperGlue, are high enough to hold SMA wires during actuation.

For the case of an SMA wire, adhesive essentially bonds to the cylindrical surface of the wire. The area of contact is therefore the surface area of the cylinder,

$$A_s = \pi d_{sma} L_{adh} \quad (1.26)$$

where  $L_{adh}$  is the measured length of the SMA wire that is exposed to adhesive, and  $d_{sma}$  is the diameter of the SMA wire. The maximum force expected from the SMA wire is then calculated based on the failure stress and the cross sectional area,

$$F_{sma,max} = \sigma_{y,sma} \pi \left( \frac{d_{sma}}{2} \right)^2 \quad (1.27)$$

where  $\sigma_{y,sma}$  is the yield stress of the SMA wire in the austenite phase (where contraction and thus force are highest), about 560 MPa [68]. Since it is only necessary for the adhesives to hold forces as high as the wire itself can hold, the bonding force defined in equation (1.28), where  $\tau_{F,adh}$  is the failure shear stress of the bond, need only be as large as  $F_{sma,max}$ .

$$F_{bond} = \tau_{F,adh} A_s \quad (1.28)$$

The experiments in Appendix A show the failure shear stress for several different adhesives at different input current values. Figure 27, reproduced from Appendix A, shows that JB Weld, Loctite E40-HT, and Loctite SuperGlue all hold a bond of about 6 MPa shear with a 100  $\mu\text{m}$  diameter SMA wire heated with a 0.25 A electrical current. Since it is infeasible to measure the temperature of these tiny wires directly without changing the temperature in the process, the temperature is inferred based on the input current relative to the listed austenite finish temperature. The recommended actuation current for 100  $\mu\text{m}$  SMA wire is 0.2 A [1], therefore Figure 27 indicates that when the wire reaches austenite finish temperature, the Loctite E40-HT is still capable of holding 10 MPa of shear stress.

To use an adhesive for mechanical connection of an SMA wire to a structure, it is first necessary to choose the SMA wire diameter and adhesive, then equate equation (1.27) to equation (1.28) and solve for the length of adhesive,  $L_{adh}$ , that must be applied to hold the required force, as shown in equation (1.29). It is also recommended that the SMA wire be scratched with fine grit sand paper and then cleaned before applying the adhesive and allowing it to fully cure according to manufacturer instructions.

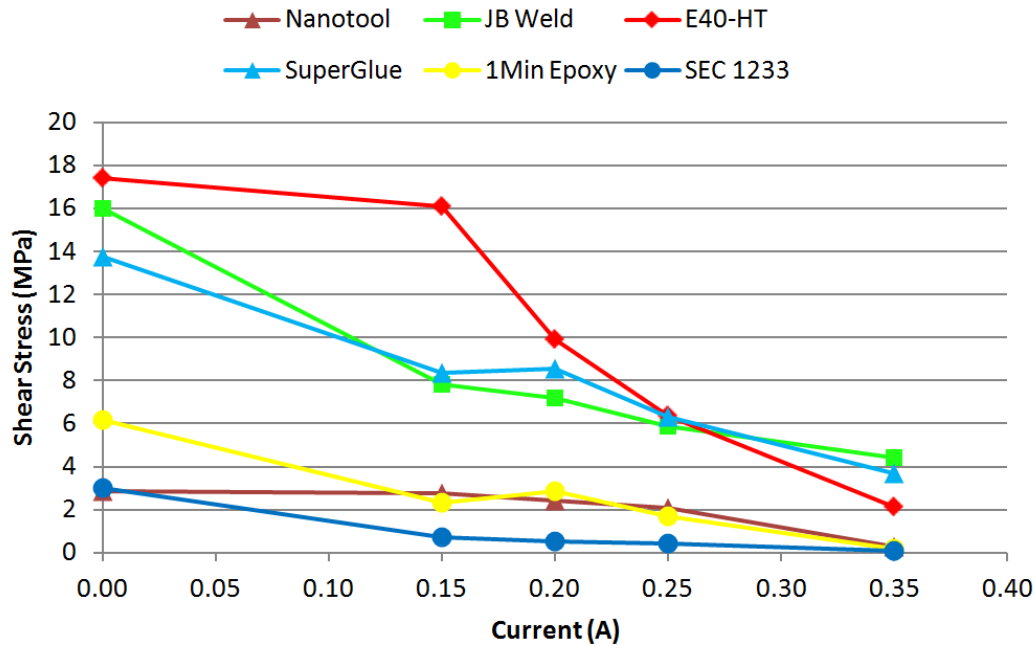


Figure 27: Shear Stress at Bond Failure between Different Adhesives and a 100  $\mu\text{m}$  Diameter SMA Wire Under Electric Current

$$L_{adh} = \frac{\sigma_{y,sma} d_{sma}}{4\tau_{F,adh}} \quad (1.29)$$

### ***Case Study Using Adhesives to Assemble Smart Inhaler Nozzle with Pre-Stressed SMA Wires***

The Smart Inhaler nozzle was assembled with pre-stressed SMA wires to most closely replicate the analog SMA-spring system discussed in section 1.1.1 (and later in section 2.1.2). Pre-stressing allows the SMA wires to return fully to the compressive-preferred martensite phase after each actuation cycle. However, the hysteretic stress-strain characteristic of SMA wire necessitates constant consideration of the stress-strain state of the material during the pre-stressing and assembly process.

Figure 28 shows a model of the pre-compressed joint with an SMA wire attached and a depiction of adhesive labeled. The length of the SMA wire that needs to be exposed to the adhesive is defined by equation (1.29). For the Smart Inhaler, 50  $\mu\text{m}$  diameter SMA wires are used, their yield stress is taken to be 560 MPa [68], and the failure shear stress of the bond is assumed to be 6 MPa, based on Figure 27. Therefore, the SMA wire should be exposed to at least 1.10 mm of either SuperGlue, Loctite E40-HT, or JB Weld, plus a reasonable safety factor if possible.

The basic procedure for assembling the nozzle with SMA wires under pre-stress is to measure the length and stiffness of the compliant joint tube, then measure the separation between the two rigid sections. The space between the two rigid sections is then set such that when the compliant joint is inserted after all of the SMA wires are attached, it will be compressed and push back on the wires with enough force to pre-stress them.

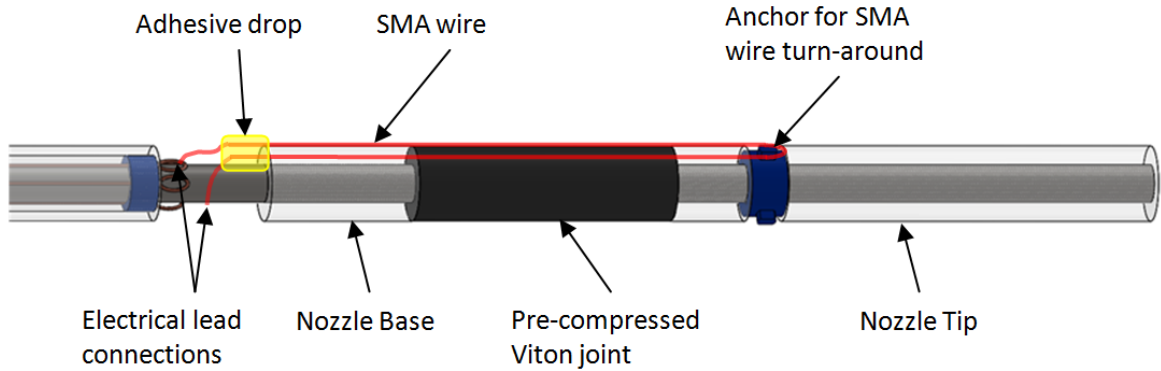


Figure 28: Diagram of an SMA Wire attached to a Pre-Compressed Compliant Joint

The five components (3 rigid and 2 flexible) that comprise the adaptive nozzle are pictured in Figure 29. The assembly setups and procedure is described in more detail in the sections below.

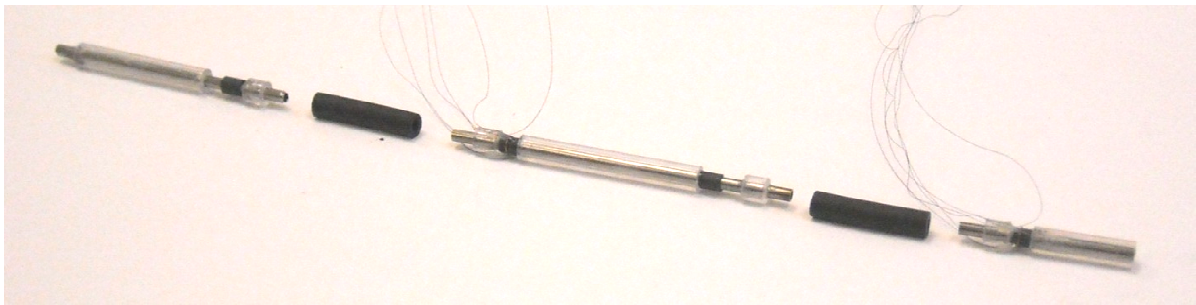


Figure 29: Three Rigid and Two Flexible Elements Used in Adaptive Nozzle Assembly

*Assembly Setups Used for Compliant Joint Measurement and SMA Wire Pre-stressing*

The setup diagrammed in Figure 30 and photographed in Figure 31 is used for measuring the length and axial stiffness of the compliant Viton rubber joint material that is placed between the nozzle tip and base, as shown in Figure 2. The assembly setups are designed to keep the nozzle base and tip aligned at all times. A small stiff rod made from tool steel is slid through both the base and tip to ensure radial (y,z) alignment is maintained, even when the pieces are moved along the x-axis, as shown in Figure 30. The nozzle base is attached in series with a Futek Model LSB200 load cell with a 9 N load limit and a Zaber T-NA08A25 linear actuator. The actuator provides a position feedback measurement that is used to locate the nozzle tip, while the nozzle base is fixed in “clamp 1”, which can rotate about the x-axis on a thrust bearing. The joint stiffness measurement process is described in the “Joint Stiffness Determination” section of the procedure.

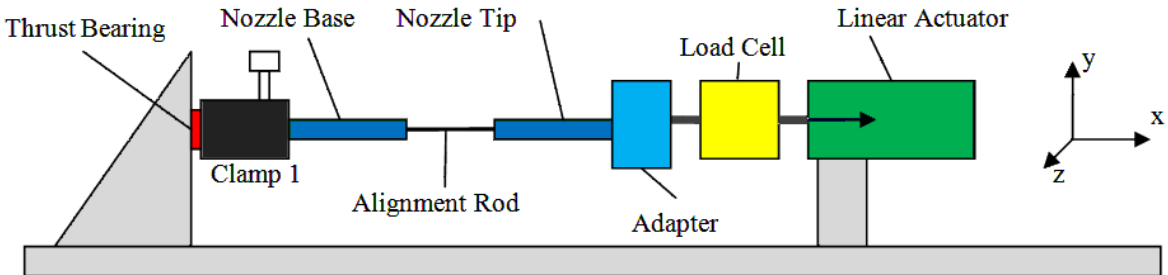


Figure 30: Setup for Pre-compressing Compliant Viton Rubber Joint

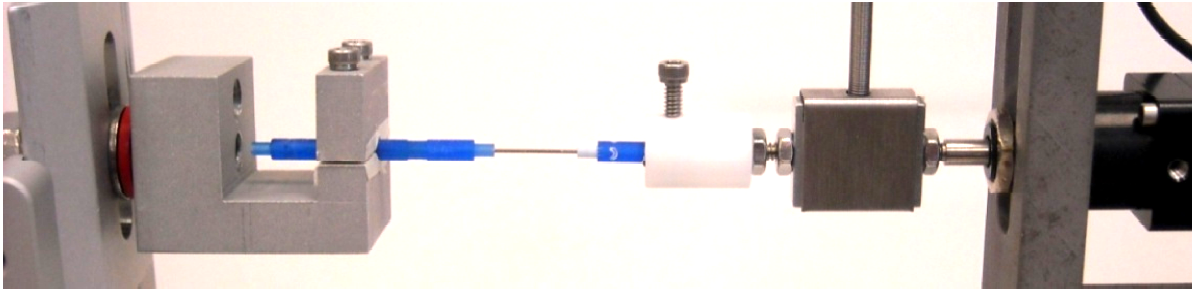


Figure 31: Photo of Setup for Pre-compressing Compliant Silicon Joint

Figure 32 and Figure 33 show the setup used to attach the SMA wires across the joint while controlling pre-stress in each wire, as described in the “SMA and Lead Wire Attachment” section of the procedure. The nozzle base is now slid onto a needled that is attached to the “bracket”. The nozzle base can rotate on the needle while staying parallel to the nozzle base. The SMA wire, shown in red in Figure 32, can be stretched beyond the nozzle base to “clamp 2,” which allows the tensile force in the SMA to be measured by the load cell, and strain to be measured by the Zaber Linear Actuator’s position feedback. The bracket is mounted on a micrometer stage so that the position of the nozzle tip can be measured with respect to the nozzle base. Note that Figure 31 and Figure 33 show a previous version of the adaptive nozzle that was 3D printed in blue.

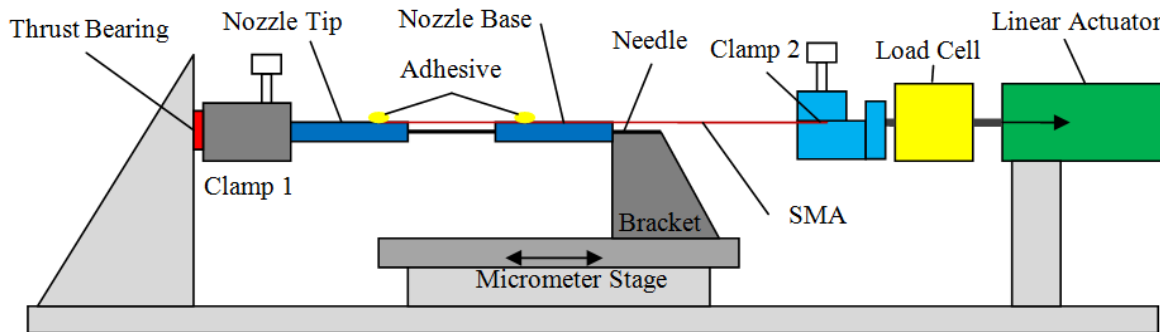


Figure 32: Setup for Pre-stressing and Attaching SMA Wires

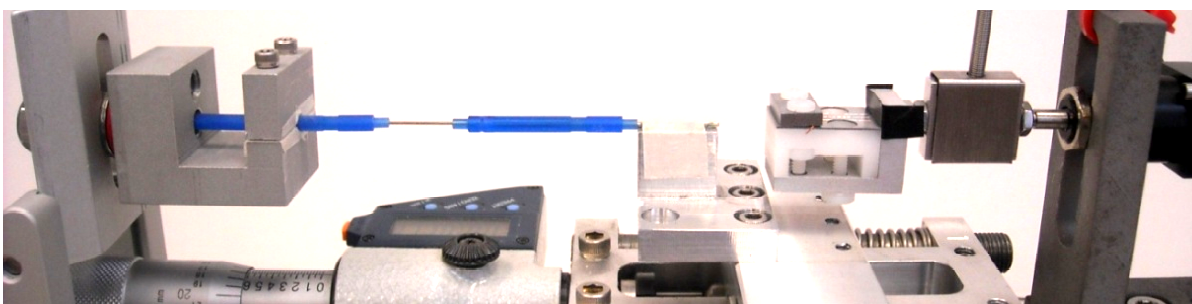


Figure 33: Photo of Setup for Pre-stressing and Attaching SMA Wires

### *Nozzle Assembly Procedure*

The procedure for attaching the SMA wires with a controlled pre-stress is listed below. The assembly consists of two parts: first the stiffness of the compliant silicone is measured using the setup in Figure 30. This will tell the fabricator by how much the joint must be compressed to produce the prescribed pre-stress in all 3 SMA actuators. Then the setup in Figure 32 is used to place the proper spacing between the nozzle tip and base to generate the needed joint compression. Also, the SMA wires are

attached with the proper pre-stress while in the setup in Figure 32. When the Viton joint is reinserted, it will be in compression and produce the proper stress in each wire.

### Wire Preparation

Prepare three 50- $\mu\text{m}$  diameter Dynalloy Flexinol [1] SMA wires for attachment using the following procedure:

1. Cut each of the 3 wires to about 10 inch length.
2. Clamp the wires and pull to 300 MPa to put the wire in  $M^+$  phase, shown in “Step 1” in Figure 34.
3. Relieve the stress in the wire and pass 0.0015 W/mm into each wire under zero stress to put the wire into the austenite phase, as shown in “Step 2” in Figure 34.
4. Turn off the heat and allow the wire to cool into the  $M^+/M^-$  twin phase, as shown in “Step 3” in Figure 34.

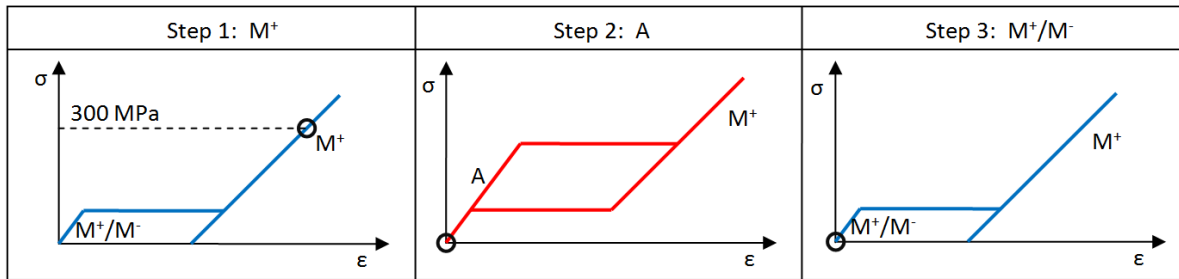


Figure 34: Stress-Strain Equilibrium after Stressing (Step1), Heating (Step 2) and Cooling (Step3)

### Joint Stiffness Determination

1. Insert Clamp the nozzle base in clamp 1 and use the “adapter” to hold the nozzle tip in series with the load cell, as shown in Figure 30.
2. Advance the Zaber until the nozzle tip contacts the nozzle base (use the load cell measurement to detect contact). Record this as a zero position,  $x_0$ .
3. Cut a piece of Viton tubing about 15 mm long. Make sure that the cut is straight, and the face of the Viton is perpendicular to the axial direction of the tubing.
4. Retract the nozzle tip and place the Viton joint between the nozzle tip and base.
5. Advance the Zaber so that the joint compresses. Stop the Zaber when the load cell measures a force that is equal to the total tensile force to be generated from all 6 wires (2 from each actuator) loaded to the desired pre-stress  $\sigma_p$

$$F_{pre} = 6\sigma_p \left( \pi r_{sma}^2 \right). \quad (1.30)$$

6. Record this position as  $x_1$  and the separation between the nozzle tip and base as  $d = x_0 - x_1$ .
7. Remove the Viton joint from the setup.

## SMA and Wire Pre-Stressing and Attachment

1. Add the micrometer stage to the setup and replace the “adapter” with “clamp 2” to create the SMA pre-stressing and attachment setup shown in Figure 32.
2. Fix the nozzle tip in clamp 1.
3. Slide the nozzle base onto the needle attached to the “bracket” in Figure 32 and advance the micrometer stage until the nozzle base touches the nozzle tip (use a microscope to detect contact).
4. Retract the micrometer stage by  $d$  and insert the Viton joint element.
5. Rotate the clamp 1 so that one of the anchors for SMA wire turn around, Figure 28, is facing up.
6. Wrap the middle of the SMA wire around the anchor and use SuperGlue to tack the wire in place as shown in Figure 35. Wait at least 10 minutes for the SuperGlue to cure.

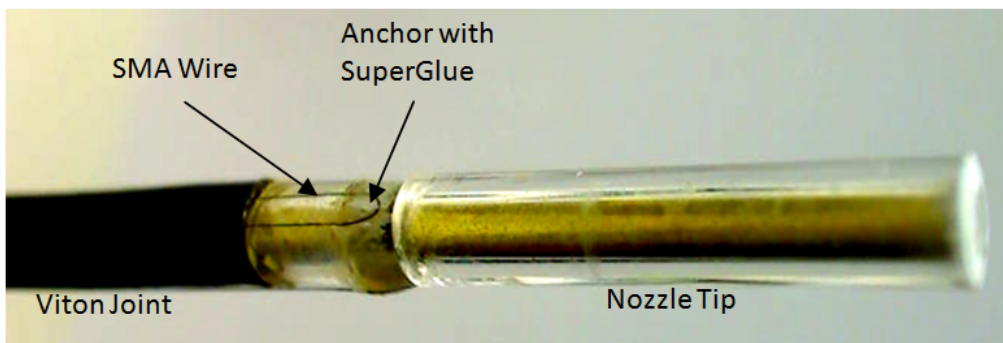


Figure 35: SMA Wire Wrapped Around Turn-Around Anchor with SuperGlue

7. Attach the SMA wire to clamp 2 and retract the Zaber slowly until the wire achieves the desired pre-stress, as measured by the load cell. This will put the wire into the state shown in Figure 36.

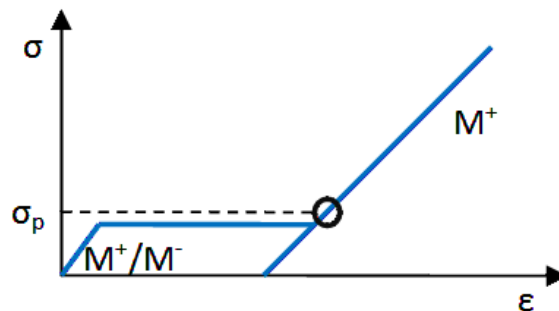


Figure 36: Stress-Strain Equilibrium after Pre-Stressing

8. Tack the SMA wire to the nozzle base using SuperGlue, as depicted in Figure 37 and photographed in Figure 38.



Figure 37: Stressed SMA Wire Tacked with SuperGlue

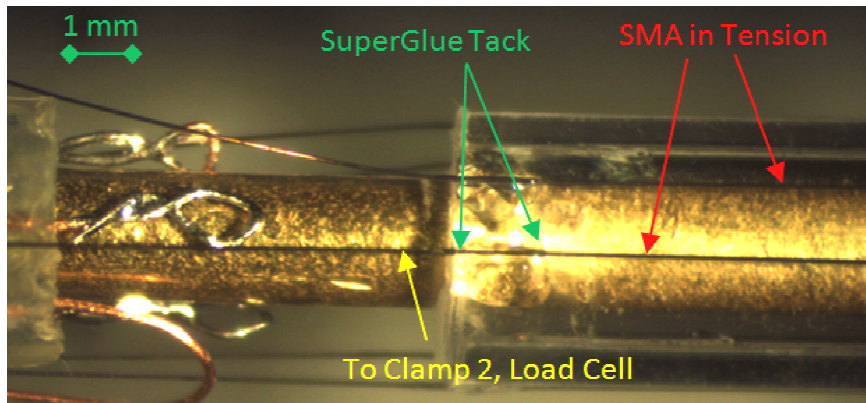


Figure 38: Close-up Photo of SMA Wire Under Tension with SuperGlue Tack

9. Wait at least 10 minutes for the SuperGlue to cure, then rotate “clamp 1” on the thrust bearing and the nozzle base on the needle. Tack the second strand of actuator 1 with SuperGlue. Repeat for all 6 SMA wires.
10. Next, the electrical connections are made via the wire loop method.
11. After the electrical connections are made, use Loctite E40-HT high temperature epoxy to reinforce the connections, as depicted in Figure 39. As calculated above, the length of SMA wire exposed to the adhesive should be at least 1.1 mm. In this case, 3 mm of wire are encased in adhesive (1.5 mm in SuperGlue and 1.5 mm in Loctite E40-HT). Allow at least 3 days to cure Loctite E40-HT before attempting actuation.



Figure 39: SMA Wires Secured with Loctite E40-HT High Temperature Epoxy

The end result of this process is a nozzle joint with 6 strands of SMA wire under a pre-stress supplied by the compression of the compliant joint. The wires are all permanently attached with adhesives. An alternative method using a bolt or screw that can rotate is discussed next.

### Adjustable Screw Method

Some of the drawbacks of using adhesives can be addressed by wrapping an SMA wire around a post that can be rotated, such as a screw. An analog of this method is in the common guitar string winder, shown in Figure 40. Wrapping a wire around a post serves to transfer most of the mechanical load to

friction between the small post and the wrapped wire. Then only a small bit of adhesive is needed to keep the SMA wire from unwrapping itself, as shown in Figure 41. Also, if at some point slack develops in the SMA wire, the screw can be rotated to remove the slack or tune the pre-stress in the wire, much like a guitar string.



Figure 40: Photo of Guitar String Winders [80]

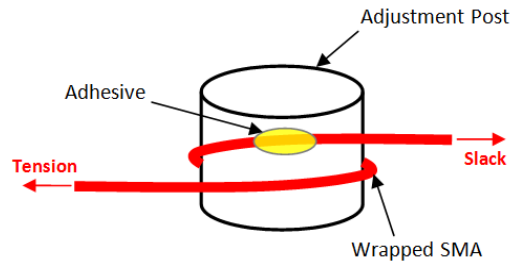


Figure 41: Diagram of Adjustable Screw Method for SMA Attachment and Tensioning

### ***Case Study in Bio-Inspired Application***

In the bio-inspired bat application presented in section 1.2.2, a brass 000-120 screw with an outer thread diameter of 0.88 mm was successfully used to hold a 75  $\mu\text{m}$  diameter SMA wire. The screw was tapped into the 3D-printed material that comprised the bat's bones. A 0.5 mm hole was left in the bone during the printing process, and the brass screw was simply turned into the hole, cutting its own threads into the softer print material. On the opposite side of the bone, a jam nut was used to apply tension on the bolt and prevent the bolt from rotating due to torque applied by the coiled SMA wire during actuation. The straight SMA actuator wire was first placed adjacent to the bolt, and a tiny drop of instant-curing SuperGlue was placed on the junction to keep the SMA in place. Then the SMA was looped around the bolt once as shown in Figure 42. Rotating the bolt gives control over the tension in the SMA wire. Behind the mechanical connection, the SMA is left slack, and the electrical connection is made to the slack wire.

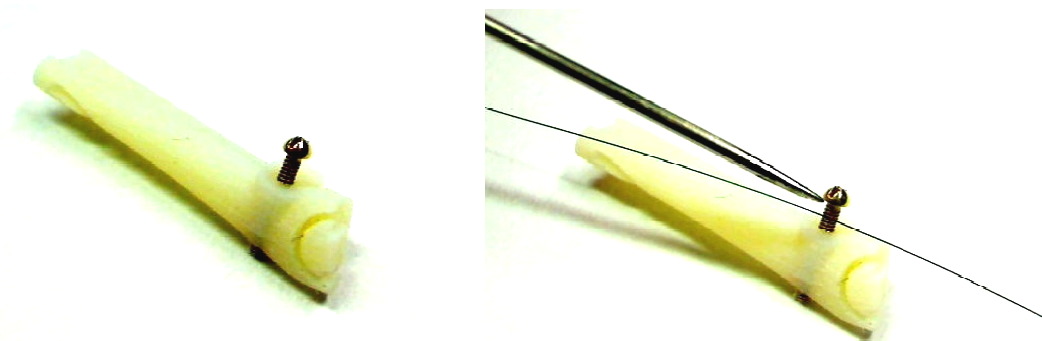


Figure 42: Structural Element with Screw for Mechanical Attachment of SMA Wire

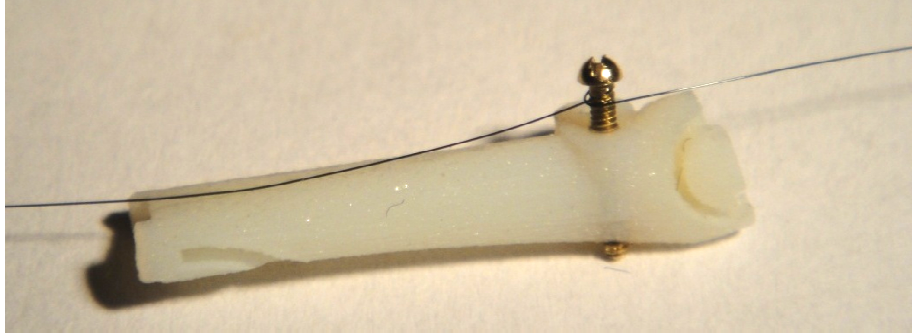


Figure 43: Demonstration of SMA Wire Attached to Bio-Inspired Bone Structure with Adjustable Screw Method

Figure 44 shows the SMA wires from the elbow and shoulder joints of the museum exhibit bat connected to small bolts. The pre-strain in the SMA wire can be tuned at any point in the fabrication or testing process by rotating these bolts.

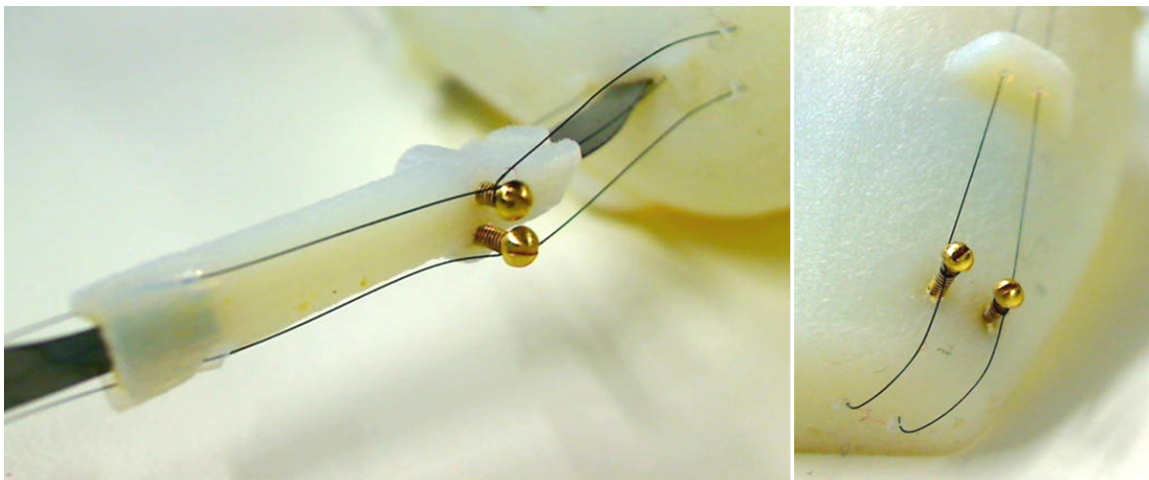


Figure 44: Adjustable Screw Method Applied to Bat Elbow and Shoulder SMA Muscles

In this method, assembly is fast and simple, and in tests the connection held without softening or failing for over 100,000 cycles. In all cases, the SMA wire itself fatigued and failed before the junction. In some cases, the SMA wire failed right at the junction. However, this issue was remedied by ensuring that the SMA wire came off the junction tangent to the post so as to avoid any stress concentration at the attachment point.

The main drawback of this method of making the mechanical connection between the SMA wire and the structure is the added bulk. The adjustment post takes up space and usually requires a jam nut. If the screw is too small compared to the SMA wire, the SMA will not be able to wind tightly around the screw without being subjected to very high stresses.

#### ***1.3.2.4 Electrical Connections between SMA and Lead Wires***

The electrical connection between the SMA wire and lead wire also needs to be stable and robust in the face of the transforming SMA wire. If the electrical connection is made at the same location as the mechanical connection, a change in tension in the wire causes a change in contact pressure and therefore contact resistance. It is critical to keep contact resistance constant, because any measurements of “wire” resistance actually include contributions from the lead wires, electrical

contacts, and parasite resistance from within the measurement electronics. Figure 45 depicts these contributions, which sum up to give the total measured resistance in equation (1.31). When a slack SMA wire is heated and changes phase it often twists or squirms in response to the small residual or thermal stresses in the wire. This can also lead to a change in contact resistance. A noisy resistance measurement not only causes a measurement error in sensor applications, but it also causes errors in the power control algorithm employed by the adaptive power supply developed at NC State University for multifunctional SMA actuators and sensors [45],[46],[69].

$$R_{Meas} = R_{SMA} + R_{C1} + R_{C2} + R_{lead1} + R_{lead2} + R_{P1} + R_{P2} \quad (1.31)$$

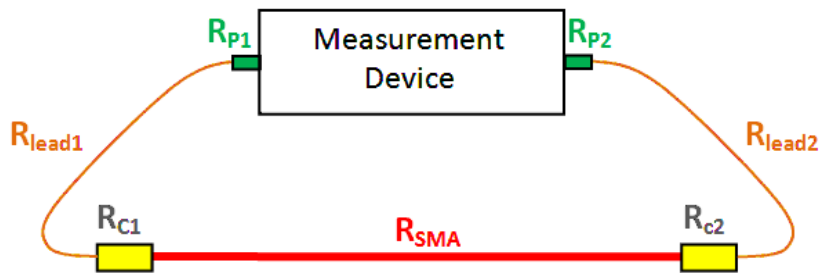


Figure 45: Diagram Showing the Contributions to SMA Resistance Measurements

In general, the effect of changing contact pressure on resistance motivates the need to put the electrical connection behind the mechanical connection. Also, when placed behind the mechanical connection the electrical connection does not need to have the mechanical strength to carry any load. Since adhesives are electrically insulating they should not be used in the area of the electrical connection. As was shown in Figure 27 and Appendix A, conductive epoxies that cure at room temperature do not hold firmly when exposed to high temperature, and the electrical connection also weakened significantly when the adhesive bond is broken.

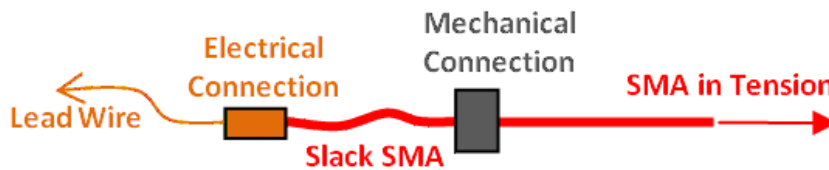


Figure 46: Diagram of Electrical Connection Behind Mechanical Connection

### Wire Loop Method

The electrical connection can be streamlined further by connecting the SMA wire directly to the lead wire, and using conductive paint to help improve conduction. This method is presented as it was applied to an adaptive Smart Inhaler nozzle, introduced in section I.iv.

### Case Study in Smart Inhaler Nozzle

In the adaptive nozzle, a 50  $\mu\text{m}$  SMA wire is attached to a 36 gauge coated copper lead wire. There are 4 lead wires – 3 channels and 1 common ground – for each of the flexible joints. The steps used to make this connection are first demonstrated and documented in the test-system shown in Figure 47,

while the same procedure is reiterated for the newest adaptive nozzle prototype in Figure 48. A description of the steps are listed below.

- Step 1 – In step 1, the SMA wires are shown before the electrical connection is made, but after the mechanical junction is made with SuperGlue adhesive.
- Step 2 – Step 2 shows the ground lead wrapped around the tube, and 1 end of the SMA wire (black) wrapped around the ground lead. The copper ground lead appears silver because it has been tinned with solder. Tinning the ground lead makes it slightly thicker, thus providing more contact area.
- Step 3 – In step 3, conductive silver paint is applied to the electrical junction. The small size of the lead wires compared to the SMA wire makes it difficult to get a consistent contact pressure while wrapping, so conductive paint helps create additional electrical pathways and keep contact resistance low.
- Step 4 – First, step 4 shows the ground connection is wrapped with silicone dielectric material. This material isolates the ground connections from the signal connections that will be laid on top of them. It also helps keep contact resistance constant by holding the SMA wire firm. Step 4 also shows the signal lead wire loop consisting of a copper wire that is formed into a ~1 mm diameter loop and then tinned.
- Step 5 – In step 5, the SMA wire is wrapped around the lead wire loop. The loose end of the SMA is then glued to the side of the tube adjacent to the original mechanical junction, labeled in Step 1.
- Step 6 – In step 6 conductive paint is added onto the wire loop at the connection point.

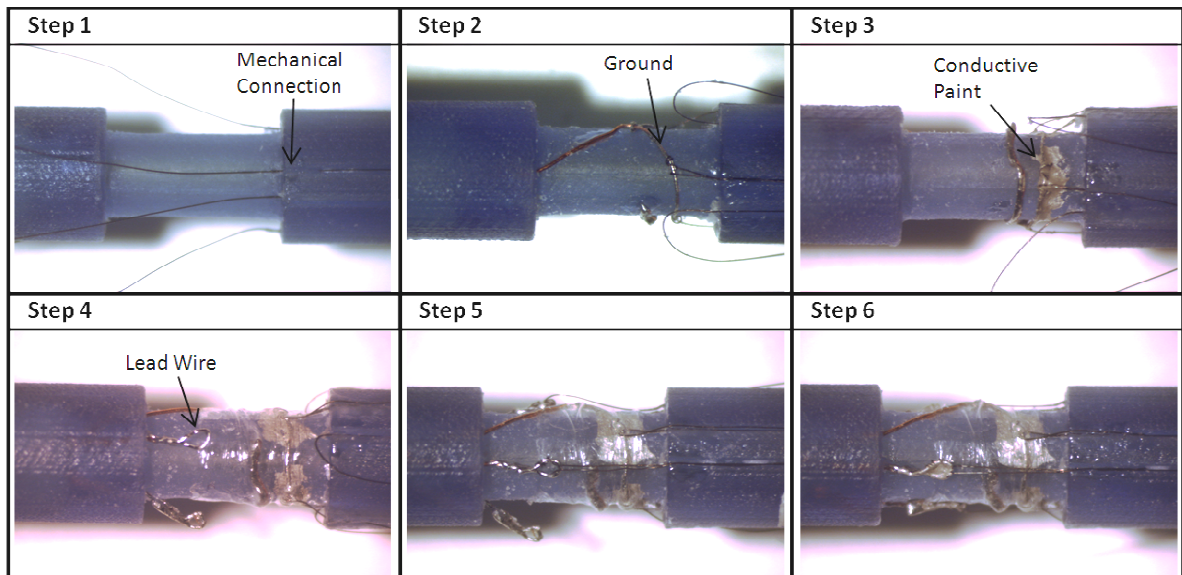


Figure 47: Demonstration Lead Wire Loop Electrical Connection Process

Figure 48 shows this same method applied to the Smart Inhaler nozzle made from layered tubes, as described in sections 1.3.2.1. In this case, the brass inner tube is maintained as the electrical ground, thus providing more surface area over which to make the ground connection.

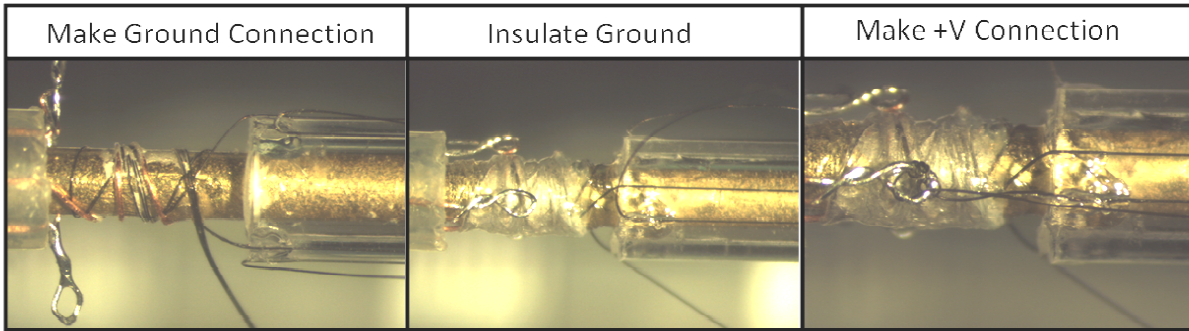


Figure 48: Lead Wire Loop Electrical Connection Process Applied to Adaptive Nozzle

Figure 49 shows the complete electrical and mechanical connection for the embedded adaptive nozzle SMA actuator wire. The electrical connection is coated with conductive paint, then the continuity of the electrical connection is checked before finally the Loctite E40-HT adhesive is added to secure the mechanical connection.

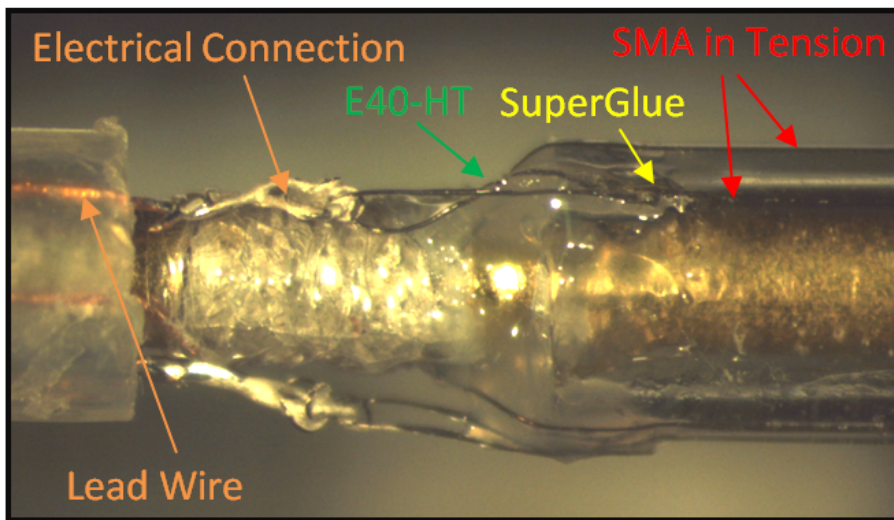


Figure 49: Adaptive Nozzle Electrical and Mechanical Connections

The connection is then encased in a sleeve of Teflon heat shrink that protects the connection and provides additional contact pressure, as shown in Figure 50.

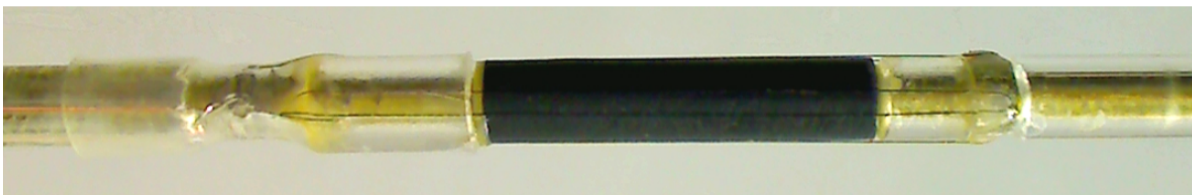


Figure 50: Adaptive Nozzle Electrical Connection Encased with Teflon Heat Shrink Tubing

This method makes very small, streamlined electrical connections, and when configured as shown in Figure 49 the lead wire loop can act as a second mechanical anchor, in case the adhesive fails. However, this method is labor intensive and occasionally causes unstable parasite resistance. Also, it is difficult to alter the connection or the pre-strain in the SMA wire once it is made.

## Pin-Socket Connections

### *Case Study in Bio-Inspired Application*

When the electrical connection is put behind the mechanical connection, as shown in Figure 46, the electrical connection does not have to carry any load. In the “pin-socket method,” a socket hole is created in a block and then a soft, conductive, tightly fitting pin is pressed into the socket along with the SMA wire. For the bat application, 4 different channels requiring 8 separate electrical connections were needed. An example of a socket block made from PVC with eight 0.79 mm diameter socket terminals is shown in Figure 51. First the SMA wire is inserted into the socket, then a copper pin with 0.81 mm diameter is pressed in, as shown in Figure 52.

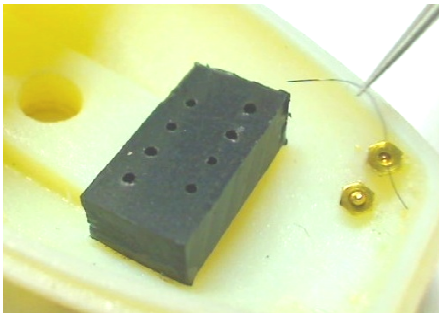


Figure 51: Socket Block with Slack End of an SMA Wire

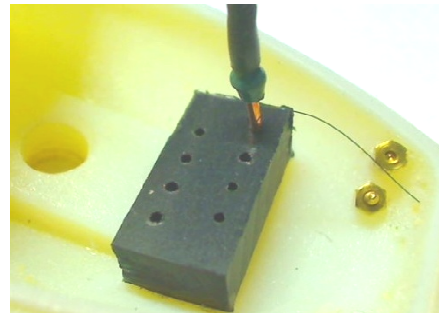


Figure 52: Socket Block with Copper Pin Holding SMA Wire

Since neither the copper pin nor the PVC socket is harder than the SMA, there is little chance of the SMA wire being cut when the pin is inserted. Also, the tight tolerance between the SMA and the pin ensures a tight connection over a larger area that results in very small ( $<0.1$  Ohm) contact resistance. Since the electrical connection is behind the mechanical junction and not exposed to changing wire stress, the contact resistance remains small and constant during heating and cooling cycles. The downside of this socket-pin method is that it is large and bulky, particularly in this implementation. For the bat, it was desirable to have all of the socket connections together on one block, and the space between the sockets makes assembly easier. It is also possible to miniaturize the socket block by separating out the channels and using 8 small tubes instead of one large block, or by printing the sockets directly into the body of the bat. The latter method is successfully employed in later versions of the bat.

### **1.3.2.5 SMA Wire Guides**

In actuator applications, the stroke provided by an SMA wire is proportional to a contraction strain scaled by the total length of the active wire. Similarly, in sensor applications a long wire can experience a larger change in the resistance and thus achieve higher resolution. Using wire guides allows a long wire to be threaded on a curved path through a structure. However, friction at contact points serves to increase the stress in the wire locally, and the sum of these local contributions causes a reduced actuation force at the attachment point. Also, a hot SMA wire conducts heat away at each contact point, resulting in a reduction in actuation stroke, as discussed in Appendix B. Ideally, a wire guide will have very low friction and thermal conductivity, and it will guide the SMA wire around a large radius of curvature so as to avoid creating a stress concentration in the wire.

Figure 53 shows wire guides employed by Bunget for a previous BATMAV prototype. These guides were meticulously formed from coated copper motor wire and glued into the body of the bat. This method requires a steady hand and a lot of labor, and the metal wire guides cause a lot of friction and heat loss at the contact points. The friction will result in a loss of stroke, increase in stress, and localized wear that could lead to fatigue and failure. The conductive cooling may prevent sections of wire from transforming to the austenite phase, also resulting in a loss of stroke, as discussed in the study of the effects of thermal boundary layers in Appendix B.

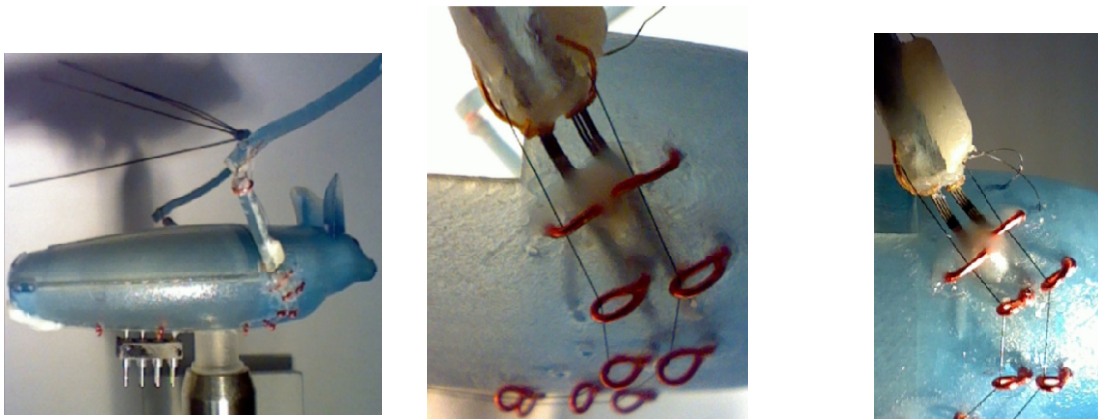


Figure 53: Wire Guide Loops from Bunget BATMAV Prototype [23]

### Case Study of Teflon Tubes in Bio-Inspired Application

The Teflon tube method offers an improvement to the wire loops shown in Figure 53. Teflon has very low friction and is resistant to wear and to temperatures over 200 C. A Teflon tube with 0.8 mm outer diameter (OD) and 0.4 mm inner diameter (ID) is shown next to a 3D printed bat wrist in Figure 54.

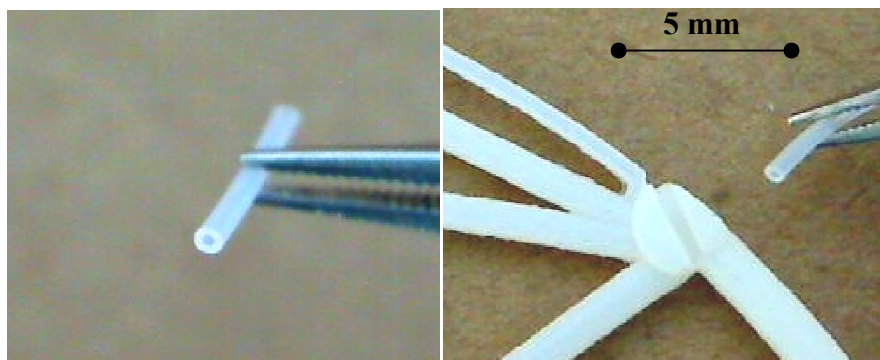


Figure 54: Teflon Tube Used for Guiding SMA Wires

The series of pictures in Figure 55 shows how Teflon tube wire guides were used as a turn-around point for an SMA wire on the wrist of the bio-inspired bat wing. In ‘Step 1’ in Figure 55, the bone structure 3D printed with a slot for a wire guide is shown along with a Teflon tube with 0.8 mm OD and 0.4 mm ID. In ‘Step 2’, the tube is inserted into to slot, and in ‘Step3’ the SMA wire is threaded through the tube. Figure 56 shows how 3 sets of Teflon wire guides are used to bring the SMA wire that actuates the elbow joint from one screw attachment point near the shoulder, through the elbow joint, around the wrist, and finally back to a second screw attachment point by the shoulder. Note that the Teflon tubes also blend in with the bone, making them ideal for the museum exhibit application.

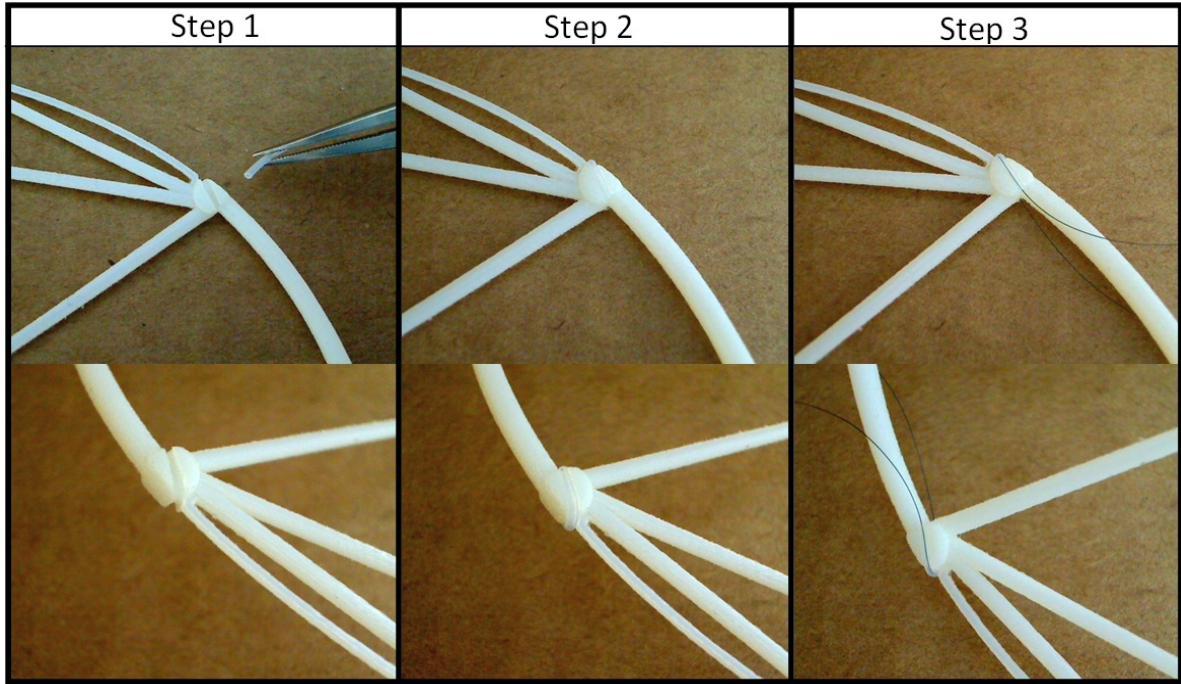


Figure 55: Teflon Tube Wire Guides in Bio-Inspired Application

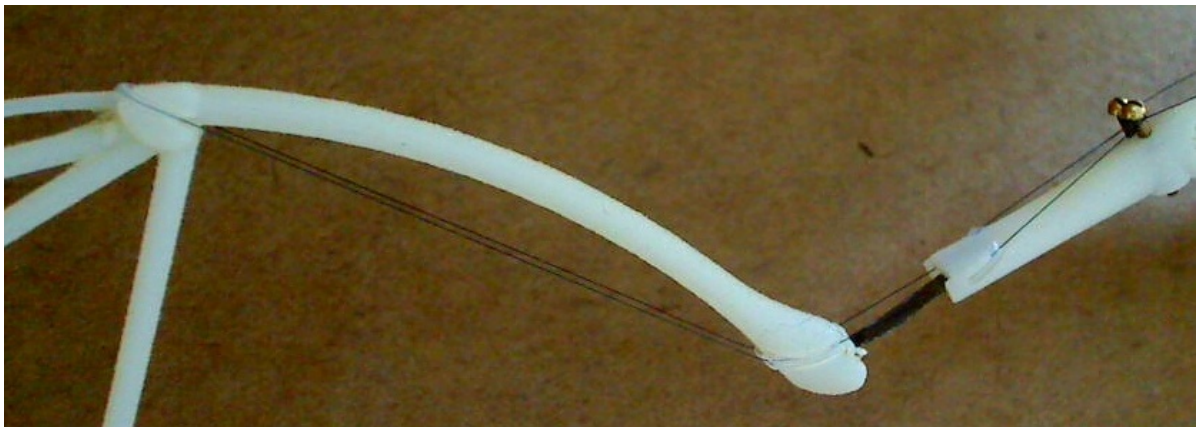


Figure 56: SMA Wire Guided Along Bat Wing with Teflon Tubes



## **1.4 Summary of Design and Fabrication for Embedded SMA Actuator Wire Applications**

Part 1 developed a systematic method for designing embedded SMA applications. The kinematics of the unique interaction between a hysteretic, non-linear material – the SMA wire – and a structure with its own force-displacement characteristic was simplified to an SMA-spring system for the purpose of demonstration. This system is studied in greater detail with side-by-side experiments and modeling in Part 2. Next a design process was outlined that directs a designer to first determine the kinematic relationship between the contraction of the SMA wire and the structural deformation, then to determine what stresses are developed in the structure and the wire by force and moment balance. The kinematic equations and force balance presented can either be applied as a simple first-order prediction; or they can be solved iteratively through an optimization algorithm that considers the objective of structural deformation subject to the constraints of the material stresses. Similarly, other methods like theory of linear elasticity or finite element analysis can be used to develop more accurate models that consider the coupling between the force and deformation problems at each step.

The design and fabrication methods presented in Part 1 have produced an adaptive Smart Inhaler nozzle and a bio-inspired flapping wing that meet the initial design objectives. The design process started with a prediction of the joint rotation that would result from a given SMA wire contraction, as determined by the kinematic relationship. Then the moments required to induce such a rotation were used to produce an estimate of the tensile force in the SMA wire via a force and moment balance. In the case of the Smart Inhaler nozzle, the estimates were used to validate that the simple geometric configuration would also produce the desired bending. For the bio-inspired wing joints, these relationships were used iteratively in an optimization algorithm to determine how the geometry could be altered to maximize bending while limiting both SMA and joint stress.

The designs were then fabricated using new techniques for mechanically joining the SMA wires to the structure and for making electrical connections between the SMA wire and lead wires. One of these techniques is based on using temperature-resistant adhesives and is detailed further in Appendix A. Also, a method of using Teflon wire guides was developed to increase the length of SMA wire that could be embedded within the structure while limiting the drawbacks of friction and thermal coupling at the contact points (detailed in Appendix B). These methods led to stable electrical and mechanical connections that produced repeatable results in the adaptive nozzle and bio-inspired wing.

### **1.4.1 Summary of Adaptive Nozzle Design and Fabrication**

The two-joint Smart Inhaler nozzle uses adhesives to create streamlined mechanical connections, and tiny wire loops to make the electrical connection. The SMA wires are assembled under pre-stress, and good repeatability is observed from one actuator to the next. The joints are able to rotate through about 16 degrees in the direction of each actuator – greater than the 15 degree objective, but less than the 25 degrees predicted by the first-order kinematic model that neglects axial compression and assumes a constant joint curvature. The distribution of Joule heating power to the 6 different

actuators allows the nozzle to be contorted to infinitely-many different configurations. The two joints and complete nozzle is shown in Figure 57 through Figure 59.



Figure 57: Top Joint



Figure 58: SMA-Actuated Dual Joint Smart Inhaler Nozzle



Figure 59: Bottom Joint

### 1.4.2 Summary of Bio-Inspired Wing Design and Fabrication

The bio-inspired flapping bat was designed using the same kinematic bending model as the nozzle. In the case of the bat, however, a force and moment balance was added and a constrained optimization algorithm was used to weigh the benefits of maximal bending against the costs of high forces. In the optimization problem, the objective was to maximize bending, and the constraints were on the peak stresses experienced in the SMA actuator wire and super-elastic SMA joint during the course of a complete joint rotation cycle. The geometric parameters, such as wire attachment points, were the design variables, and the optimization algorithm produced the best geometry possible based on the simplified kinematic and force models. Testing of the bat showed that the shoulder was capable of repeating a rotation of 80 degrees 100,000 times in response to a 0.3 Hz cyclic input wave with 1.1 W peak power. The elbow was designed to rotate less than the shoulder, so it only bends 60 degrees. In some tests the SMA actuator wire failed around 100,000 cycles, and in others the super-elastic joint failed, also right around 100,000 cycles.

The final bat, pictured in Figure 60, uses small bolts as mechanical attachment junctions that enable tuning of the wire pre-stress after assembly. Very stable electrical connections are made behind the mechanical connection with a plug and pin method. Also, Teflon tubes are employed extensively to guide the SMA wires around the natural curves of the bat arms and body without subjecting them to

significant friction or contact cooling. This enables the implementation of long “muscle” wires with large actuation strokes.

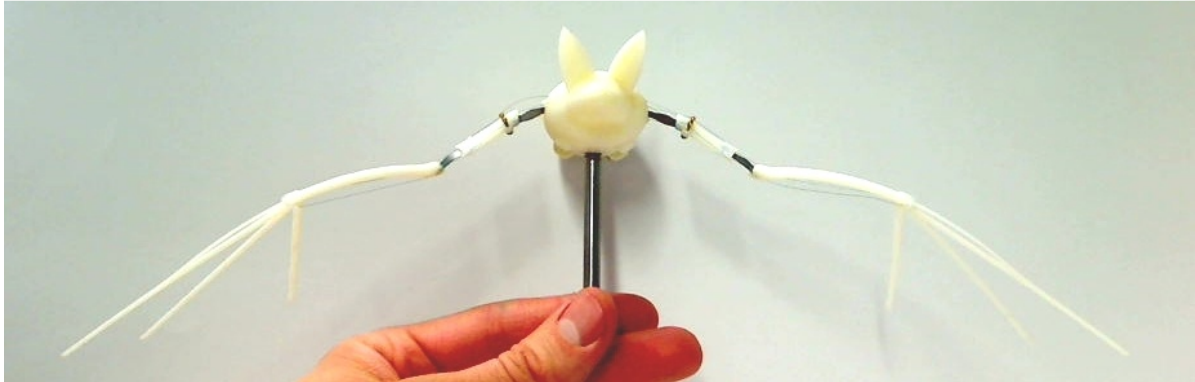


Figure 60: Bio-Inspired Bat with Two SMA-Actuated Shoulder and Elbow

In the case of both the bat and the nozzle, the process described in Part 1 produced a theoretical basis for the initial designs, and the kinematic and force models identified trends so that the design improved with subsequent prototype generations. Additionally, the case studies are accompanied by a summary of successful fabrication techniques that can be reliably employed in future embedded SMA actuator wire applications.

## 1.5 Future Work for Part 1

The design and fabrication successes in Part 1 also inspire future work. Design is often based on predicting the behavior of a system before building it, and those predictions are never perfect. Further, fabrication often involves developing an ad hoc solution to the problem at hand, so it is impossible for all of the questions to ever be answered. A number of points come to mind for improvement:

- Couple the force and bending problems using an implementation of linear elasticity such as Euler-Bernoulli beam theory to get a more accurate prediction of joint bending and peak SMA stresses. This will relax the first order assumption that the joint bends on a uniform arc and provide a better model for use with geometric design optimization.
- Explore different methods for cutting super-elastic SMA ribbons or SMA actuators that are not already drawn into wire form. Although SMA wires are convenient, many of the electrical and mechanical attachment challenges could be solved by cutting the actuator out of a sheet while leaving an attachment feature behind. However, cutting SMA material is not trivial because local heating or plastic deformation can change the properties of the material.
- Improve the understanding of the effects of thermo-mechanical coupling on actuator performance by simulating a 1D SMA wire with a polycrystalline SMA model and implementing more realistic thermal boundary conditions that are somewhere between isothermal and adiabatic.



# Part 2: SMA Wire Modeling, Characterization, and Multifunctional Sensing and Control



## 2.1 Modeling and Characterization of SMA Actuator Systems

A systematic design process and reliable, repeatable fabrication are prerequisites for successfully creating an embedded SMA actuator or sensor device. However, extracting meaningful sensor data from the available measurements and then accurately controlling that device requires a much greater understanding of the material's behavior in the context of the relevant system. The goal of Part 2 is to develop such an understanding through a series of carefully conducted characterization experiments side-by-side with a physics-based material model. The model is used to identify qualitative trends and gain an understanding of how the physics of the material manifests itself in the behavior of the coupled SMA-structure system. This understanding is then be used to motivate potential sensor mapping methods and control schemes that truly exploit the multi-functional capability of SMA wires.

Two different SMA-structure systems with relevance to embedded SMA actuator and sensor applications are studied via physics-based modeling and experimental characterization. The first is the single SMA-spring that approximates many actuator systems where the structure provides a passive restoring force, as was discussed in section 1.1.1. The second system adds an opposing SMA wire that provides an active restoring force. A simplification of the physics-based model developed by Seelecke, Mueller, and Achenbach [28],[32] is derived for the case of a 1D thin wire. That material model is then implemented to simulate the practical actuator systems studied.

### 2.1.1 SMA Single-Crystal Model

An implementation of the SMA material model is developed to simulate the coupled electro-thermo-mechanical behavior of an SMA wire that is heated by a controlled input power. The implementation simplifies the system to 1D and assumes adiabatic thermal boundary conditions at the wire endpoints, resulting in a uniform temperature profile and eliminating the need for finite element analysis. Also, R-phase and 2-way effects are ignored because the SMA is almost constantly in tension. The compression-induced  $M^-$  phase is not observed for this same reason; however, it is included in the model formulation for completeness.

The behavior of the SMA material is simulated by a single-crystal, free-energy based model described below and in further detail by Heintz [42] and Seelecke [31],[44]. A Helmholtz free energy landscape is used to determine the probability of the single crystal of material changing phase. These transition probabilities then drive the evolution of the phase fractions – the volume ratio of all material that is in a given phase – that can be used to quantify mechanical properties. The energy landscape is dependent on temperature, so the thermal evolution is also tracked. Table 4 shows the three differential equations that form the basis of the numerical model. The terms in each relation and their bearing on the characteristic stress-strain behavior of an SMA wire are described in the sections below.

The differential equations that drive the SMA behavior are implemented into a Simulink model that facilitates coupling of multiple SMA wires and structural elements. The inputs to the Simulink model are controlled by a MATLAB script that cycles through different wire pre-stresses, actuation frequencies, and input power amplitudes. The different output variable arrays are then saved for later plotting.

Table 4: Numerical Model – Coupled Temperature and Phase Fraction Evolution Equations

Description	Differential Equation
Change in martensite plus phase fraction	$\dot{x}^+ = -x^+ p^{+A} + x^A p^{A+}$
Change in martensite minus phase fraction	$\dot{x}^- = -x^- p^{-A} + x^A p^{A-}$
Change in wire temperature	$\rho c \dot{T} = 2h(T - T_0) / R + j - H(\dot{x}^+ + \dot{x}^-)$

### 2.1.1.1 Phase Fraction Evolution Equations

The time rate of change of the phase fractions is governed by equations (2.1) and (2.2).

$$\dot{x}^+ = -x^+ p^{+A} + x^A p^{A+} \quad (2.1)$$

$$\dot{x}^- = -x^- p^{-A} + x^A p^{A-} \quad (2.2)$$

where  $p^{\alpha\beta}$  is the transition probability between phase  $\alpha$  and phase  $\beta$ . Also,  $x^A$ ,  $x^+$ , and  $x^-$  are the volume fractions of the austenite, tensile-preferred martensite, and compression-preferred martensite phases, respectively. The change in austenite is simply  $\dot{x}^A = 1 - \dot{x}^+ - \dot{x}^-$ .

### 2.1.1.2 Phase Transition Probabilities

The probabilities of an SMA constitutive element transitioning from one phase to another are the result of barriers in the energy landscape. They ultimately reduce to functions of temperature and stress shown in equations (2.3) and (2.4).

$$p^{\pm A}(\sigma, T) = \frac{1}{\tau_x} \frac{\exp\left[-\frac{V_{LE}}{2E_M k_B T} (\sigma_M \mp \sigma)^2\right]}{\text{erfc}\left[\sqrt{\frac{V_{LE}}{2E_M k_B T}} (\sigma_M \mp \sigma)\right]} \quad (2.3)$$

$$p^{A\pm}(\sigma, T) = \frac{1}{\tau_x} \frac{\exp\left[-\frac{V_{LE}}{2E_M k_B T} (\sigma_M \mp \sigma)^2\right]}{\text{erfc}\left[\sqrt{\frac{V_{LE}}{2E_A k_B T}} (\sigma_A + \sigma)\right] + \text{erfc}\left[\sqrt{\frac{V_{LE}}{2E_A k_B T}} (\sigma_A - \sigma)\right]} \quad (2.4)$$

The meaning of the terms in equations (2.3) and (2.4) are given in Table 5. The derivation of the transition probabilities is based in statistical physics and can be seen in detail in [42] and [44].

Table 5: List of Variables Used in Transition Probability Calculations

Parameter	Description [units]	Unit
$V_{LE}$	Lattice element activation volume	$m^3$
$\tau_x$	Transition attempt frequency of the layer	$s^{-1}$
$k_B$	Boltzmann constant	$J/K$
$c$	Specific heat	$\frac{J}{kgK}$
$\rho$	Density of Nitinol	$\frac{kg}{m^3}$
$R_{sma}$	Radius of SMA wire	$\mu m$
$L_0$	Length of SMA wire	$mm$
$E_A$	Austenite Young's modulus	$GPa$
$E_M$	Martensite Young's modulus	$GPa$
$\varepsilon_T$	Transformation strain	
$\sigma_A$	Transformation stress (A to M)	$Pa$
$\sigma_M$	Transformation stress (M to A)	$Pa$
$\sigma$	Wire stress	$Pa$
$\Delta\sigma$	Hysteresis loop width	$MPa$
$\sigma_{AL}$	$\sigma_A$ at low temperature	$MPa$
$d\sigma/dT$	Thermal dependence of stress	$\frac{MPa}{K}$
$H$	Latent heat of phase transformation	$\frac{W}{m^3}$
$h$	Convective cooling coefficient	$\frac{W}{m^2K}$
$T$	Current wire temperature	$K$
$T_L$	Temperature dependence parameter	$K$

Figure 61 shows how the transformation stresses are defined in the context of a typical single-crystal SMA stress-strain diagram. From Figure 61, the martensite to austenite transformation stress can be written as shown in equation (2.5).

$$\sigma_M = \sigma_A - \Delta\sigma \quad (2.5)$$

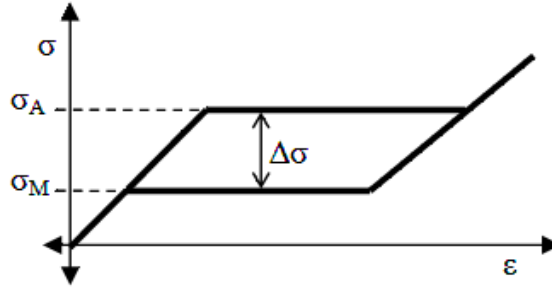


Figure 61: Diagram of Model Parameters on Stress-Strain Hysteresis Loop

The value of  $\sigma_A(T)$  is defined by equation (2.6).

$$\sigma_A(T) = \sigma_{AL} + \frac{d\sigma}{dT}(T - T_L) \quad (2.6)$$

The parameter  $\sigma_{AL}$  is the plateau stress at a predetermined “low” temperature,  $T_L$ , which is set such that  $\sigma_A$  is less than zero when  $T$  is less than the austenitic start temperature, as found on the product specification [1]. From equation (2.6),  $d\sigma/dT$  describes how much the hysteresis loop in a stress-strain diagram will rise when the temperature of the material increases, and should be set based on experimental data showing the stress-strain behavior at two or more temperatures.

### 2.1.1.3 Thermal Equilibrium Equation

The time rate of change of SMA temperature  $T$  is a function of the electrical power passed through the SMA wire, the rate of heating or cooling due to the latent heats of phase transformations, and the convective exchange between the surface of the wire and the ambient environment. The balance of internal energy reduces to equation (2.7)

$$\rho c \dot{T} = 2h(T - T_0)/R + j - H(\dot{x}^+ + \dot{x}^-) \quad (2.7)$$

where  $j$  is the volume power density of applied joule heating,  $H$  is the latent heat of transformation for martensite [11],  $c$  is the specific heat, and  $\rho$  is the density of the SMA [1]. The heat convection coefficient,  $h$ , is set by looking at experiments run at two different frequencies. Further discussion on the terms in the internal energy balance can also be found in Appendix B, where heat conduction is also considered.

### 2.1.1.4 Stress-Strain Relation

The constitutive relationship between the applied stress  $\sigma$  and the resultant strain  $\varepsilon$  in a single-crystal SMA material is given by equation (2.8). The inverse relation of stress in terms of strain is shown in equation (2.9).

$$\varepsilon = x^A \left( \frac{\sigma}{E_A} \right) + x^+ \left( \frac{\sigma}{E_M} + \varepsilon_T \right) + x^- \left( \frac{\sigma}{E_M} - \varepsilon_T \right) \quad (2.8)$$

$$\sigma = \frac{\varepsilon - \varepsilon_T (x^+ - x^-)}{\left( \frac{x^A}{E_A} + \frac{x^+ + x^-}{E_M} \right)} \quad (2.9)$$

The modulus of austenite and martensite are  $E_A$  and  $E_M$ , respectively. The strain value  $\varepsilon_T$  represents the maximum recoverable strain, as indicated in Figure 62.

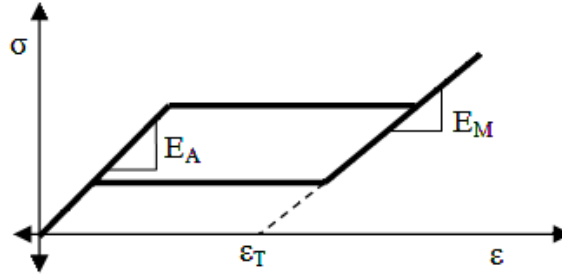


Figure 62: Typical SMA Stress-Strain Curve with Austenitic and Martensitic Elastic Moduli

### 2.1.1.5 Resistance Model

This model implementation extends the model in [42] by including a relationship between the current phase fractions and SMA resistance. The average resistivity in the SMA is a function of the resistivity of the wire in each phase scaled by the fraction of each phase present, as shown in equation (2.10)

$$\rho_{SMA}(T) = \left[ x^A \rho_A(T) + x^+ \rho_+(T) + x^- \rho_-(T) \right] \quad (2.10)$$

where  $\rho_A(T)$ ,  $\rho_+(T)$ , and  $\rho_-(T)$  are the temperature-dependent resistivity's of each component phase. The temperature dependence of each resistivity value is defined in equation (2.11) through equation (2.13)

$$\rho_A(T) = \rho_{0A} (1 + \alpha^A \Delta T) \quad (2.11)$$

$$\rho_+(T) = \rho_{0+} (1 + \alpha^+ \Delta T) \quad (2.12)$$

$$\rho_-(T) = \rho_{0-} (1 + \alpha^- \Delta T) \quad (2.13)$$

where  $\alpha^i$  is the percentage change in resistivity per degree Kelvin for material phase  $i$ . The total resistance of the SMA wire is then given by equation (2.14)

$$\Omega(T, x^A, x^+, x^-) = \frac{\rho_{SMA}(T, x^A, x^+, x^-) L_0}{A_0} \quad (2.14)$$

where  $L_0$  and  $A_0$  are the fully-austenitic reference length and cross-sectional area of the wire, respectively. This model captures the effects caused by the changing temperature of the wire as well as the change in phase. The thermal effect is captured explicitly by equations (2.11) - (2.13). The implementation of the resistance model in the opposing SMA system to be presented in section 2.1.3.2 (and Appendix B) will also include explicit contributions from deformation due to the elastic straining and lateral contraction.

The temperature dependence coefficients, shown in Table 8, were set so that the slope of the resistance-power curve of the fully martensitic and fully austenitic wires agreed between experiment and simulation. Similarly, the phase resistivity's were set so that the change in resistance of the macroscopic wire due to phase transformation agreed between experiments and simulation.

## 2.1.2 Single SMA-Spring System

Once defined, the simplified material model is implemented into a system that is relevant to embedded SMA applications. For practical SMA actuator applications, a restoring force is needed to enable repeated actuation. This restoring force is often provided by structural elements that flex when the wire is heated and thus actuated (contracted), then act as a spring to lengthen the SMA wire upon cooling. The addition of a pre-stretched linear bias spring in series with an SMA wire, as shown in Figure 63, provides a generalization of that restoring force. The spring also alters the stress-strain response of SMA material by constraining it to be linear.

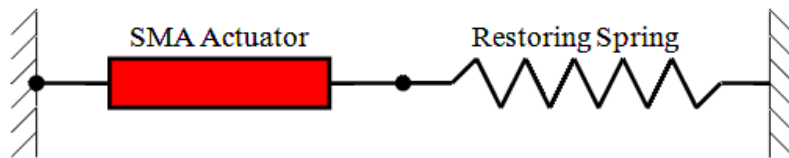


Figure 63: Diagram of SMA and Spring in Series

Figure 64 illustrates the effect of actuator behavior with increasing input power, and thus wire temperature, similar to Figure 8 in Part 1. Depictions of the stress-strain responses of an SMA wire at increasing power levels are plotted, as well as the characteristic stress-strain curve of a spring (for a given pre-stress). Note that the characteristics of the spring and SMA wire have stresses of different sign. This is because a contraction of the SMA wire causes a lengthening of the spring, and vice versa.

In Figure 64, the left branch of the hysteresis loops that pass through the origin represents the stress-strain behavior expected from material while it is in the austenite phase. The right branches represent the characteristic behavior of the tensile-preferred martensite phase. When the strictly linear load-deformation characteristic of the spring causes the material to find equilibrium on one of the horizontal plateaus, the wire is a mixture of the two phases.

The actuator equilibrium points are the intersection points between the SMA and spring characteristic lines. For an SMA wire pre-stressed to  $\sigma_p$  as shown in the top-left panel in Figure 64, the stress-strain equilibrium is indicated by triangles. Upon thermal loading, the hysteresis loop will rise and

equilibrium will follow the bottom branch, indicated by black triangles pointing up. Upon, thermal unloading, the equilibrium will follow the top branch as indicated by the gray, downward-pointing triangles. This difference in path from loading to unloading will result in a hysteresis in the temperature (or input power) vs. strain, stress, and resistance curves.

If additional pre-stress is added, the location of the spring characteristic and x-axis intercept will be shifted to the right, and the equilibrium position will be shifted up and to the right, as shown by the light gray lines in the top-left and bottom-right panels in Figure 64. As a result, additional pre-stress will necessitate a higher heating input energy to achieve complete phase transformation. This is apparent in the bottom-right panel in Figure 64; the higher pre-stress results in equilibrium, indicated by the gray circle, that is not fully on the austenite branch at  $T_4$ . This behavior is modeled and presented extensively in the literature [40]-[44],[47]-[51], but now the effect on SMA resistance as pre-stress is added.

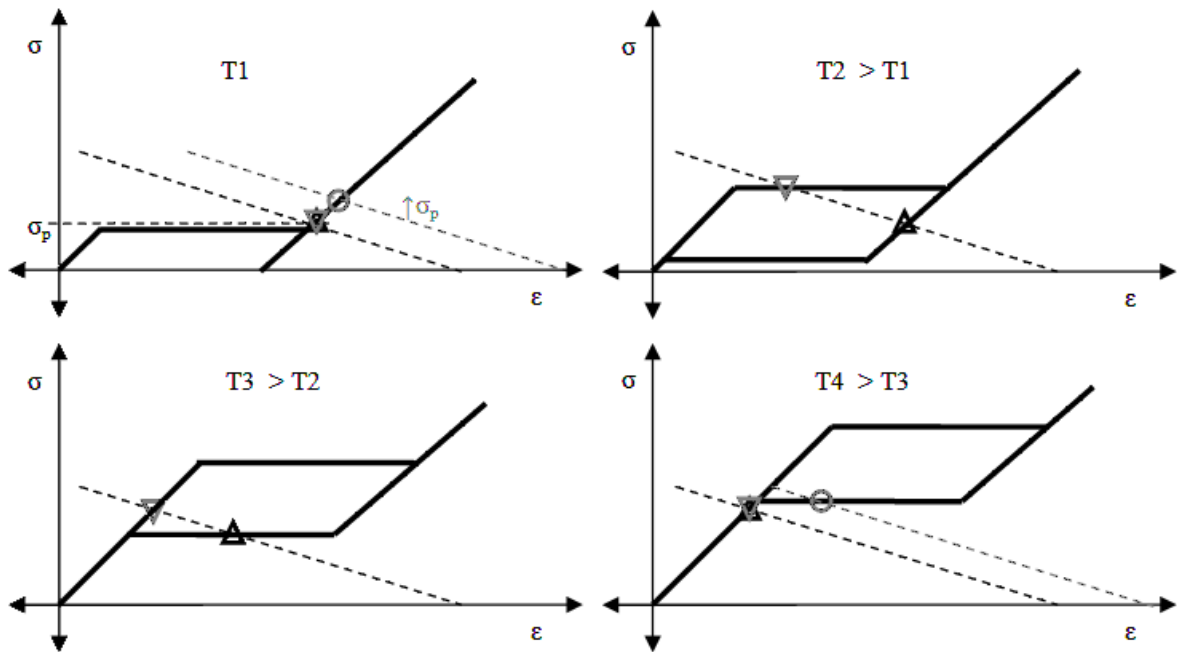


Figure 64: Stress-Strain Equilibrium Diagrams for an SMA Wire and Spring at Different Temperatures

Also, most researchers compare SMA stress, strain, and resistance to a constant input voltage or current. However, wire temperature is more directly related to the input power. When subjected to a constant current, a wire will heat more as the wire is strained and its resistance increases. The opposite occurs when the wire is heated with a constant voltage. Finally, studies correlating SMA resistance to strain [36],[52]-[54] that are needed to enable the use of SMA wires as position sensors are few, and none are available for the case of an SMA actuator system under power-control.

### **2.1.2.1 Objectives of Single SMA-Spring System Study**

The objective of the single SMA-spring system study presented in this section is to characterize numerically and experimentally the behavior of a shape memory alloy actuator system consisting of an SMA wire and spring in series. The effect of actuator pre-stress and actuation frequency are

studied, and the stress, strain, and resistance characteristics are plotted against Joule heating power. A simplification of a previously presented physics-based model [31] is implemented to provide a framework for studying the material's response to the input most relevant to SMA actuator applications: controlled heating power inputs at various cycling frequencies. Further, a new model is developed to predict SMA resistance based on SMA wire temperature and phase fractions. Simulations are then compared to measurements taken using a multi-functional power supply [45],[46]. The resistance measurements are studied with the aim of using resistance measurements as a position feedback sensor in future applications. The SMA wire studied in experiments is a 50  $\mu\text{m}$  HT option Flexinol wire from Dynalloy [1] and the spring is a cantilever beam with an equivalent linear spring stiffness of 0.34 N/mm.

### 2.1.2.2 SMA Model Implementation and Parameters

#### Kinematic and Force Balance

To simulate the coupled SMA-spring system shown in Figure 65, the material stress-strain in equation (2.8) is adjusted to include a the force contribution from the spring. The force equilibrium for the system in Figure 65 is given by

$$F_{SMA} = -F_k. \quad (2.15)$$

where  $F_k = k\delta$  is the force in the spring. The deflection of the SMA junction shown in Figure 65 is defined as

$$\delta = L_{0,SMA} (\varepsilon - \varepsilon_p). \quad (2.16)$$

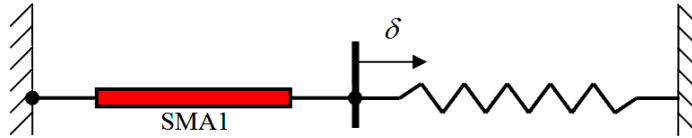


Figure 65: Sketch of Coordinate System for Single SMA Wire and Spring System

The pre-strain  $\varepsilon_p$  is determined by calculating the strain in the SMA wire that will generate the desired pre-stress via equation (2.8). It is common for the pre-stress to be chosen such that the SMA wire will be 100% in the  $M^+$  phase, in which case equation (2.8) simplifies to

$$\varepsilon_p = \frac{\sigma_p}{E_M} + \varepsilon_T. \quad (2.17)$$

In order to compare spring force to SMA wire stress the spring force is normalized by the cross-sectional area of the SMA wire,  $\sigma_k = \frac{F_k}{A_c}$ , the force equilibrium in equation (2.23) can be written in terms of stresses

$$\sigma = -\sigma_k. \quad (2.18)$$

Substituting the constitutive stress-strain relationship (9) for each wire yields

$$\frac{\varepsilon - \varepsilon_T (x^+ - x^-)}{\left( \frac{x^A}{E_A} + \frac{x^+ + x^-}{E_M} \right)} = -\frac{kL_{0,SMA}}{A_c} (\varepsilon - \varepsilon_p). \quad (2.19)$$

The equilibrium strain is found by solving for  $\varepsilon$ ,

$$\varepsilon = \left( \frac{A}{B} - k\varepsilon_p \right) \left( \frac{1}{B} - \frac{kL_{0,SMA}}{A_c} \right)^{-1}, \quad (2.20)$$

where

$$A = \varepsilon_T (x^+ - x^-), \quad (2.21)$$

and

$$B = \left( \frac{x^A}{E_A} + \frac{x^+ + x^-}{E_M} \right). \quad (2.22)$$

Finally the stress  $\sigma$  can be calculated directly using equation (2.9).

### Modeling Parameters

The modeling parameters used in simulations of the single SMA-Spring system are listed in Table 6. Parameters relating to the resistance model are shown in Table 7.

Table 6: SMA Wire and Heat Transfer Model Parameters

Parameter	Description [units]	Value	Unit
$V_{LE}$	Lattice element activation volume	$5 \times 10^{-23}$	$m^3$
$\tau_x$	Transition attempt frequency of the layer	0.01	$s^{-1}$
$k_B$	Boltzmann constant	$1.38044 \times 10^{-23}$	$J/K$
$c$	Specific heat	600	$\frac{J}{kgK}$
$\rho$	Density of Nitinol	6400	$\frac{kg}{m^3}$
$R_{sma}$	Radius of SMA wire	25	$\mu m$
$L_0$	Length of SMA wire	53.35	$mm$
$k$	Linear spring constant	0.34	$\frac{N}{mm}$
$E_A$	Austenite Young's modulus	75.0	$GPa$
$E_M$	Martensite Young's modulus	28.0	$GPa$
$\varepsilon_T$	Transformation Strain	0.024	
$\Delta\sigma$	Hysteresis loop width	150	$MPa$
$\sigma_{AL}$	$\sigma_A$ at low temperature	190	$MPa$
$d\sigma/dT$	Thermal dependence of stress	4.6	$\frac{MPa}{K}$
$H$	Latent heat of phase transformation	3.75	$\frac{W}{m^3}$
$h$	Convective cooling coefficient	600	$\frac{W}{m^2K}$
$T_L$	Temperature dependence parameter	318	$K$

Table 7: SMA Wire Resistance Model Parameters

Parameter	Description [units]	Value	Unit
$\rho_{0A}$	Resistivity of Austenite phase	$8.9 \times 10^{-8}$	$\Omega m$
$\rho_{0\pm}$	Resistivity of martensite phase	$10.2 \times 10^{-8}$	$\Omega m$
$\alpha^A$	Temperature dependence of Austenite phase	0.0002	$K^{-1}$
$\alpha^\pm$	Temperature dependence of martensite phase	0.00015	$K^{-1}$

### 2.1.2.3 Effect of Using a Single Crystal Model to Simulate a Polycrystalline Material

When looking at results in the next two sections it is important to note that this model assumes a perfect single-crystal SMA. However, in reality an SMA wire is composed of many crystals, all of which have slightly different properties, such as transition temperature and stress. The properties of the bulk wire then become an average of the properties of the different crystals. Figure 66 shows the single crystal stress-strain characteristic in black with sharp edges along with a representation of the behavior expected from a real, polycrystalline material, shown in gray. The polycrystalline material

will have smooth phase transitions resulting from different grains transforming at slightly different times.

As in Figure 64, a characteristic of a linear spring is overlaid, and the equilibrium points are highlighted, with black squares showing equilibrium with the single-crystal SMA and gray circles showing equilibrium with the polycrystalline SMA. Also note that in Figure 66 the subscripts “s” correlate to results derived from the single-crystal plot and the subscripts “p” from the polycrystalline.

For a typical SMA wire, the maximum recoverable strain,  $\varepsilon_T$  in the top panel of Figure 66, is often taken to be between 4-5% [1]. However, the addition of the spring reduces the maximum recoverable strain when compared to a system with a constant applied stress (as in a hanging mass) by ensuring that the wire is under a higher stress when the SMA wire is heated and contracted into the austenite phase than when it is cool and martensitic. The stress induced by the spring causes elastic straining along the austenite branch, shown by  $\varepsilon_{s,2}$  in the bottom panel of Figure 66. As a result,  $\delta_s$  will be less than  $\varepsilon_T$ .

An additional reduction in stroke is apparent because of the polycrystalline nature of an actual SMA wire. The expected strokes of a single-crystal and polycrystalline actuator are labeled by  $\delta_p$  and  $\delta_s$ , respectively. Clearly, when placed in series with a spring, a polycrystalline SMA wire will exhibit substantially less stroke than would be predicted by a single-crystal model. The smooth curves delay transition to 100% austenite or martensite, so the maximum possible stroke is rarely realized. This phenomenon becomes apparent in comparisons between experimental and initial simulated solutions. However, to account for this known shortcoming in the model, the  $\varepsilon_T$  parameter is simply reduced to 2.4% for the implementation of the single SMA-spring system. This ensures that the scale of the strain, and thus stress as coupled via the spring constant, remain comparable between the simulation and the experiments.

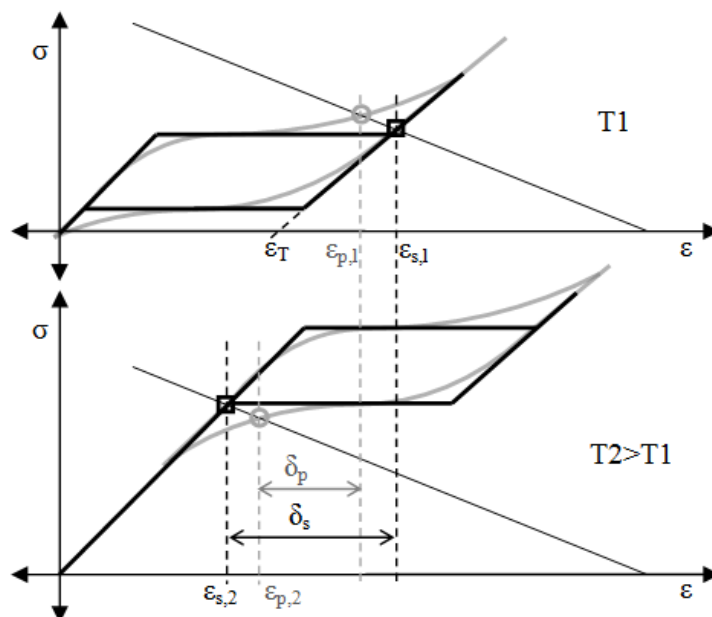


Figure 66: Depiction of Single Crystal (black) and Polycrystalline (gray) Stress-Strain Characteristics and Expected Stroke

An additional limitation of the single-crystal model is apparent on pre-stressing. Since the pre-stressing process is force (stress) controlled, the single-crystal model can only find equilibrium on either the austenite branch or the martensite branch, as shown in the left panel of Figure 67. The horizontal plateau is unattainable during force-controlled loading. Further, the two-way effect causes the wire to find an equilibrium with a higher fraction of martensite plus than martensite minus at low temperature under zero stress. This causes the stress-strain curve to cross the x-axis to the right of the origin at  $\epsilon_{0M}$ , which often measures up to 2% strain, as indicated by the dotted gray line in Figure 67. The smooth transitions of the polycrystalline characteristic and change in characteristic due to the two-way effect change the equilibriums, as shown in the right panel of Figure 67.

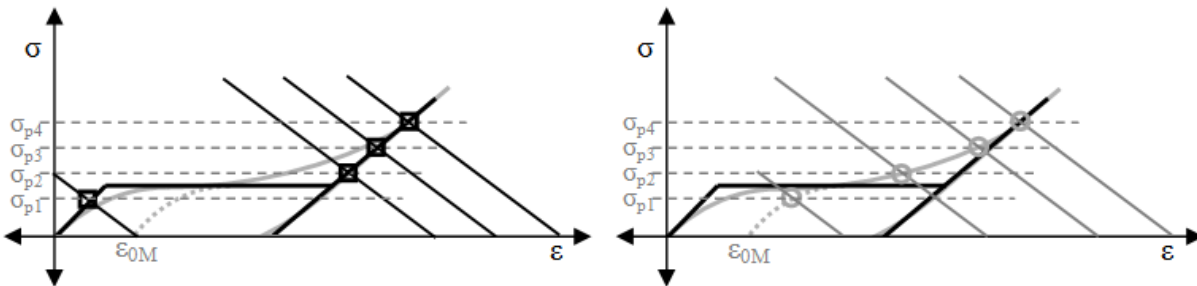


Figure 67: Equilibriums Attainable during Pre-stressing in a Single Crystal (left) and Polycrystalline (right) Material.

#### 2.1.2.4 Experiment Setup

A simple tensile-testing setup is used to characterize the behavior of the SMA actuator wire in series with a flexure spring. The electrical power used to heat the wire through Joule heating is input through a pulse-width-modulation (PWM) based power controller [45],[46]. Since the increase in temperature due to Joule heating is proportional to the power input, controlling power gives the best control over SMA temperature. A constant, continuous current source would cause less heating as the wire shortens and its resistance decreases.

The power supply ensures that the total power put into the wire remains constant, even as the resistance of the SMA wire changes during actuation. It does this by pulsing a current wave with constant amplitude at high (~1 kHz) frequency, while adjusting the duty cycle of the pulse to adjust the total power going into the wire every millisecond. Since the heating and cooling processes happen much more slowly than 1 ms, the temperature of the wire is not affected by the individual pulses, only the average of many pulses. At the same time as the current is pulsed, the voltage across the SMA wire is measured. As the wire is heated and strained during a tensile test its resistance changes; however, since peak current is constant, the peak voltage measured during each pulse can be used to calculate the wire resistance directly. This resistance measurement is also used to update the duty cycle of the constant current pulse for the next cycle.

The tensile test setup used to characterize the SMA wire is diagrammed in Figure 68 and photographed in Figure 69. The 50  $\mu\text{m}$  Flexinol SMA wire is connected in series with a spring-steel cantilever flexure with stiffness of 0.34 N/mm, as shown in Figure 68. On the right boundary, a clamp transmits the tensile load to a Futek Model LSB200 load cell with a 9 N (4.6 GPa stress, for a

50  $\mu\text{m}$  diameter wire) load limit that is oversampled and filtered for a peak resolution of 0.14 mN (0.1 Mpa) and a Zaber Model T-NA08A25 linear actuator with 0.6  $\mu\text{m}$  controller resolution. The linear actuator provides position feedback, so the position of the right boundary of the SMA wire can be effectively tracked. A Micro-Epsilon optoNCDT 1300 laser displacement sensor with 25  $\mu\text{m}$  resolution is used to track the deflection of the flexure, and thus the left boundary of the wire while the wire is actuated. All of the components are aligned on a ThorLabs rail and enclosed in a 0.5x0.6x0.2 m acrylic box to isolate the wire from environmental disturbances.

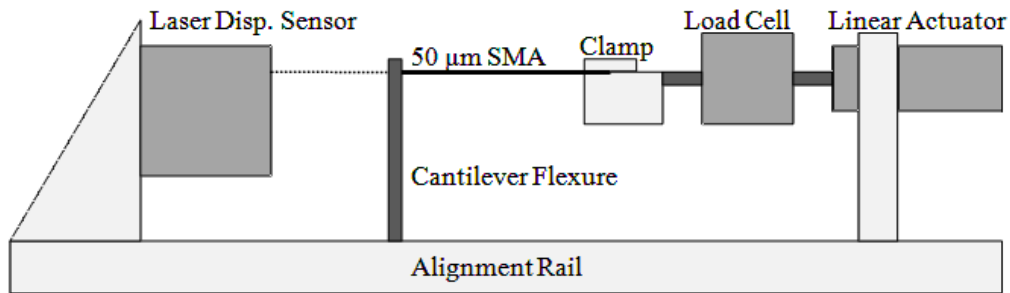


Figure 68: Diagram of SMA-Flexure Test Setup

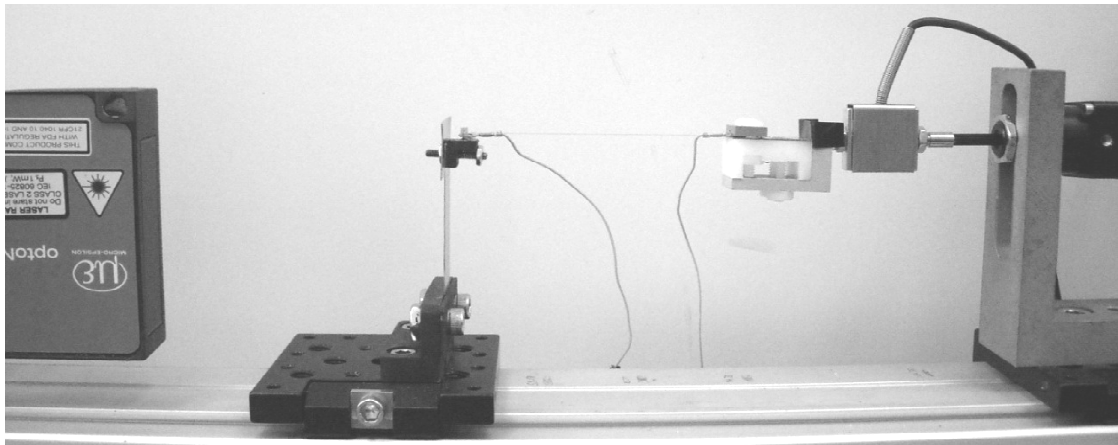


Figure 69: Photograph of SMA-Flexure Testing Setup

### 2.1.2.5 Experiment Procedure

Because of the hysteretic nature of SMA wires, the procedure used to conduct the tensile tests is essential to understanding the results. Also, the wire was actuated through 50 cycles to eliminate drift prior to the start of experimentation. The steps taken to prepare the wire used in each test are documented below.

1. Secure the wire between the clamp and the flexure mount, ensuring that there is slack in the wire.
2. Heat the wire under 0 stress with 0.012 W/mm input power for 10 s. Neglecting incomplete phase transformation due to conductive cooling at the wire endpoints (Appendix B), this will transform the wire to  $\sim 100\%$  austenite.
3. With the heat still applied, retract the linear actuator until the load cell and laser displacement sensor detect a small force and displacement, respectively. Record the wire length as the austenitic length,  $L_{0A}$ .

4. Turn off the power into the wire, and allow the wire to cool for 10 s to the martensitic twin phase. Note that the two-way effect will cause a greater percentage of the wire to be in the martensite plus phase.
5. Retract the linear actuator until the load cell and laser displacement sensor detect a small force and displacement, respectively. Record the wire length as the martensitic length,  $L_{0M}$ .
6. Retract the linear actuator until the load cell measures a stress in the wire equal to the desired pre-stress for this test.
7. Stop the linear actuator and begin cycling the power input 10 times in a triangle wave with the desired frequency and amplitude, as shown in Figure 70.
8. Repeat steps 1-7 for all desired pre-stresses and input power amplitudes and frequencies.

### 2.1.2.6 Tensile Test Inputs

For each of the desired pre-stress values, 9 different input power signals shown in Figure 70 were used to actuate the SMA wire. Each signal was allowed to run for 10 cycles. The frequencies used were 0.1, 0.5, and 1 Hz, and the amplitudes were 0.004, 0.008, and 0.012 W/mm. Since the wire's nominal length was 50 mm, these power densities result in 0.2, 0.4, and 0.6 W input power amplitudes. Preliminary results showed that 0.008 W/mm was sufficient to induce complete phase transformation at all pre-stress values, so the plots taken at this power amplitude value are presented in the following sections.

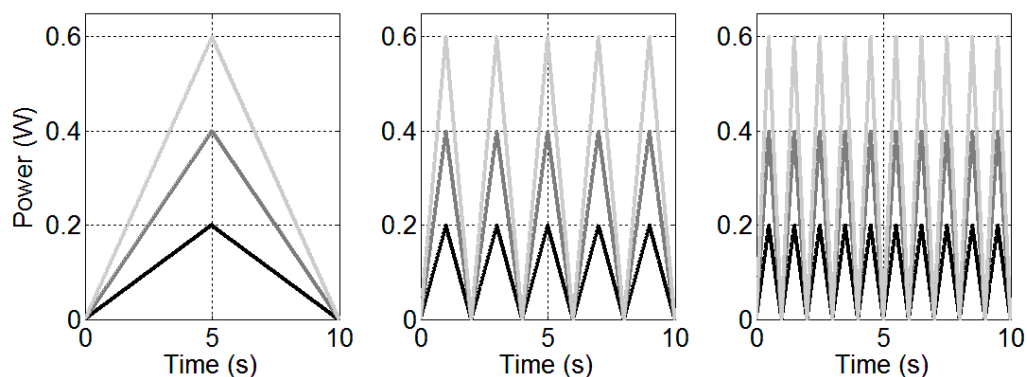


Figure 70: Input Power Signals Shown over 10 s at 0.1 Hz (left), 0.5 Hz (middle), and 1.0 Hz (right)

### 2.1.2.7 Numerical and Experimental Results

The numerical and experimental results are compared and the effect of changing wire pre-stress and actuation frequency is studied. Careful attention is paid to the relationship between wire strain and resistance, since this is the characteristic that will enable an SMA wire to be used as a position feedback sensor during actuation. In all plots, experimental results are shown in the left panel and simulated results in the right panel.

#### Effect of SMA Pre-stress.

In this section, the effect of the wire pre-stress on the characteristic behavior of an SMA wire actuated at low (0.1 Hz) frequencies is examined. Figure 71 shows how the wire strain changes as input power is cycled. As pre-stress is increased, the hysteresis loops move up and to the right on the power-strain

curves. This is because a larger input power is needed to overcome a larger pre-stress and induce wire contraction. This behavior is accurately captured by the model; however, the model underestimates the magnitude of the upward motion of the hysteresis. The discrepancy results from the fact that a single crystal model is employed in these simulations. In a single crystal model, phase transformation results in an equilibrium state that is either on the horizontal plateau of the hysteresis, entirely on the austenitic branch, or entirely on the martensitic branch. In reality, the material makes a smooth transition between the plateau and martensitic branch since not all grains change phase at the same instant. A more realistic depiction of stress-strain behavior is indicated by the gray line in Figure 66. This means that the 50 MPa incremental increases in pre-stress actually may result in equilibrium states between the austenitic and martensitic branches, as shown in Figure 67. In the case of the model, the material is already on the stiff martensite branch after 50 MPa, so any additional stress will only cause only small 0.07 % increases in strain per 50 MPa stress increase.

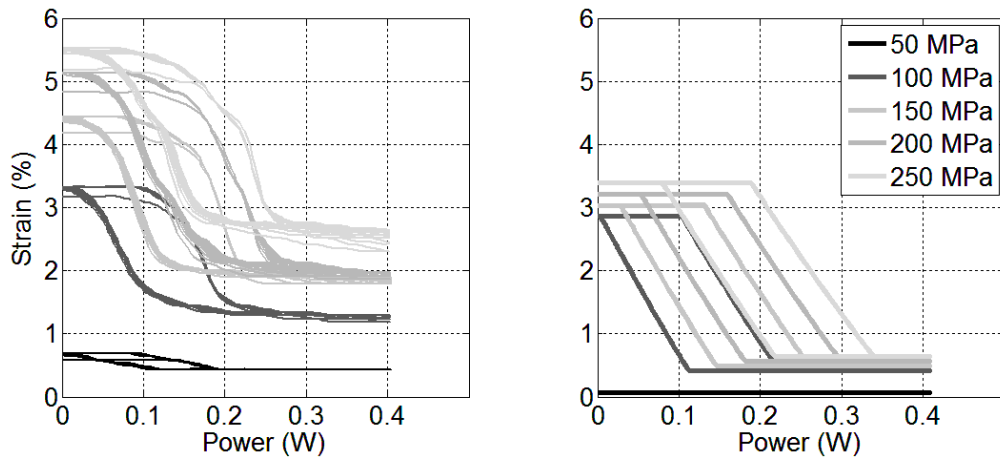


Figure 71: Power vs. Strain for Different Pre-stresses with 0.1 Hz Heating Frequency

Figure 72 shows that increased pre-stress causes the power-stress hysteresis to move up, as expected. Also, note that the curves show that phase transformation is delayed (it requires a larger power input) when pre-stress is higher. This is the same mechanism that causes the hysteresis loops in Figure 71 to move to the right. Note that the 50 MPa pre-stress case exhibited very little change in stress, and thus strain. This is because the 50 MPa pre-stress was unable to place the wire in the martensite plus phase prior to power cycling. The magnitude of the measured stresses are different from the simulated stresses because the simulation requires that pre-stressing place the SMA on the austenite line or the martensite line, but the actual wire is polycrystalline and can be placed at points in between, as discussed in Section 2.1.2.2.

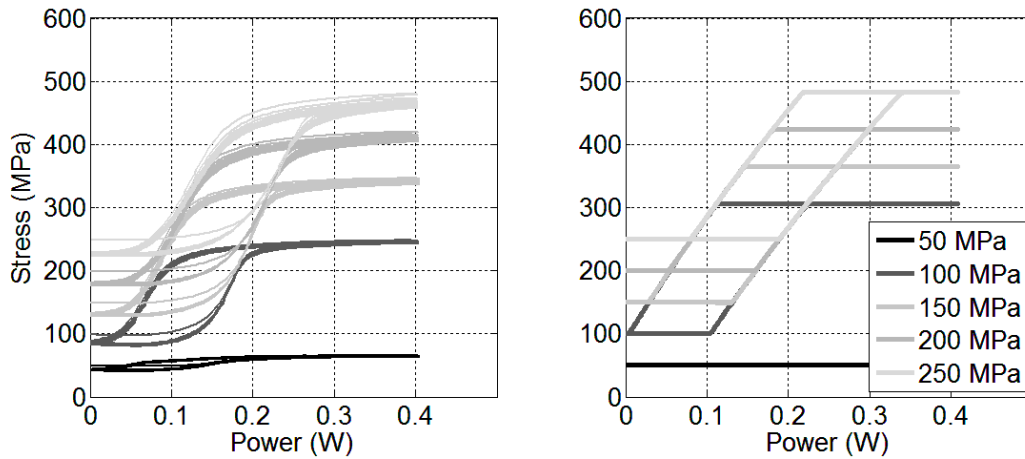


Figure 72: Power vs. Stress for Different Pre-stresses with 0.1 Hz Heating Frequency

The resistance plots in Figure 73 show that resistance follows approximately the same characteristic as strain in Figure 71. However, the thermal contribution causes the resistance of the wire to increase as power input and thus temperature, are increased. Once phase transformation and wire contraction are complete, the wire continues to heat due to further increases in input power, so resistance begins to increase again. This is apparent for power inputs larger than 0.3 W. The slope of this increase is found in Table 7 as  $\alpha^4$ .

The small loops on the top left of each hysteresis curve result from the rate-dependent cooling of the wire. Since the wire can only cool as quickly as it conducts heat into the ambient environment, the temperature during power unloading is expected to be slightly higher than during power loading. This results in a slightly higher resistance during power loading – the effect is especially noticeable prior to transformation while the wire is still in the martensitic phase.

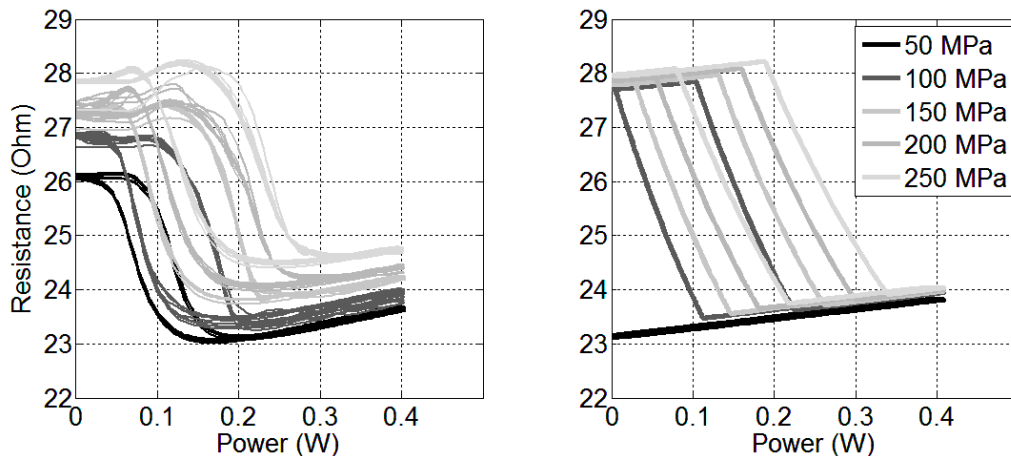


Figure 73: Power vs. Resistance for Different Pre-stresses with 0.1 Hz Heating Frequency

Figure 74 shows the stress-strain plots during the cycled power actuation. Since the stress and strain are constrained by the characteristic of the flexure that is in series with the SMA wire, the relationship is a straight line with slope equivalent to the stiffness of the flexure: about 325 N/m. The polycrystalline nature of the real SMA wire is evident in the experimental results once again. As pre-

stress is increased, the measured characteristics move further out on the strain axis than predicted by the simulation, just as in Figure 71. The non-linearity that is apparent at high stress levels in the experimental stress-strain curves is a result of using an imperfect flexure.

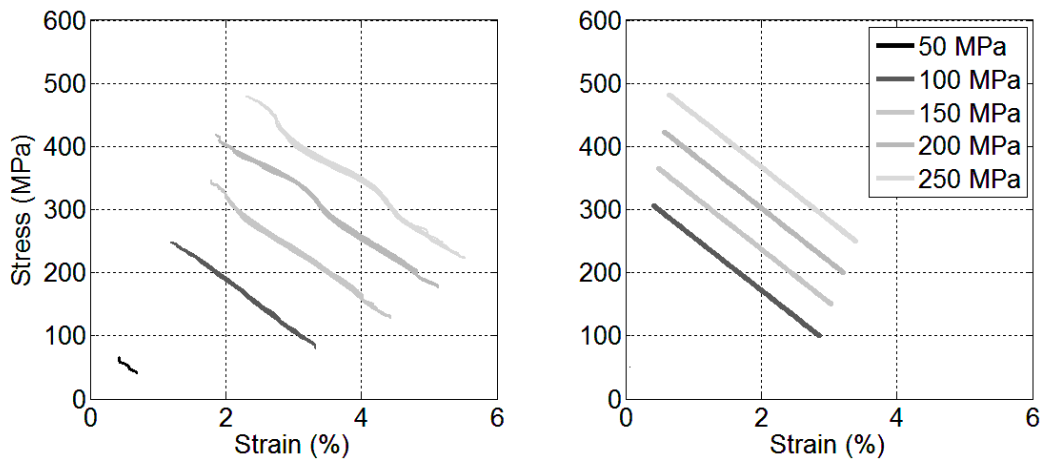


Figure 74: Stress vs. Strain for Different Pre-stresses with 0.1 Hz Heating Frequency

Figure 75 shows the relationship between strain and SMA wire resistance. It is interesting to note that because the strain-dependent term dominates the resistance, the strain-resistance relationship is nearly linear while phase transformation is occurring. However, since the wire continues to heat even after the phase transformation is complete, there is a slight drop in the resistance that occurs after maximum strain is reached. Also, because the resistivity of the martensitic phase is slightly higher than the resistivity of the austenitic phase, there is a narrow hysteresis on thermal unloading. It is important to note that the linearity and repeatability of this strain-resistance characteristic is essential for any application that endeavors to use the SMA wire as a position feedback sensor. For the thermal loading case shown the characteristics show reasonably good linearity and repeatability with only a limited hysteresis.

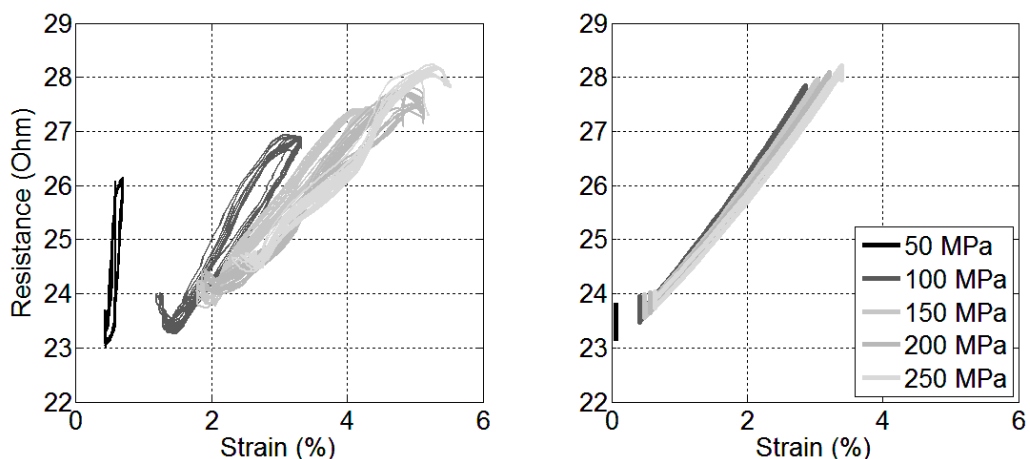


Figure 75: Resistance vs. Strain for Different Pre-stresses with 0.1 Hz Heating Frequency

### Effect of Actuation Frequency

The frequency of the cycled input power has a significant impact on some of the characteristic behavior. This is because the heating and cooling of the wire is rate-dependent. The wire can be heated almost as quickly as desired by simply pushing a larger electrical power through it. However, the wire can only cool as quickly as it can transfer heat out of its surface and into the ambient environment. Since this process is relatively slow, its effects are apparent at thermal loading rates faster than about 0.2 Hz. Figure 76 shows how the rate of loading affects the power-strain curve for a wire pre-stressed to 150 MPa. All three curves start at the same spot: 0 W, and about 3 % strain generated from the 150 MPa pre-stress. However, for rapid heating (1 Hz) the wire is unable to completely heat and contract by the time the power input reaches its maximum and starts to reduce again. It continues to contract as the wire starts to cool, then begins to lengthen again after power is reduced below about 0.22 W. However, it cannot completely cool and lengthen before the power begins to increase again. As a result, the strain starts cycles 2 through 10 at about 2.2 % (for the experimental case shown in the left panel). Similar behavior is observed for the 0.5 Hz actuation frequency, while 0.1 Hz is chosen to be approximately quasi-static – further reductions in actuation frequency have a negligible effect on the hysteresis.

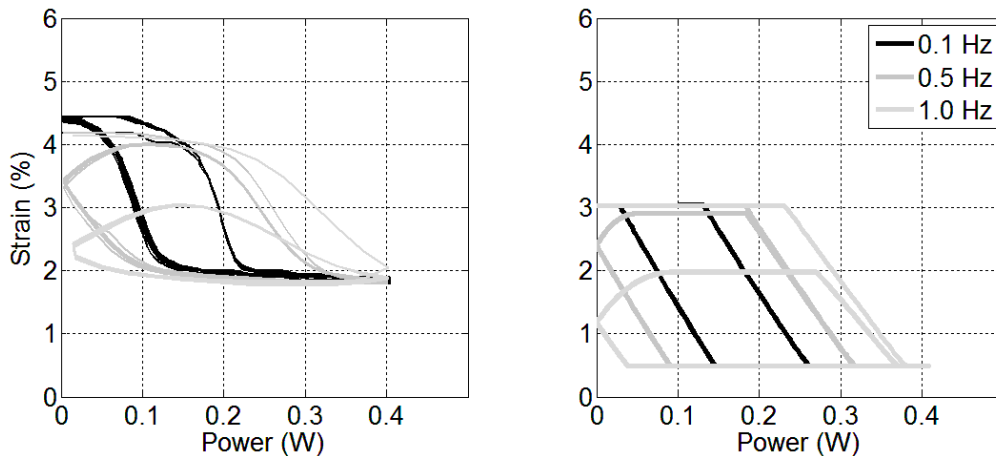


Figure 76: Power vs. Strain for Different Heating Frequencies with 150 MPa Pre-stress

Figure 77 shows the resulting stress as power is cycled. The same effect is evident, and simulations verify that a widening of the hysteresis loop is expected along with the reduction in stress (and strain) amplitude.

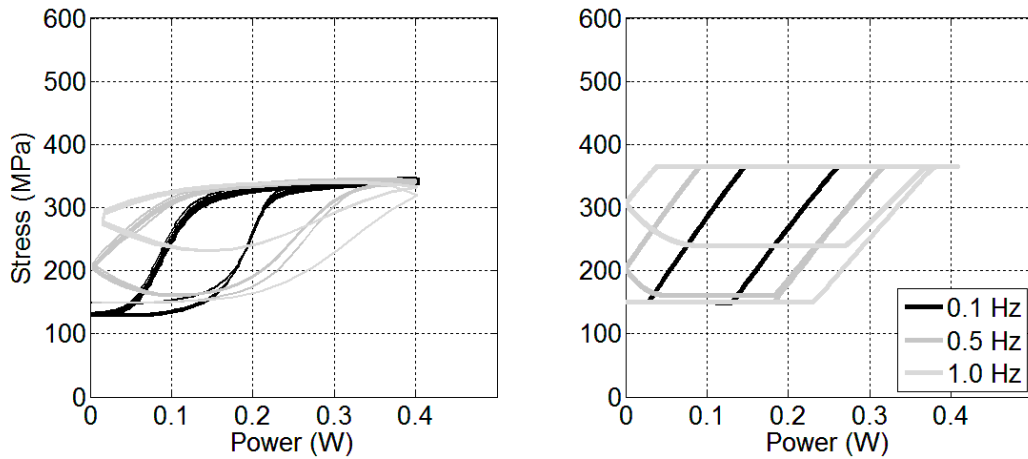


Figure 77: Power vs. Stress for Different Heating Frequencies with 150 MPa Pre-stress

Since resistance measurement is largely dependent on strain, the rate dependent effects are evident in Figure 78 as well. The simulations once again clearly predict the widening of the hysteresis loop as well as the smaller loops at the top-left of the characteristics that result from the dual dependence of resistance on wire strain and temperature.

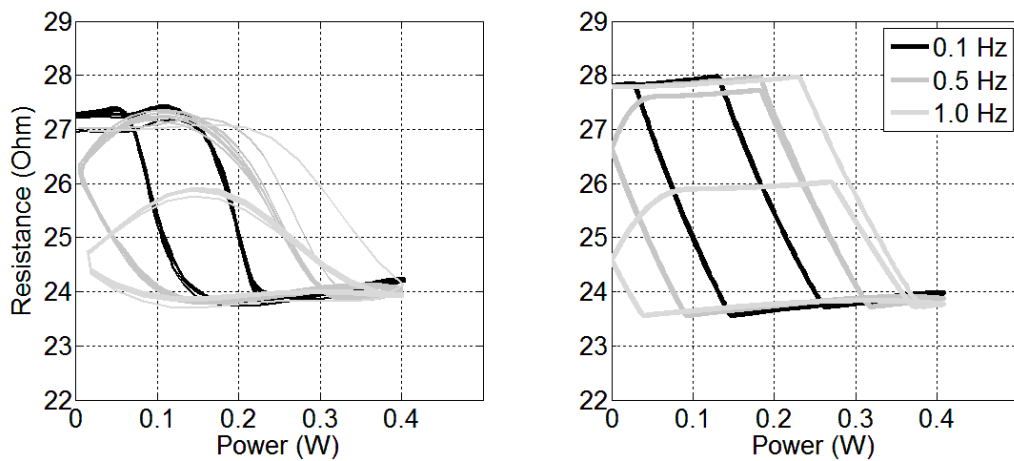


Figure 78: Power vs. Resistance for Different Heating Frequencies with 150 MPa Pre-stress

Once again, the stress-strain relationship is constrained by the load-deformation characteristic of the flexure. The simulated results in the right panel of Figure 79 show that all of the lines are coincident, because only one pre-stress (150 MPa) is shown in the plot. The actuation frequency has no affect on the shape of the stress-strain or resistance-strain plots. However, higher frequency inputs result in an incomplete phase transformation and reduction of stroke. For this reason the strain and resistance do not return to their initial values after the first cycle. Figure 80 shows how the correlation between length and resistivity changes with actuation frequency. Aside from the effect caused by incomplete phase transformation, the shapes of the strain-resistance characteristics are largely independent of frequency.

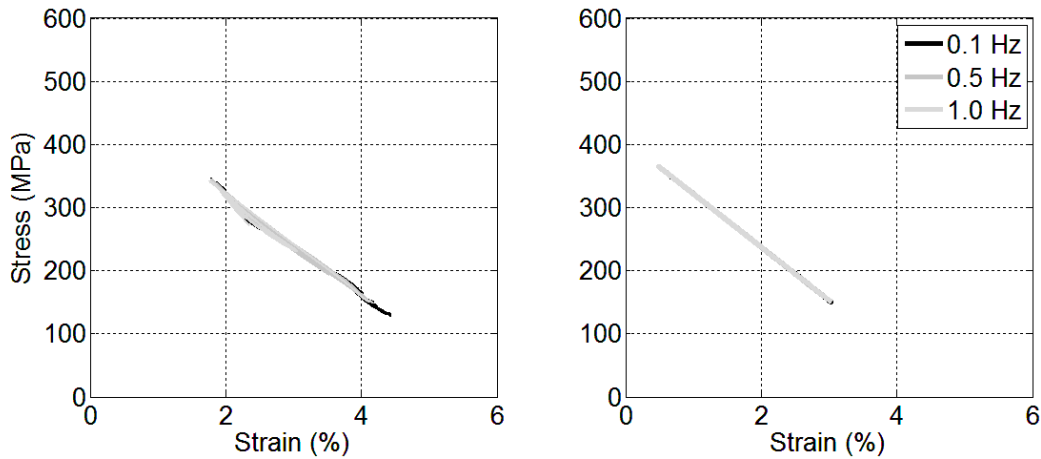


Figure 79: Stress vs. Strain for Different Heating Frequencies with 150 MPa Pre-stress

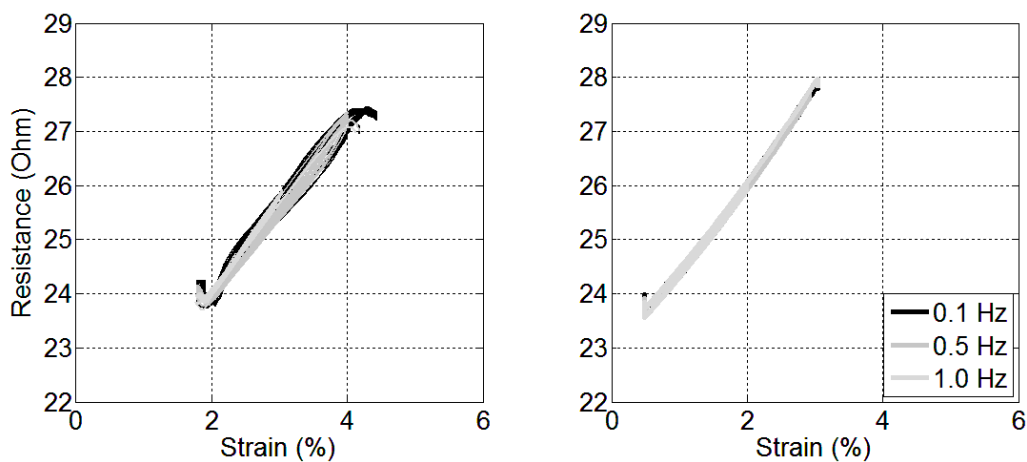


Figure 80: Resistance vs. Strain for Different Heating Frequencies with 150 MPa Pre-stress

The effects of the incomplete phase transformation are highlighted further in Figure 81 and Figure 82. In Figure 81, which shows the strain-resistance characteristic at 0.5 Hz actuation frequency, the resistance does not have time to decrease due to passive cooling before the next heating cycle begins. Figure 82 shows that when actuated at 1.0 Hz, the wire is not even able to completely transform back to its longest, highest-resistance martensitic state. This effect is also evident in Figure 76 and Figure 78. However, this rate-dependent effect is irrelevant for controls applications because the characteristic (i.e. the slope and intercept) of the relationship between the resistance measurement and wire strain is still independent of frequency, as shown in Figure 80. Using the resistance vs. strain plot as a sensor mapping is discussed in greater detail in section 2.2.1.

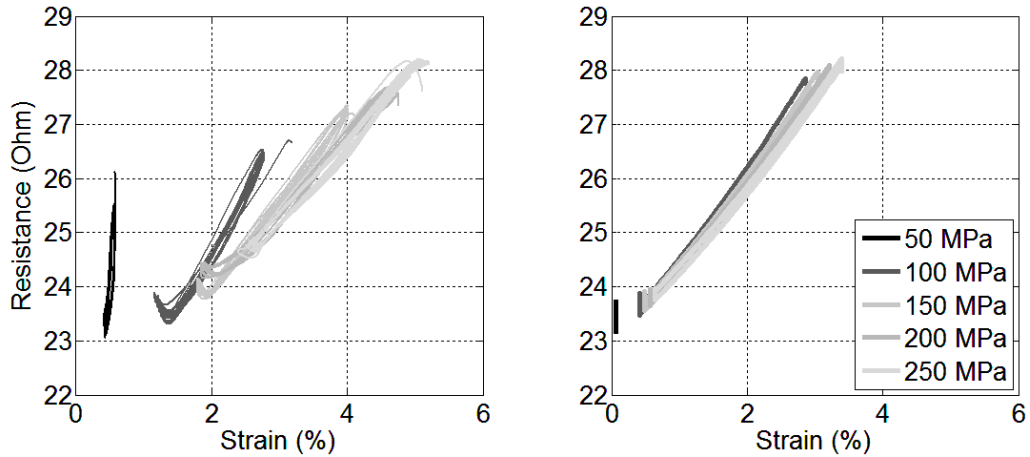


Figure 81: Resistance vs. Strain for Different Pre-stresses with 0.5 Hz Heating Frequency

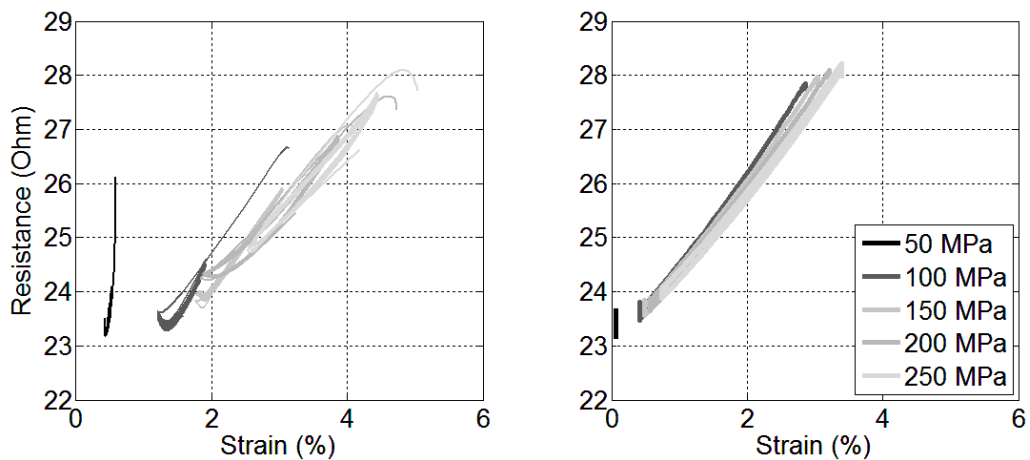


Figure 82: Resistance vs. Strain for Different Pre-stresses with 1.0 Hz Heating Frequency

### 2.1.2.8 Conclusions from Single SMA-Spring System

A number of important conclusions can be extracted from the side-by-side experimental-simulation study on the system of a single SMA wire in series with a spring. First, the comparisons between the experimental and simulated results show that the numerical model can accurately capture the physics of several pre-stress and rate dependent characteristics. When possible, model parameters were extracted from literature. Otherwise they are chosen based to provide the best possible visual comparison for one or two select experiments, then maintained for all of the different pre-stress and rate inputs. The model and experiments show a translation of characteristics in response to changing pre-stress, and a widening of hysteresis loops at higher actuation frequencies.

The added resistance model based on an assumed strain and temperature dependence for both the austenite and martensite SMA phases captures the changes in resistance caused by phase transition and temperature change. The experimental and simulated results suggest that the strain-resistance curve is roughly linear within the actuation range; only a narrow hysteresis resulting from the small difference between the resistivity of the austenite and martensite phases is observed. The linearity and repeatability of this relationship, particularly at high pre-stresses, is encouraging for applications that endeavor to use the resistance measurement as a position feedback sensor, such as will be

presented in section 2.2.1. Also, results show that actuation frequency does not affect the relationship between strain and resistance. However, this relationship is only valid within a certain range of input powers – once power is increased beyond a certain threshold, additional heating causes an increase in resistance rather than a contraction-induced decrease. Regardless, an understanding of the errors and limitations of the resistance measurement will help ensure that a position feedback controller will perform predictably in a practical setting.

### 2.1.3 Opposing SMA System

In the single SMA-spring system studied in the previous section, the SMA wire induces deformation of the structure when it contracts due to heating while the passive structural element provides a restoring force that lengthens the wire again upon cooling, such as is depicted in the left panel of Figure 83. In the configuration in the right panel of Figure 83, an opposing SMA wire can provide an active restoring force, thus increasing the potential actuation frequency and control over positioning. Figure 84 shows a simplification of the dual-SMA system.

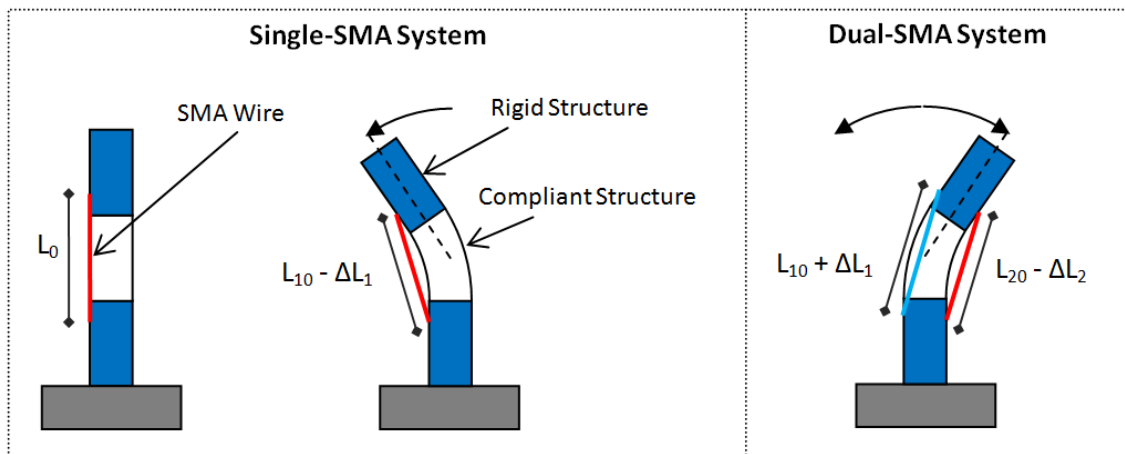


Figure 83: Diagram of Embedded SMA Application with Single-SMA (left) and Dual-SMA Actuation (right)

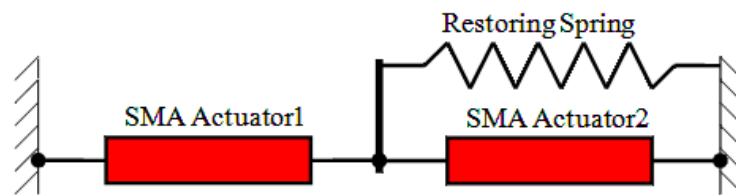


Figure 84: Opposing SMA-Spring System

#### 2.1.3.1 Objectives

In this section the behavior of the opposing SMA system is systematically studied in a controlled setting. The stress, strain, and resistance of both wires in the coupled system are measured and simulated. Simulations are once again provided solely as a means to identify the physical mechanisms behind observed behavior rather than to provide an optimal curve fit. For some results, one wire is prescribed a constant heating power, while the power into the second wire is cycled. In other tests, the input power is alternated between one wire and the other, and the effect of the initial stress or strain state (pre-stress or pre-strain) of the SMA wires as well as the actuation frequency are studied. Results are discussed in the context of using the SMA resistance as a strain or structural deformation measurement in future multi-functional controls applications.

#### 2.1.3.2 SMA Model Implementation and Parameters

A number of adjustments to the force balance and kinematic relations are needed to add a second opposing SMA wire to the simulation. Then the two SMA wires are each modeled with their own sets of phase fractions and temperature, but they are coupled by the kinematics and force equations.

## Mechanical Equilibrium of Opposing SMA-Spring System

The force equilibrium for the system in Figure 84 is given by

$$F_{SMA1} = F_{SMA2} - F_k. \quad (2.23)$$

where  $F_k = k\delta$  is the force in the spring. The deflection of the SMA junction is defined as

$$\delta = L_{0,SMA1} (\varepsilon_1 - \varepsilon_p) = L_{0,SMA2} (\varepsilon_p - \varepsilon_2). \quad (2.24)$$

Using (2.24) and taking  $L_{0,SMA1} = L_{0,SMA2}$ , the strain in the wires are related by

$$\varepsilon_2 = 2\varepsilon_p - \varepsilon_1. \quad (2.25)$$

The pre-strain  $\varepsilon_p$  is controlled to be equal in both SMA wires, and the force in the spring is taken to be zero when the strain of both SMA's is equal to  $\varepsilon_p$ .

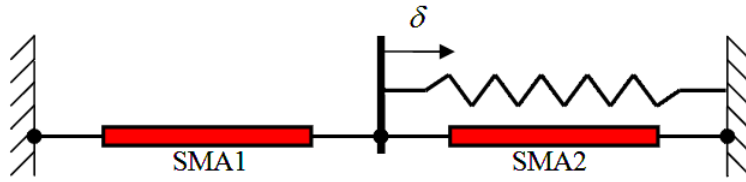


Figure 85: Sketch of Coordinate System for Coupled SMA Wire and Spring System

Figure 86 shows the stress-strain characteristics of both SMA wires and the spring (dotted line) in the left and center panels, with both plotted on the same set of axes in the right panel. Note that in order to plot both characteristics on the same set of axes, the strain in SMA 2 must be negated and translated by  $2\varepsilon_p$  as in equation (2.25).

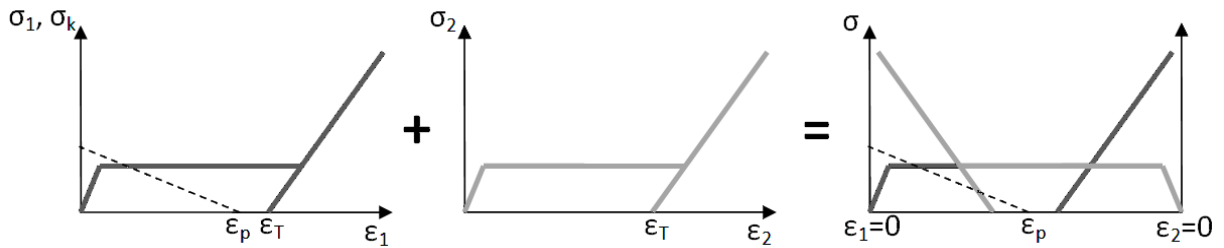


Figure 86: Stress-Strain Characteristics of SMA Wires and Spring

When the spring force is normalized by the cross-sectional area of the SMA wires,  $\sigma_k = \frac{F_k}{A_c}$ , the force equilibrium in equation (2.23) can be written in terms of stresses

$$\sigma_1 = \sigma_2 - \sigma_k. \quad (2.26)$$

Substituting the constitutive stress-strain relationship from equation (2.9) for each wire yields

$$\frac{\varepsilon_1 - \varepsilon_T (x_1^+ - x_1^-)}{\left(\frac{x_1^A}{E_A} + \frac{x_1^+ + x_1^-}{E_M}\right)} = \frac{\varepsilon_2 - \varepsilon_T (x_2^+ - x_2^-)}{\left(\frac{x_2^A}{E_A} + \frac{x_2^+ + x_2^-}{E_M}\right)} - \frac{kL_{0,SMA1}}{A_c} (\varepsilon_1 - \varepsilon_p). \quad (2.27)$$

The equilibrium strain is found by substituting equation (2.25) and solving for  $\varepsilon_1$ ,

$$\varepsilon_1 = \left( \frac{A_1}{B_1} + \frac{2\varepsilon_p - A_2}{B_2} - k\varepsilon_p \right) \left( \frac{1}{B_1} + \frac{1}{B_2} - \frac{kL_0}{A_c} \right)^{-1}, \quad (2.28)$$

where

$$A_i = \varepsilon_T (x_i^+ - x_i^-), \quad (2.29)$$

and

$$B_i = \left( \frac{x_i^A}{E_A} + \frac{x_i^+ + x_i^-}{E_M} \right). \quad (2.30)$$

Finally,  $\varepsilon_2$  and the stresses in each wire,  $\sigma_1$  and  $\sigma_2$ , can be calculated directly using equation (2.25) and equation (9).

### Updated Resistance Model

For the simulations of the dual-SMA system the resistance model is an extension of the model used to study the single SMA-Spring system. As before, the resistivity of the material is a sum of phase fractions scaled by the nominal resistivity of a length of wire in each phase

$$\rho_{SMA}(T) = \left[ x^A \rho_A(T) + x^+ \rho_+(T) + x^- \rho_-(T) \right]. \quad (2.31)$$

In equation (10), the nominal resistivity's  $\rho_A(T)$ ,  $\rho_+(T)$ , and  $\rho_-(T)$  are temperature-dependent. The temperature dependence of each resistivity value is defined in equation (2.32) through equation (2.34).

$$\rho_A(T) = \rho_{0A} (1 + \alpha^A \Delta T) \quad (2.32)$$

$$\rho_+(T) = \rho_{0+} (1 + \alpha^+ \Delta T) \quad (2.33)$$

$$\rho_-(T) = \rho_{0-} (1 + \alpha^- \Delta T) \quad (2.34)$$

where  $\alpha^{A,+,-}$  are the thermal dependence on resistivity of each phase.

The updated model also accounts for the elastic deformation of the wire, also presented in Appendix B [57], because elastic strain causes the wire to stretch and the cross-sectional area to be reduced. The elastic component of the strain is derived from equation (2.8), only without the term accounting for strain change due to phase transformation,  $\varepsilon_T$ . Therefore, elastic strain is solved as

$$\varepsilon_e = \sigma \left( \frac{x_+ - x_-}{E_m} + \frac{x_A}{E_A} \right). \quad (2.35)$$

Elastic strain alters the active length of the SMA via equation (2.36), and the cross-sectional area via equation (2.37), where  $\nu$  is the Poisson's ratio and is taken as 0.3 [67].

$$L(\varepsilon_e) = L_0 (1 + \varepsilon_e) \quad (2.36)$$

$$A(\varepsilon_e) = \pi R_0^2 (1 - \nu \varepsilon_e)^2 \quad (2.37)$$

Finally, the total resistance of the SMA wire can be calculated as the product of the temperature and phase dependent resistivity and the elastic-strain dependent length, divided by the area, as shown in equation (2.38). Table 9 shows the parameters used for the SMA resistance model.

$$\Omega(T, x^A, x^+, x^-, \varepsilon_e) = \frac{\rho_{SMA}(T) L(\varepsilon_e)}{A(\varepsilon_e)} \quad (2.38)$$

### Modeling Parameters

The modeling parameters used to simulate the opposing SMA system are listed in Table 8 and Table 9.

Table 8: SMA Wire and Heat Transfer Model Parameters

Parameter	Value	Unit	Description
$E_A$	71.1e9	Pa	Modulus of austenite
$E_M$	30.9e9	Pa	Modulus of martensite
$\varepsilon_T$	0.041		Maximum recoverable strain
$V_d$	1e-22	$m^3$	Volume element size
$\tau_x$	1e-2	s	Scale factor on transition probability
$\rho$	6.4e3	$kg/m^3$	Density of Nitinol
$H$	24e3	J/kg	Latent heat of phase transformation
$h$	160	$W/m^2/K$	Heat convection coefficient
$c_v$	600	J/kg/K	Specific heat
$r_{SMA}$	25	$\mu m$	Radius of SMA wire
$L_0$	50	mm	Length of SMA wire
$k$	0.098	N/mm	Linear spring constant
$\sigma_L$	135e6	Pa	Austenitic transformation stress
$\Delta\sigma_T$	6e6	Pa	Stress-strain plateau temp. dependence
$T_L$	310	K	Austenitic conversion temperature
$\Delta\sigma$	200e6	Pa	Width of stress-strain hysteresis

Table 9: SMA Resistance Model Parameters

Parameter	Value	Unit	Description
$\rho_{0A}$	8.9e-7	$\Omega m$	Resistivity of austenite phase
$\rho_{0\pm}$	10.2e-7	$\Omega m$	Resistivity of martensite phase
$\alpha^A$	0.0002	$K^{-1}$	Temp. dependence of austenite phase
$\alpha^\pm$	0.0003	$K^{-1}$	Temp. dependence of martensite phase

### 2.1.3.3 Experimental Setup

The tensile test setup used to characterize the SMA wire is diagrammed in Figure 87 and photographed in Figure 88. The two 50  $\mu m$  diameter Flexinol SMA (Dynalloy Inc., Tustin, CA) [1] wires are connected to each other at the SMA junction. This junction is a cylinder that tracks on a ‘frictionless’ slide bushing. During certain stages of the pre-treatment procedure, the SMA junction cylinder is allowed to slide freely to ensure that both the SMA wires are under the same tensile stress. When the actuation experiment cycles are run, the cylinder is locked in the slide bushing so that the spring flexure will be forced to deflect along with the SMA wires. On the right boundary, the tensile load is transmitted to a Futek Model LSB200 load cell with a 9 N (4.6 GPa stress, for a 50  $\mu m$  diameter wire) load limit that is oversampled and filtered for a peak resolution of 0.14 mN (0.1 MPa) and Zaber Model TNA08A25 linear actuator. The linear actuator provides position feedback, so the

position of the right boundary of the SMA wire  $x_1$  can be effectively tracked with 0.6  $\mu\text{m}$  resolution. A Keyence LK-G82 laser displacement sensor with 0.2  $\mu\text{m}$  resolution is used to track the motion at the SMA junction (and cantilever flexure) at  $x_2$ . The length of each SMA wire can be determined using

$$L_{SMA2} = L_0 + x_1 - x_2 \quad (2.39)$$

and

$$L_{SMA1} = L_0 + x_2, \quad (2.40)$$

where  $L_0$  is the nominal length of the SMA wire, taken to be 50 mm for these experiments. The load cell measures the tensile force in SMA 2 directly. Since the cantilever flexure has a known, linear stiffness, the force in SMA 1 can be calculated from

$$F_1 = F_2 - kx_2. \quad (2.41)$$

Then stress scales by the cross-sectional area of the 50  $\mu\text{m}$  diameter SMA wire. All of the components are aligned on a breadboard and enclosed in an acrylic box to isolate the wire from environmental disturbances.

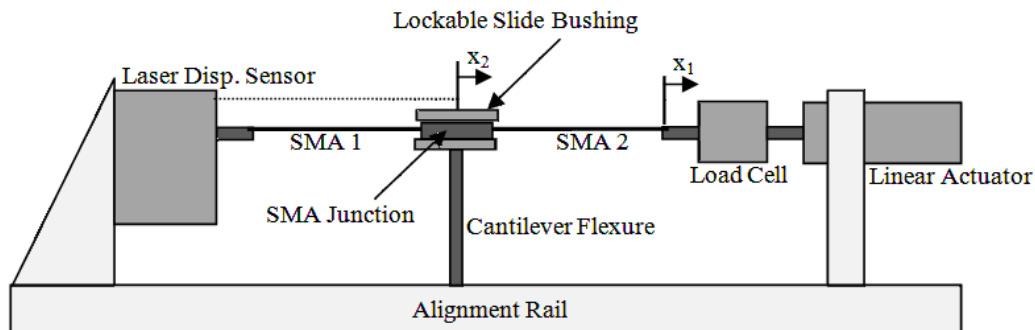


Figure 87: Diagram of SMA-Flexure Test Setup

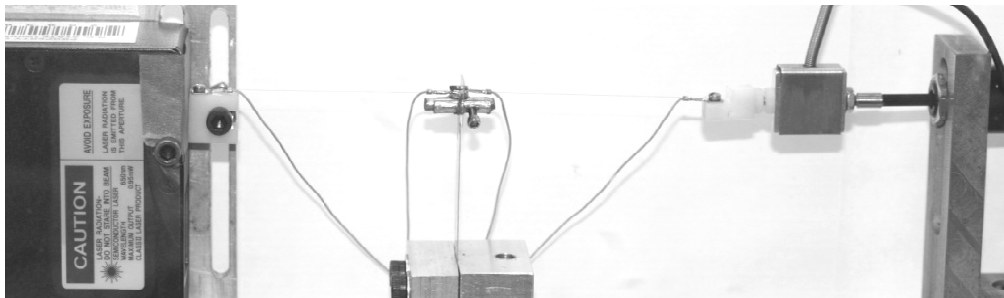


Figure 88: Photograph of SMA-Flexure Testing Setup

### 2.1.3.4 Experiment Procedure

When dealing with non-linear, hysteretic wires the treatment of the wires must be carefully controlled and reported throughout the duration of the experiment for test results to be meaningful and

reproducible. This is particularly true when two SMA wires are coupled together, and the treatment history of one wire affects the behavior of the other. In all of the experiments discussed in this paper, the wires go through a pre-treatment (memory-clearing) procedure and are then either pre-strained or pre-stressed to a certain level before the experiment cycling begins. For the results shown in this paper, two different types of actuation cycles are run. In “constant opposing power” experiments, the power input into SMA 2 is maintained at a constant level, and then the power into SMA Wire 1 is cycled using a triangle wave as shown in the left panel of Figure 90. In “alternating actuation” experiments, the wires are cycled one at a time using triangle waves that are out of phase, as shown in the right panel of Figure 90.

### Pre-Treatment

1. Unclamp the slide bushing so that the SMA junction can slide freely with respect to the spring flexure.
2. Heat both SMA wires with 0.3 W while under 0 stress to transform them into the austenite phase.
3. While the power is still high, retract the linear actuator until the load cell detects a small force. Record the actuator position and the austenitic reference length,  $L_{0A}$ . Record the position of the linear actuator as  $x_{1A}$ .
4. Allow both wires to cool under zero stress to the martensitic twin phase. Note that some slack will develop as the martensite plus phase is favored due to the two-way effect.

### Pre-Straining

1. Retract the linear actuator to position  $x_{1A} - 2L_{0A}\epsilon_{p0}$  to put both wires at a strain level of  $\epsilon_{p0}$ , as shown in the left plot in Figure 89.
2. Extend the linear actuator until the load cell detects no force.
3. Record this position as  $\epsilon_{p1}$ , as shown in Figure 89. This is the point from which experiment cycles will begin.
4. Lock the slide bushing so that the spring flexure deflect when the SMA junction moves.

### Pre-Stressing

1. Retract the linear actuator until the load cell detects a stress of  $\sigma_{p1}$ , as shown in the right plot in Figure 89. This is the point from which experiment cycles will begin.
2. Lock the slide bushing so that the spring flexure deflect when the SMA junction moves.

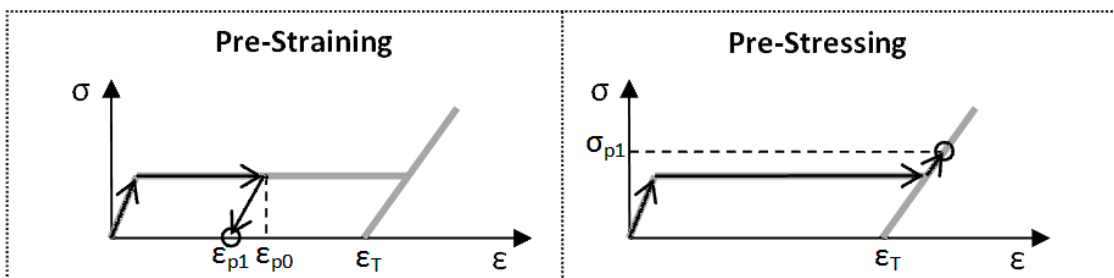


Figure 89: Stress-Strain Diagram of Pre-Straining (left) and Pre-Stressing (right) Procedure

### Constant Opposing Power Experiment Cycles

1. Heat SMA Wire 2 with a pre-determined power amplitude between 0 and 0.25 W.
2. After 5 s, begin cycling the power to SMA 1 five times using a triangle wave with an amplitude of 0.25 W at a frequency of 0.1 Hz. The input power signals for  $P_{SMA2}$  equal to 0.15 W is shown in the left panel of Figure 90, with Wire 2 input shown in gray and Wire 1 in black.

### Alternating Actuation Experiment Cycles

1. Cycle Wire 1 then Wire 2 five times each using alternating triangle waves at the amplitudes and frequencies listed in Table 10. Note that power amplitude is increased as actuation frequency is increased.
2. Repeat for the pre-strain, pre-stress, and frequency/amplitude combinations shown in Table 10.

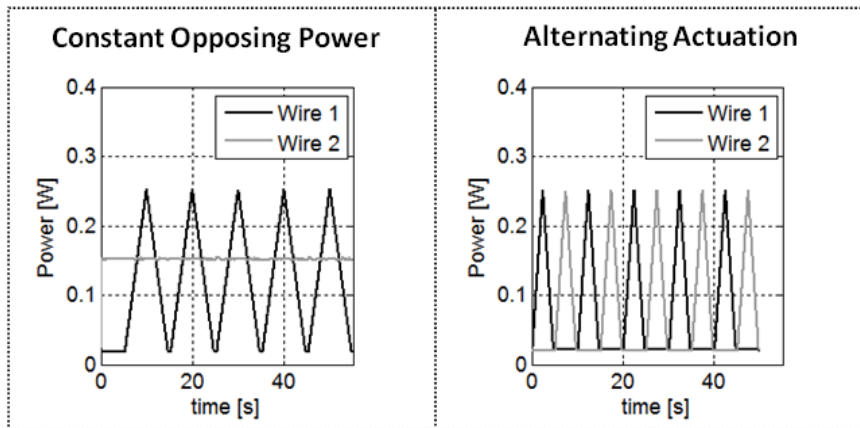


Figure 90: Power input to SMA Wires during Constant Opposing Power (left) and Alternating Actuation (right) Experiments.

Table 10: Pre-Strain, Pre-Stress and Actuation Frequency/Amplitudes for Alternating Actuation Experiments

$\epsilon_{p0}$ (%)	$\sigma_p$ (MPa)	freq. (Hz)	P (W)
2.5	50	0.1	0.25
3.0	100	0.2	0.30
3.5	150	0.5	0.35
4.0	200	1.0	0.40
4.5		2.0	0.45

#### 2.1.3.5 Results and Discussion

Results are presented for the experiments run with constant power in the opposing SMA wire and for alternating actuation cycles. In the constant opposing power experiments, the impact of changing the opposing power is evaluated. In alternating cycles experiments, the effect of changing the pre-strain or pre-stress and the actuation frequency is presented.

#### Constant Opposing Power

In the constant opposing power experiments, the power into SMA Wire 2 is set at a constant value, then the power into Wire 1 is cycled. Figure 91 shows an approximation of the expected stress-strain equilibrium during the course of a constant opposing power experiment. Since the addition of the

linear spring serves only to tilt the landscape by slightly increasing the stress in one wire compared to the other, its effect is not included in the approximation. In Figure 91, the black circle represents the current stress-strain state.

At the start of the experiment, both wires are at room temperature and pre-strained to 3.33% as shown in panel A of Figure 91. Then Wire 2 is heated with the pre-determined power (0.13 W) as shown in panel B. This process effectively adds a pre-stress to Wire 1 by pulling it into the martensite plus phase. Then as Wire 1 is heated (panel C and D) and cooled (panel E and F), Wire 2 serves as a non-linear, hysteretic spring element in series with Wire 1. The resulting stress-strain pathway of Wire 2 during this mock experiment is plotted with a dotted line.

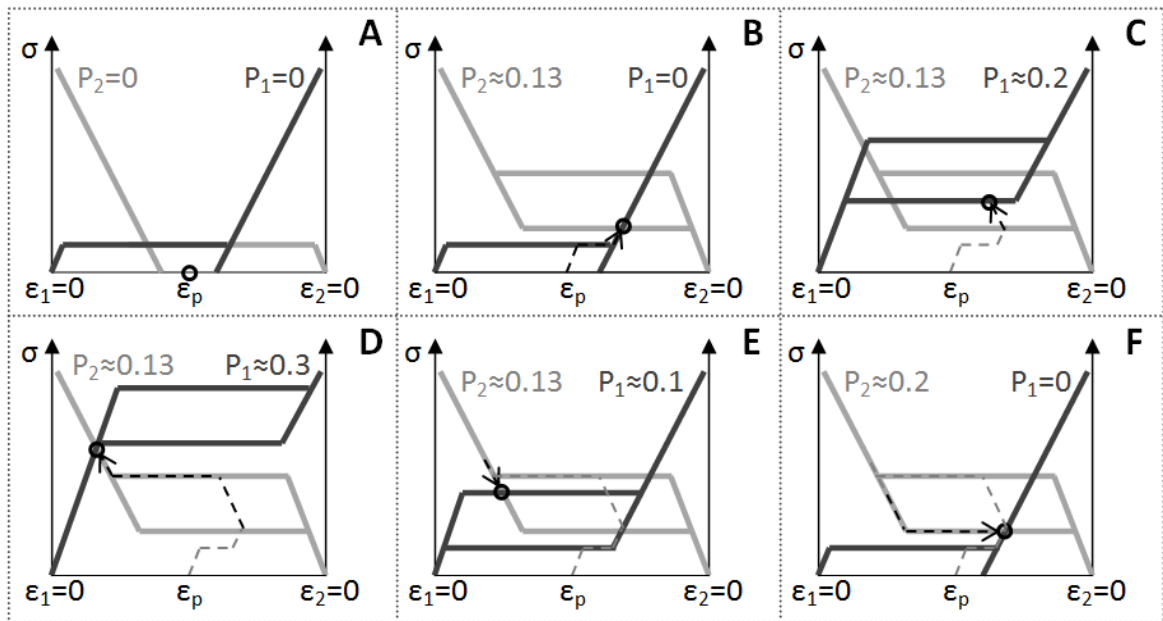


Figure 91: Single-Crystal Approximation of the Stress-Strain Behavior during Constant Opposing Power Experiment

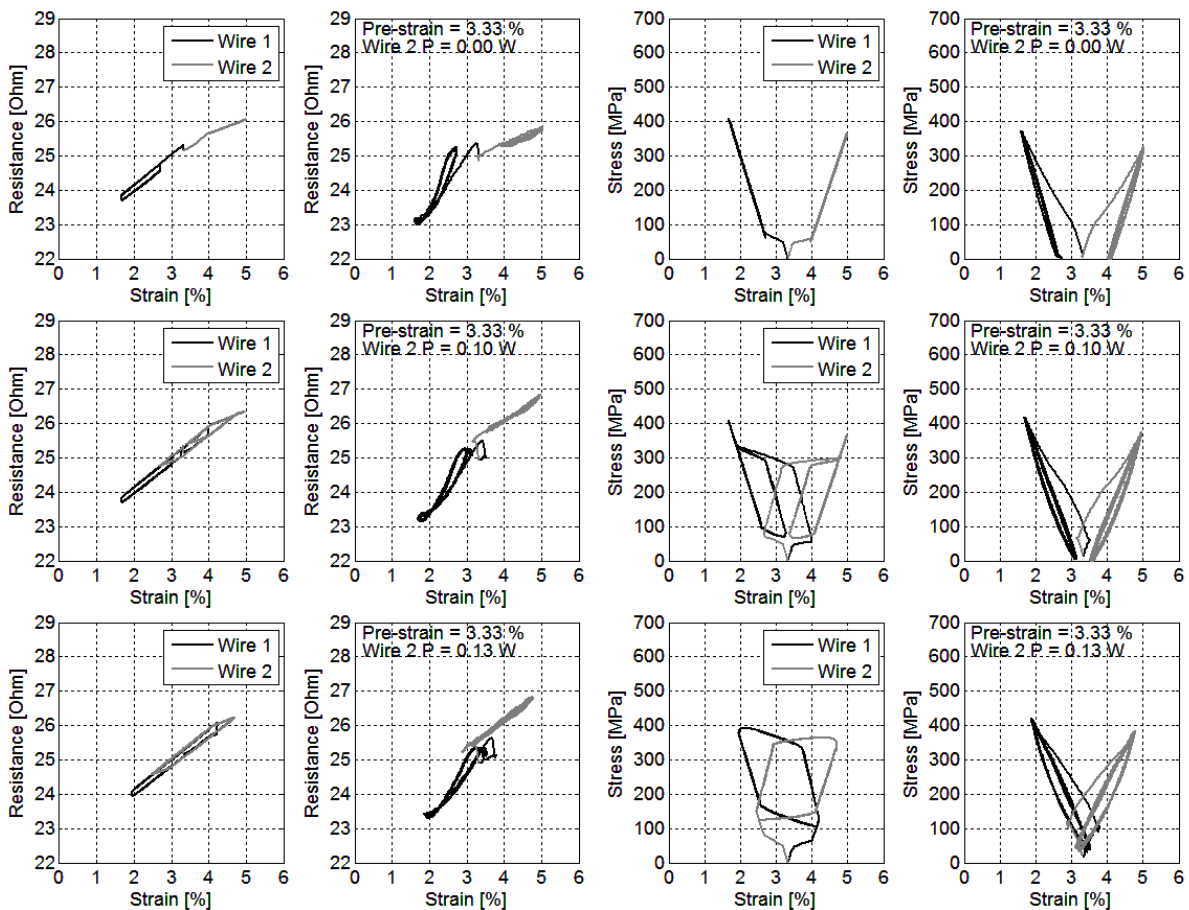
The results in this section show the stress and resistance vs. strain characteristics for both wires. In all plots, the simulated results are on the left, while the experimental results are on the right. The fixed power input to Wire 2 increases from the top row to bottom row in Figure 92.

When Wire 2 is given zero input power, as shown in the top row, its martensitic characteristic defines the equilibrium stress-strain state for the coupled system after the first cycle. As a result, the resistance of Wire 2 only changes due to elastic deformation of the martensite plus phase as the load from Wire 1 cycles. The resistance of Wire 1 changes due to its change in temperature, phase fraction, and elastic strain. The coupling of the thermal and mechanical effects as well as the change in phase induced hysteresis in Wire 1. Note that the power into Wire 1 is cycled at 0.1 Hz so that the thermal problem is approximately quasi-static.

As the power to Wire 2 is increased, the hysteretic behavior becomes visible in the stress-strain characteristics, just as predicted by the model and the mock experiment shown in Figure 91. Interestingly, even as power to Wire 2 is increased to the point where it is able to transform itself back

to austenite after being stressed to martensite, the experiments show no hysteresis in the resistance of Wire 2. The model predicts hysteresis because the modeled resistance is related to phase fractions (as well as elastic strain and temperature).

However, a translation and a change in slope is observed in the measured resistance-strain curve of Wire 2 as its fixed heating power is increased. When power into Wire 2 is high, Wire 2 resistance is reduced significantly at low stress as a result of the increased presence of the austenite phase. For Wire 2 power inputs greater than 0.13 W the slope for Wire 2's resistance-strain plot increases, indicating a greater change in resistance for the same change in strain. This is evidence that the phase change is at least partially responsible for the larger change in resistance. As Wire 2 input power is increased to 0.25 W, as shown in the bottom row of Figure 92, the “effective pre-stress” on Wire 1 becomes so high that very little phase change is able to occur while its power is cycled, and the slope of the resistance-strain line is reduced once again. The lack of hysteresis despite the clear indications of phase change was also observed in the study in Appendix B [57], and may be attributed to mixing of the coupled electro-thermo-mechanical effects as well as the smoothing effects that result from the polycrystalline nature of a real wire.



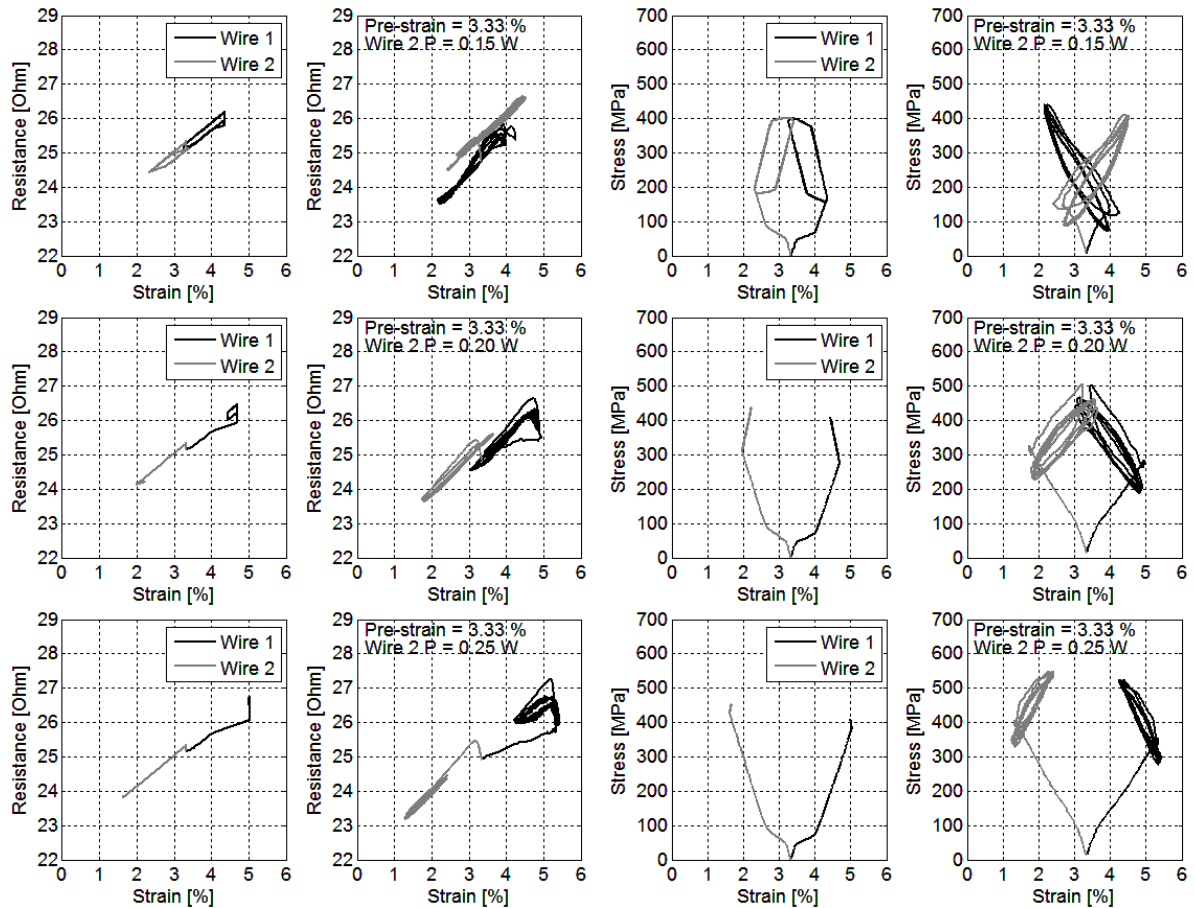


Figure 92: Simulated (left) and Experimental (right) Resistance and Stress vs. Strain for Various Wire 2 Power Inputs

### Alternating Cycles

In this section, results are shown from experiments where the power input is alternated between Wire1 and Wire 2, as shown in the right panel of Figure 90. Figure 93 diagrams the stress-strain equilibrium at different stages of the alternating-cycle experiments. Both wires start at pre-strain of  $\epsilon_p$  as shown in panel A. When Wire 1 begins to heat, the bottom branch of its hysteresis loop rises and the stress-strain equilibrium is constrained along a minor loading loop of Wire 2, as shown in panel B. As power into Wire 1 rises further, Wire 2 is strained up its  $M^+$  line as shown in panel C. After cooling of Wire 1, panel D shows that the equilibrium is expected to be different from the starting position. Then the same behavior is expected on the heating and cooling of Wire 2 as indicated by panels E and F.

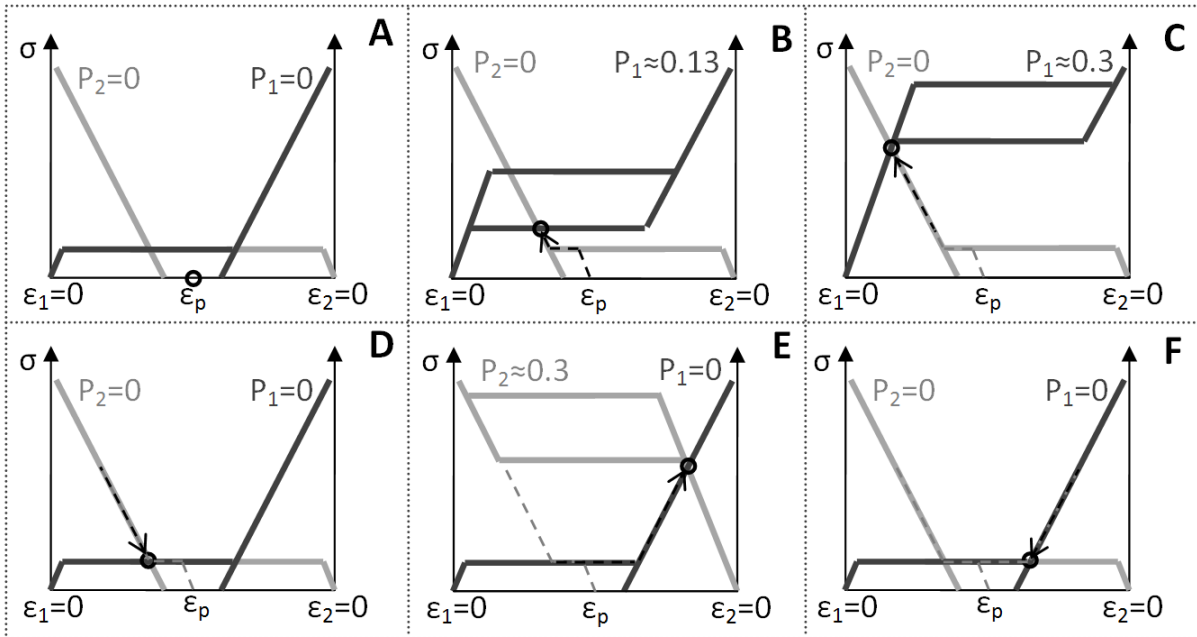


Figure 93: Single-Crystal Approximation the Stress-Strain Behavior during Alternating Cycles Experiment

In the results, the affect of wire pre-strain or pre-stress is first discussed for 0.1 Hz, “quasi-static” input triangle waves. This discussion is essential for determining the stroke and force output that can be developed for a specific application. Then a single pre-strain value (3.33%) is chosen and the experiments are run at different frequencies to demonstrate how an opposing wire configuration can maintain the high stroke range at cycling frequencies up to 2 Hz (in still air).

### Effect of Changing Pre-Strain

Each row of plots in Figure 94 shows the resistance and stress vs. strain behavior for the SMA Wires at a different pre-strain. In a typical experiment with pre-strain of 2.48%, for example, Wire 1 is heated, resulting in a contraction from 2.48% to about 0.7%. This contraction is accompanied by an equal elongation of Wire 2 into the  $M^+$  phase to 4.3%. Then Wire 2 is heated and contracts to 0.7%, while Wire 1 is elongated. Since these tests are run at a slow, 0.1 Hz cycling frequency, the each wire has enough time to cool and relax before the opposing wire is heated. As a result, there is a period where the wires are essentially slack (zero stress) between cycles.

The stress-strain plots show that increasing the pre-strain from 2.48% to 3.65% serves to increase the maximum stress from 200 MPa to 400 MPa without having a significant impact on stroke that remains roughly constant at  $\pm 1.8\%$ . If a lower input power were used, it is likely that increasing pre-strain would have resulted in a reduction in stroke, as one wire would not have been heated enough to overcome the opposing force of the other. These observations are critical, as a lower pre-strain will allow prolonged cycling life in high-stroke applications by limiting the peak stress in the SMA wires.

The resistance-strain plots show that the pre-strain also has an impact on the width of the hysteresis. In general, the experiments show that lower pre-strains result in wider hysteresis. However, this effect is not captured by the single-crystal model. Non-linearity occurs on thermal unloading because there is insufficient stress to immediately bias all of the material grains from the austenite phase to the

tensile-induced  $M^+$  phase. Instead, some of the material grains are able to transform to the  $M^-$  phase forming the twin  $M^+ / M^-$  structure that has the same high resistivity as  $M^+$ , but the low strain of austenite. The top (thermal unloading) branch of the resistance-strain plot shows when starting from the lowest strain state (0.7%), the resistance initially increases rapidly with little measured change in strain.

This effect is critical for sensing applications that endeavor to use the resistance measurement as a strain or displacement measurement while the wire is being actuated. Hysteresis in the characteristic necessitates a complex resistance to strain mapping method. Also, for low pre-strains the wire that is not being actuated is essentially slack and in the martensite phase, so its resistance does not change until it is elastically strained up the  $M^+$  phase. Once again, while the power input to a wire is not being changed its resistance-strain curve shows no hysteresis.

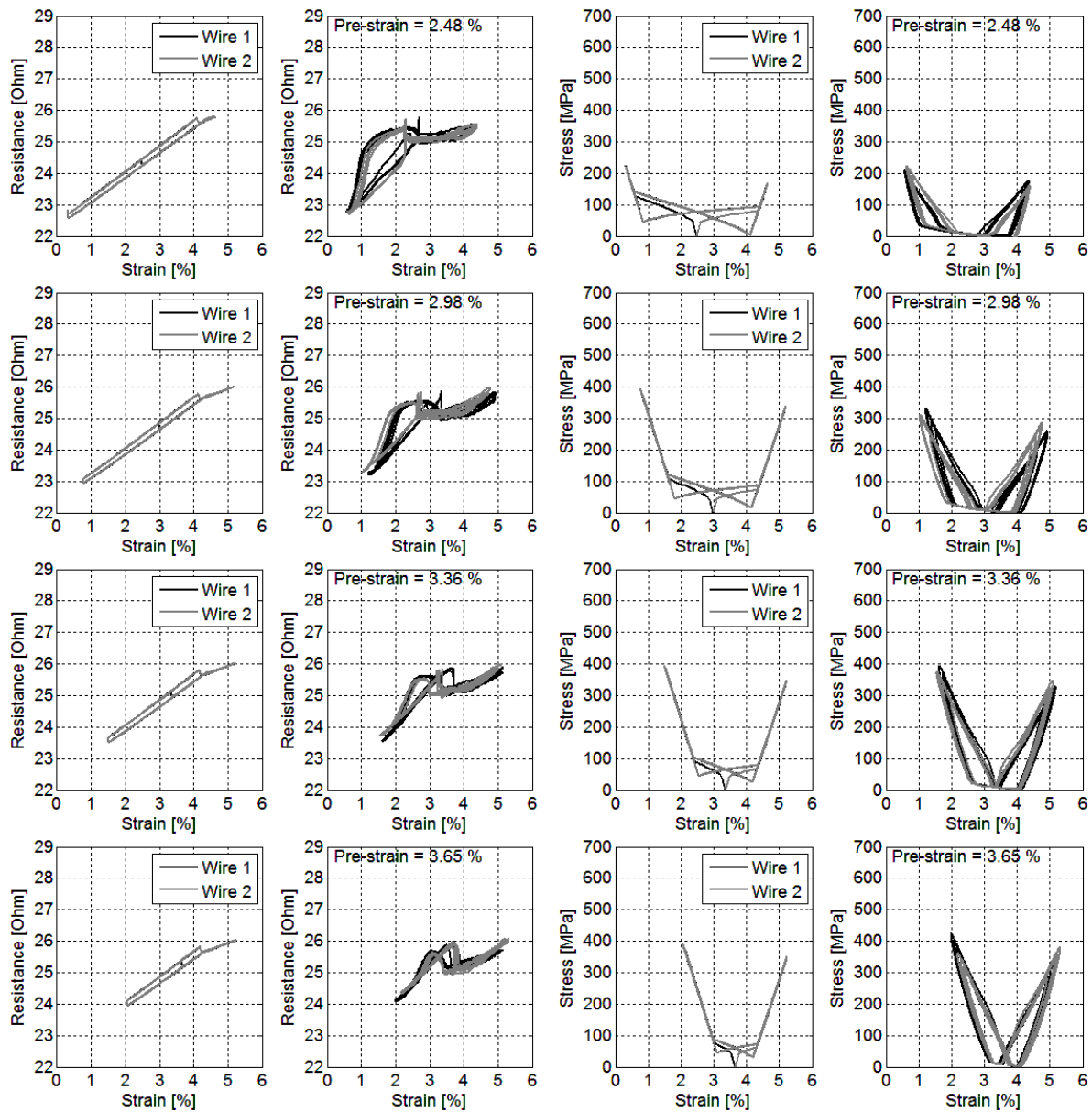


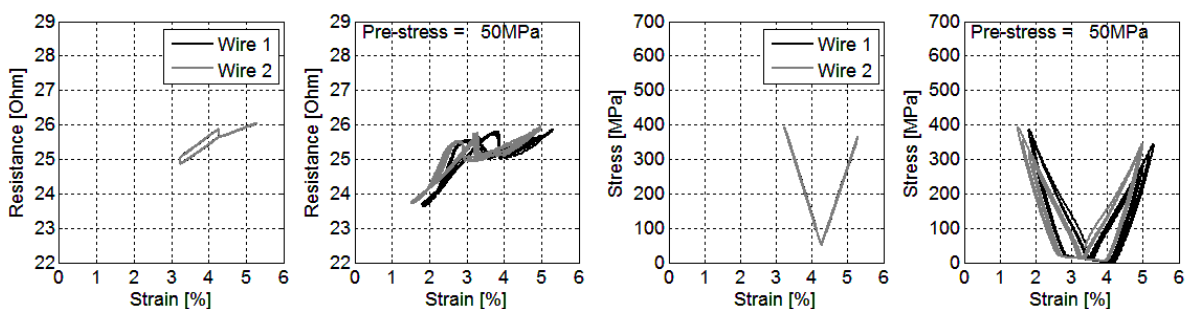
Figure 94: Simulated (left) and Experimental (right) Resistance and Stress vs. Strain for Various Pre-Strain Values

### Effect of Changing Pre-Stress

When the SMA wire is pre-stressed instead of pre-strained, the wire essentially starts on the  $M^+$  line of the stress-strain curve. This results in a high peak stress of 400 MPa and a reduction in stroke at higher pre-stress cases where the applied power is insufficient to overcome the high stresses. However, as described in section 2.1.2.3, since the material is actually polycrystalline, the low values of pre-stress actually result in a wire that is still a mixture of  $M^+$  and  $M^-$  after pre-stressing is finished. When the wire experiences high stress on the first loading cycle, the  $M^-$  grains are mostly eliminated. Therefore, the wire returns to a lower stress value upon cooling. This is why the experimental results show the stress dropping to zero after the first cycle of the 50 MPa pre-stress case, while the single crystal model does not.

The resistance plot for the 50 MPa case shows similar hysteresis as the 3.36% pre-strain case because of the amount of  $M^-$  that is still present in the wire after pre-stressing. However, the resistance plots of higher pre-stress cases have very little hysteresis while contraction is occurring. The hysteresis loop in the middle of the resistance-strain plot is a result of the thermal contribution to the resistance. When a wire is heated to a temperature that is too low to start transformation, the resistance initially rises due to the rise in wire temperature. Once transformation begins, the wire changes to the austenite phase and both strain and resistance are reduced. On the cooling part of the cycle, the transformation finishes at a different temperature than it started on the heating cycle, resulting in small square-like hysteresis loop around 3.6% strain that forms between the end of the cooling of Wire 1 and the beginning of heating of Wire 2.

On either side of the hysteresis, the resistance-strain plots for pre-stresses greater than 50 MPa show two distinct lines. The left portion of the plot (strain less than the initial strain induced by pre-stress,  $\sim 4.3\%$  strain for the simulations) shows the behavior of the wire while it is being actuated – this line results from the resistance change due to both elastic straining and phase transformation, and thus it has a steep slope. The segment of line to the right of the hysteresis loop (strain greater than 4.3%) shows how the resistance changes when the wire is elastically strained in the martensite phase. This line has a shallower slope because it does not include significant contributions from phase transformation. For controls applications, these linear, non-hysteretic segments may allow for a linear mapping from resistance to strain to be employed under certain conditions, as will be discussed in section 2.2.1. The shifting of this line (and reduction of slope) when the opposing wire is actuated also motivates a mapping method that considers the state of both coupled wires.



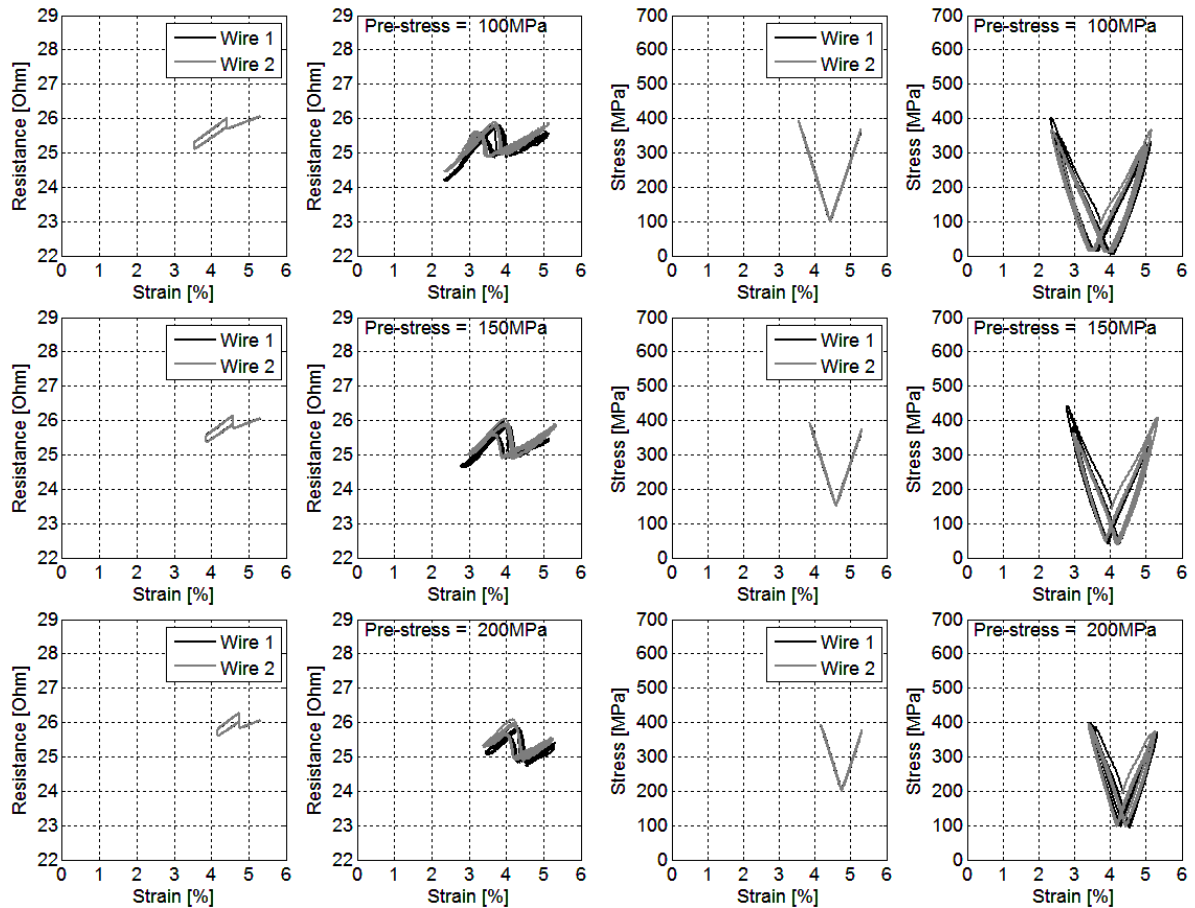


Figure 95: Simulated (left) and Experimental (right) Resistance and Stress vs. Strain for Various Pre-Stress Values

### Actuation Frequency

Figure 96 shows how actuation cycling frequency impacts the resistance and stress vs. strain behavior for a wire pre-stressed to 3.33%. In order to allow for sufficient heating at the higher frequencies, the peak input power was increased with frequency. For frequencies of 0.1, 0.5, 1.0, and 2.0 Hz, the peak input power was 0.25, 0.35, 0.40, and 0.45 W, respectively, as shown in Table 10. Results show that a stroke range of  $\pm 1.5\%$  is maintained all the way up to 1 Hz for the 50  $\mu\text{m}$  diameter wires tested in still air. However, at frequencies higher than 0.5 Hz, the wire is not able to cool back to the martensite phase before the next cycle begins, so the wire is never fully relaxed into the zero stress state. Also, above 0.1 Hz the heating and cooling process can no longer be considered quasi-static, so the thermal contribution to the resistance continues to change, even after the power to one wire is off and the other is on. As a result, at high frequencies hysteresis appears in the right segment of the resistance-strain curve, whereas at low frequencies the right side is non-hysteretic because it shows the behavior of a totally cooled wire being elastically strained on the martensite branch. Since this is a thermal effect, it is corroborated by the model.

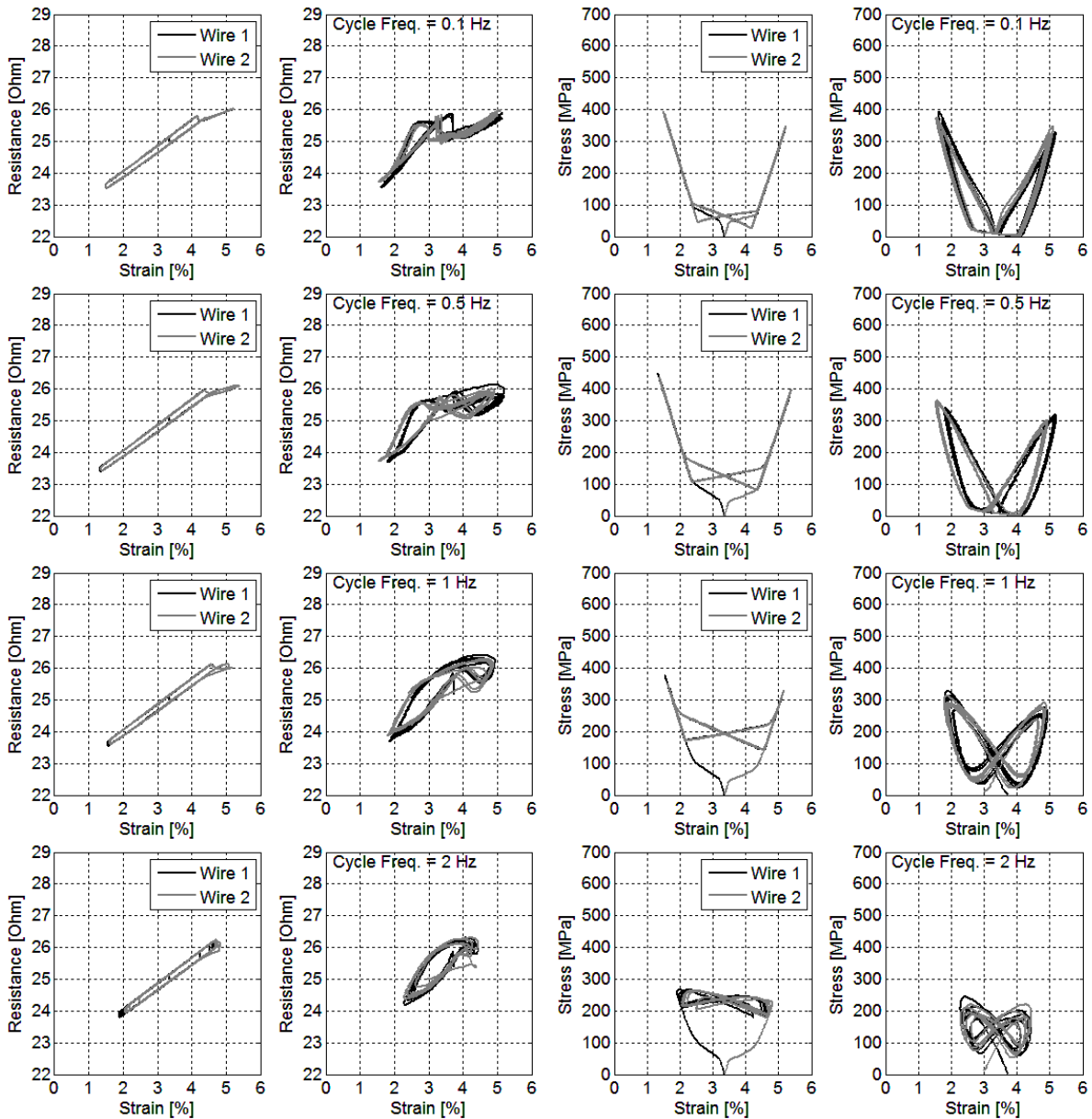


Figure 96: Resistance and Stress vs. Strain for Alternating Actuation Tests at Different Frequencies for a Pre-strain of 3.33%.

### 2.1.3.6 Conclusion from the Opposing SMA-Spring System

Clearly, the behavior of two coupled hysteretic elements is complicated. However, systematic study of the system consisting of two opposing SMA wires and a spring flexure has demonstrated many wire characteristics that are relevant to multi-functional sensor/actuator applications. First, straining these 50  $\mu\text{m}$  diameter Flexinol SMA wires [1] to 2.5% pre-strain produces a large  $\pm 1.8\%$  stroke at a small peak stress of 200 MPa. Increasing pre-strain reduces stroke and exposes the wires to higher stresses. Pre-stressing the wires to over 100 MPa represents the extreme cases of pre-straining and also results in high stress and low stroke. Therefore, low pre-strain values are desirable for actuation applications that endeavor to achieve large stroke over many cycles.

However, the resistance-strain plot at low pre-strain values develops a wide hysteresis that complicates mapping for sensing applications. For example, in the 2.48% pre-strain case, a measured

resistance value of  $24.5 \Omega$  could indicate that the SMA wire is strained anywhere between 1 and 2.3%. For the pre-stressed tests, the resistance-strain plot is nearly linear and non-hysteretic over certain ranges, so a single measured resistance value can be easily mapped to a strain with an error less than 15% of full scale.

Results also show that coupling opposing SMA actuators allows for a stroke of  $\pm 1.2\%$  even at high, 2 Hz cycling frequency in still air. The actuation rate would be increased substantially if the wire were exposed to moving air or water that removes the heat from the wire much more quickly, allowing the wire to elongate back to the martensite phase and then be heated rapidly via Joule heating again. Unfortunately, when heat cannot be removed rapidly enough by the surrounding environment the thermal problem cannot be considered quasi-static. As a result, the thermal contribution to the resistance measurement complicates resistance-strain sensor mappings by introducing a cooling lag and thus hysteresis. This cooling lag was not observed in the single SMA-spring system because there was no concurrent increase in opposing force from the second wire, only the passive force from the linear spring flexure.

Despite the obvious design trade-offs between actuation stroke/frequency and sensing accuracy, these experiments and simulations provide a framework from which operation envelopes can be anticipated and model-based mapping methods can be calibrated. So long as the SMA wire's behavior is repeatable and the physical mechanisms behind the hysteresis and nonlinearities can be deciphered, an accurate sensor can be calibrated and used in conjunction with actuation. Then the multi-functionality of the material can be fully exploited in embedded SMA applications, such as the adaptive Smart Inhaler nozzle characterized in the next section.



## 2.1.4 Smart Inhaler Nozzle Joint

The Smart Inhaler nozzle joint shown in Figure 97 and introduced extensively in Part 1, is very much like the opposing SMA setup discussed in section 2.1.3. Each actuator wire is opposed by two others; however they are oriented 120 degrees apart, so the two opposing SMA wires have only half the moment arm of the first.

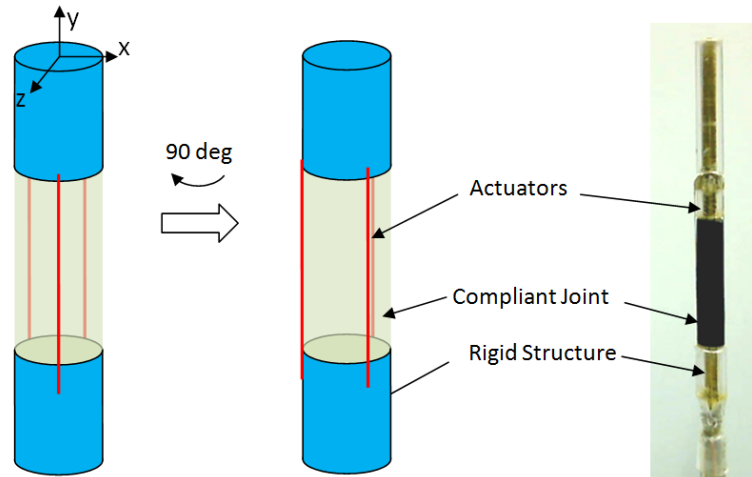


Figure 97: Adaptive Smart Inhaler Nozzle Joint

### 2.1.4.1 Objectives

The adaptive nozzle design and assembly process outlined in section 1.3.2 was carefully controlled such that all 6 SMA wires were attached in the same way. While some variation from one SMA actuator to the next is inevitable, calibration is possible if the behavior of each individual actuator is repeatable. The goal of this section is to characterize all 6 SMA actuator wires to determine the effectiveness of the assembly process and validate the repeatability of each joint for future calibration purposes. Characterization relates the heating power input to the response of the wire resistance and strain, as well as the response of the structure in terms of the nozzle tip displacement. Also, the resistance vs. tip displacement plots are discussed as a potential sensor diagram for future closed-loop control that uses the SMA wire as both actuator and sensor.

### 2.1.4.2 Experiment Setup

The setup used for measuring the SMA wire strain and nozzle deformation during testing is shown in Figure 98. Two cameras are analyzed by LabVIEW pattern matching software (Machine Vision) to track the displacement of 2 different track-points in different planes. The top-view camera measures the displacement of the nozzle tip indicated by a green circle while the side-view camera measures the strain of the SMA wire by tracking the location of the wire endpoints, shown in yellow. Since the bottom end of the SMA wire is fixed, it is set as the origin and only the top end of the wire is tracked. The nozzle is clamped in a rotational stage so that the three actuators at each joint can be tested independently. The 6-channel power controller [46] is employed to simultaneously control and measure input power control and take resistance measurements.

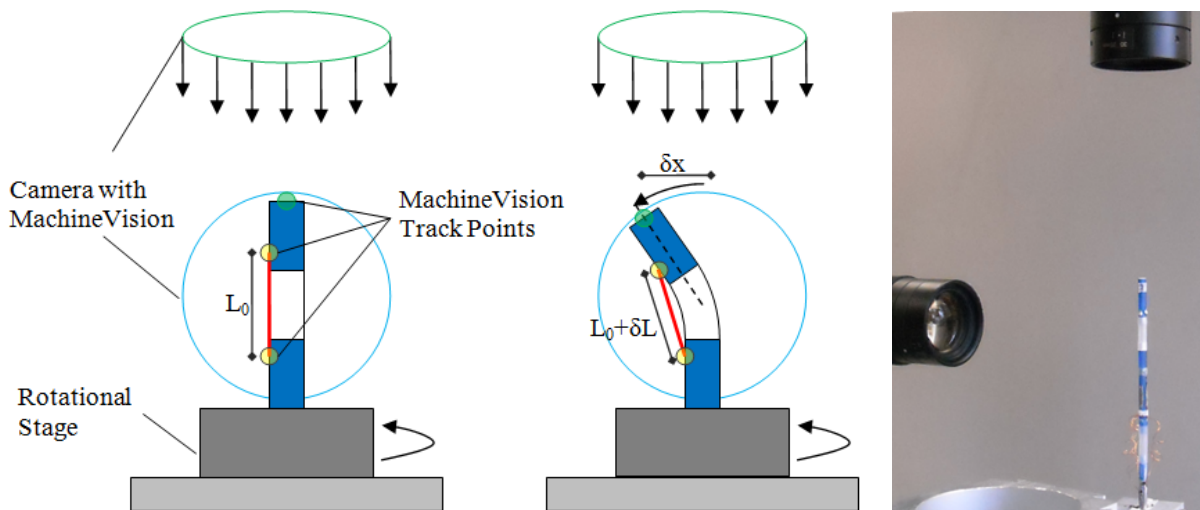


Figure 98: Diagram of Test Setup Used to Measure SMA Strain and Nozzle Tip Displacement Showing Un-deformed (left) and Deformed (middle) Nozzle Tip. Photographed on Right.

### 2.1.4.3 Flexible Joint Test Results

The time history of the heating power input for actuator 1 in the top joint is shown in the top plot of Figure 99. The SMA wire is 50  $\mu\text{m}$  diameter and has a total length of 56 mm (28 mm out and back), so the heating power density is 0.005 W/mm of SMA wire. In the characterization tests of joint 1 (actuators 1, 2, and 3), the heating input is cycled at 0.1 Hz so that the thermal problem is roughly quasi-static.

Figure 99 also shows the measured SMA resistance and strain, as well as the measured nozzle tip displacement resolved into the direction of actuator 1. As expected, heating power input causes a drop in SMA resistance due to phase change and wire contraction, the measured strain reduces from the strain induced by the pre-stressing process, about 4.1 %, to about 2%, and the tip displaces about 6 mm in the direction of actuator 1 from its unheated equilibrium position.

Figure 100 through Figure 102 show the hysteresis plots for the three top joint actuators. The power vs. displacement and resistance vs. tip displacement show a hysteretic character similar to the power-strain and resistance-strain plots of the analog SMA-spring system discussed in section 2.1.2. The strain vs. tip displacement relationship is constrained by the kinematics of the joint rotation, not the SMA material, so it has no hysteresis.

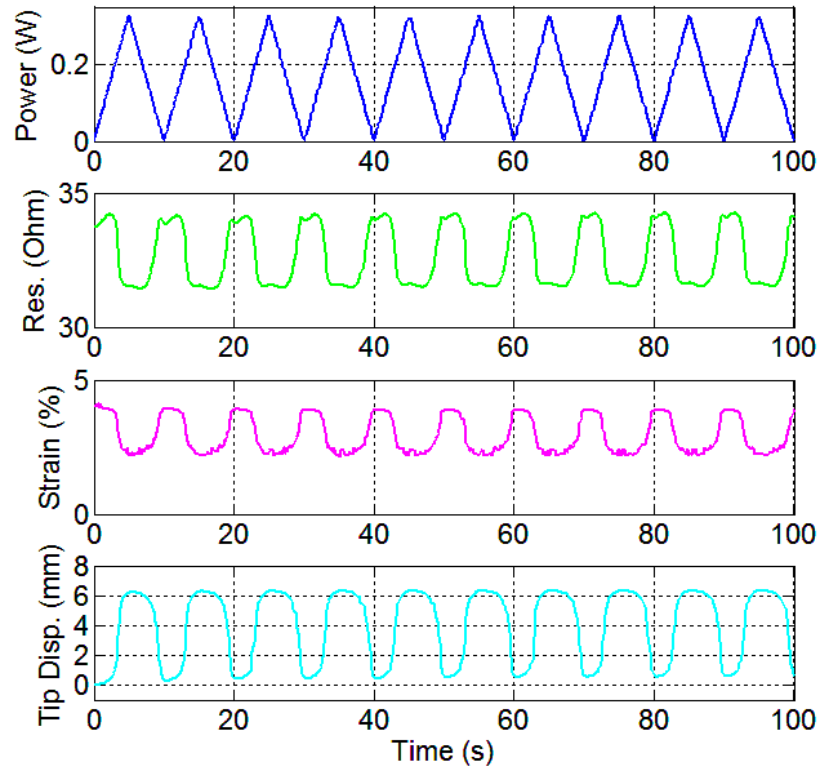


Figure 99: Time History of Power Input, SMA Resistance and Strain, and Nozzle Tip Displacement for Actuator 1 at 0.1 Hz

The hysteresis plots show reasonable repeatability from actuator 1 through actuator 3, validating the steps taken during fabrication. There is a slight difference in the magnitude of the resistance of actuator 1, most likely because of a small variation in the contact resistance between the SMA wire and the lead wire connected by the wire loop method presented in section 1.3.2.4. Also, the strain change is not uniform between the 3 actuators. All three SMA wires start at 4.1 % pre-strain, but actuator 1 finishes at 2.1%, actuator 2 at 0.7 %, and actuator 3 at 1.6 %. However, the tip displacement in all three actuator directions reaches its maximum at between 6.0 and 6.5%. The variation in measured strain could be a result of a direction-dependent variation in structural stiffness of the joint. This would cause an accompanying variation in the pre-stress (and therefore pre-strain) in the three actuators once the compliant joint is inserted as discussed in section 1.3.2.3. A pre-strain reference point is needed for plotting, and it is assumed to be 4.1% for all actuators, but it seems that actuators 1 and 3 may actually have a smaller pre-strain and thus smaller recoverable strain. Fortunately the behavior is stable and repeatable from one cycle to the next, so the variation between actuators can be calibrated and compensated in sensing and controls applications.

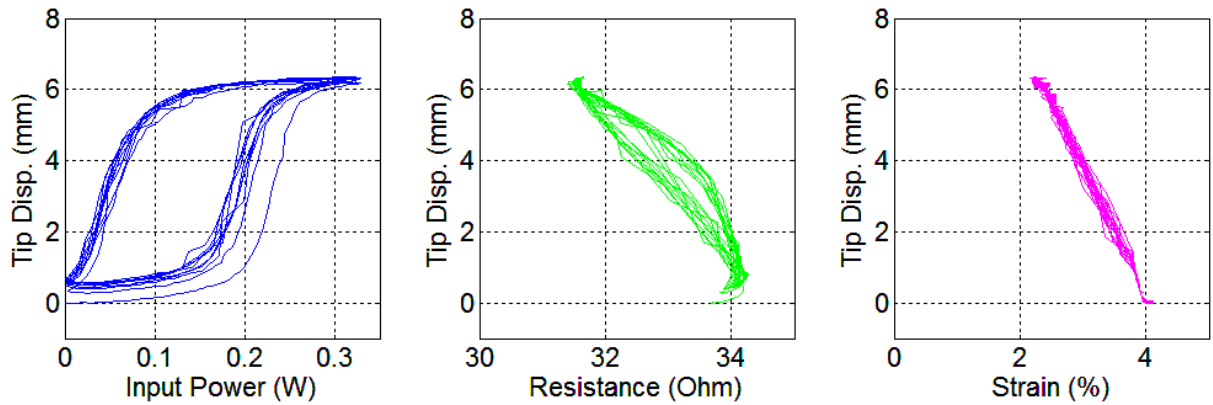


Figure 100: Hysteresis Plots for Top Joint Actuator 1 at 0.1 Hz

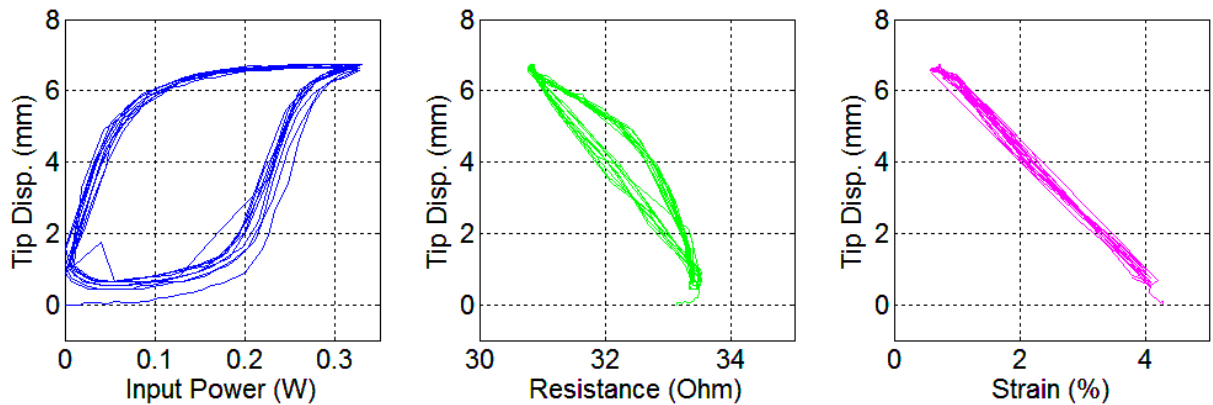


Figure 101: Hysteresis Plots for Top Joint Actuator 2 at 0.1 Hz

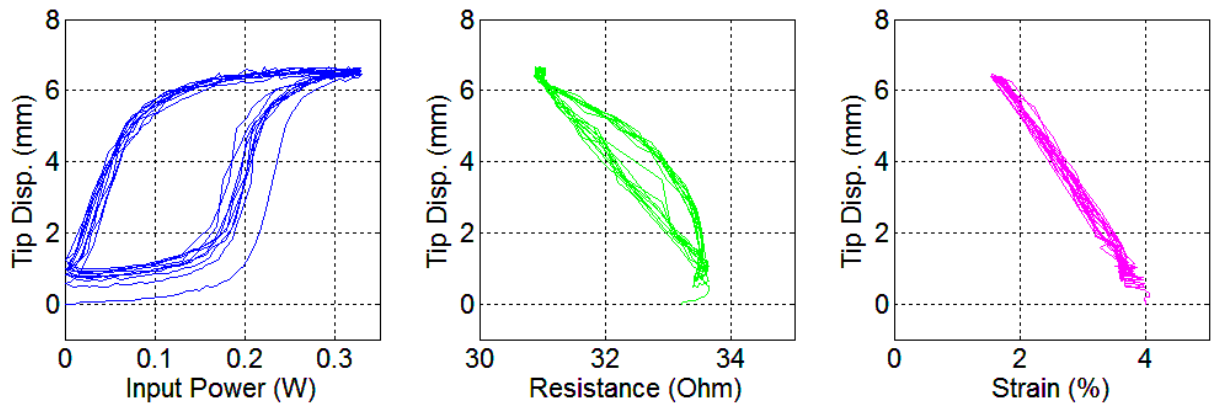


Figure 102: Hysteresis Plots for Top Joint Actuator 3 at 0.1 Hz

The stable character of the SMA resistance vs. tip displacement plots is encouraging for sensor applications. A sensor application would use the resistance of the SMA wire as a measurement for tip displacement, so the plots shown in Figure 103 would serve as sensor diagrams measuring displacement in each of the actuator directions. The hysteresis in these diagrams as well as the small hooks that occur before and after phase transformation (as discussed in section 2.1.2.7) pose a sensing challenge. However, because the SMA wires were pre-stressed instead of pre-strained, the hysteresis is narrow as discussed in section 2.1.3.5. Section 2.2.3 discusses methods for overcoming the hysteresis in sensing applications.

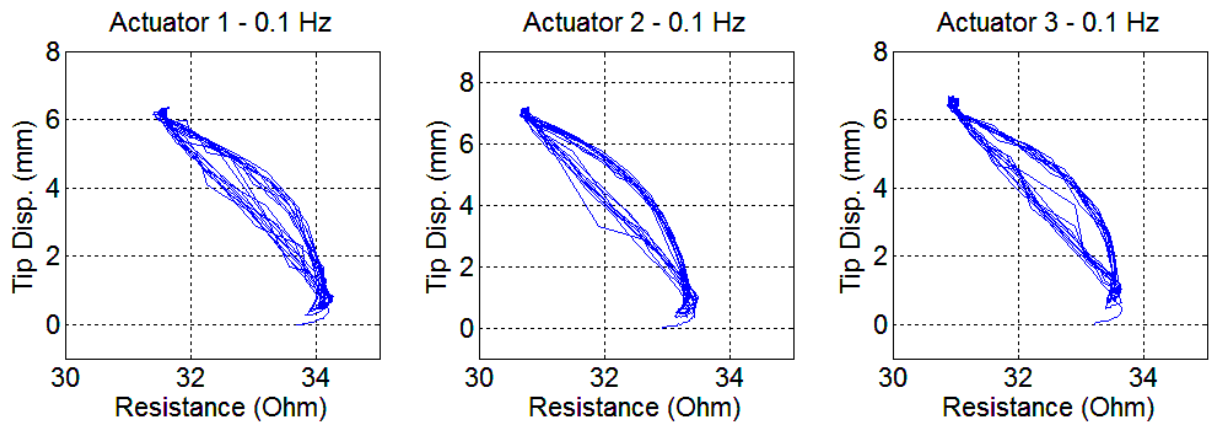


Figure 103: Top Joint Sensor Diagrams: Resistance vs. Tip Displacement in Actuator Direction 1, 2, or 3 at 0.1 Hz

Figure 104 shows how the resistance vs. tip displacement plots change when the actuators are cycled at a higher frequency. At 0.5 Hz, the passive cooling process cannot complete before the next heating cycle begins, so the nozzle tip is not able to return to its zero position. As a result, the plots follow inner loops on subsequent cycles. However, the position of the hysteresis within the plot box does not change.

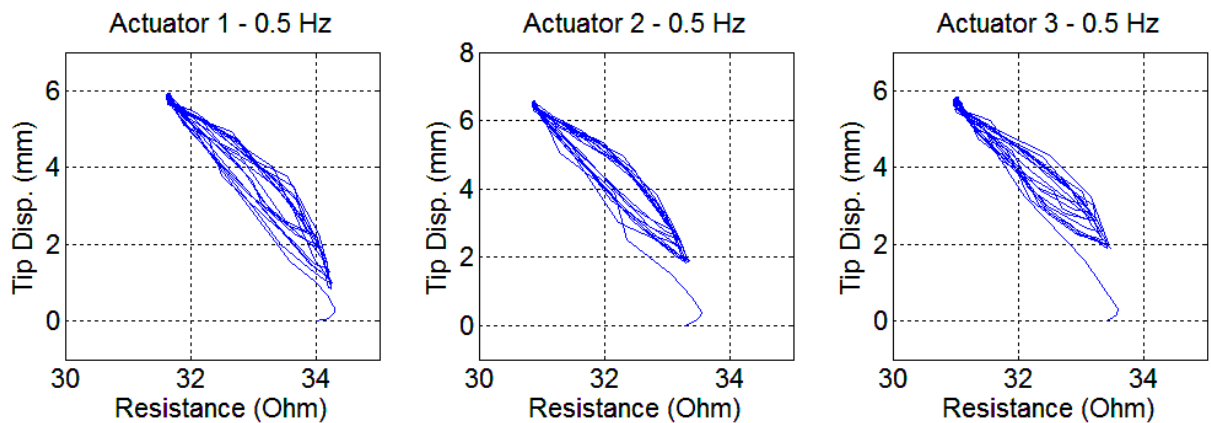


Figure 104: Top Joint Sensor Diagrams: Resistance vs. Tip Displacement in Actuator Direction 1, 2, or 3 at 0.5 Hz

The same results are shown for the actuators 4, 5, and 6 of the bottom joint in Figure 105 through Figure 109. When the bottom joint rotates it must move a longer section of nozzle, including the top joint. It therefore carries more inertia and is cycled at a lower 0.4 Hz frequency so that the passive cooling and the structural spring-back process can remain quasi-static. There is once again some variation in the strain vs. tip displacement measurements, but there is also still good stability in the characteristics from one cycle to the next.

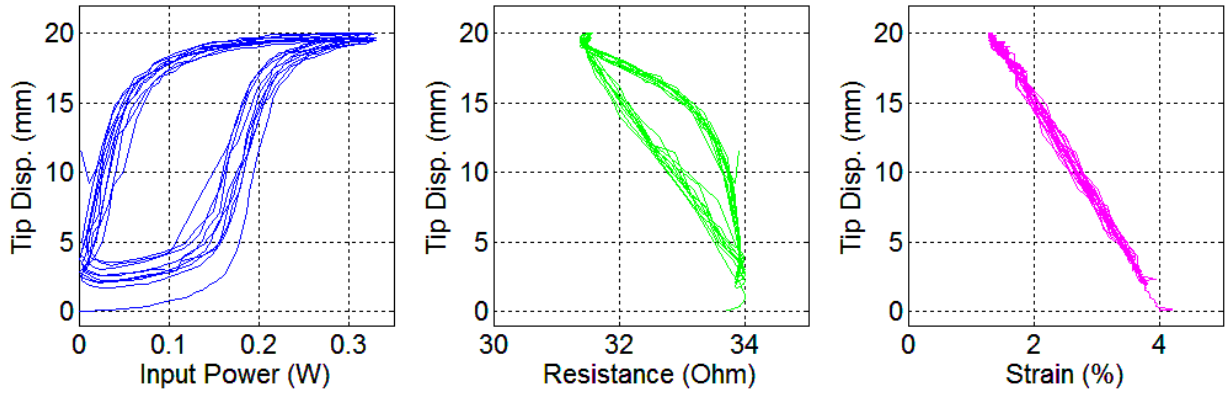


Figure 105: Hysteresis Plots for Bottom Joint Actuator 4 at 0.04 Hz

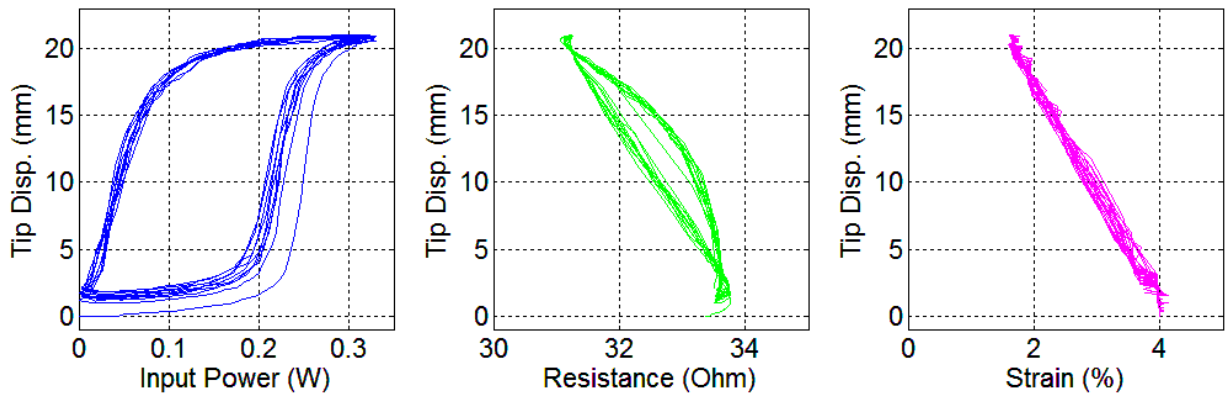


Figure 106: Hysteresis Plots for Bottom Joint Actuator 5 at 0.04 Hz

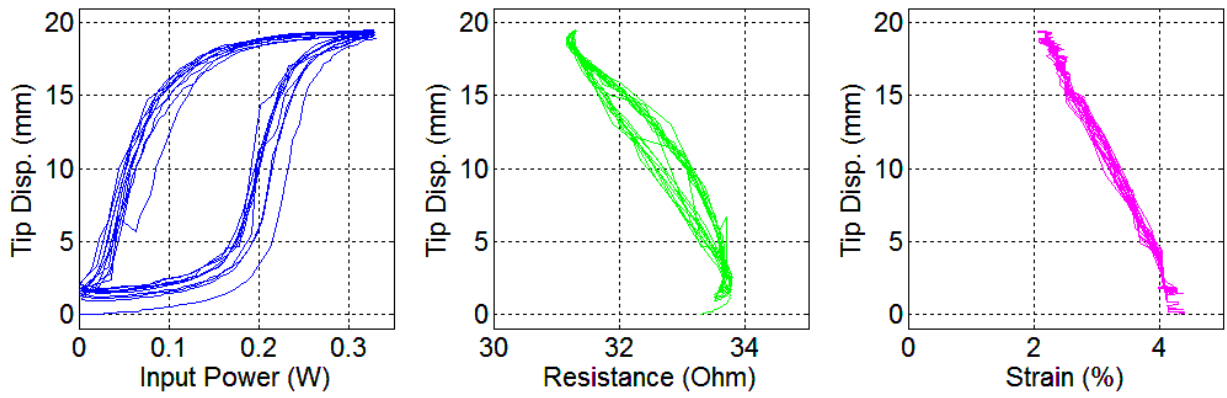


Figure 107: Hysteresis Plots for Bottom Joint Actuator 6 at 0.04 Hz

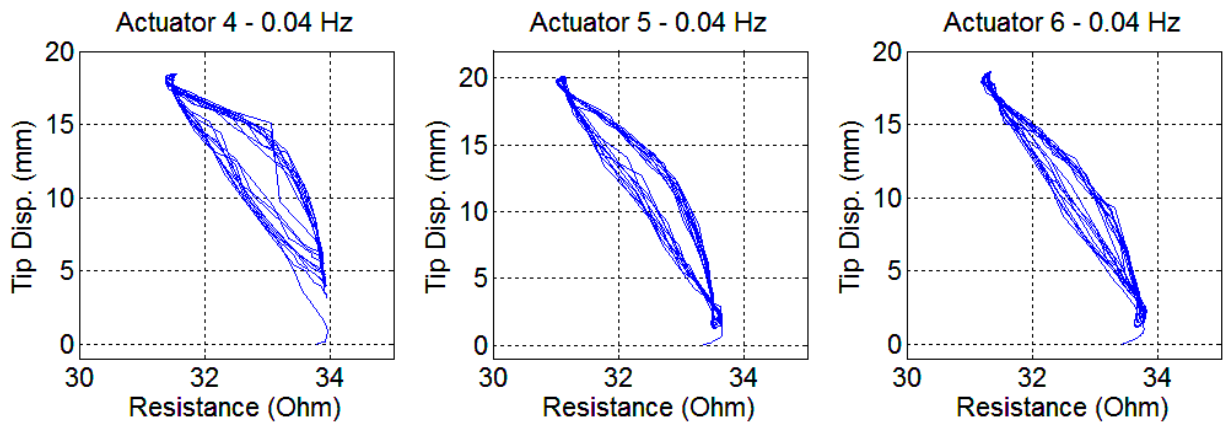


Figure 108: Bottom Joint Sensor Diagrams: Resistance vs. Tip Displacement in Actuator Direction 4, 5, or 6 at 0.04 Hz

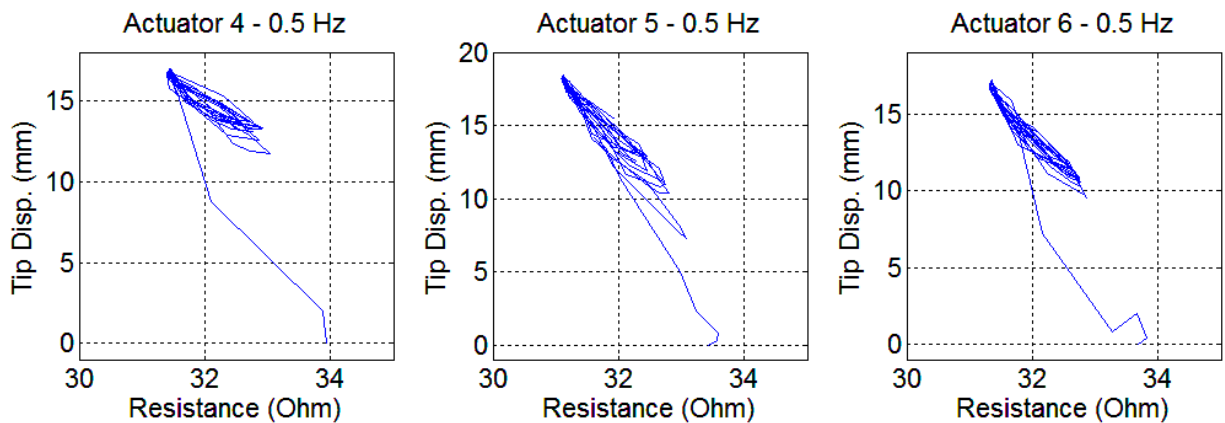


Figure 109: Bottom Joint Sensor Diagrams: Resistance vs. Tip Displacement in Actuator Direction 4, 5, or 6 at 0.5 Hz

Figure 110 shows the time history of an alternating power input test, where each actuator in the top joint was heated then cooled one at a time. In this case, the tip displacement plot in Figure 110 shows the magnitude of displacement, not the component of displacement resolved in any actuator direction. When viewed from above, the nozzle tip follows the trace shown in Figure 111, resembling a Mercedes star.

One interesting feature of the resistance plot in Figure 110 is the bump that occurs early in the heating cycle of each actuator. For example, the bump measured in the resistance of wire 1 (red) between 0 and 2 seconds. This is a result of the stretching that occurred in wire 1 while wire 3 was heated during a previous cycle (not shown). When wire 1 cools under low stress, some grain of  $M^-$  are able to develop alongside the  $M^+$ , resulting in a somewhat shorter wire without observable slack. When the opposing wire (wire 3) heats, wire 1 is stressed into almost entirely  $M^+$ , and then when wire 3 cools, wire 1 is unable to recover the  $M^-$  phase and slack develops. As soon as heating of wire 1 begins at  $t = 0$ s, this slack is recovered very quickly. Once the slack is removed, the additional force needed to deform the structure necessitates more heat, resulting in the  $\sim 2$  s delay, during which time the resistance of the wire actually increases slightly due to the thermal dependence of resistivity. This process repeats for each actuator over the 100 s experiment shown in Figure 110.

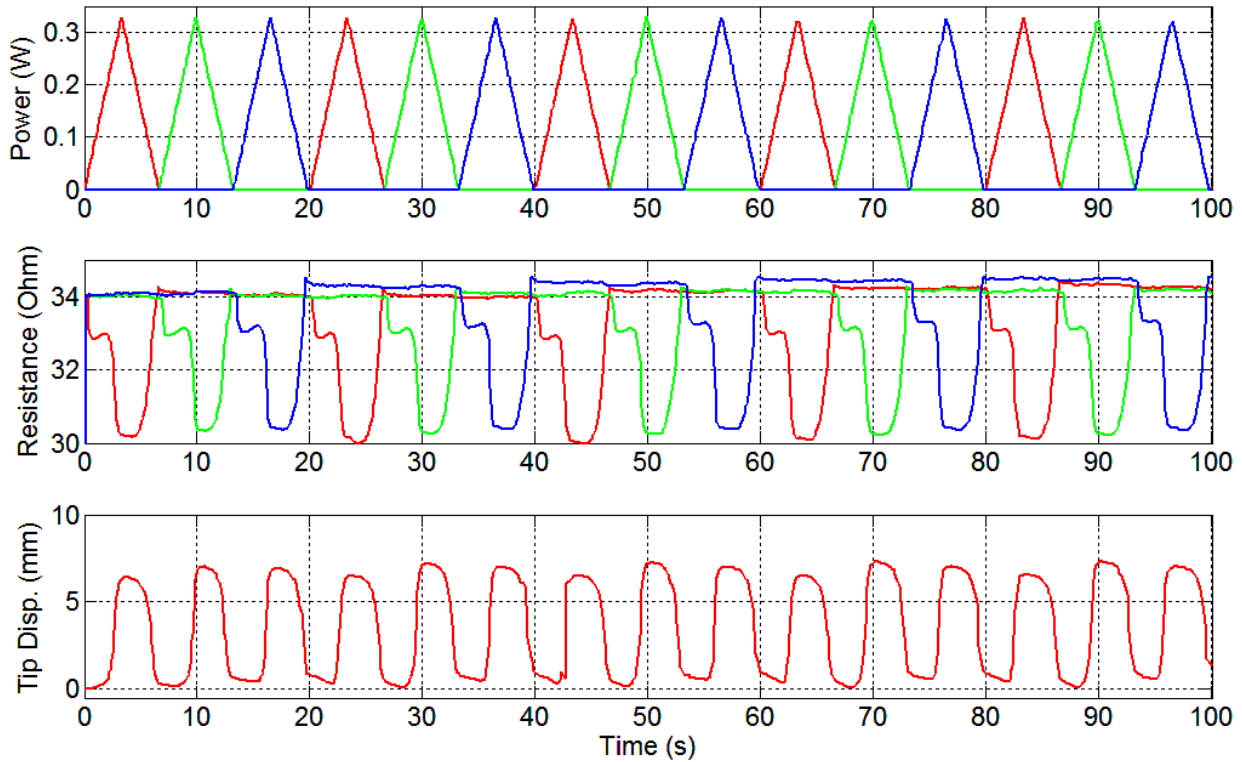


Figure 110: Time Histories for Top Joint Actuator 1 (red), 2 (green) and 3 (blue) for Mercedes Star Input at 0.05 Hz

Figure 111 shows how the nozzle tip deflects in the direction of the actuated SMA wire, each oriented 120 degrees apart. Note that actuator 1 is aligned with the positive y axis and actuator 2 follows clockwise, into the positive x and negative y quadrant. The trace has a slightly skewed appearance because actuator 1 is still about 0.5 mm from the origin when the nozzle tip is pulled in the actuator 2 direction, and subsequently actuator 2 is still ~0.5 mm from the origin when actuator 3 is heated. This is to be expected, and occurs because as wire 1 contracts, wires 2 and 3 are stretched. Then when wire 1 is cooled again slack develops in wires 2 and 3, and the restoring force provided by the structure alone is insufficient to bring the tip back to center.

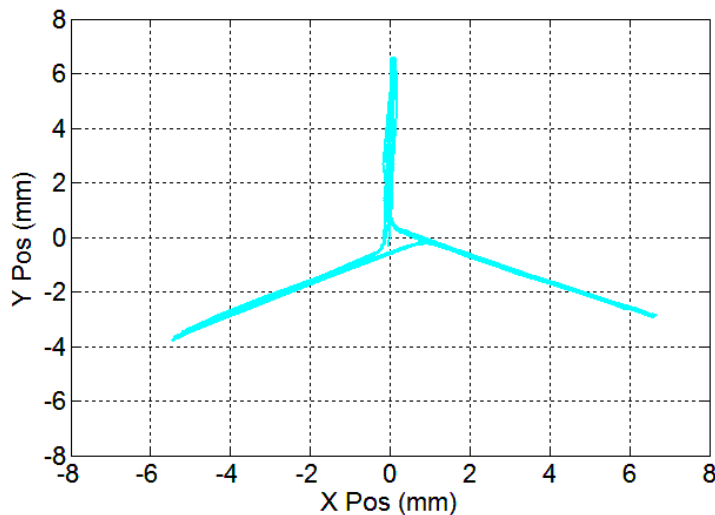


Figure 111: Tip Displacement of Top Joint Mercedes Star Input

#### ***2.1.4.4 Conclusions from Nozzle Testing***

The results of nozzle testing validate that the fabrication processes discussed in Part 1 produced a stable electrical and mechanical connection between the SMA wires and nozzle structure. This leads to repeatable behavior from one cycle to the next. Although each actuator does not behave identically, they have qualitatively similar performance and repeatability, so the variations can be calibrated for sensing and controls purposes.

Also, the sensor diagrams in Figure 103, Figure 104, Figure 108, and Figure 109 show that pre-stressing the SMA wires helped keep hysteresis in the resistance vs. tip displacement curves narrow, as was predicted by the discussion in section 2.1.3.5. In the sensing and control schemes in the sections that follow, the narrower hysteresis helps to simplify the sensor mapping method and reduce measurement errors.



## 2.2 Sensing and Controls with Multifunctional SMA Wires

The multi-functional capabilities of SMA wires can be exploited by measuring the resistance change of the wire during phase change and correlating it to the strain change in the SMA and accompanying deformation of the structure. The sensor information can then be used as the input to a feedback controller that commands a heating power. In effect, the material has the ability to measure its own length change, then react to a small change in heating power to bring that measured length to a desired set-point. In such an implementation, not only is the actuator system streamlined by removing conventional motors, but the need for an additional feedback sensor is also eliminated.

The goal of this section is to develop a simple method for sensor mapping, then implement the mapping into closed-loop control of the systems discussed in Part 2 – starting with the single SMA-spring system and building up to the adaptive nozzle joint. While the complex behavior of SMA wires may inspire a wide range of sensor mapping and controls methods, this work focuses on developing the simplest functional sensor mapping technique and basic PID feedback control. This approach reduces the complexity of mapping or controller dynamics, thus making the material-driven errors easier to identify. Then physics-based methods for reducing errors and improving performance are discussed along with other areas for future work.

### 2.2.1 Sensor Mapping and Control of Single SMA-Spring System

As before, the first system studied is the single SMA-spring system discussed in section 2.1.2 and diagramed again in Figure 112. The characteristics measured in section 2.1.2 are used to motivate a method for sensor mapping, then this method is applied to closed-loop control of the same flexure system used in characterization. The coordinate frame is established such that  $\delta = 0$  when  $\varepsilon = \varepsilon_{pre}$ .

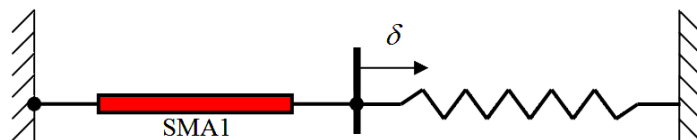


Figure 112: Single SMA-Spring System

#### 2.2.1.1 Resistance to Deflection Sensor Mapping

The simplifying assumption behind the scheme for mapping resistance to deflection is that resistance relates approximately linearly and non-hysteretically to SMA wire strain (and thus flexure deflection) while phase transformation is occurring. Under this assumption, the plots in Figure 113 are used to motivate a general scheme for creating a position feedback sensor out of a SMA-spring system. In the plots in Figure 113, reproduced from the characterization experiments in section 2.1.2, the 150 MPa pre-stress case is isolated and used to generate a resistance to displacement mapping based on characteristic data. Other pre-stress or pre-strain situations would require a separate mapping. The resistance vs. strain plot in the left panel of Figure 113 is qualitatively equivalent to resistance vs. displacement because in the flexure setup shown in Figure 69 strain is calculated directly from the measurement of flexure displacement scaled by the length of the SMA wire. The characteristic for the

150 MPa case is highlighted in green, and a linear curve fit (blue) is generated to approximate the relationship.

The objective of the mapping is to get a relation for displacement as a function of resistance. First, in equation (2.42) resistance is mapped linearly to strain. Then the deflection of the flexure,  $\delta$ , is scaled with the change in length of the SMA wire, as shown in equation (2.43). Finally, equation (2.42) is substituted into equation (2.43) and constant coefficients are combined such that  $k = L_{0,SMA}k_1$  and  $\delta_0 = L_{0,SMA}(\varepsilon_0 - \varepsilon_{pre})$  to create Equation (2.44) that maps resistance directly to deflection.

$$\varepsilon = k_1R + \varepsilon_0 \quad (2.42)$$

$$\delta = L_{0,SMA}(\varepsilon - \varepsilon_{pre}) \quad (2.43)$$

$$\delta = kR + \delta_0 \quad (2.44)$$

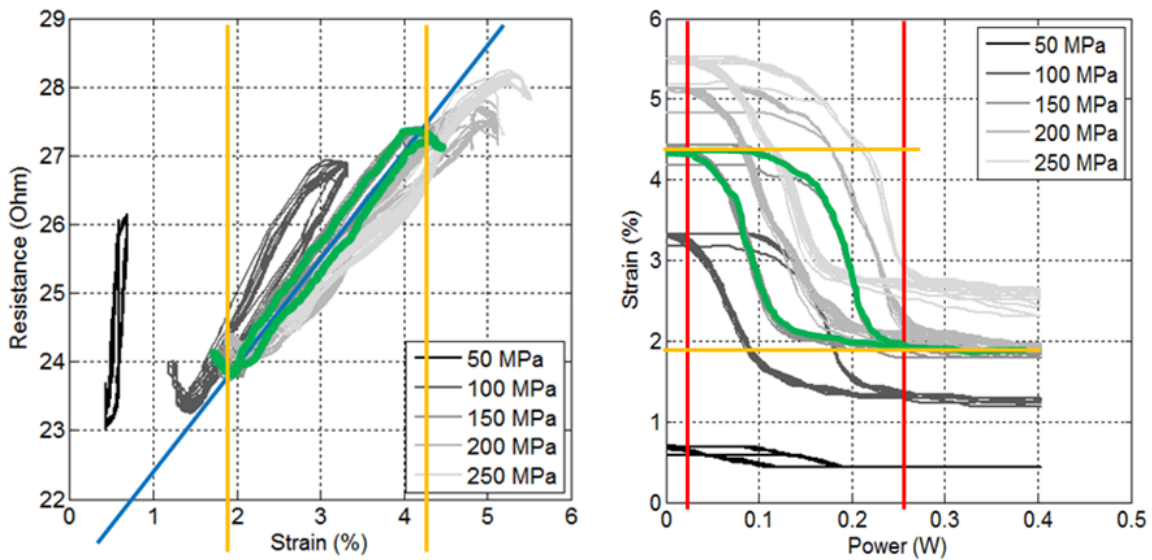


Figure 113: Example of Using Characteristics of a SMA-Spring System to Generate a Displacement Sensor Mapping

Next, Figure 113 shows how the range of the sensor characteristic must be limited to avoid the hooked regions at the extremes of the R- $\varepsilon$  relationship, where a single resistance value correlates to multiple strain (displacement) measurements. As discussed in section 2.1.2.7, these hooks result from heating the SMA wire without inducing phase transformation, as is the case before the wire temperature reaches austenite start temperature and when additional heat is added after phase transformation is complete. During these non-transformation periods, heating the SMA wire causes its resistance to increase, just as is the case in a non-active metal. In order to prevent the hooked areas from causing mapping errors, the range of input power is simply limited to the range that induces transformation, as indicated by the red vertical lines in the right panel of Figure 113 – so for the case shown, the power input would be limited to between 0.03 and 0.23 W. Although at first this

procedure limits the authority that a user may have over input power for high-speed control applications, one can easily imagine a controller that relaxes the range limitations for a short periods of time while tracking error is large.

### 2.2.1.2 Feedback Control Scheme

Once the mapping coefficients in equation (2.44) and the power ranges are obtained, the mapping can be employed in a simple feedback controller. The block diagram in Figure 114 shows how the Joule heating power and electrical resistance that are measured by a custom-built power controller [46] are passed into the mapping algorithm. Then the deflection,  $\delta$ , is commanded, and a simple PI controller dictates the command power for the next loop. The PI gains were tuned manually and then maintained for all experiments, but no significant effort was made to optimize them. Additional control features, such as a feed-forward algorithm, a mechanism to relax input power range limitations for a short period of time while tracking errors are large, or model-based controller could be employed. However, the primary focus is to analyze the performance of the mapping under the assumptions mentioned.

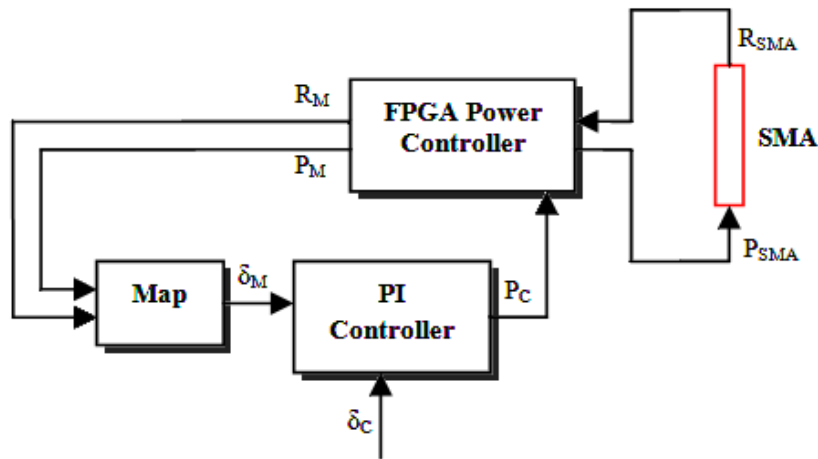


Figure 114: Controller and Mapping Block Diagram

### 2.2.1.3 Closed-Loop Control of SMA-Spring System

The performance of the controller and the accuracy of the resistance-based position feedback measurement were tested in response to sinusoid inputs at 0.2 Hz, 1.0 Hz, and 2.0 Hz as well step inputs. Figure 115 shows that at 0.2 Hz, the controller is able to force the SMA to follow the command positions very well. Tracking error, which is equal to the difference between the command position,  $\delta_C$ , and the resistance-based position measurement,  $\delta_{M,res}$ ,

$$E_T = \delta_C - \delta_{M,res} \quad (2.45)$$

is 8  $\mu\text{m}$  RMS (root mean square). This error is only measured over the last  $\frac{3}{4}$  of the time series to avoid the larger initial peaks and make results comparable from one experiment to the next, and it represents the average deviation from 0 error. The more significant error come from the

measurement. The measurement error calculated by subtracting the resistance-based displacement measurement from the laser-based measurements,  $\delta_{M,laser}$ ,

$$E_M = \delta_{M,laser} - \delta_{M,res} \quad (2.46)$$

is 21  $\mu\text{m}$  RMS with a peak to peak error of 50  $\mu\text{m}$ , or about 8% of full scale. These two metrics are labeled on the “Error” plots in Figure 115 through Figure 118, and compiled in Table 11. The measurement error has a tendency to change sign each time the displacement reverses direction. This is not surprising, because the resistance vs. strain characteristic in Figure 113 has a slight hysteresis. This hysteresis affects the measurement accuracy every time the phase transformation process switches direction.

The right plot in Figure 115 shows the SMA resistance plotted vs. displacement as measured by the laser (red) and the resistance-based mapping (blue). Of course the mapping shows up as a straight line, since mapped displacement is calculated directly from the resistance measurement via the slope and intercept of the best-fit line. In this implementation, the linear approximation is appears effective.

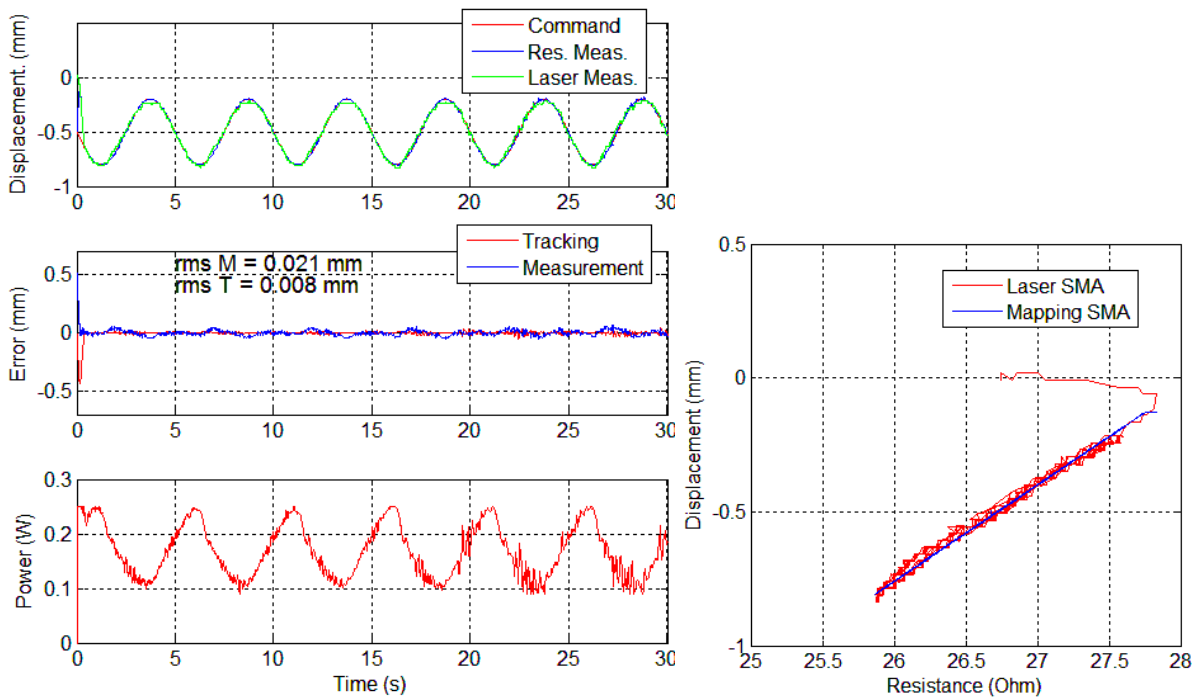


Figure 115: Position Tracking of 0.2 Hz Sinusoid (left) and Sensor Diagram Showing Displacement as measured by the Laser and the R- $\delta$  Mapping (right)

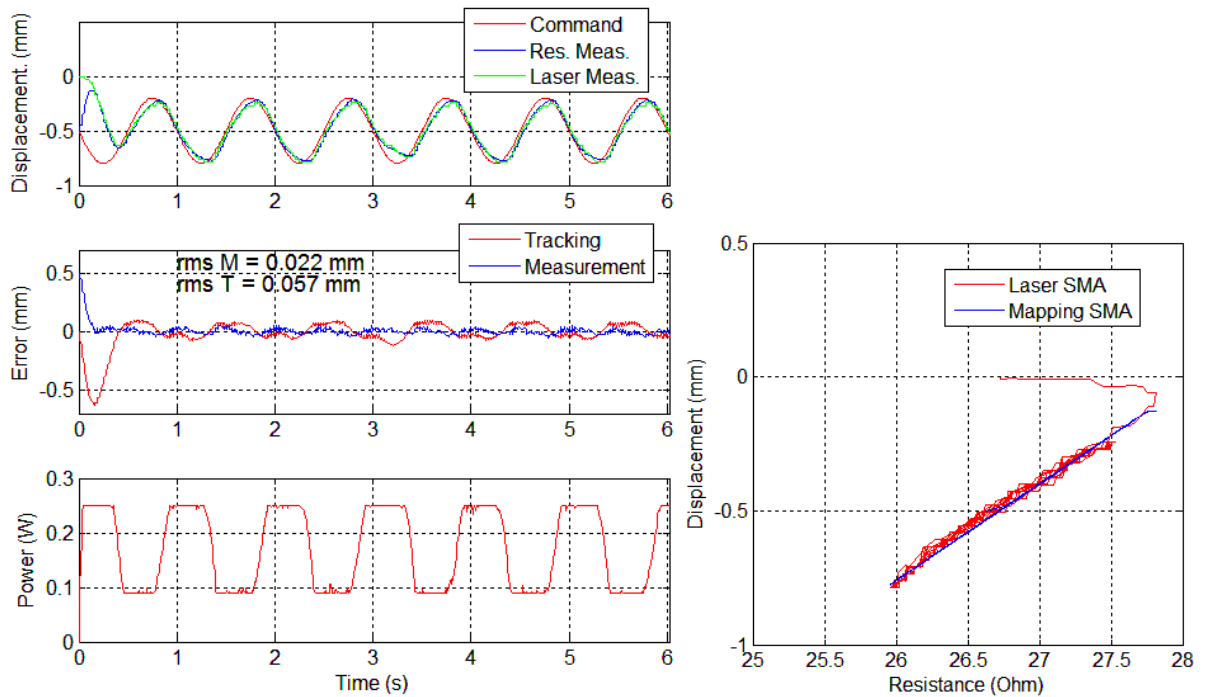


Figure 116: Position Tracking of 1.0 Hz Sinusoid (left) and Sensor Diagram Showing Displacement as measured by the Laser and the R- $\delta$  Mapping (right)

When the input frequency is increased to 2.0 Hz in Figure 117. The measurement error is once again 22  $\mu\text{m}$  RMS, and it still changes direction with each cycle; however, now the lag causes a very large tracking error. The power plots in Figure 116 and Figure 117 show how power quickly switches from the upper limit to the lower.

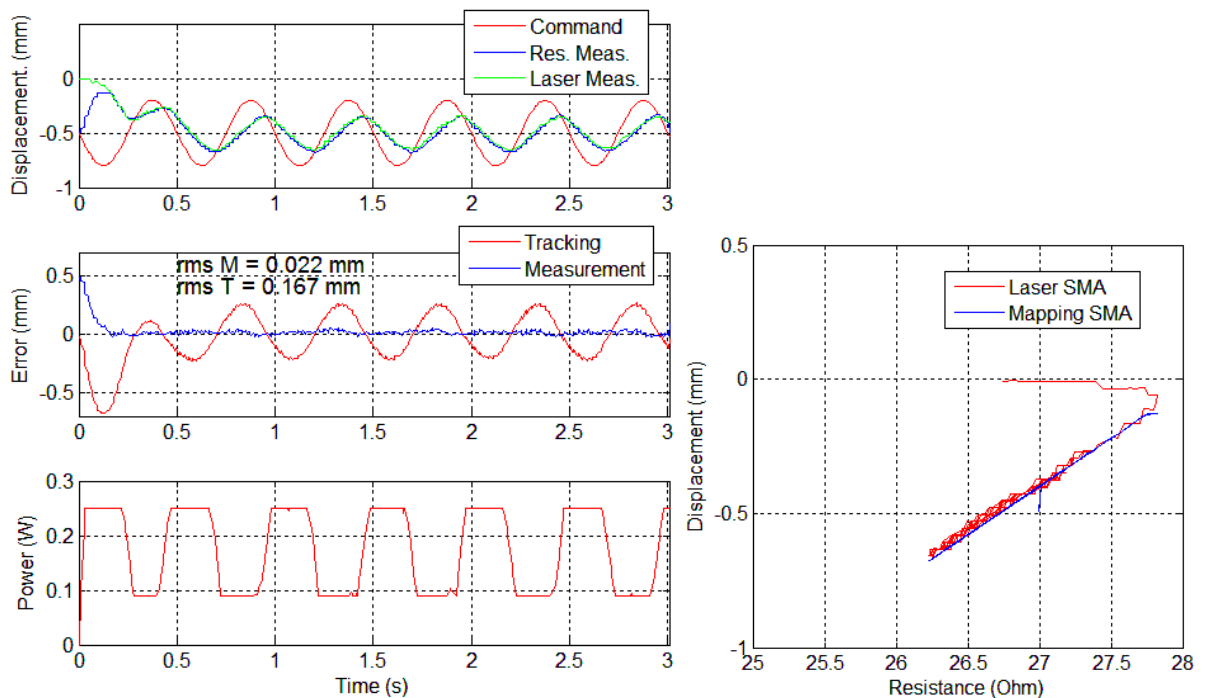


Figure 117: Position Tracking of 2.0 Hz Sinusoid (left) and Sensor Diagram Showing Displacement as measured by the Laser and the R- $\delta$  Mapping (right)

The most extreme cycling rate is captured by a step input, shown in Figure 118. The position plots show that for the upper power limit established, it takes about 0.35 s for the SMA wire to contract by 0.4 mm, correlating to a strain change of about 2%.

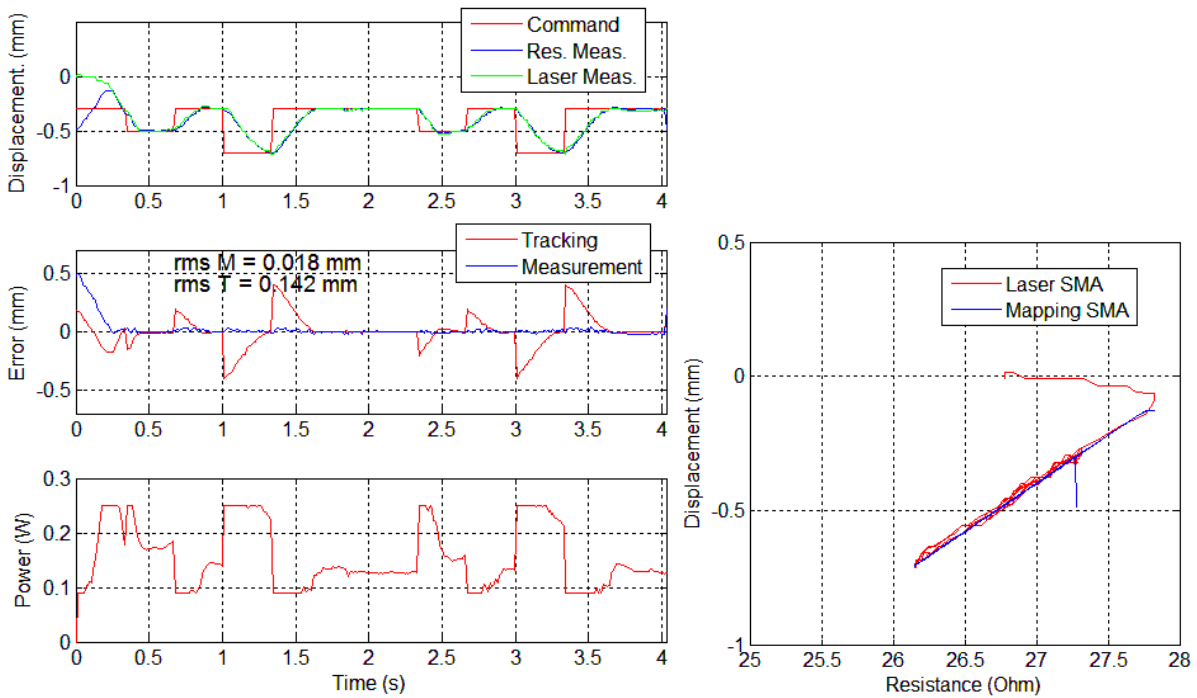


Figure 118: Position Tracking of Variable Step Input (left) and Sensor Diagram Showing Displacement as measured by the Laser and the R- $\delta$  Mapping (right)

### 2.2.1.4 Conclusions from Single SMA-Spring Sensor Mapping and Control

The simplest possible sensor mapping fit a line to the resistance vs. deflection plot and then limited the power to prevent the wire from being heated or cooled without phase transformation. This produced a sensor with peak to peak accuracy of better than 50  $\mu\text{m}$  over a range of 0.6 mm, or about 9% of full scale. Also, this measurement accuracy was robust to input wave frequency and type, as shown in the summary of RMS errors in Table 11. The controller is able to drive enough power to fully actuate the wire and eliminate a positive tracking error in less than 0.4 s; however, this could be reduced significantly if the max heating power were not limited. Also the passive cooling process makes eliminating negative tracking errors slower and subject to environmental conditions. One way to regain control authority over negative tracking errors is to add a second opposing SMA wire, as is discussed in the next section.

Table 11: RMS Tracking and Measurement Error for Single SMA-Spring System Pre-stressed to 150 MPa.

	Track. Err. (mm RMS)	Meas. Err. (mm RMS)
0.2 Hz	0.008	0.021
1.0 Hz	0.057	0.022
2.0 Hz	0.176	0.022
Step	0.142	0.018

## 2.2.2 Sensor Mapping and Control of Opposing SMA System

The opposing SMA system in Figure 119 has the potential to improve sensing by providing two separate resistance measurements that can be combined to produce a single deflection measurement. Also, the opposing SMA actuator can improve control authority and actuation frequency, as discussed in section 2.1.3.

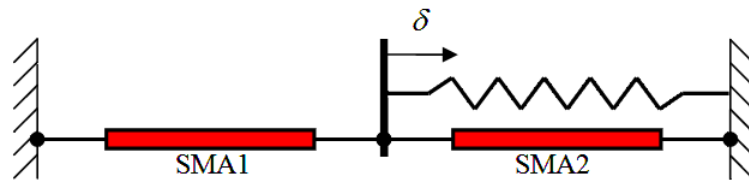


Figure 119: Opposing SMA-Spring System

### 2.2.2.1 Automated Sensor Mapping and Feedback Control Scheme

Sensor mapping of the opposing SMA system is similar to the single SMA system, in that a linear fit with an accompanying slope and intercept is made to the resistance vs. deflection curve, as shown in equation (2.44). However, in the case of the dual-SMA system, each wire displacement will have its own displacement measurement,  $\delta_1$  and  $\delta_2$ , and slope and intercept. The two displacement measurements must then be reconciled into one measurement of the flexure displacement. This can be done in many ways; however, in order to reduce the human variables inevitable in an ad hoc controller implementation, an automated mapping and control scheme was used to systematically study performance. The steps in the mapping scheme are to:

- **Calibrate** mapping coefficients and power limits for both actuators.
- **Convert** the two actuator measurements into a single displacement measurement.
- **Control** the input power via a PID control algorithm.
- **Choose** which actuator to power.

Those steps are shown in the block diagram in Figure 120 and described in greater detail below.

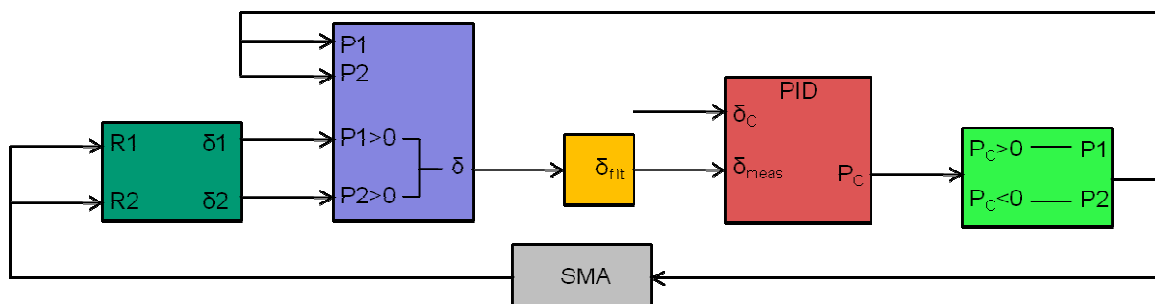


Figure 120: Block Diagram of Opposing SMA System Sensor Mapping and Control Scheme

### Calibrate

The first step is to calibrate the sensor mapping coefficients to convert the measured resistance of the SMA wires to two separate displacement measurements (dark green block in Figure 120). This is done by running an automated actuation test, using a procedure identical to the “constant opposing power” experiment procedure in section 2.1.3.4. In this first implementation, an opposing power of 0

was used, and the sensor mapping is applied to the SMA wire being actuated. Figure 121 shows an approximation of a fit (black) done on the cycled actuator's resistance vs. strain plot (red).

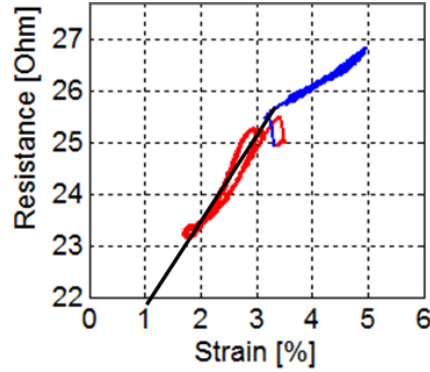


Figure 121: Sensor Diagram for Coupled SMA System

The calibration is repeated for the second SMA wire, then the sensor mapping coefficients can be written in matrix format,

$$\begin{bmatrix} \delta_1 \\ \delta_2 \end{bmatrix} = \begin{bmatrix} k_1 & 0 \\ 0 & k_2 \end{bmatrix} \begin{bmatrix} R_1 \\ R_2 \end{bmatrix} + \begin{bmatrix} \delta_{01} \\ \delta_{02} \end{bmatrix}. \quad (2.47)$$

The power limits were also identified during the automated calibration procedure. The lower limit was chosen by identifying the input power that corresponded to the highest measured resistance after the first cycle. The experiments in section 2.1.3 showed that no minimum resistance value can be identified because the large opposing force from the second SMA wire prevents complete phase transformation in the first, so no upper power limit is needed to keep the SMA wire within the accurate measurement range.

### Convert

The two separate measurements in equation (2.47) are then converted to a single measurement. This is done by reviewing the power command from the previous control step. Since the mapping coefficients were determined for an SMA wire during cyclic actuation, the sensing scheme chooses the measurement from the SMA wire that was being powered in the previous control step, as indicated by the purple block in Figure 120.

Unfortunately, this method of simply choosing one measurement value or the other leads to inherent instability near zero tracking error where control power switches from one actuator to the other. This occurs because inherent measurement errors cause the two SMA wires produce slightly different measurements, leading to noise in the chosen  $\delta$  value. To reduce the chatter, a 4 point running average filter is applied to the displacement measurement in the yellow block in Figure 120. Since the heating and cooling process occurs slowly compared to the control loop ( $\sim 300$  Hz), the averaging does not introduce significant measurement lag.

## Control

The filtered measurement value is then fed into a simple PID algorithm. The gains are once again chosen such that the system does not become unstable, then maintained through all experiments. The minimum power limit is imposed at all times, and a maximum power limit for the controller of 0.32 W is chosen to prevent the wire from overheating. However, in this implementation a 0.35 W burst of power is allowed for a short period of time when tracking errors greater than 0.2 mm.

## Choose

The PID controller produced a positive control power to compensate negative tracking errors and negative control power to compensate positive tracking errors. For negative tracking errors, the control power was applied to SMA 1, as labeled in Figure 119. For positive tracking errors, the control power was negated and applied to SMA 2.

### ***2.2.2.2 Calibration and Experiment Procedure***

The mapping and control scheme was tested on the same experimental setup described in section 2.1.3.3 and diagrammed in Figure 87. Two opposing 50  $\mu\text{m}$  diameter Flexinol SMA wire from Dynalloy [1] are used for testing. The entire calibration scheme was automated to eliminate any potential bias from a user. Once again, the hysteretic nature of the material requires that the pretreatment steps be documented as well so that the initial state of the wire is known. Also, many of the sources of error in the results can be identified because they are a direct result of the particular steps taken during calibration.

### **Automated Pretreatment and Calibration Procedure**

The pretreatment and calibration steps are fully automated using the real-time operating system onboard a National Instruments cRIO 9074 input/output device with LabVIEW 2010. The pretreatment procedure is identical to that used in the experimental characterization of the coupled SMA system in section 2.1.3.4. Also, after pretreatment the SMA wires are either pre-stressed or pre-strained depending on the case being tested. This procedure is also the same as in section 2.1.3.4. The listing of these procedures is repeated below:

#### Pre-Treatment

1. Unclamp the slide bushing so that the SMA junction can slide freely with respect to the spring flexure.
2. Heat both SMA wires with 0.3 W while under 0 stress to transform them into the austenite phase.
3. While the power is still high, retract the linear actuator until the load cell detects a small force. Record the actuator position as  $x_{1,A}$  and the austenitic reference length as  $L_{0,A}$ .
4. Allow both wires to cool under zero stress to the martensitic twin phase. Note that some slack will develop as the martensite plus phase is favored due to the two-way effect.

### Pre-Straining

5. Retract the linear actuator to position  $x_{1A} - 2L_{0A}\varepsilon_{p0}$  to put both wires at a strain level of  $\varepsilon_{p0}$ , as shown in the left plot in Figure 89.
6. Extend the linear actuator until the load cell detects no force.
7. Record this position as  $\varepsilon_{p1}$ , as shown in Figure 89. This is the point from which experiment cycles will begin.
8. Lock the slide bushing so that the spring flexure deflect when the SMA junction moves.

### Pre-Stressing

5. Retract the linear actuator until the load cell detects a stress of  $\sigma_{p1}$ , as shown in the right plot in Figure 89. This is the point from which calibration cycles will begin.
6. Lock the slide bushing so that the spring flexure deflect when the SMA junction moves.

### Calibration Cycles and Mapping Procedure

1. Cycle the power to SMA 1 five times using a triangle wave with an amplitude of 0.25 W at a frequency of 0.1 Hz.
2. Eliminate the data from the first cycle.
3. Find the data-point with the highest measured resistance, and set the associated input power at  $P_{\min}$ , the lower bound on power input.
4. Calculate the slope and intercept,  $k_1$  and  $\delta_{01}$ , of the resistance vs. displacement curve for the last 4 cycles using a least-square fit method.
5. Repeat steps 1-4 for SMA 2 to find  $k_2$  and  $\delta_{02}$ .

### Controller Experiment Procedure

1. Turn off the heating power to both SMA wires for 5 s after the calibration steps to allow them to cool.
2. Choose the set-point waveform and run 10 cycles with the mapping and control scheme implemented as discussed in section 2.2.2.1. Note: in some comparison tests the resistance to displacement mapping is ignored and the laser displacement sensor is used directly as the position feedback measurement.
3. Turn off the heat power to both SMA wires for 5 s while data from one experiment is being saved so that the wires are cool at the start of the next experiment.

#### **2.2.2.3 Results of Opposing SMA Control**

For the results shown, mapping and controller performance is studied in response to an sinusoid input with a commanded displacement of  $\pm 0.4$  mm at 0.2, 1.0, and 2.0 Hz along with a variable step waveform. Results also compare a case where the wires are pre-strained to 3.47% to a case where the wires are pre-stressed to 100 MPa. For each case an additional experiment is run where the resistance to displacement mapping is removed from the control loop and the laser displacement sensor is used directly as the feedback measurement. Since the Keyence LK-G82 laser displacement sensor measures much faster than the control loop rate (50 kHz compared to  $\sim 400$  Hz) and is very accurate

(0.2  $\mu\text{m}$  resolution), it is used as the “ideal” sensor to help differentiate between the controller performance from the mapping performance.

In the right panel of each figure, the displacement measurement determined via resistance mapping is plotted overtop the laser measurement. These plots give some indication of how well the resistance-based measurements align with measurements from an ideal sensor. Unlike in the single SMA system, the resistance-based mapping does not show up on these plots as a simple straight line. As discussed in the “Convert” section above, the two SMA wires provide separate displacement measurements, and the measurement from the wire that is currently subjected to a heating power is chosen to represent the displacement of the flexure. When SMA 1 is being heated, the sensor mapping is the magenta line in the displacement vs. resistance plots and the red line is the validation from the laser sensor. When SMA 2 is heated, the controller uses the sensor mapping plotted in cyan (and blue). Although the magenta and cyan lines are initially calculated directly from the linear mapping coefficients, they do not appear as straight lines because of the filtering that occurs after the displacement measurement is chosen. The running average causes measurements by SMA 2 to be skewed by the measurements from SMA 1 in a previous time step, that was slightly different.

In almost all of the plots shown, the tracking error switches between positive and negative, meaning that the control power switches between SMA 1 and SMA 2 frequently. This switch is always associated with a small bump in measurement error, and therefore tracking error. The controller’s attempt to compensate for this contributes to noise in the system and thus the RMS of the measurement and tracking error.

Another observation that can be made for all of the plots in the pre-strained case is that SMA 1 has a higher minimum power input than SMA 2. Recall that this power input was automatically determined as the power that induced the maximum resistance value during the calibration experiments. SMA 1 consistently shows up with a higher minimum power because of friction in the slide bearing of the experimental setup. Since SMA 1 is behind the slide bearing, it invariably ends up under slightly less tensile force than SMA 2, with the difference being the friction in the bearing. This is apparent from review of the pre-treatment and pre-straining steps. Since some slack forms in SMA 1 after pre-straining, the first little bit of heating power actually causes a reduction in resistance as slack is eliminated, just as was observed in the time history of the nozzle tests in Figure 110. Once the slack is removed, the heating power must increase substantially before the flexure and opposing SMA can be deformed and further contraction can occur. In the meantime, the increasing heating power causes the resistance to increase again until phase transformation begins and the resistance finally reaches the maximum that is used to bound the lower limit of power. So in effect, the minimum power is constantly maintained to ensure that no slack can form in the wires and that they are always on the verge of beginning martensite to austenite phase transformation. Since SMA 1 has more slack than SMA 2, a higher minimum power is needed to eliminate the slack in SMA 1 than in SMA 2. The pre-stressing procedure does not allow any slack to form, so the minimum power levels for SMA 1 and SMA 2 in the pre-stress section (next) are equal.

## Pre-Strained SMA Wires

Figure 122 through Figure 129 show results for SMA wires pre-strained to 3.47%. The behavior observed is much more complex than in the single-SMA case. Once again measurement and tracking errors are quantified via their RMS value, displayed on the “Error” plots. The measurement error is between 59 and 93  $\mu\text{m}$  RMS for all of the pre-strain cases. The RMS of tracking error is highly dependent on the input waveform and is not the primary focus in this work because it is more a metric of controller performance rather than sensor mapping accuracy. Also, it is important to note that there are many different possible methods of implementing the sensor mapping and control scheme. These results focus on only a single method, and its merits and deficiencies are discussed. Other methods may be suitable in different applications and will be subject for future work.

To start, the displacement is shown tracking a slow sine wave in Figure 122, where the controller uses the resistance-based measurement as the feedback sensor. Bumps in measurement error can be observed each time tracking error (and thus control power) switches direction. These bumps are one of the reasons why the errors in the low frequency test of the opposing SMA system are greater than the errors in the low frequency test of the single SMA system in Figure 115. However, in the case of the opposing SMA system, the displacement amplitude is slightly higher, and the SMA wires are pre-strained rather than pre-stressed.

When comparing Figure 122 with Figure 123, where the laser sensor is used as feedback, the chatter is reduced because there is no longer a discontinuity in the measurement. The reduction in noise brings down both measurement (equation (2.46)) and tracking error, now defined as

$$E_T = \delta_C - \delta_{M,laser} \quad (2.48)$$

for the experiments where the laser is the feedback sensor. There is still a small bump in tracking error when the control power switches from one SMA wire to the other. Although it is not used in the feedback loop, the resistance-based measurement is still plotted in magenta and cyan on the resistance vs. displacement plots, and the bumps in measurement error defined by equation (2.46) can still be observed.

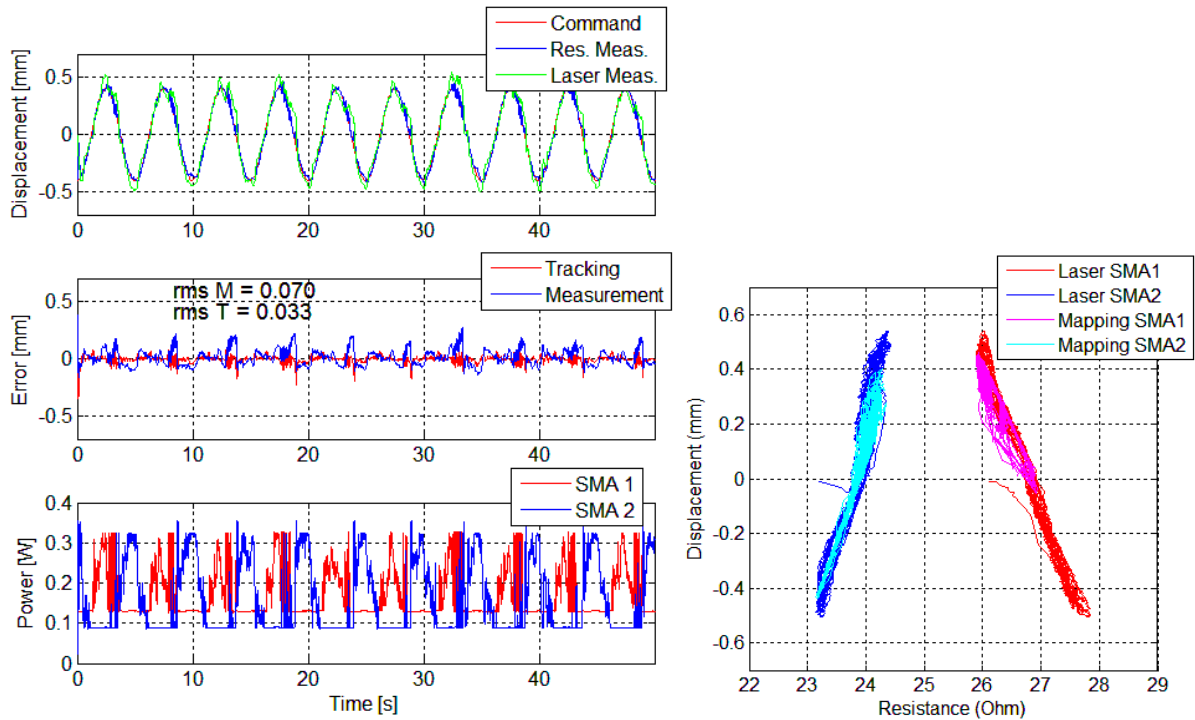


Figure 122: Tracking (left) and Sensor Diagram (right) of a 0.2 Hz Sinusoid using Resistance Mapping as Feedback Measurement for 3.47% Pre-Strained SMA Wires

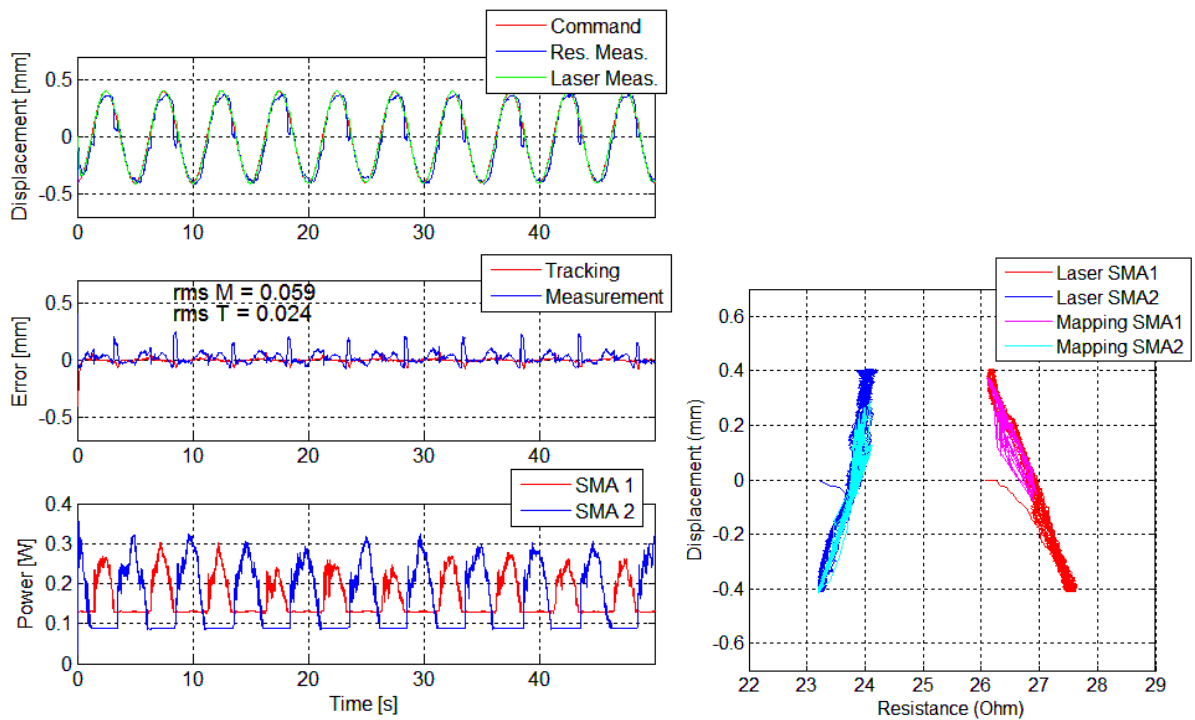


Figure 123: Tracking (left) and Sensor Diagram (right) of a 0.2 Hz Sinusoid using Laser Sensor as Feedback Measurement for 3.47% Pre-Strained SMA Wires

When actuation frequency is increased to 1.0 Hz in Figure 124 and Figure 125, a lag becomes visible and tracking error increases significantly as a result. Since the controller cannot quite keep up, the tracking error is more distinctly positive or negative, so the SMA wire that is used as the sensor switches less frequently. Like in the single SMA system, measurement error is much less effected by

the increase in command frequency than tracking error. The plot in Figure 125 shows that the laser sensor once again provides a more effective feedback sensor, helping to bring down both errors.

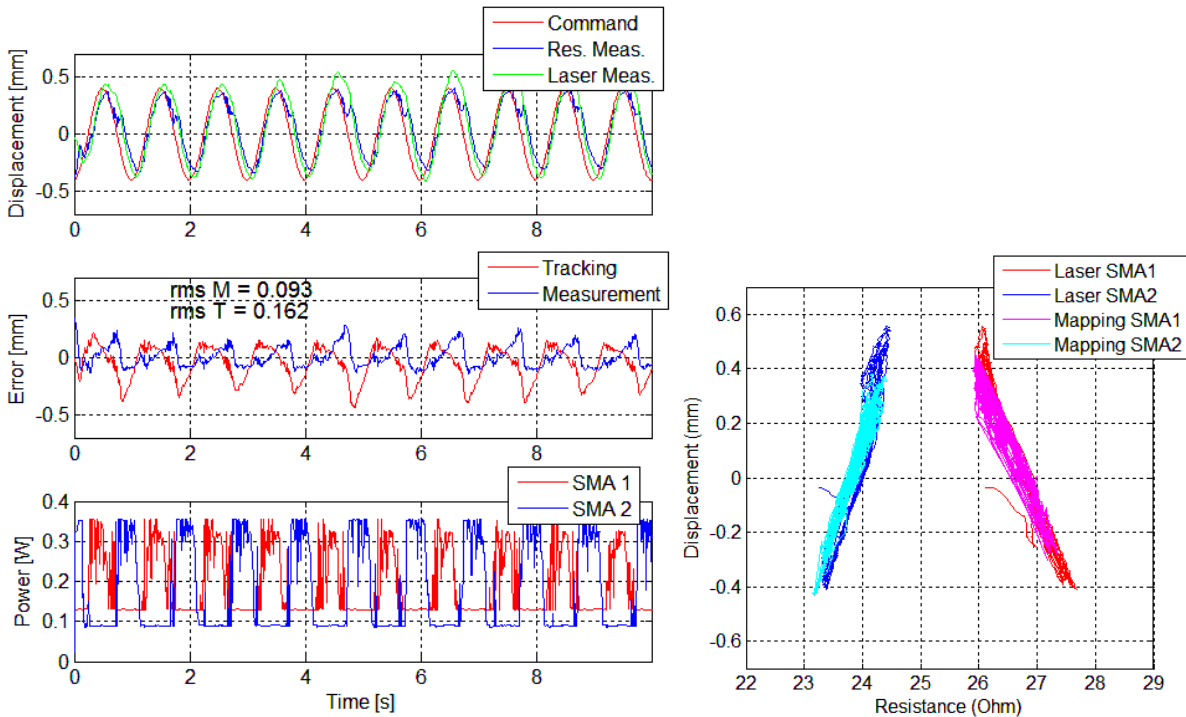


Figure 124: Tracking (left) and Sensor Diagram (right) of a 1.0 Hz Sinusoid using Resistance Mapping as Feedback Measurement for 3.47% Pre-Strained SMA Wires

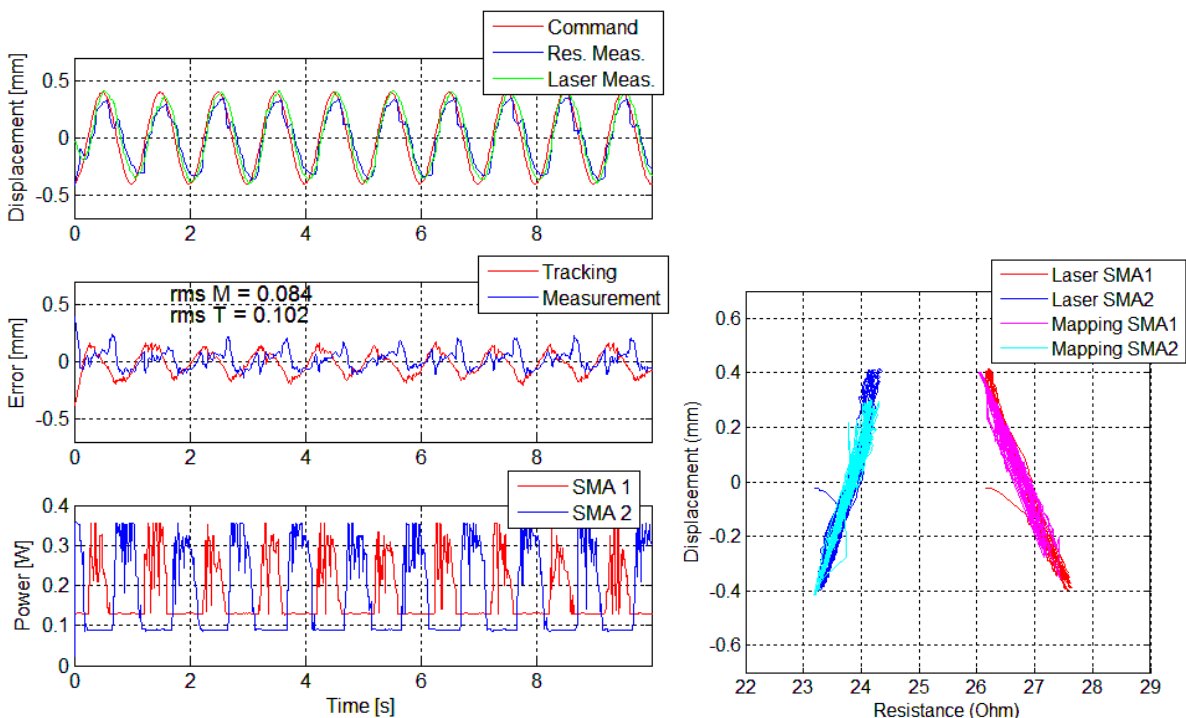


Figure 125: Tracking (left) and Sensor Diagram (right) of a 1.0 Hz Sinusoid using Laser Sensor as Feedback Measurement for 3.47% Pre-Strained SMA Wires

These trends continue to 2 Hz in Figure 126 and Figure 127. However, as frequency increases the choice of sensor becomes less important because error is dominated by the controller's inability to

track the input. This could be predicted from the fact that measurement error is more or less constant. As tracking error increases the choice of sensor become less critical.

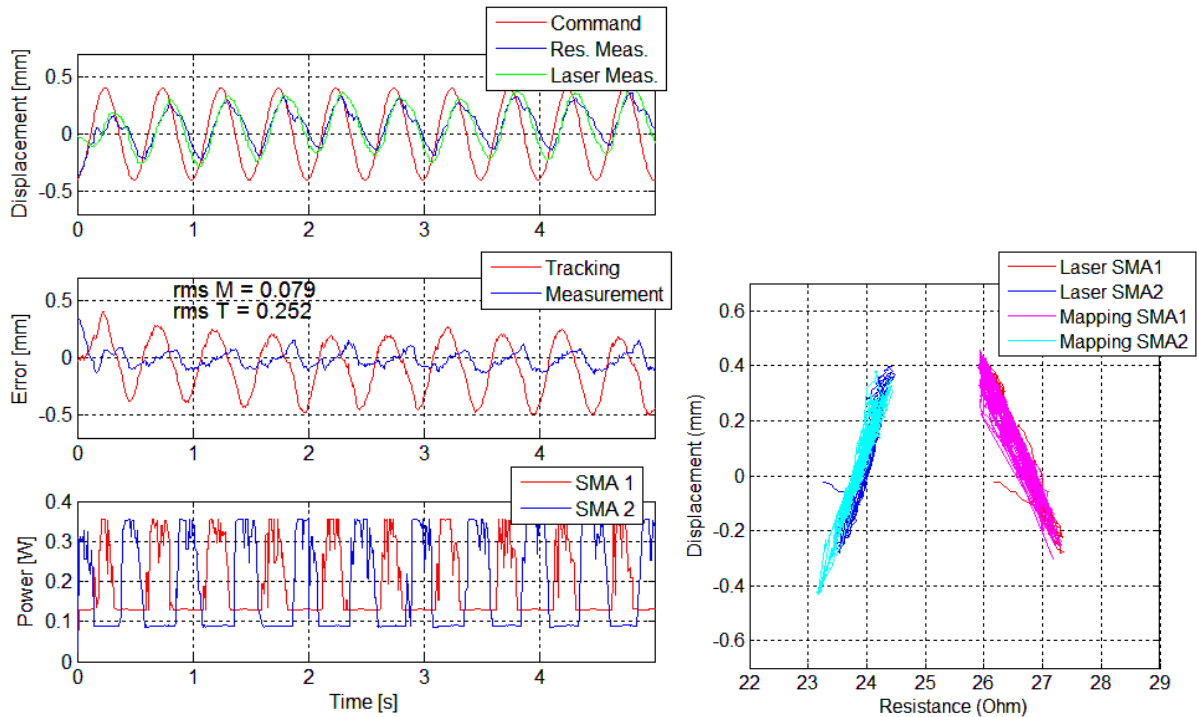


Figure 126: Tracking (left) and Sensor Diagram (right) of a 2.0 Hz Sinusoid using Resistance Mapping as Feedback Measurement for 3.47% Pre-Strained SMA Wires

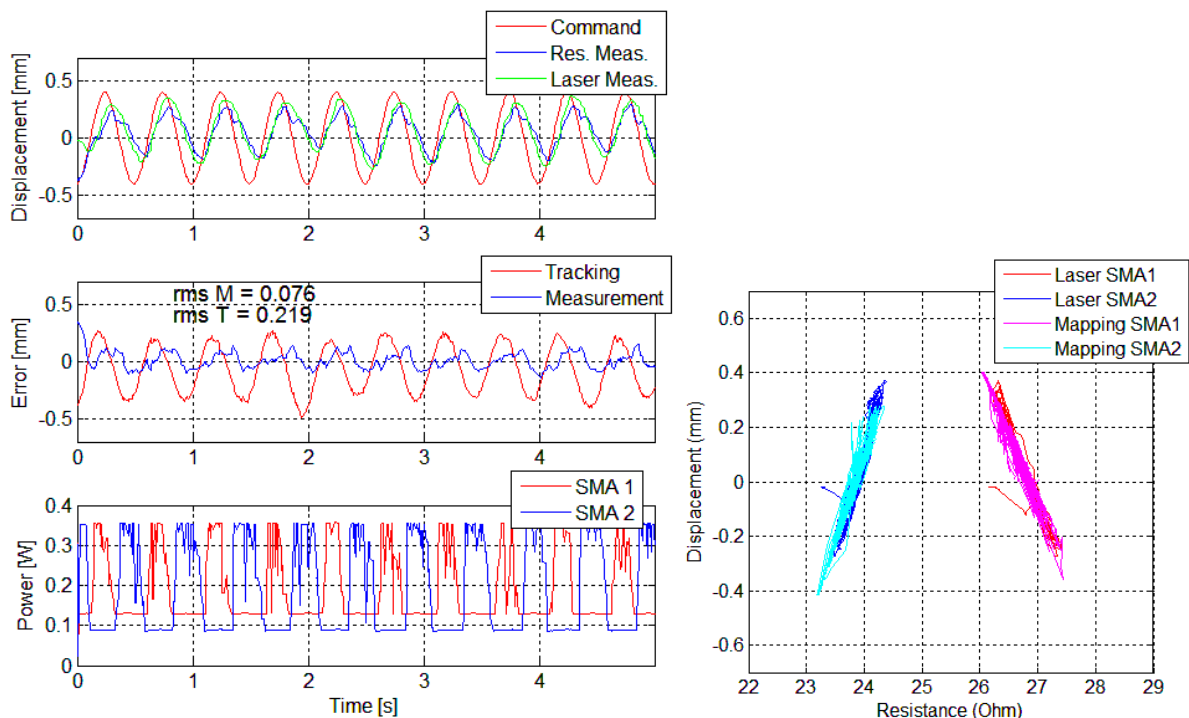


Figure 127: Tracking (left) and Sensor Diagram (right) of a 2.0 Hz Sinusoid using Laser Sensor as Feedback Measurement for 3.47% Pre-Strained SMA Wires

Figure 128 and Figure 129 show the system's response to a variable step function. The step function provides a challenge for the resistance-based sensor because of the constant switching of control

power direction required to hold the displacement constant on a plateau. As a result, using the laser sensor significantly reduces the noise in the control power input and measured errors.

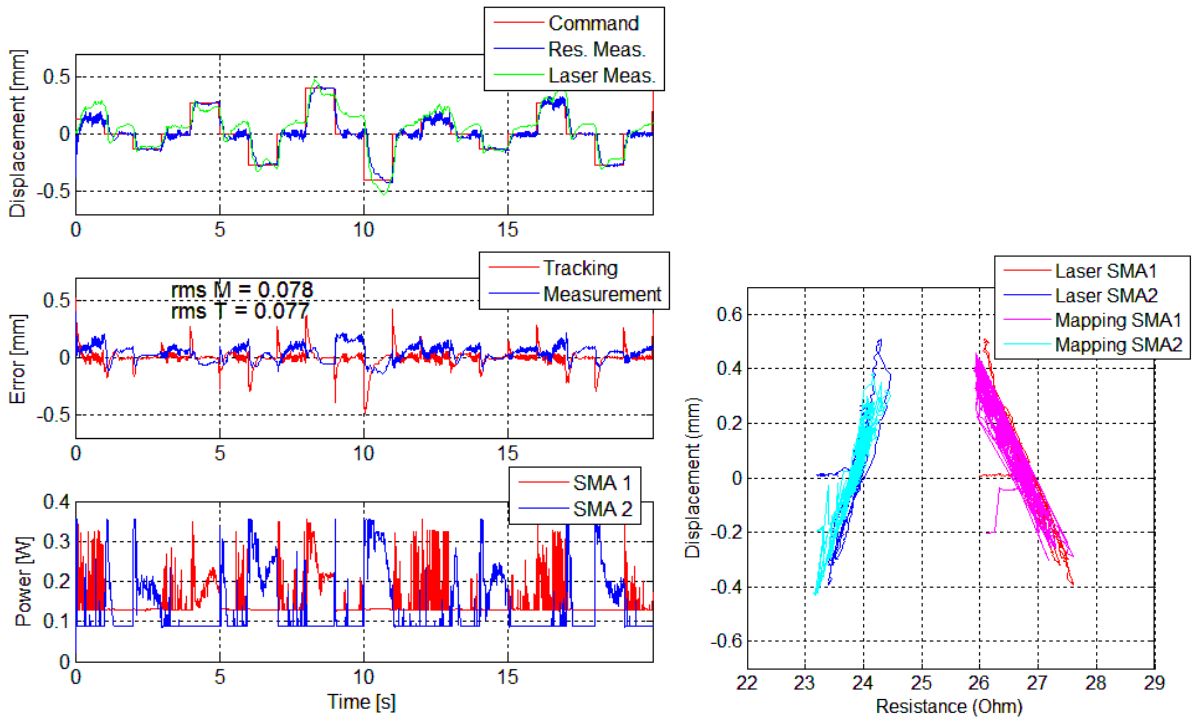


Figure 128: Tracking (left) and Sensor Diagram (right) of a Step Function using Resistance Mapping as Feedback Measurement for 3.47% Pre-Strained SMA Wires

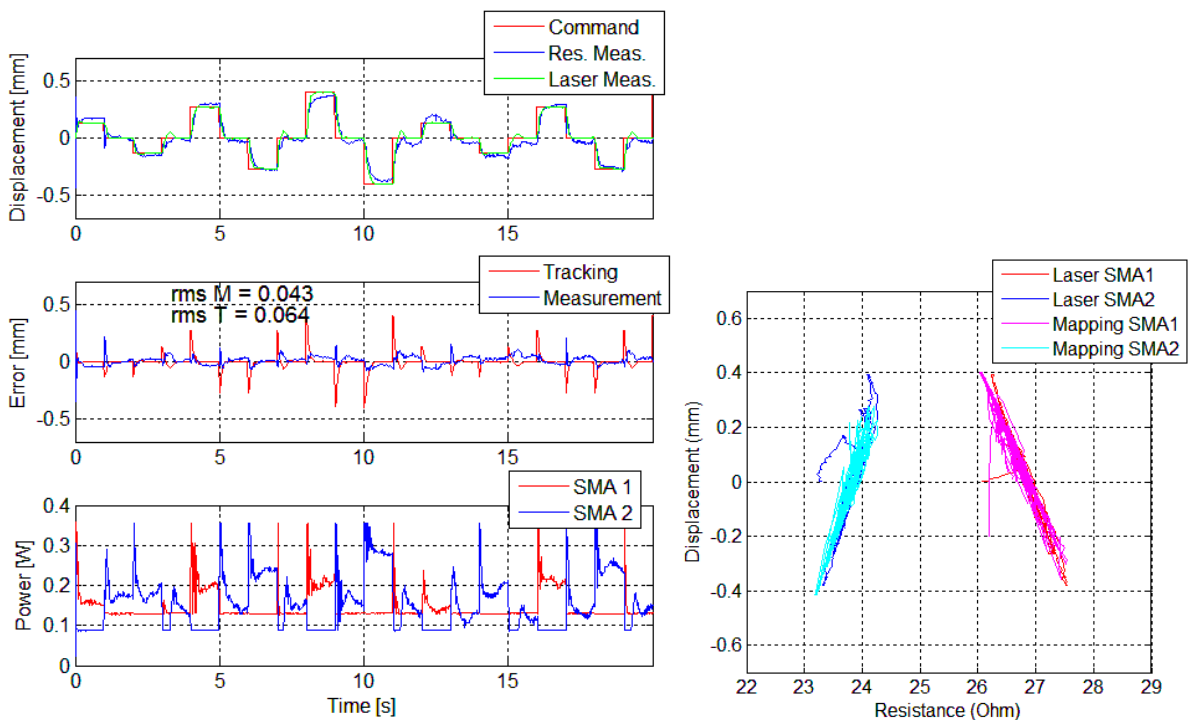


Figure 129: Tracking (left) and Sensor Diagram (right) of a Step Function using Laser Sensor as Feedback Measurement for 3.47% Pre-Strained SMA Wires

## Pre-Stressed SMA Wires

The conclusions from characterization of the coupled SMA system (section 2.1.3.6) suggested that the SMA wires would make better sensors when pre-stressed then when pre-strained because pre-stressing reduces the hysteresis in the resistance vs. strain relation and helps prevent formation of slack. However, the results that follow (compiled in Table 12) indicate that pre-stressing actually increased measurement error slightly, while tracking error remained virtually unaffected.

One cause for the increase in measurement error in the pre-stress case may be that the high opposing forces prevent resistance from getting low enough to reach the maximum and minimum of the commanded displacement. Note in Figure 130 and Figure 131: even at low frequency the resistance-based measurement never reaches the -0.4 mm displacement value. Once the opposing wire is pulled entirely into the  $M^+$  phase, the actuating wire requires a much larger heating power to overcome the opposing force. The higher temperatures cause an increase in resistance that is not associated with a decrease in SMA strain. This is the same mechanism that causes the resistance-strain plots to shift depending on pre-stress of the single SMA-spring system, as shown in Figure 75 and Figure 113. This effect causes a bump in measurement error to occur not only during the switch from one SMA to the other, but also at the maxima of displacement that is out of range of the resistance-based measurement. These physics motivate the coupled mapping approach implement in control of the adaptive nozzle discussed in the next section.

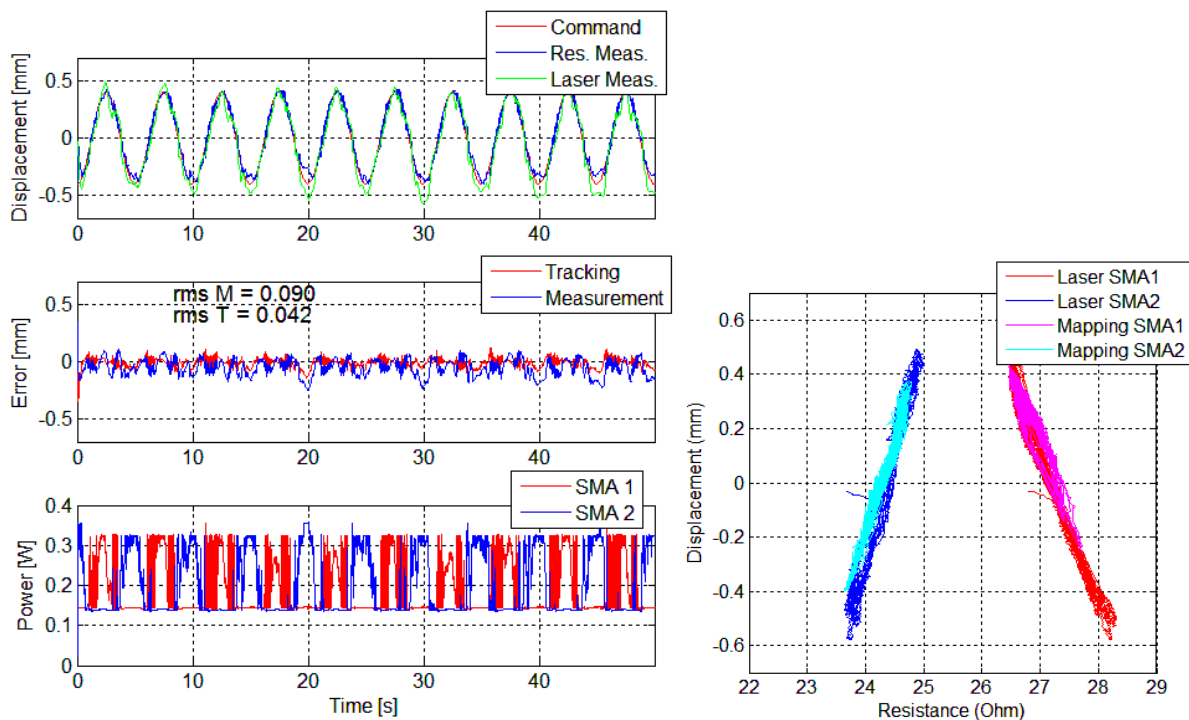


Figure 130: Tracking (left) and Sensor Diagram (right) of a 0.2 Hz Sinusoid using Resistance Mapping as Feedback Measurement for 100 MPa Pre-Stressed SMA Wires

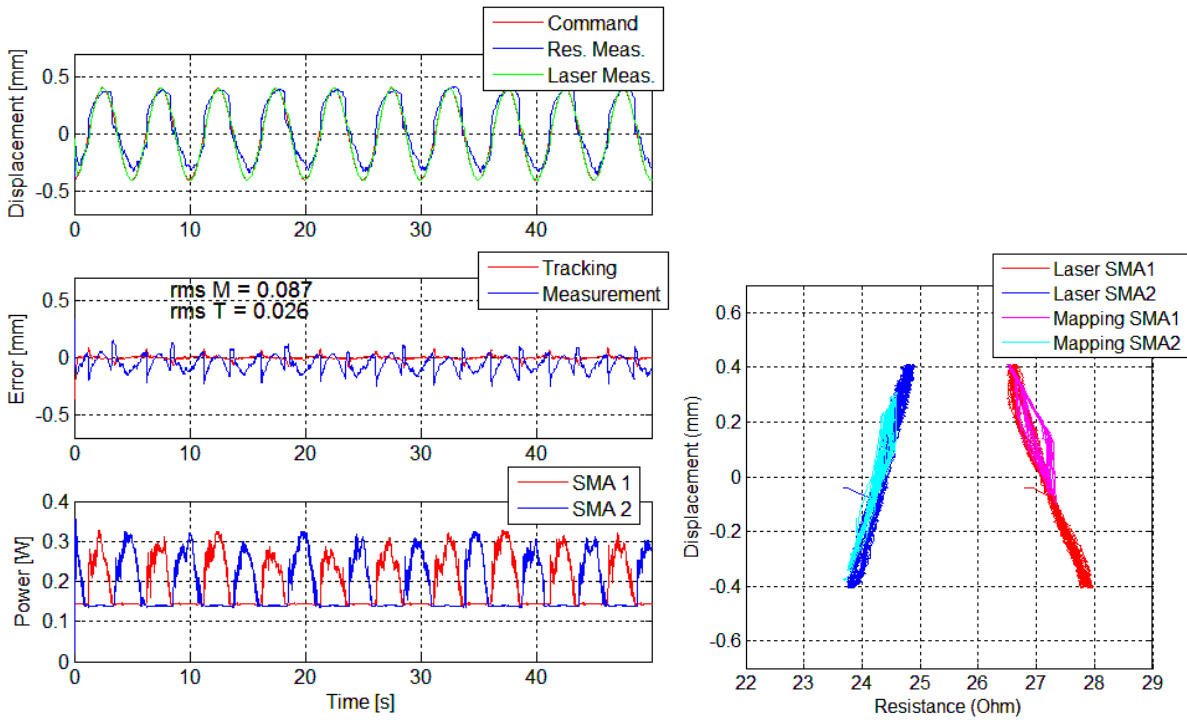


Figure 131: Tracking (left) and Sensor Diagram (right) of a 0.2 Hz Sinusoid using Laser Sensor as Feedback Measurement for 100 MPa Pre-Stressed SMA Wires

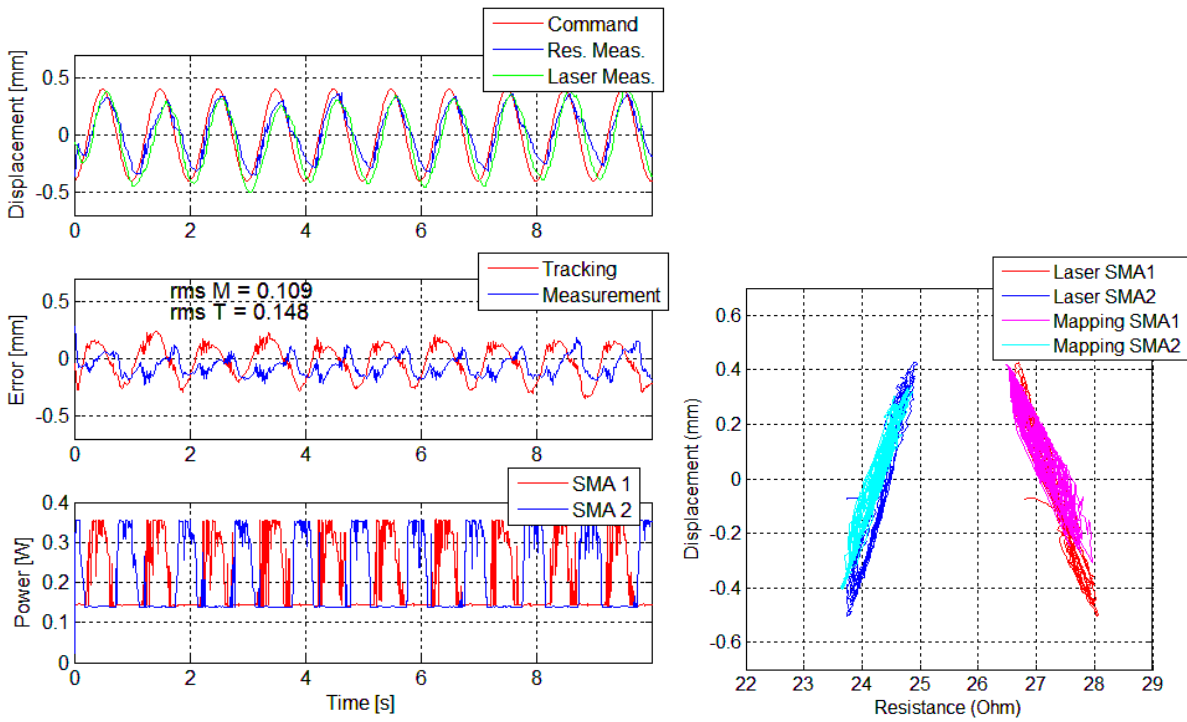


Figure 132: Tracking (left) and Sensor Diagram (right) of a 1.0 Hz Sinusoid using Resistance Mapping as Feedback Measurement for 100 MPa Pre-Stressed SMA Wires

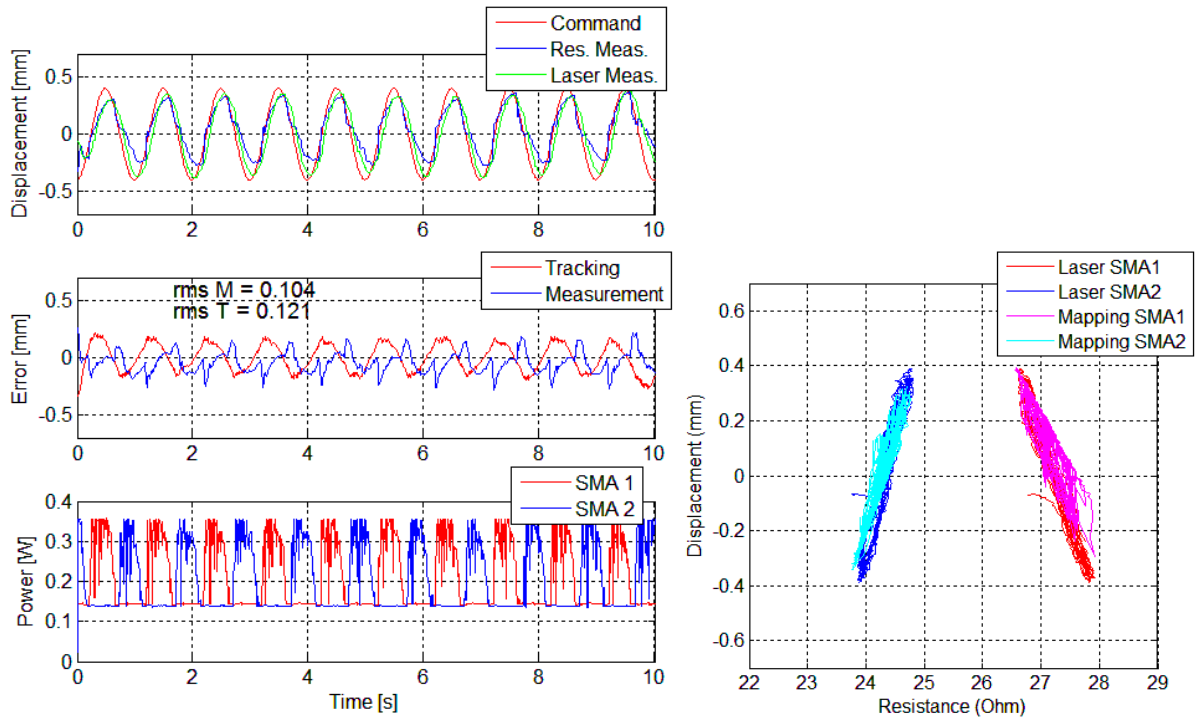


Figure 133: Tracking (left) and Sensor Diagram (right) of a 1.0 Hz Sinusoid using Laser Sensor as Feedback Measurement for 100 MPa Pre-Stressed SMA Wires

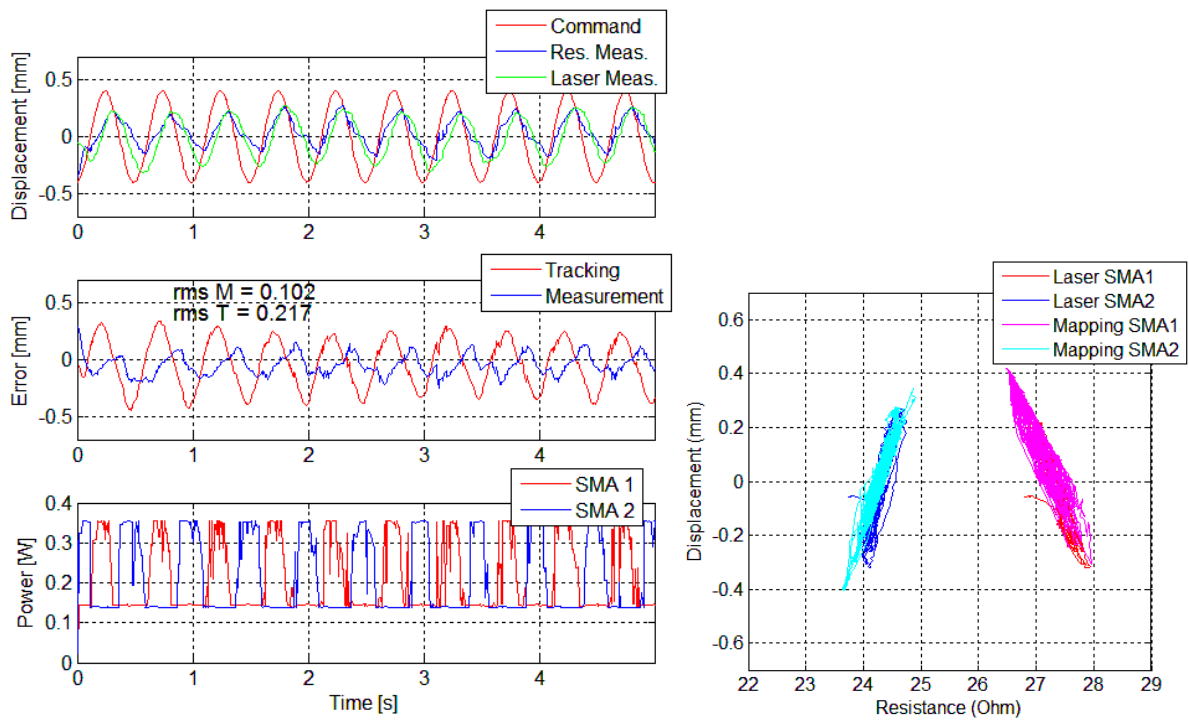


Figure 134: Tracking (left) and Sensor Diagram (right) of a 2.0 Hz Sinusoid using Resistance Mapping as Feedback Measurement for 100 MPa Pre-Stressed SMA Wires

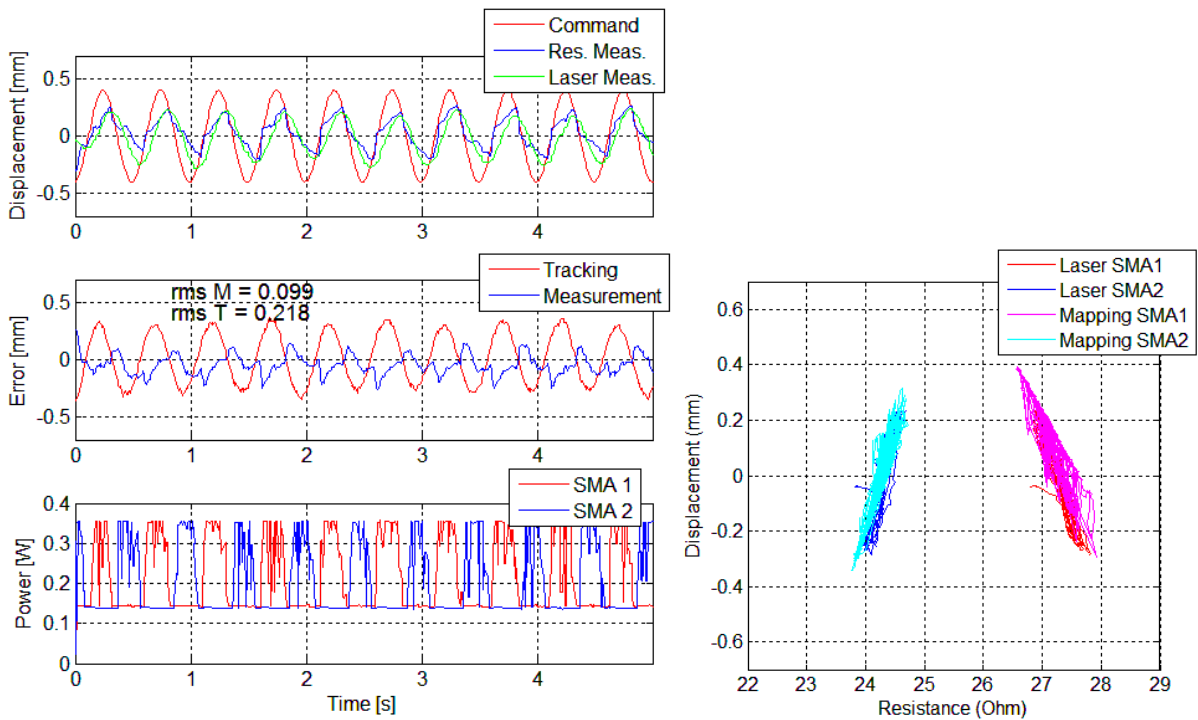


Figure 135: Tracking (left) and Sensor Diagram (right) of a 2.0 Hz Sinusoid using Laser Sensor as Feedback Measurement for 100 MPa Pre-Stressed SMA Wires

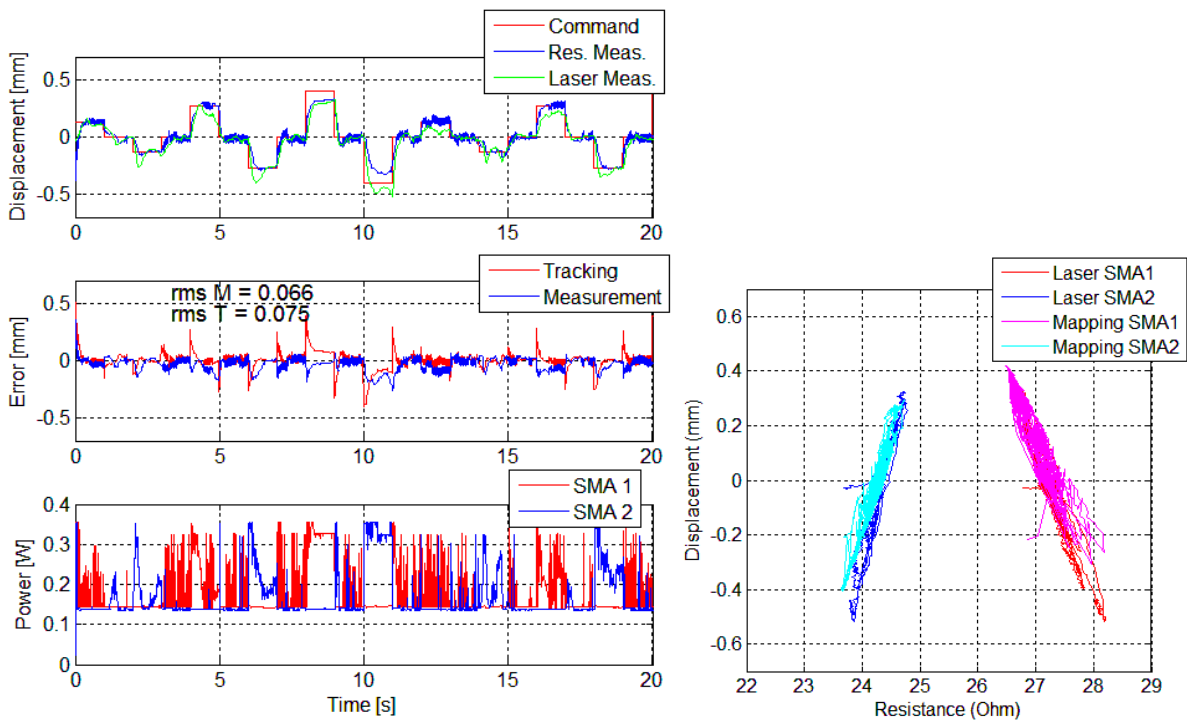


Figure 136: Tracking (left) and Sensor Diagram (right) of a Step Function using Resistance Mapping as Feedback Measurement for 100 MPa Pre-Stressed SMA Wires

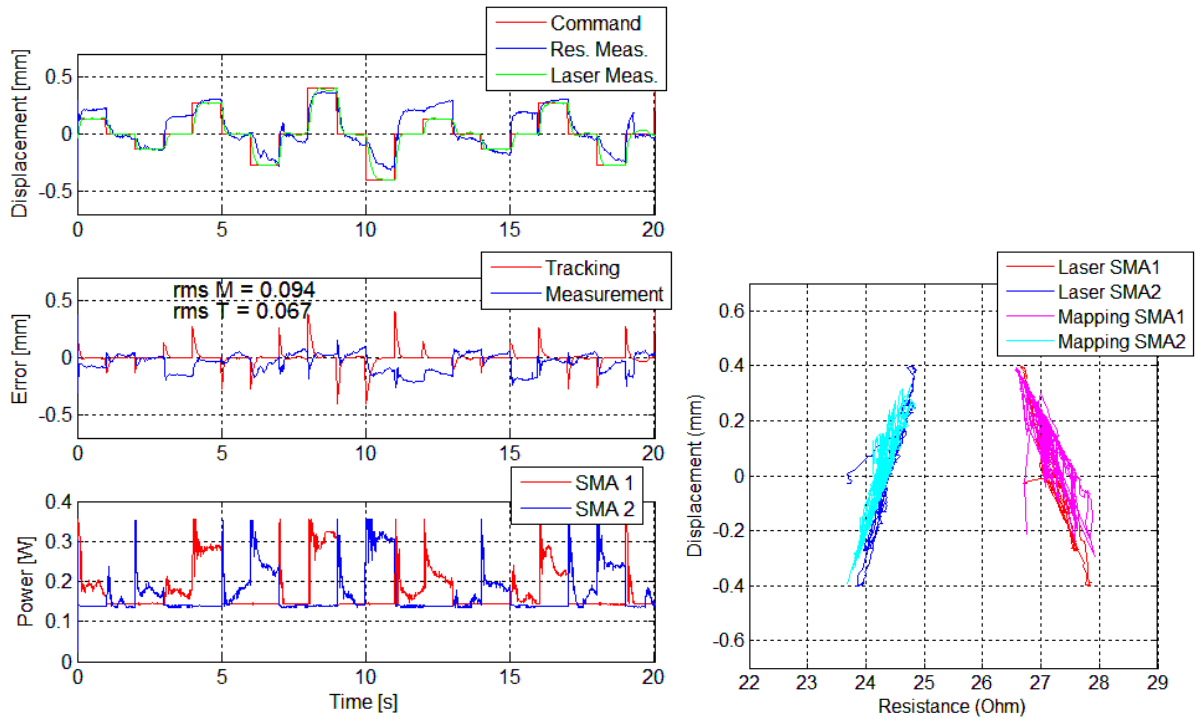


Figure 137: Tracking (left) and Sensor Diagram (right) of a Step Function using Laser Sensor as Feedback Measurement for 100 MPa Pre-Stressed SMA Wires

#### 2.2.2.4 Conclusions from Coupled SMA Controls Experiments

These results demonstrate the challenges of working with the opposing SMA wire system, and it is not surprising that coupling two hysteretic, non-linear elements together complicates the problem. The variation in the reaction force from the opposing SMA has a significant impact on the resistance vs. deformation characteristic and therefore the sensor diagram. This leads to an increase in measurement error compared to the single SMA system, where the reaction force was supplied by a simple linear spring. However, as shown in Table 12, measurement error remains fairly constant through the different test inputs. In the pre-stressed tests, the functional range of the resistance-based mapping sensor was insufficient to cover the displacement range, causing a slight increase in the RMS of measurement error. So the increase in error does not necessarily invalidate the method.

Table 12: RMS of Tracking and Measurement Errors Using Resistance-Based and Laser Feedback Sensor

Experiment	Resistance-Based Sensor		Laser Sensor	
	Track. Err. (mm)	Meas. Err. (mm)	Track. Err. (mm)	Meas. Err. (mm)
Pre-strain, 0.2 Hz	0.033	0.070	0.024	0.059
Pre-strain, 1.0 Hz	0.162	0.093	0.102	0.084
Pre-strain, 2.0 Hz	0.252	0.079	0.219	0.076
Pre-strain, Step	0.077	0.078	0.064	0.043
Pre-stress, 0.2 Hz	0.042	0.090	0.026	0.087
Pre-stress, 1.0 Hz	0.148	0.109	0.121	0.104
Pre-stress, 2.0 Hz	0.217	0.102	0.218	0.099
Pre-stress, Step	0.075	0.066	0.067	0.094

These results also may inspire a method to improve the sensor mapping. The variation in the opposing force causes a shift in the resistance vs. displacement plot, so a scheme can be imagined

where the opposing force is somehow estimated, then used to adjust the mapping coefficients. This could, for example, make better use of the available resistance and power input data from both SMA wires to improve sensor mapping. If mapping accuracy is made to be more robust to changes in the opposing force, the opposing actuator system can offer advantages, such as higher actuation frequency, bi-directional control authority, and the possibility of eliminating the biasing spring entirely. In the meantime, the information gained from this simplified setup provides a baseline for understanding the behavior of an even more complex embedded SMA system: the Smart Inhaler nozzle joint.

### 2.2.3 Sensor Mapping and Control of Smart Inhaler Nozzle Joint

Figure 138 depicts how the adaptive nozzle joint is another example of an opposing SMA system; as a result it shares many characteristics with the system described in the previous section. However, the nozzle joint has a third actuator that enables arbitrary bending in the top-view plane. This third actuator adds additional steps to the calibration and mapping procedure, and it adds more complexity to the control scheme. Nevertheless, lessons learned from the systems studied in section 2.2.1 and 2.2.2 are of great value in developing the mapping and control scheme for the adaptive nozzle joint.

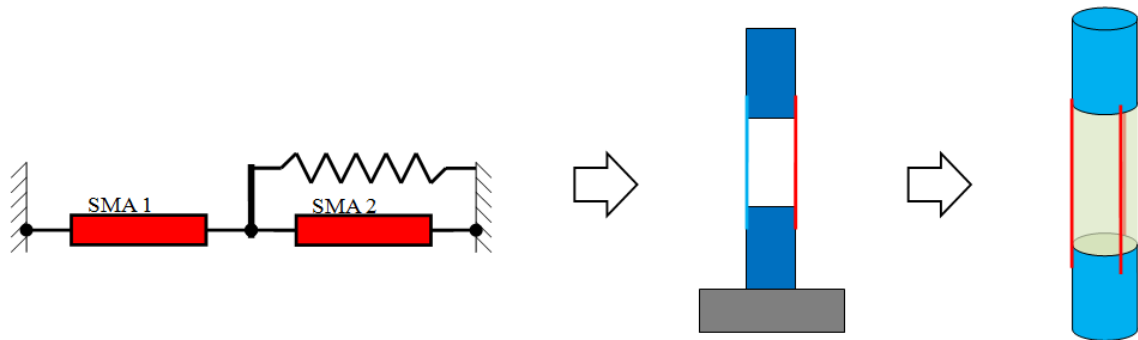


Figure 138: Adaptive Nozzle Joint as an Opposing Actuator System

#### 2.2.3.1 Resistance to Deflection Mapping

The following section describes how the resistances of the three SMA wires in a Smart Inhaler nozzle joint are mapped to the nozzle tip position. In the case of the Smart Inhaler application, the geometry of the nozzle dictates that the strain in an SMA wire will map linearly to nozzle tip deflection along the direction of that actuator, so long as rotation angles are small. For the first implementation discussed in this section, the role of the coupled force from the opposing SMA actuators wires are neglected. A subsequent method presents a coupled mapping technique that uses the varying power input to opposing wires to alter the resistance to deformation mapping along the first direction.

As before, it is important that the mapping and calibration procedures be well documented and motivated by the physics. Otherwise the hysteretic nature of SMA wires may lead to mappings that are not reproducible. The procedures documented below are automated to eliminate operator bias. They are used to:

- Align the coordinate system of the top-view camera with the center position of the nozzle.
- Transform the coordinate system from the  $[x,y]$  frame of the camera to the  $[\delta_1, \delta_2, \delta_3]$  frame of the nozzle joint.
- Calibrate the mapping coefficients, including R- $\delta$  slopes, offsets, and power ranges.

The centering of the camera system is important because the camera is used to measure nozzle deformation during calibration and to determine measurement errors during controller validation.

#### Camera Coordinate System Centering Procedure

The goal of centering the camera coordinate system is to place the non-deformed nozzle in the center of the camera's coordinate frame, then align the motion induced by contraction of actuator 1 with the

camera's y axis, as indicated in Figure 139. In Figure 139, contraction of actuator 1 (behind) is assumed to induce bending in the  $\delta_1$  direction.

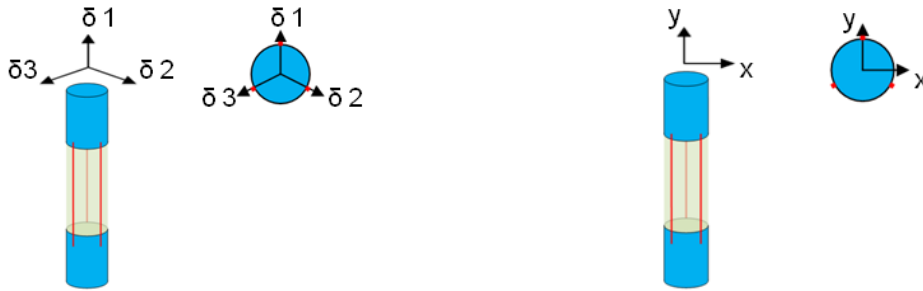


Figure 139: Alignment of Nozzle [ $\delta_1, \delta_2, \delta_3$ ] Coordinate System with Camera [ $x, y$ ] Coordinate System

The steps for centering the camera coordinate system are outlined below:

1. Heat all 3 actuators simultaneously for 5 s with 0.25 W. This exposes all of the wires to high stress to effectively erase their memory of their previous state. Upon cooling, the wires should return to a  $M^+$  state.
2. Command 5 cycles of a triangle input wave with an amplitude of 0.25 W and frequency of 0.1 Hz to actuator 1.
3. Using top view camera with LabVIEW pattern recognition software, track the x-y position of the nozzle tip.
4. Once the 5 cycles are finished, throw away the x-y data associated with the first cycle and fit a line to the remaining x-y data using a least square method. Save the slope and y-intercept of this line.
5. Repeat steps 1 through 4 for each of the other 2 actuator channels.
6. Find the intersection points of the three lines obtained, shown by  $P_{12}$ ,  $P_{23}$ , and  $P_{13}$  in the left panel of Figure 140.
7. Find the average of  $P_{12}$ ,  $P_{23}$ , and  $P_{13}$  and take this as the center of the nozzle coordinate frame.
8. Determine the angle  $\theta$  based on the slope of  $\delta_1$  then translate and rotate the nozzle frame to align with the camera frame.

The right panel in Figure 140 shows an example of the calibration process. The gray lines show the initial cycles in a non-oriented coordinate system, and the black lines show the same cycles rerun in the oriented coordinate system. Note that for the case shown, the coordinate frame was translated 0.16 mm in x and 1.64 mm in y, and it was rotated 133.8 degrees clockwise.

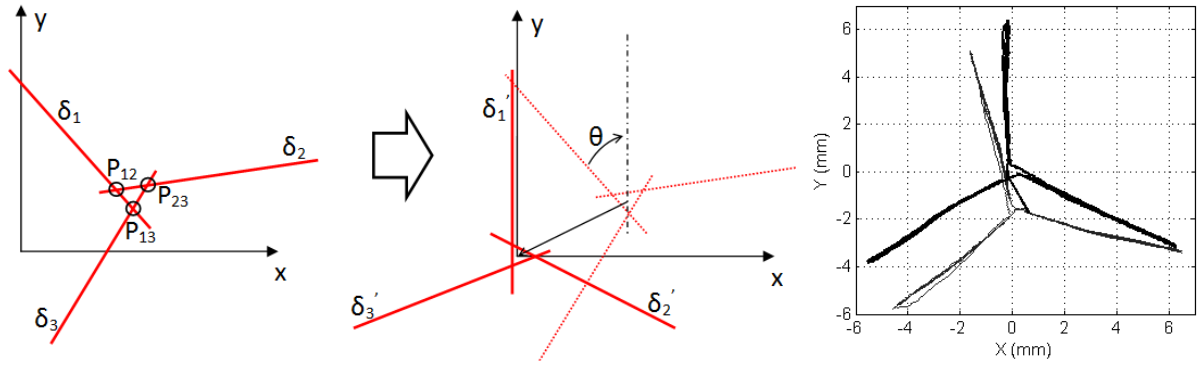


Figure 140: Alignment of Camera and Nozzle Coordinate Frame Pre-Alignment (left), Aligned (middle) and Tested (right)

### Three Axis Coordinate Transformation

In general, the strains of actuator 1, 2, and 3 are assumed to induce nozzle deflection only along each actuator axis,  $\delta_1$ ,  $\delta_2$ , and  $\delta_3$ , respectively. So in effect, the system is modeled as 3 independent single SMA-spring systems diagrammed in Figure 112. These deflections are then superimposed to give the final position of the nozzle tip. Figure 141 shows how a deflection in the  $\delta_1$  and  $\delta_2$  directions can be equated to a position in the  $x$ - $y$  frame. The form of the coordinate system transformation is important, particularly because the  $[\delta_1, \delta_2, \delta_3]$  coordinate system over-constrains a point, so only the two  $\delta$  axes that are adjacent to the point being mapped can be considered. So in the case shown in Figure 141, only the  $\delta_1$  and  $\delta_2$  axes are considered, and contributions made by  $\delta_3$  are taken to be 0 and neglected. This assumption is valid, because in positioning controls applications, positioning the nozzle tip between the  $\delta_1$  and  $\delta_2$  axes requires that there be no power to actuator 3, effectively rendering it as a passive part of the structure. The transformation in equations (2.49)-(2.51) are used to convert deflections in the  $[\delta_1, \delta_2, \delta_3]$  coordinate system to  $[x,y]$ . Each equation is only valid for points in one third of the  $[\delta_1, \delta_2, \delta_3]$  coordinate system.

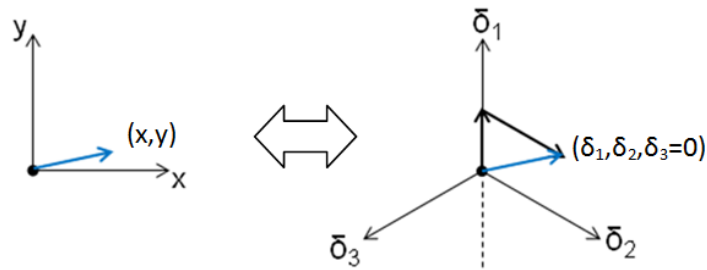


Figure 141: Superposition of Nozzle Deflections in  $\delta_1$  and  $\delta_2$  Directions

The  $[\delta_1, \delta_2, \delta_3]$  to  $[x,y]$  coordinate transform for points between the  $\delta_1$  and  $\delta_2$  axes is,

$$\begin{bmatrix} x \\ y \end{bmatrix} = \begin{bmatrix} 0 & \frac{\sqrt{3}}{2} & 0 \\ 1 & -\frac{1}{2} & 0 \end{bmatrix} \begin{bmatrix} \delta_1 \\ \delta_2 \\ \delta_3 \end{bmatrix}, \quad (2.49)$$

the  $[\delta_1, \delta_2, \delta_3]$  to  $[x,y]$  coordinate transform for points between the  $\delta_2$  and  $\delta_3$  axes is,

$$\begin{bmatrix} x \\ y \end{bmatrix} = \begin{bmatrix} 0 & \frac{\sqrt{3}}{2} & -\frac{\sqrt{3}}{2} \\ 0 & -\frac{1}{2} & -\frac{1}{2} \end{bmatrix} \begin{bmatrix} \delta_1 \\ \delta_2 \\ \delta_3 \end{bmatrix}, \quad (2.50)$$

and the  $[\delta_1, \delta_2, \delta_3]$  to  $[x,y]$  coordinate transform for points between the  $\delta_3$  and  $\delta_1$  axes is,

$$\begin{bmatrix} x \\ y \end{bmatrix} = \begin{bmatrix} 0 & 0 & -\frac{\sqrt{3}}{2} \\ 1 & 0 & -\frac{1}{2} \end{bmatrix} \begin{bmatrix} \delta_1 \\ \delta_2 \\ \delta_3 \end{bmatrix}. \quad (2.51)$$

The inverse transformation is given in equations (2.53)-(2.55). Once again, each  $[x,y]$  to  $[\delta_1, \delta_2, \delta_3]$  coordinate transform is only valid in one third of the coordinate frame. The angle between the y-axis and the  $[x,y]$  point  $\phi$ , counting positive clockwise, is first determined via

$$\phi = \tan^{-1}\left(\frac{x}{y}\right). \quad (2.52)$$

For  $0 \leq \phi < \pi/3$ , the  $[x,y]$  to  $[\delta_1, \delta_2, \delta_3]$  coordinate transform is

$$\begin{bmatrix} \delta_1 \\ \delta_2 \\ \delta_3 \end{bmatrix} = \begin{bmatrix} \frac{\sqrt{3}}{3} & 1 \\ \frac{2\sqrt{3}}{2} & 0 \\ 0 & 0 \end{bmatrix} \begin{bmatrix} x \\ y \end{bmatrix}, \quad (2.53)$$

for  $\pi/3 \leq \phi < 2\pi/3$ , the  $[x,y]$  to  $[\delta_1, \delta_2, \delta_3]$  coordinate transform is

$$\begin{bmatrix} \delta_1 \\ \delta_2 \\ \delta_3 \end{bmatrix} = \begin{bmatrix} 0 & 0 \\ \frac{\sqrt{3}}{3} & -1 \\ \frac{\sqrt{3}}{3} & -1 \end{bmatrix} \begin{bmatrix} x \\ y \end{bmatrix}, \quad (2.54)$$

and for  $2\pi/3 \leq \phi < 2\pi$ , the  $[x,y]$  to  $[\delta_1, \delta_2, \delta_3]$  coordinate transform is

$$\begin{bmatrix} \delta_1 \\ \delta_2 \\ \delta_3 \end{bmatrix} = \begin{bmatrix} -\frac{\sqrt{3}}{3} & 1 \\ 0 & 0 \\ -\frac{2\sqrt{3}}{3} & 0 \end{bmatrix} \begin{bmatrix} x \\ y \end{bmatrix} \quad (2.55)$$

This case-wise transformation is critical in controls applications. For example, equation (2.53) shows how a commanded (x,y) position is converted to desired deflections of the 3 actuators. However, note that once again equation (2.53) is only valid in the third of the  $[\delta_1, \delta_2, \delta_3]$  coordinate system between the  $\delta_1$  and  $\delta_2$  axes, and that the commanded deflection in the direction of actuator 3,  $\delta_3$ , will be 0. This method does have potential drawbacks. In a controller that excludes the  $\delta_3$  actuator when positions are commanded between the  $\delta_1$  and  $\delta_2$  axes, the only mechanism for moving the nozzle tip in the  $\delta_3$  direction becomes setting the power to actuators 1 and 2 to zero and waiting for them to cool while the passive structural element pulls the nozzle back in the  $\delta_3$  direction. In this way, the nozzle joint mimics the single SMA-spring system studied in section 2.2.1.

### Resistance to Deflection Mapping Concept

In this first implementation of R- $\delta$  mapping, it is assumed that the forces generated by one actuator have no impact on the slope and intercept of the R- $\delta$  line of the others. As a result, when equation (2.44) is expanded to include all three actuators, the resistance to deformation mapping for the nozzle is defined in equation (2.56). Although all of the actuators were assembled using an identical procedure, independently calibrating the characteristic slopes and intercepts for each actuator channel gives one the ability to compensate for inconsistencies between the three actuators identified in section 2.1.4.3.

$$\begin{bmatrix} \delta_1 \\ \delta_2 \\ \delta_3 \end{bmatrix} = \begin{bmatrix} k_1 & 0 & 0 \\ 0 & k_2 & 0 \\ 0 & 0 & k_3 \end{bmatrix} \begin{bmatrix} R_1 \\ R_2 \\ R_3 \end{bmatrix} + \begin{bmatrix} \delta_{01} \\ \delta_{02} \\ \delta_{03} \end{bmatrix} \quad (2.56)$$

This is the simplest viable mapping, and equation (2.56) in concert with the coordinate system transformation in equation (2.49) through (2.51) gives a complete mapping from the resistance of the three actuator wires to the deflection of the nozzle tip in the [x,y] coordinate system. This measurement can then be compared to position data simultaneously taken by the camera system. Since the camera system is used to initially calibrate the k and  $\delta_0$  values, comparing the camera data to deflections measured via the resistance mapping gives a good indication of the validity of the assumptions that inspired the mapping concept, and it also enables a measurement error to be quantified.

### Sensor Mapping Procedure

The procedure used to determine the  $k$  and  $\delta_0$  values follows directly after the completion of the camera coordinate system centering procedure described above. The first step is to determine the power limits discussed in the previous controller implementations. The ideal procedure for this would be to cycle the input power into each actuator and plot the  $R$ - $\delta$  characteristics. These plots would be expected to look like the resistance vs. displacement plots in Figure 103, reproduced in the right panel of Figure 142, since nozzle deflection is assumed to be linearly dependent on SMA wire. Then the power that induces the maximum and minimum resistances in the SMA wire would be taken as the minimum and maximum power limits, respectively, as was diagrammed in Figure 113. The  $R$ - $\delta$  curve of SMA actuator 1 measured after the memory clearing process (step 1 above) is shown in the left panel of Figure 142. Clearly, the calibration process produced a different plot than characterization. Most notably, the calibration data shows a substantial plateau at the bottom where there is a resistance change of  $-1.7 \Omega$ , but no measured deflection. This behavior is similar to what was observed in Figure 110, where the SMA wires were actuated one after another to generate the Mercedes star trace.

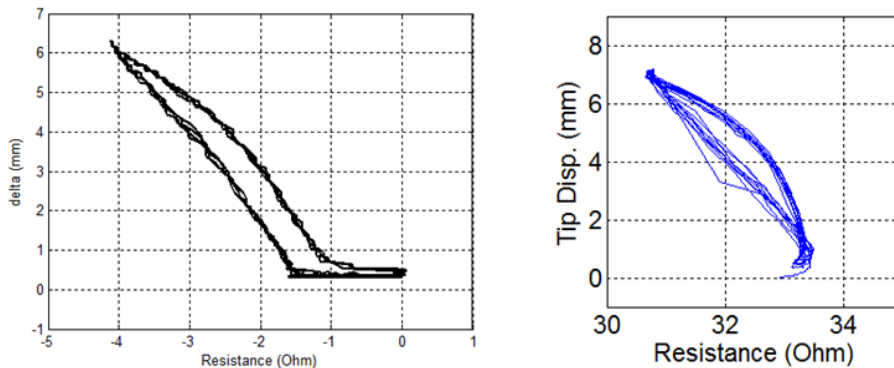


Figure 142: Calibration (left) and Characterization (right) Resistance vs. Nozzle Deflection Plot for Power Cycled between 0-0.25 W

The unexpected behavior observed in the bottom right of the calibration  $R$ - $\delta$  relationship can be explained by considering the physical mechanisms behind the resistance change and the steps taken before the calibration cycles were run. It is observed that low input heating powers do not cause a slight increase in resistance, as is expected prior to the beginning of phase transformation. Rather, a point starting at the bottom-right of the  $R$ - $\delta$  characteristic follows the bottom branch of the hysteresis loop during heating. This branch begins with a significant reduction in resistance (about  $1.7 \text{ Ohm}$ ) that does not result in any deformation of the nozzle along that axis. In the case of the Mercedes trace, this behavior was attributed to slack that developed when the opposing SMA wires actuated. In this case there is no visible slack, but there is a similar explanation for a reduction in resistance that does not result in wire strain (and thus nozzle deflection) that is derived from the effects of heating all 3 SMA wires at once and allowing them to cool under stress.

The left side (panels A-D) of Figure 143 shows the stress-strain and resistance-strain behavior for a “single-crystal” SMA wire. At low temperature, the pre-stressed wire is expected to be fully martensitic, as indicated by panel A. The resistance, panel B, is slightly below the maximum attainable resistance value. As the wire is heated to just below the austenite start temperature (panel

C), the resistance rises slightly as it would for any metal (panel D). Since phase transformation has not yet begun there is no reduction in resistance due to transformation to the austenite phase.

The right side (panels E-H) of Figure 143 show the behavior that might be expected from a real, polycrystalline material that is cooled under the stress. At low temperature and the same stress as before, the wire is not fully on the  $M^+$  line, as shown in panel E. Rather, the material is a mixture of  $M^+ / M^-$ , biased towards  $M^+$  due to the positive stress. However, since the resistance of  $M^-$  is the same as  $M^+$ , the wire will have the resistance indicated in panel F, just as it did in panel B. The difference is, that because of the martensite minus grains, the strain values are different. Once heating begins, the first thing that happens is that some of the  $M^+ / M^-$  twins change to austenite. This results in a significant reduction in resistance, but no change in strain, as indicated in panel H. This analysis explains the behavior observed in the left panel of Figure 142. It also explains the behavior exhibited in the 50 MPa pre-stress case from the single SMA-spring characterization experiments shown in section 2.1.2.

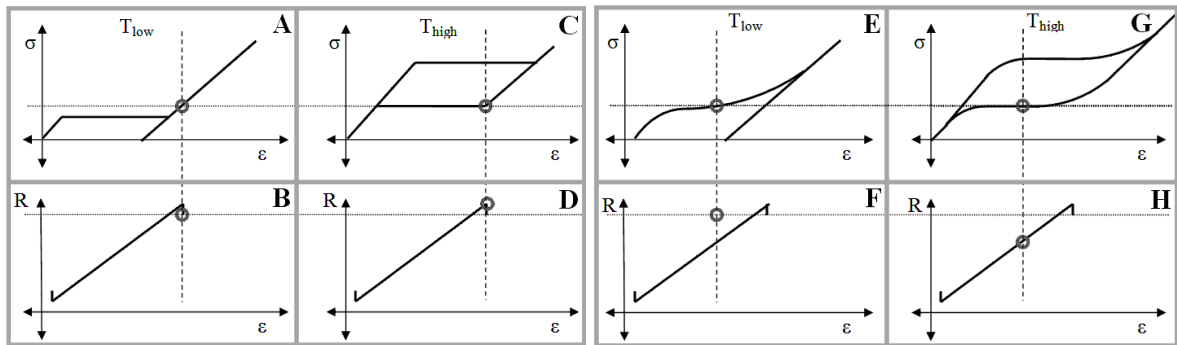


Figure 143: Stress, Strain, and Resistance Behavior for Idealized Single-Crystal (left) and Poly-Crystal (right) SMA Wire

Since the mapping from resistance to deflection is taken to be linear, a large reduction in resistance with no change in strain (or thus deflection) results in a large measurement error. To avoid this, a minimum power input is maintained, just as it was in previous controller implementations. However, this minimum power cannot be chosen based on the power needed to get attain maximum resistance. Rather, it is chosen based on the power needed to start nozzle deflection.

As was shown in Figure 143, the SMA wires are probably never totally on the  $M^+$  line. As a result, they are expected to have non-linear, hysteretic force-displacement characteristics that act in parallel with that of the passive structural element, just as in the case of the opposing SMA-spring system in sections 2.1.3 and 2.2.2. This invariably leads to hysteresis in the R- $\delta$  curve of the SMA wire being actuated. Additionally, in the nozzle joint control application multiple wires are being actuated at once. A changing thermal state in opposing wires causes them to effectively output more force, also affecting all of the other wires in the system. All of these coupling effects motivate the need for considering the state of opposing wires when generating the R- $\delta$  mappings. However, as a first attempt, the R- $\delta$  mappings are made independent of coupling considerations. The updated calibration procedure is listed below. The plot in Figure 144 shows a typical R- $\delta$  characteristic with power limits imposed. A line is fit to this curve to approximate displacement along each actuator direction.

1. Actuate all 3 actuators simultaneously for 5 s with 0.25 W to effectively erase their memory of their previous state. Upon cooling under stress, the wires return to a martensitic state on the top plateau of the stress-strain hysteresis loop.
2. Command 5 cycles of a triangle input wave with an amplitude of 0.27 W and a frequency of 0.1 Hz to actuator channel 1. Track the x-y position of the nozzle tip using the top view camera with Machine Vision.
3. Convert the [x,y] position to the  $[\delta_1, \delta_2, \delta_3]$  coordinate system using equation (2.53).
4. Plot the  $\delta_1$  data against the  $R_1$  data.
5. Eliminate the data points for the first cycle, and chose the point where  $\delta_1$  was sufficiently high for the application (6 mm in this case). Take the measured power at this point as the upper power limit,  $P_{upper}$ .
6. Identify the point where deflection began, and set the corresponding power input as the lower power limit  $P_{lower}$ .
7. Repeat steps 1 through 4, for actuator channels 2 and 3 and determine the upper and lower power limits for each channel.

Once power limits are determined the procedure for determining the R- $\delta$  characteristics is as follows:

8. Actuate all 3 actuators simultaneously for 5 s with  $P_{upper,i}$  W. This exposes all of the wires to high stress to effectively erase their memory of their previous state. Upon cooling under stress, the wires return to a martensitic state on the top plateau of the stress-strain hysteresis loop.
9. Command 5 cycles of a triangle input wave between  $P_{lower,1}$  and  $P_{upper,1}$  W and a frequency of 0.1 Hz to actuator channel 1.
10. Eliminate the data points for the first cycle, and apply a least square linear fit to the remaining data. The slope of this line is  $k_1$  and the y-intercept is  $\delta_{01}$ .
11. Repeat steps 8 through 10 for actuator channels 2 and 3 to fill the k matrix and  $\delta$  offset vector in equation (2.56).

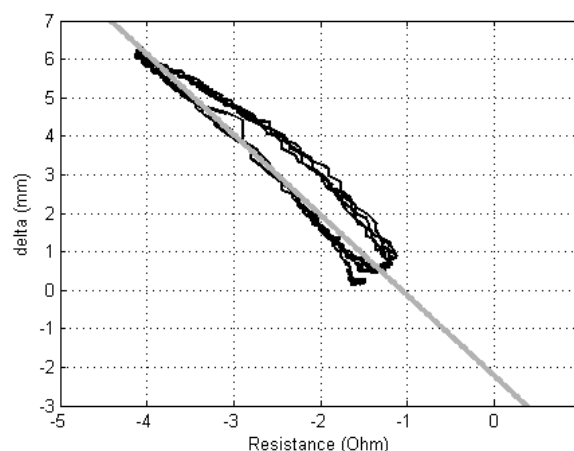


Figure 144: Typical Resistance-Deformation Plot with Minimum Power Limit of 0.05 W

The set of mapping coefficients determined experimentally are shown in Table 13. The performance of this simple mapping and a PID controller are shown in section 2.2.3.2; however, the coupled mapping concept is introduced next.

Table 13: Resistance to Deflection Mapping Coefficients for SMA-Actuated Joint

Channel	Slope (mm/Ohm)			Intercept (mm)		
	$k_1$	$k_2$	$k_3$	$\delta_{01}$	$\delta_{02}$	$\delta_{03}$
Value	-2.019	-2.315	-2.208	-1.994	-2.514	-1.685

### Coupled Mapping Concept

One of the main assumptions made in the uncoupled mapping case discussed above was that the resistance-deformation line of one actuator was not influenced by forces applied by the other actuators—i.e. the nozzle was modeled as 3 independent SMA-spring systems. However, because the wires oppose each other, the system is actually coupled, as shown in Figure 144, reproduced from the opposing SMA characterization in section 2.1.3. In the system in Figure 144, the spring is uncompressed when the stress and strain in opposing wires are equal. As actuator 1 contracts, the other actuators are forced to lengthen, along with the spring. If the opposing actuators are fully in the  $M^+$  phase, then they simply act as additional linear springs in parallel with the structural spring.

The assumption behind the coupling procedure described in this section is that forces exerted by the opposing actuators serves to alter the  $R$ - $\delta$  characteristic of the first actuator by effectively increasing its pre-stress. This should affect the  $R$ - $\delta$  plot in the same way that increasing the pre-stress affected the  $R$ - $\epsilon$  plot from the single SMA-spring system reproduced in the left of Figure 146. It is possible to couple the opposing actuator based on either its measured resistance, its measured deflection (as mapped by resistance), or its input power. In this first attempt at a coupled actuator, the power input to the opposing actuators is used to alter the slope and intercept of the  $R$ - $\delta$  mapping line of the first actuator, as shown in the right of Figure 146.

To first order, it is assumed that the slopes and intercepts of the  $R$ - $\delta$  plot for one actuator vary linearly with the change in power of opposing actuators. In future implementations, the resistance of opposing actuators will be coupled, since it is already assumed that resistance maps linearly to strain and presumably force, in the opposing actuators. Equations (2.57) and (2.58) show how the previous (uncoupled) values of slopes, now written as  $[k_{10}, k_{20}, k_{30}]$ , are updated by sensitivity coefficients scaled by the resistance of the other actuators. The analogous transformation is applied for the offset deflection vector, and the new  $k$  and  $\delta_0$  values are applied via Equation (2.56) to produce the coupled mapping.

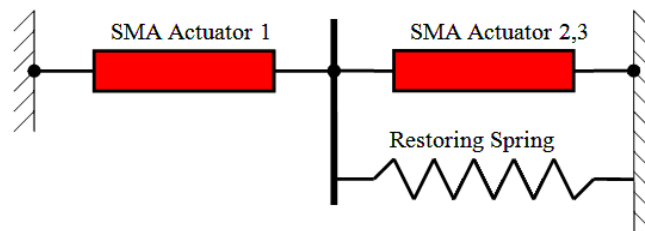


Figure 145: Coupled SMA-Spring Diagram

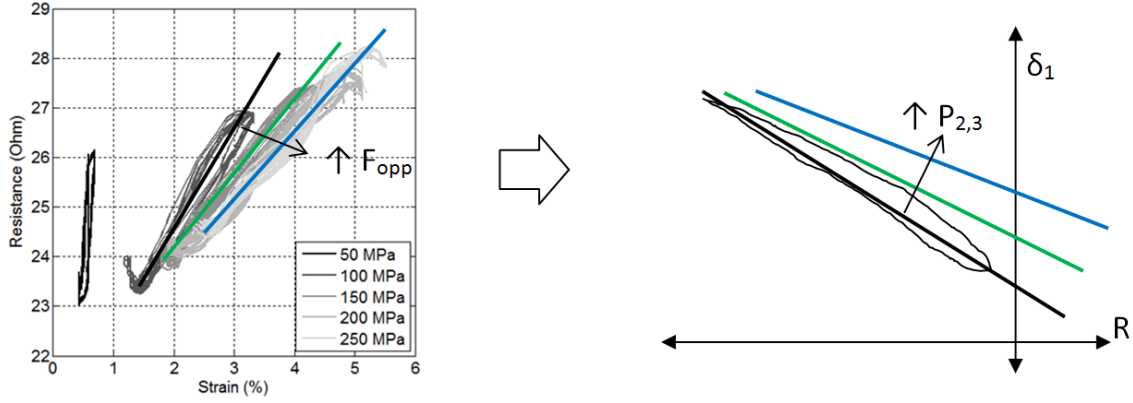


Figure 146: Diagram of Shifting R- $\delta$  Characteristics as a Result of Increasing Force

$$\begin{bmatrix} k_1 \\ k_2 \\ k_3 \end{bmatrix} = \begin{bmatrix} k_{10} \\ k_{20} \\ k_{30} \end{bmatrix} + \begin{bmatrix} 0 & S_{k12} & S_{k13} \\ S_{k21} & 0 & S_{k23} \\ S_{k31} & S_{k32} & 0 \end{bmatrix} \begin{bmatrix} P_1 \\ P_2 \\ P_3 \end{bmatrix} \quad (2.57)$$

$$\begin{bmatrix} \delta_{01} \\ \delta_{02} \\ \delta_{03} \end{bmatrix} = \begin{bmatrix} \delta_{01\_0} \\ \delta_{02\_0} \\ \delta_{03\_0} \end{bmatrix} + \begin{bmatrix} 0 & S_{\delta12} & S_{\delta13} \\ S_{\delta21} & 0 & S_{\delta23} \\ S_{\delta31} & S_{\delta32} & 0 \end{bmatrix} \begin{bmatrix} P_1 \\ P_2 \\ P_3 \end{bmatrix} \quad (2.58)$$

### Coupled Mapping Procedure

The procedure for calibrating the coupled mapping coefficients is described below. The case presented makes the slope of 1 actuator dependent on its own R- $\delta$  mapping line, altered by the changing power inputs (temperatures) of the other actuators.

1. Follow steps 1-3 in the sensor mapping procedure above to determine the uncoupled  $k_{10}$  and  $\delta_{010}$  coefficients for actuator 1. Plot the coefficients as shown in Figure 147.
2. Repeat the calibration procedure above, but command a simultaneous constant power of  $0.25 \cdot P_{\text{upper},2}$  to channel 2. Calculate the coupled mapping coefficients  $k_{121}$  and  $\delta_{021}$  plotted in Figure 147.
3. Repeat with a power of  $0.50 \cdot P_{\text{upper},2}$  commanded to channel 2. Calculate the coupled mapping coefficients  $k_{122}$  and  $\delta_{022}$  plotted in Figure 147. Then fit a line to the  $k$  and  $\delta_0$  points – the slopes of these lines are the sensitivity of the slope or intercept of actuator 1 to power inputs in channel 2.

Repeat this procedure for all other actuator and coupling actuator combinations and fill the S matrices in equations (2.57) and (2.58).

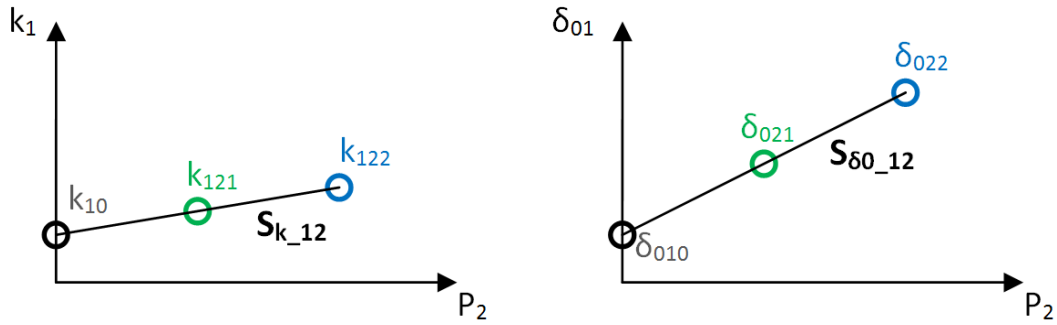


Figure 147: Plot Showing How Sensitivity Matrix Coefficients are Determined Based on Coupled Mapping Coefficients

The experimentally determined coupling coefficients are shown in the matrices in equations (2.59) and (2.60).

$$S_k = \begin{bmatrix} 0 & 0.69 & 0.48 \\ 1.04 & 0 & 0.76 \\ 0.96 & 0.28 & 0 \end{bmatrix} \quad (2.59)$$

$$S_{\delta_0} = \begin{bmatrix} 0 & 9.46 & 11.24 \\ 10.94 & 0 & 6.55 \\ 11.11 & 9.32 & 0 \end{bmatrix} \quad (2.60)$$

### 2.2.3.2 Controller Implementation and Testing

Once the mapping coefficients are determined, the same controller used in the single SMA-spring system, diagrammed in Figure 114, is implemented. However, in the case of the nozzle, all of the power inputs and resistance outputs are vectors of 3 elements, one for each actuator channel. The power limits are imposed on all channels, and the PI gains are set and maintained, but not optimized. The primary focus at this stage is to validate the mapping concept and test it in the context of a controls application, not to optimize the controller itself.

#### Uncoupled Mapping

Results for the uncoupled mapping case (i.e.  $S_k=S_{\delta_0}=[0]$ ) are shown in Figure 148. The controller was programmed to command a Mercedes star (top) and a circle shape (bottom) in Figure 148. These results show a large measurement error of up to 4 mm, but generally small tracking errors. This is expected, because an inaccurate mapping will lead directly to measurement errors, since measurement error is the difference from the position mapped via the SMA resistances and the position measured by the validation camera, as in equation (2.46). However, the controller is still able to keep tracking errors small by bringing the mapped position measurement close to the commanded position. As in the other sensor/controller experiments, the measurement errors increase upon direction reversal because of the hysteresis in the R- $\delta$  characteristic that was neglected in the mapping scheme.

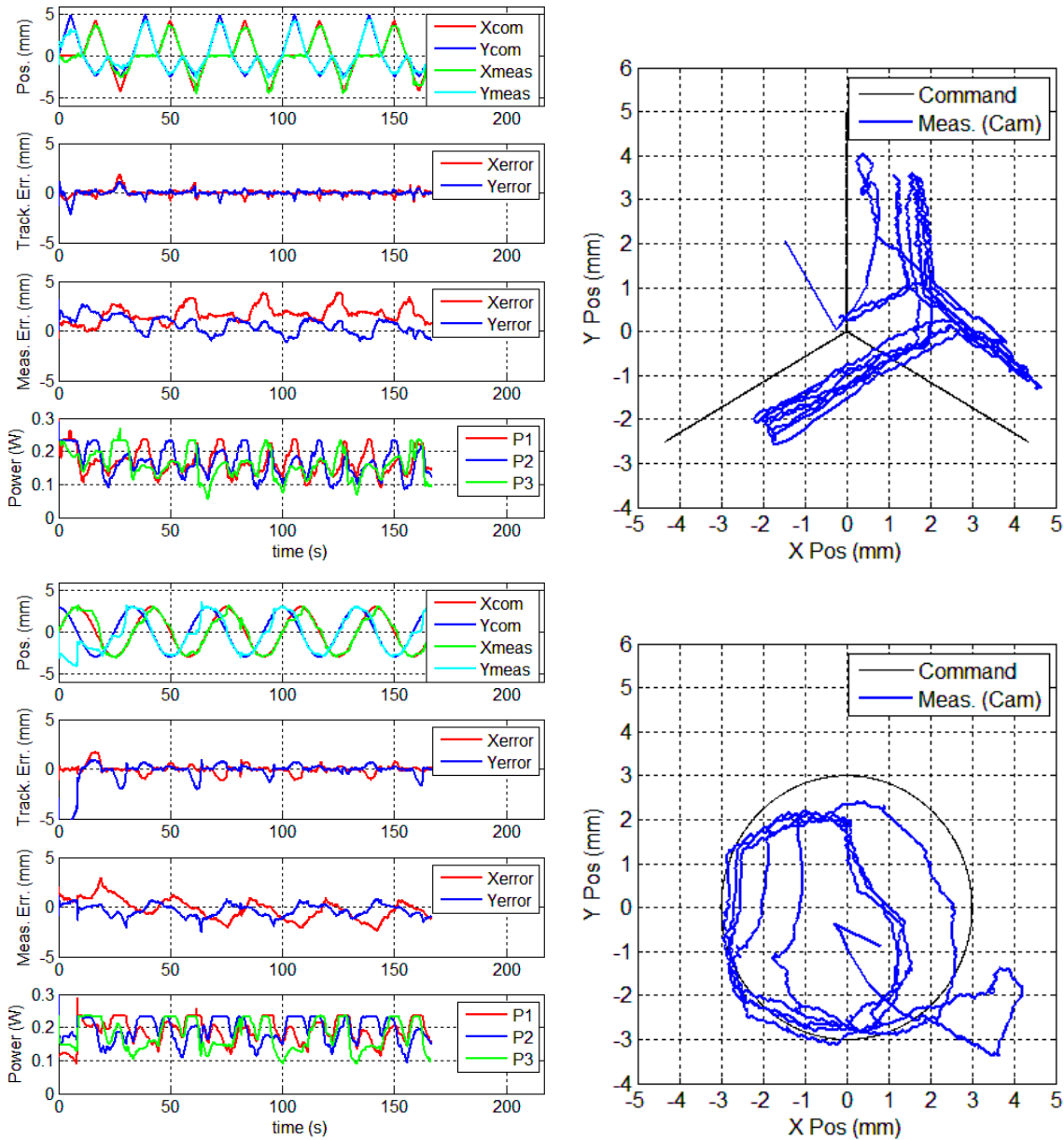


Figure 148: Mapping and Controller Performance to Mercedes Star (top) and Circle (bottom) Command Trajectories using Uncoupled R- $\delta$  Mapping

### Power-Coupled Mapping

Figure 149 shows that the same test run using the power-coupled mapping technique and the same controller. The measurement error is less than 2 mm, half what it was with the uncoupled mapping method. There is a slightly larger tracking error. This is not surprising because the mapped position measurements are constantly being updated as the power input to the other wires changes. This noise makes it more difficult for the controller to maintain good tracking. If resistance were used as the coupling parameter, tracking error might be expected to be reduced. Regardless, the plots of the x-y trajectories clearly show improved performance when the coupled mapping technique is employed.

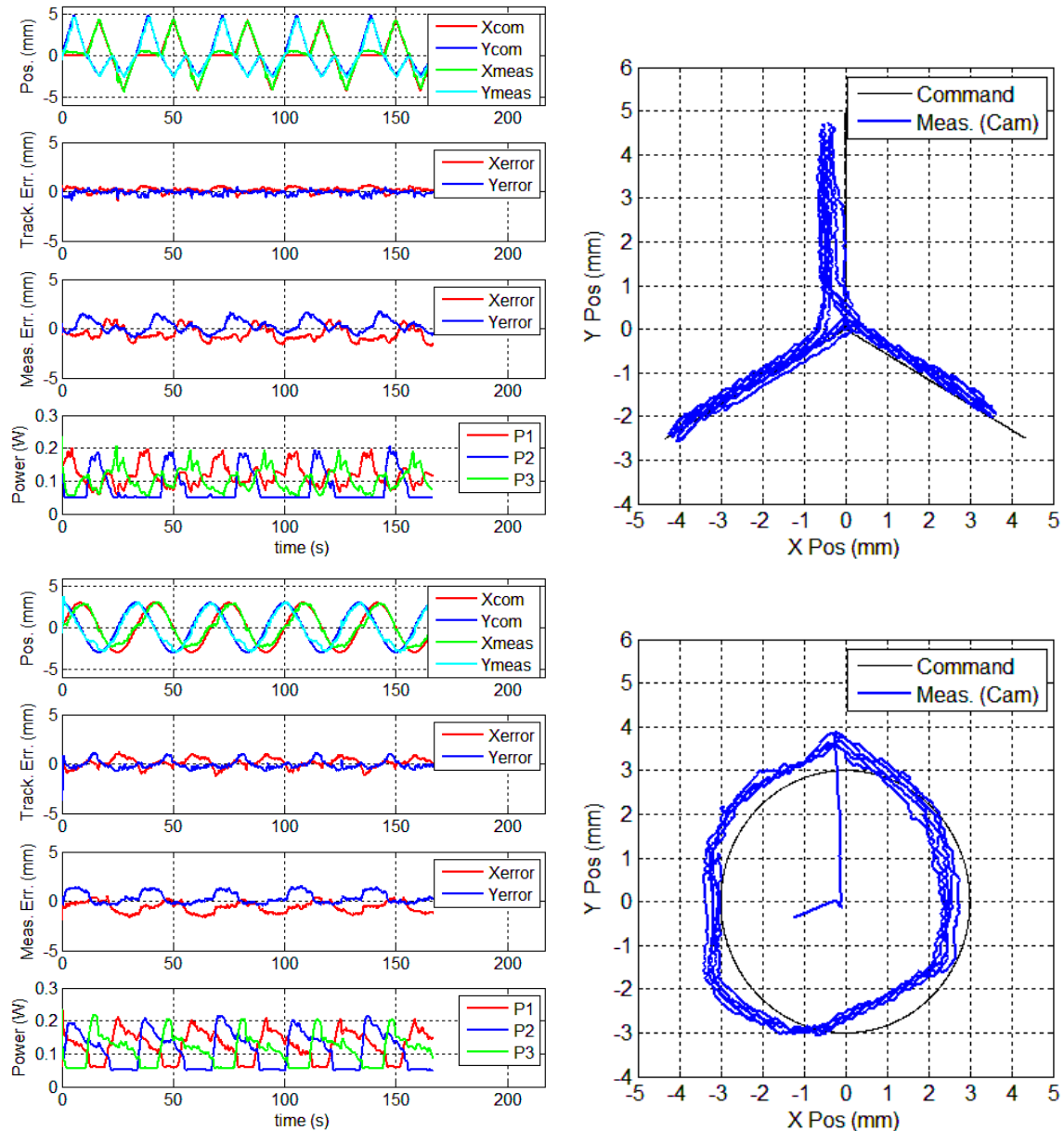


Figure 149: Mapping and Controller Performance to Mercedes Star (top) and Circle (bottom) Command Trajectories using Coupled R- $\delta$  Mapping Concept

### 2.2.3.3 Conclusions

The adaptive Smart Inhaler nozzle joint exploits the multi-functionality of SMA wires in an embedded SMA sensor/actuator application. While measurement errors are at times large ( $\sim 30\%$  full scale), the results show that there is potential to using the resistance measurement across an SMA wire as a strain, and thus displacement sensor. However, mapping resistance to deflection is complicated, particularly when the SMA wires are not sufficiently pre-stressed or SMA actuators are coupled to other opposing SMA actuators. For an application with multiple opposing SMA wires, such as the adaptive nozzle, changing force output in one wire alters the mapping plot of opposing wires. Also, because the stress-strain behavior of the coupled wires is non-linear and hysteretic, coupling begins to add significant hysteresis to the load-deformation characteristic of the entire structure, and thus to the resistance vs. strain plots of the SMA wires embedded within the structure. However, it was found

that including a mapping scheme that considers not only the resistance of one wire to sense its own strain, but also the power input of opposing wires, greatly improves mapping accuracy. This coupling method effectively utilizes more of the available heating power and resistance information based on lessons learned from the simplified SMA spring systems.

## 2.3 Summary of Part 2

Part 2 builds an understanding of SMA actuator wire behavior by studying three systems: a single SMA and linear spring in series, opposing SMA wires coupled with a linear spring, and an adaptive Smart Inhaler nozzle joint. The first two simplified systems are easy to model and validate experimentally, and they represent a wide range of possible embedded actuator applications. The study of the single SMA-flexure system demonstrates the effects of pre-stress and actuation frequency on the stress, strain, and resistance of 50  $\mu\text{m}$  diameter Flexinol SMA wire [1]. A new resistance model is discussed to correlate the resistance of the SMA wire to modeled phase fractions and temperature. In the single SMA-spring system the load-displacement characteristic is constrained by the linear spring, and the nearly linear, non-hysteretic character of the resistance vs. strain plot shows significant potential for sensing applications.

The opposing SMA system explores the complications that arise when non-linear, hysteretic elements are coupled together. In this case, one SMA constrains the force-displacement behavior of the other, causing a cross-linked interdependence between the actuation state of the two wires. For example an increase in force from wire 2 necessitates an increase in temperature into wire 1 for the strains in the two wires to be maintained. This change in force also shifts the resistance vs. strain curve that would be used in applications that endeavor to use the resistance measurement as a displacement sensor. One example of such a system is the adaptive Smart inhaler nozzle, that employs 3 opposing SMA wires in a Mercedes star configuration. The adaptive nozzle is characterized as the first step of developing a resistance to deflection sensor mapping.

The systematic study of these systems alongside physics-based simulations leads to many practical conclusions. For example, it is demonstrated that pre-stressing SMA wires helps to reduce the hysteresis in the resistance vs. strain characteristic, while pre-straining helps reduce stress in the opposing SMA system at a cost of wider hysteresis. Also, results show that this coupled system is capable of actuating over larger ranges at a higher frequency than the single SMA-spring system because the opposing SMA wire provides an active restoring force. Most discussions are made in the context of using the resistance vs. strain plot as a sensor diagram, and the systematic opposing-SMA experiments offer clues for how to calibrate the coupled sensor diagrams for such a system.

Part 2 also makes a first attempt at using the gained understanding of the simplified systems to implement an SMA wire resistance to structural displacement sensor mapping, and using this measurement in closed-loop control. As a first attempt at controlling the simplest, single SMA-flexure system, a line is fit to the resistance vs. flexure displacement plot and the power is limited to avoid non-linear regions. Results show that peak to peak sensor errors are less than 10% of full scale, but the displacement of a flexure can only be actively controlled in one direction. Moving the spring flexure in the other direction requires waiting for the SMA wire to cool and the flexure to stretch the wire back out again.

This deficiency is remedied by adding a second opposing SMA wire, but at a cost of increased measurement errors. The same linear fit mapping is applied to both SMA wires in the opposing SMA system, and the measurement from the wire being heated is chosen as the flexure displacement measurement. This method leads to larger measurement errors on the order of 30% of full scale. For the adaptive nozzle, a coupled sensor calibration and mapping scheme is presented that uses the power input to the opposing SMA actuators to shift the resistance vs. displacement sensor line. This coupling method reduced measurement errors by about 50% compared to the uncoupled mapping technique. Further development of more accurate sensor mapping and control techniques is left for future work.

## 2.4 Future Work for Part 2

The simplified analog SMA-spring systems studied in Part 2 provide a base of understanding for SMA wires in the context of actuator applications. However, there are many useful ways of applying that understanding that have yet to be explored and are therefore points for future work. These include:

- Adjust the coupled mapping technique used on the adaptive nozzle joint to shift one actuator's resistance vs. deformation mapping based on the change in resistance of the opposing wires, instead of the change in power. The motivation behind the coupled mapping concept is that force of the opposing wires effectively alters the pre-stress in the first wire. Resistance may provide a more relevant measure of opposing force than heating power input.
- Improve sensing accuracy by applying model-based resistance to deformation mapping instead of a simple linear fit. This could be as simple as estimating the SMA temperature by tracking the history of power input to each wire and using it to capture some of the transient heating and cooling effects, or it could involve a full implementation of a poly-crystalline SMA model or neural network that approximates hysteresis.
- Apply different control schemes to the multifunctional sensor-actuator wires. The current work only discusses PI or PID control, with limits set on power input to help resolve mapping ambiguity. There is substantial room for improvement with optimal or model-based control.

# References

- [1] Dynalloy.com. "Flexinol Technical Design and Data." < <http://www.dynalloy.com/TechData.html>>. (2009).
- [2] Duerig T., Stoeckel, D. and Johnson, D. "SMA – Smart Materials for Medical Applications." Proceedings of SPIE - The International Society for Optical Engineering, v 4763, p 7-15, 2002.
- [3] Veeramani, A. S., Buckner, G. D., Owen, S. E., Cook, R. C., and Bolotin, G., "Modeling the dynamic behavior of a shape memory alloy actuated catheter." *Smart Materials and Structures*. 17, 2008.
- [4] Crews, J. H., "Development of a Shape Memory Alloy Actuated Robotic Catheter for Endocardial Ablation: Modeling, Design Optimization, and Control." Doctoral Dissertation, North Carolina State University. Raleigh, NC. 2011.
- [5] Stepan, L. L., Levi, D. S., and Carman, G. P. "A thin-film nitinol heart valve." ASME Journal of Biomechanical Engineering. Vol. 127, Nov. 2005.
- [6] Calkins, F. T. and Mabe J. "Shape memory alloy based morphing aerostructures." *Journal of Mechanical Design*. Vol. 132, Nov. 2008.
- [7] Kohl, M., Popp, M., and Krevet, B. "Shape memory micromechanisms for microvalve applications." *Proceedings of SPIE*. v 5387, p 106-117. 2004.
- [8] Gravatt, L. M., Mabe J. H., Calkins, F. T., and Hartl, D. J. "Characterization of varied geometry shape memory alloy beams." *Proc. SPIE*. 7645, 2010.
- [9] Epps, J. J., and Chopra, I., "In-flight tracking of helicopter rotor blades using shape memory alloy actuators." *Smart Materials and Structures*. Vol. 10, p. 104-111, 2001.
- [10] Fu, "Characterization of TiNi shape-memory alloy thin films for MEMS applications." *Surface Coatings Technology*. Vol. 145, p. 107, 2001.
- [11] Fu, Y. Du, H., Huan, W., Zhang, S., and Hu. M. "TiNi-based thin films in MEMS applications: a review." *Sensors and Actuators A*, 112 p. 395-408, 2004.
- [12] Clausi, D., Gradin, H., Braun, S., Peirs, J., Reynaerts D., Stemme, G., and Van Der Wijngaart, W. "Wafer-level mechanical and electrical integration of SMA wires to silicon MEMS using electroplating." *Proceedings of the IEEE International Conference on Micro Electro Mechanical Systems (MEMS)*, p 1281-1284, 2011.
- [13] Kohl, M. and Skrobaneck, K. D. "Linear microactuators based on the shape memory effect." *Sensors and Actuators A*. 70. p 104-111. 1998.
- [14] Kohl, M. "Shape Memory Microactuators." Springer-Verlag. Berlin, Heidelberg. 2004.
- [15] Lan, C-C, Yang, and Y-N, "A computational design method for a shape memory alloy actuated compliant finger," *Journal of Mechanical Design*, vol. 131, pp. 21009-1 - 21009-9, 2009.
- [16] Cha, K., Kim, G, Kim, J., and Jeong, S. "A study on anthropomorphic robot hand simulation driven by SMA wire using segment control." *Key Engineering Materials* v 345-346, pt.2, 1249-52. 2007.
- [17] Rossi, C., Barrientos, A., and Cuellar, W. C. "SMA control for bio-mimetic fish locomotion." ICINCO 2010 - Proceedings of the 7th International Conference on Informatics in Control, Automation and Robotics, v 2, p 147-152, 2010.
- [18] Manciasci, A., Gorini, S., aPernorio, G. and Dario, P. "A SMA actuated earthworm." *Proceedings - IEEE International Conference on Robotics and Automation*, v 2004, n 4, p 3282-3287, 2004.
- [19] Pausley, M. E. and Seelecke, S. "Multifunctional SMA-based Smart Inhaler system for improved aerosol drug deliver – Design and fabrication." *Proceedings of SPIE Active and Passive Smart Structures and Integrated Systems*. (2008).
- [20] Kleinstreuer, C., Zhang, Z., Li, Z, Roberts, W. L., and Rojas, C., "A new methodology for targeting drug-aerosols in the human respiratory system." *International Journal of Heat and Mass Transfer*. Vol 51, no. 23-24, p. 5578-5589. Nov. 2008.
- [21] Zhang, Z., Kleinstreuer, C., and Kim, C. S., "Comparison of analytical and CFD models with regard to micron particle deposition in a human 16-generation tracheobronchial airway model." *Journal of Aerosol Science*. Vol. 40, no. 1, p. 16-28. Jan 2009.
- [22] Bunget, G. and Seelecke, S. "BATMAV: A biologically-inspired micro-air vehicle for flapping flight – Kinematic modeling." *Proceedings of SPIE – Active and Passive Smart Structures and Integrated Systems*. 2008.
- [23] Bunget, G. "BATMAV – A Bio-Inspired Micro-Aerial Vehicle for Flapping Flight." Doctoral Dissertation, North Carolina State University. Raleigh, NC. 2011.
- [24] Jayender, J., Azizian, M., and Patel, R. V., "Autonomous image-guided robot-assisted active catheter insertion." *IEEE Transactions on Robotics*. Vol. 24, no. 4, Aug. 2008.

- [25] Chen, Q., Levy, C., "Vibration analysis and control of flexible beam by using smart damping structures." *Composites: Part B*. 30, p. 395-406, 1999.
- [26] Saadat, S., Salichs, J., Noori, M., Hou, Z., Davoodi, H., Bar-on, I., Suzuki, Y., and Masuda, A., "An overview of vibration and seismic application of NiTi shape memory alloy." *Smart Materials and Structures*. 11, 218-229, 2002.
- [27] Cho, M., and Kim, S., "Structural Morphing Using Two-Way Shape Memory Effect of SMA." *International Journal of Solids and Structures*. Vol. 42, p 1759-1776, 2005.
- [28] Furst, S., and Seelecke, S. "Experimental validation of different methods for controlling a flexible nozzle using embedded SMA wires as both positioning actuator and sensor." *Proceedings of SPIE Active and Passive Smart Structures and Integrated Systems*. (2011).
- [29] Ma, N., Song, G., Lee H-G. Position control of shape memory alloy actuators with internal electrical resistance feedback using neural networks, 2004, *Smart materials & structures*, Volume 13, Issue 4, p. 777.
- [30] Raparelli T, Zobel P B and Durante, SMA wire position control with electrical resistance feedback, 2002, *Proc. 3rd World Conf. on Structural Control*, Volume 2, pp. 391-8.
- [31] Seelecke, S., Muller, I., "Shape memory alloy actuators in smart structures: Modeling and simulation." *Appl. Mech. Rev.* vol. 57, no. 1, Jan. 2004.
- [32] Achenbach, M. "A model for an alloy with shape memory," *Int'l J of Plasticity*. vol 5; 371-396, 1989.
- [33] Cheminsky, Y., Duval, A., Piotrowski, B., aZineb, T. B., Tahari, V., and Patoor, E. "Numerical tool for SMA material simulation: application to composite structure design." *Smart Materials and Structures*. 18 (10). 2009.
- [34] Vanderplaats, G. N. *Multidiscipline Design Optimization*. Garret N. Vanderplaats, Monterey, CA. 2007.
- [35] Ikuta K, Tsukamoto M, Hirose S. Shape memory alloy servo actuator system with electrical resistance feedback and application for active endoscope, 1988, *IEEE Int. Conf. on Robotics and Automation*, Volume 1, pp 427-30.
- [36] Novák, V., et al., Electric resistance variation of NiTi shape memory alloy wires in thermomechanical tests: Experiments and simulation. *Materials Science and Engineering: A*, 2008. 481-482: p. 127-133.
- [37] Teh, Y. H. and Featherstone, R. "Frequency response analysis of shape memory alloy actuators." *Proc. of SPIE International Conference on Smart Materials and Nanotechnology in Engineering*. v 6423, 2007.
- [38] Teh, Y. H. and Featherstone, R. "An architecture for fast and accurate control of shape memory alloy actuators." *International Journal of Robotics Research*. v 27, n 5, p 595-611, May 2008.
- [39] Frautschi, J. and S. Seelecke. Finite element simulation of adaptive aerospace structures with SMA actuators. in *Smart Structures and Materials 2003: Modeling, Signal Processing, and Control*. 2003. San Diego, CA, USA: SPIE.
- [40] Chang, B. C., Shaw, J. A., and Iadicola, M. A., "Thermodynamics of shape memory alloy wires: modeling, experiments, and application." *Continuum Mech. Thermodyn*. 18: 83-118, 2006.
- [41] Boyd, J. G., and Lagoudas, D. C. "Thermodynamic Constitutive Model for Shape Memory Materials. Part 1. The Monolithic Shape Memory Alloy." *International Journal of Plasticity*. v 12, n 6, p 805-842. 1996.
- [42] Heintze, O., A Computationally Efficient Free Energy Model for Shape Memory Alloys - Experiments and Theory, NCSU Doctoral Thesis, 2004.
- [43] Yang, S., and Seelecke, S. "FE analysis of SMA-based bio-inspired bone-joint system." *Smart Materials and Structures*. 18. 2009.
- [44] Seelecke, S. "Modeling the Dynamic Behavior of Shape Memory Alloys." *International Journal of Non-Linear Mechanics*. 37; 1363-1374. 2002.
- [45] Talla, V, M. Pausley, and S. Seelecke, A Novel Driver for SMA Actuators with Simultaneous Power Control and Resistance Measurement, *J. of Mechatronics* (submitted)
- [46] Hangekar, R., Seelecke, S., "A Multi-Channel Power Controller for Actuation and Control of Multiple SMA Actuators." *Proceedings of the ASME 2009 Conference on Smart Materials, Adaptive Structures and Intelligent Systems*, (2009).
- [47] Heintze, O. and S. Seelecke, "A coupled thermomechanical model for shape memory alloys." *Materials Science & Engineering: A*, 2008. 481-482: p. 389-394.
- [48] Massad, J. E. and Smith, R. C. "A homogenized free energy model for hysteresis in thin-film shape memory alloys." *Thin Solid Films*. 489(1-2), pp. 266-290, 2005.
- [49] Cheminsky, Y., Duval, A., Patoor, E., and Ben Zineb, T. "Constitutive model for shape memory alloys including phase transformation, Martensitic reorientation and twins accommodation." *Mechanics of Materials*. Vol. 43. Jul. 2011.
- [50] Lagoudas, D. *Shape Memory Alloys: Modeling and Engineering Applications*. Springer, New York, NY. 2008.

- [51] Brinson, L. C. "One-dimensional constitutive behavior of shape memory alloys: Thermomechanical derivation with non-constant material functions and redefined martensite internal variable." *Journal of Intelligent Systems and Structures*. 4, 1993.
- [52] He, Z., Gall, K. R., and Brinson, L. C. "Use of electrical resistance testing to redefine the transformation kinetics and phase diagram for shape-memory alloys." *Metallurgical and Materials Transactions A*. vol. 37A, March 2006.
- [53] Antonucci, V., Faiella, G., Giordano, M., Mennella, F., and Nicolais, L. "Electrical resistivity study and characterization during NiTi phase transformations." *Thermochimica Acta*. 462, 2007.
- [54] Churchill, C. B., and Shaw, J. A. "Shakedown Response of Conditioned Shape Memory Alloy Wire." *Behavior and Mechanics of Multifunctional and Composite Materials*. Vol. 6928. 2008.
- [55] Pausley, M., Furst, S., and Seelecke, S. "Assessment of various modeling approaches for SMA actuators: experimental characterization." *Proceedings of SPIE Active and Passive Smart Structures and Integrated Systems*. (2009).
- [56] Smith, R. C., Seelecke, S., Zoubeida, O., and Smith, J. "A Free Energy Model for Hysteresis in Ferroelectric Materials." *Journal of Intelligent Material Systems and Structures*. 14; 719. 2003.
- [57] Furst, S. J., Crews, J. H., and Seelecke, S. "Numerical and Experimental Analysis of the Effect of a Thermal-Boundary-Layer Induced Inhomogeneity on the Behavior of SMA Wire." *Continuum Mechanics and Thermodynamics*. (submitted).
- [58] Chang, B. C., Shaw, J. A., and Iadicola, M. A., "Thermodynamics of shape memory alloy wires: modeling, experiments, and application." *Continuum Mech. Thermodyn*. 18: 83-118, 2006.
- [59] Muller, I. and Wilmski, K. "A model for a pseudoelastic body." *Il Nuovo Cimento della Societa Italiana di Fisica: B*. vol 57; 283-318, 1980.
- [60] Huo, Y. "A mathematical model for the hysteresis in shape memory alloys." *Continuum Mechanics and Thermodynamics*. vol 1; 283-303, 1989.
- [61] Heintz, Olaf. "A Computationally Efficient Free Energy Model for Shape Memory Alloys – Experiments and Theory." *Doctoral Dissertation, North Carolina State University*. Raleigh, NC. 2004.
- [62] Q Li, "Modeling and finite element analysis of smart materials," *Doctoral Dissertation, North Carolina State University*, 2006.
- [63] Langelaar, M. and van Keulen, F., "Modeling of shape memory alloy shells for design optimization," *Computers and structures*, vol. 86, pp. 955-963, 2008.
- [64] Richter, F., Kastner, O., and Eggeler, G. "Implementation of the Muller-Achenbach-Seelecke Model for Shape Memory Alloys in ABAQUS," *Journal of Materials Engineering and Performance*, vol. 18, no. 5-6, pp. 626-630, 2009.
- [65] Cho, M., and Kim, S., "Structural Morphing Using Two-Way Shape Memory Effect of SMA." *International Journal of Solids and Structures*. Vol. 42, p 1759-1776, 2005.
- [66] Fu, "Characterization of TiNi shape-memory alloy thin films for MEMS applications." *Surface Coatings Technology*. Vol. 145, p. 107, 2001.
- [67] Furst, S. J. and Seelecke, S. "Modeling and Experimental Characterization of the Stress, Strain, and Resistance of SMA Actuator-Wires with Controlled Power Input." *Journal of Intelligent Material Systems and Structures*. Submitted. May, 2011.
- [68] *Matweb.com*. "Nitinol – NiTi Shape Memory Alloy; High/Low Temperature Phase". 2011, <<http://www.matweb.com/search/QuickText.aspx?SearchText=nitinol>>.
- [69] Hangekar, R. C. "A Multi-Channel Power Controller for Actuation and Control of Shape Memory Alloy Actuators." *Masters Thesis*. North Carolina State University. Raleigh, NC. 2010.
- [70] Yang, S. and Seelecke, S. "Finite Element Analysis of SMA Beam Bending Using COMSOL." *Proceedings of SPIE*. v 7289, 2009.
- [71] Yang, S. and Seelecke, S. "FE Analysis of SMA-Based Bio-Inspired Bone-Joint System." *Smart Materials and Structures*. v 18, n 10. 2010.
- [72] Heintze, O. and S. Seelecke, A coupled thermomechanical model for shape memory alloys, *Materials Science & Engineering: A*, 2008. 481-482: p. 389-394.
- [73] Chang, B. C., Shaw, J. A., and Iadicola, M. A., "Thermodynamics of shape memory alloy wires: modeling, experiments, and application." *Continuum Mech. Thermodyn*. 18: 83-118, 2006.
- [74] Poon, C-k., Lau, K-t., and Zhou, L-m., "Design of pull-out stress for prestrained wire/polymer hybrid composites." *Composites: Part B*. 36, p 25-31, 2005.
- [75] Payandeh, Y., Meraghi, F., Patoor, E., Eberhardt, A. Debonding initiation in a NiTi shape memory wire-epoxy matrix composite. Influence of martensitic transformation." *Materials and Design*. v 31, n 3, p1077-1084. March 2010.
- [76] Boyd, J. G., and Lagoudas, D. C., "Thermomechanical Response of Shape Memory Composites." *Journal of Intelligent Systems and Structures*. Vol. 5, p. 333-346, 1994.

- [77] Jonnalagadda, K., Kline, G. E., and Sottos, N. R., "Local displacements and load transfer in shape memory alloy composites." *Experimental Mechanics*. Vol. 37, no.1, p 78-86, Mar. 1997.
- [78] Sadrnezhaad, S. K., Nemati, N. H., and Bagheri, R., "Improved adhesion of NiTi wire to silicone matrix for smart composite medical applications." *Materials and Design*. 30, p. 3667-3672, 2009
- [79] Smith, N. A., Antoun, C. G., Ellis, A. B., and Crone, W. C., "Improved adhesion between nickel-titanium shape memory alloy and a polymer via silane coupling agents." *Composites Part A: Applied Science and Manufacturing*. Vol. 35 no. 11, p. 1307-1312, Nov. 2004.
- [80] "Saitenkurbel – Guitar String Winder 2.jpg" September 1, 2009 via wikimedia, Creative Commons License.

# Appendices



# Appendix A: Adhesive Strength Experiments

## A.1 Using Adhesives for Mechanical Attachments

This appendix presents a set of experiments that quantify the shear strength of the bond between an SMA wire and various common and specialized adhesives. Adhesives offer one of the most streamlined, customizable mechanical connections possible, but their reliability in bonding with an SMA wire that is heating, cooling, and changing phase is not well known. In these experiments, the effect of wire heating current on adhesive strength is studied along with the transient slipping or softening behavior that may result from prolonged exposure to repeated mechanical and thermal loading. The effect of treating the SMA with acetone prior to adhesive application is also studied.

## A.2 Adhesive Experiment Setup

A simple tensile testing setup is used to measure the tensile force in an SMA wire attached to a drop of adhesive, as depicted in Figure 150. The droplet of adhesive is placed in a 0.5 mm wide and deep trough in the removable inserts shown in Figure 154. Employing many removable inserts allows multiple samples to be cured simultaneously. The force is measured using a strain-gage-based load cell (Futek Model LSB200) with a 2lb (~9N) load limit. A ball screw linear actuator (Zaber Model TNA08A25) is used to pull on the wire. Flexinol wire with 100  $\mu\text{m}$  diameter from Dynalloy [1] is used in all of the tests reported. Wires smaller than 100  $\mu\text{m}$  diameter have a larger surface area to cross-sectional area ratio. As a result, the smallest feasible adhesive drop developed a bonding area that was often too large for the bond to fail before the wire yielded.

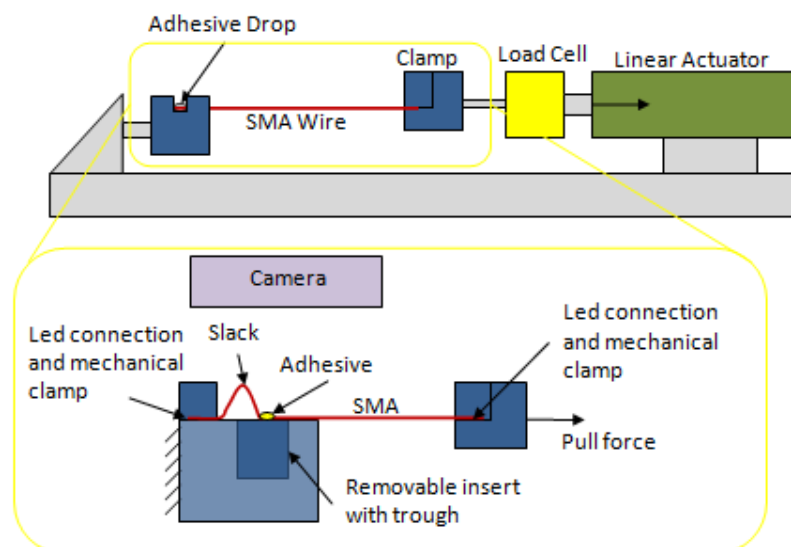


Figure 150: Tensile Test Setup Diagram

The insert holder shown in Figure 152 is fixed to a rail, and removable inserts, each holding one adhesive sample at a time, are placed in the holder for testing. A clamp at the back of the insert

holder provides an electrical and mechanical contact. However, when an adhesive is being tested slack is left between the adhesive drop and the mechanical clamp on the insert holder to ensure that the adhesive carries the load, not the clamp.

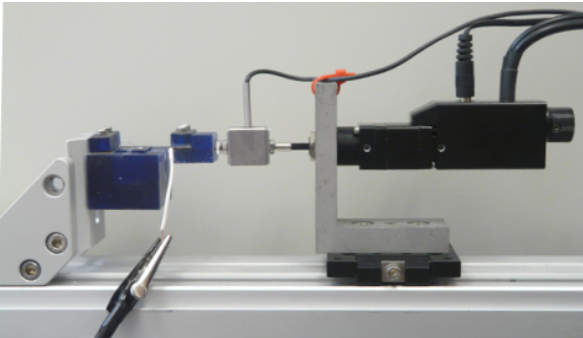


Figure 151: Tensile Test Setup Photo

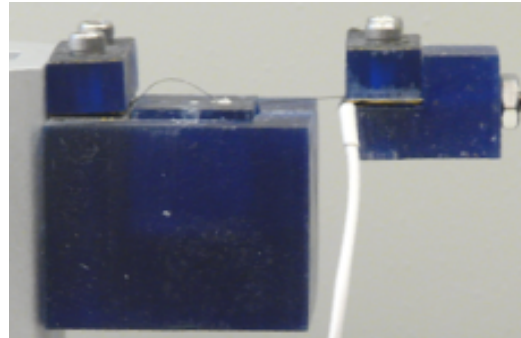


Figure 152: Close-up of Clamps and Adhesive

A photograph of the entire setup is shown in Figure 151, and a close-up view of the clamps, adhesive, and SMA wire is shown in Figure 152. The trough in the removable inserts causes the adhesive to form into a droplet with walls that are perpendicular to the SMA wire direction. The length of wire that is exposed to the adhesive, labeled  $L_{adh}$  in Figure 153, is measured under a microscope, and these vertical walls make the measurements easier and more accurate. A photograph of an adhesive drop holding a 100  $\mu\text{m}$  diameter SMA wire taken under a microscope is shown in Figure 153.

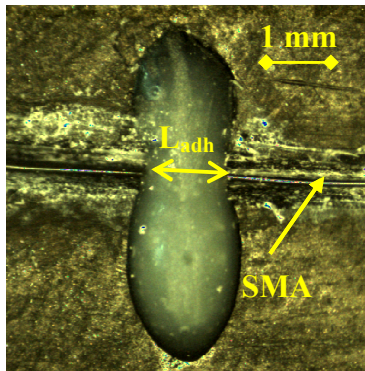


Figure 153: Microscopic view of adhesive drop and SMA Wire in trough

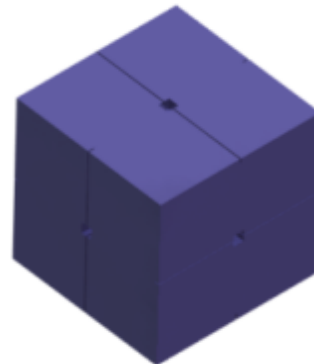


Figure 154: Model of removable insert

### A.3 Adhesive Testing Procedure and Matrix

Two separate tests, “constant current” and “constant displacement”, were run on the setup described above to determine the strength of the adhesive. In both tests different adhesives were used to hold the tensile load while either wire heating current or end displacement, and therefore engineering strain, was cycled. These two tests required samples be prepared such that the SMA wire was exposed to a measureable length of adhesive that held the load while the wire was in tension. A description of the procedure and experimental matrix for each test and sample preparation is given in the following sections.

### A.3.1 Sample Preparation for Adhesive Tests

The test samples were prepared by a repeatable procedure so that results could be averaged and compared statistically. One of the goals of this study is to characterize the effect of treating the SMA wires with acetone compared to using a new, untreated wire, so the acetone treatment procedure is included. Also, the preparation method for Loctite SuperGlue was different from the other epoxies because SuperGlue has very low viscosity prior to cure.

Each SMA wire was glued to a removable insert, pictured in Figure 154. The removable inserts were printed using a Visijet 3D printer. The prototyped objects have a waxy film residue from the printing process that greatly reduced the ability of adhesives to bond to the inserts. Soaking the 3D printed parts in mineral oil for about 1 minute, then acetone for another minute, removed much of this film and greatly improved the bond between the prototyping material and the adhesives. This ensures that the bond fails at the interface between the adhesive and the SMA wire rather than the interface between the adhesive and the removable insert.

For each sample tested, a 40 mm length of SMA wire was cut. If no washing procedure was prescribed for a given sample, the sample was cut from a new role of SMA wire and handled with bare hands. For the washed samples, the following steps, shown in Figure 155, were taken:

- 1) Wear latex gloves at all times while handling the SMA wire.
- 2) Soak a piece of lens paper with acetone and wipe all sides of the SMA wire several times.
- 3) Use a clean, dry piece of lens paper to wipe all sides of the SMA wire.
- 4) Place the prepared wires in a clean area on top of a piece of lens paper to ensure that no contamination occurs.



Figure 155: Materials used when cleaning residue from a SMA wire

The adhesives tested, listed in Table 14, represent both common adhesives and specialty adhesives. Nanotool is a UV-cure resin with embedded ceramic particles that give it thermally insulating properties. JB Weld is a common all-purpose epoxy for a wide range of materials, including metals and plastics. Loctite SuperGlue is a fast-curing contact adhesive. E40-HT and 1-min Epoxy are

Loctite brand adhesives that claim temperature-resistance and fast-curing, respectively. ResinLabs SEC1233 is a two-part epoxy that has dissolved silver particles that make it conductive. All of the adhesives used can be cured at room temperature, but Nanotool requires UV light.

Table 14: Adhesives tested

Adhesive	Name	Description
1	Nanotool	UV cure stereolithography material
2	JB Weld	All-purpose 2-part epoxy
3	Loctite SuperGlue	Single-part fast-curing contact adhesive
4	Loctite E40-HT	High temperature 2-part epoxy
5	Loctite 1-min Epoxy	Quick setting 2-part epoxy
6	ResinLabs SEC1233	Conductive 2-part epoxy

All of the adhesives aside from Loctite SuperGlue have viscosity roughly comparable to honey. On the small scale, JB Weld has a fine-grain, sandy appearance, and ResinLabs SEC1233 conductive epoxy has the consistency of paste, not forming into droplets. However, all of these viscous adhesives can be handled in the following way:

1. Place the SMA wire lengthwise in a clean trough on one of the faces of the removable insert and tape it in place with masking tape such that about 15 mm hangs off each side of the block.
2. Mix the prescribed epoxy as directed by the datasheet.
3. Place the block under a stereoscope with about 25x zoom.
4. Place a single drop of the mixed adhesive on the end of a needle transfer it into the trough (above the SMA wire). The droplet should be less than 2 mm across for all adhesives except for Nanotool. When Nanotool is used, 2-4 mm of the wire should be exposed to adhesive.
5. Lift the SMA wire out of the trough then push it back down to ensure that the adhesive droplet surrounds all sides of the wire.
6. Place the sample in a safe, clean place to cure according to datasheet instructions.
7. Measure the length of the SMA wire that is exposed to the adhesive using a reticle in the stereoscope eyepiece (0.002"/divide was used for these experiments).

The low-viscosity SuperGlue must be handled slightly differently. SuperGlue samples are not attached in the trough. Rather, the SMA wire is taped down on a face of the removable insert, and a droplet of glue is placed next to the wire. Then a needle is used to drag a small line of glue over the wire, as shown in Figure 156. Care is given to ensure that all sides of the wire are exposed to the adhesive.

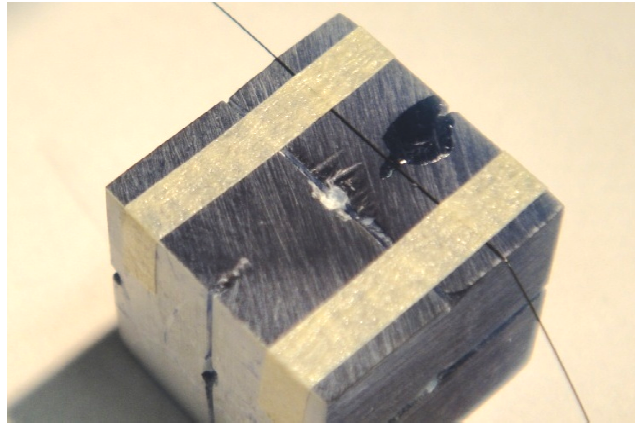


Figure 156: Photo of Removable Insert Prepared with SuperGlue Sample

### A.3.2 Experiment Matrix

The matrix used for testing adhesive strength as a function of different parameters is shown in Table 15. The test for each set of parameters in Table 15 was repeated ten times for each adhesive. Both the measured length of the SMA wire that was exposed to the adhesive and the failure force were recorded for each of the repetitions. The SMA wire surface preparation field was only varied on adhesives 1-4. The adhesives and parameter key are listed in Table 15.

Table 15: Experiment Parameter Matrix

Adhesive	Test	Preparation	Pre-strain (%)	Current (mA)
1-6	Constant displacement	Washed or Unwashed	Fixed 2, 3, or 4	Cycle
1-6	Constant current	Washed or Unwashed	0	Fixed 0, 150, 200, or 250

### A.3.3 Procedure for Constant Displacement Tests

In the constant displacement test the length of the wire was fixed and the input current was cycled to simulate a thermal-mechanical loading scenario that would be expected in a typical actuation application. The wire was first heated under zero stress to clear the material memory, then pre-strained to either 2, 3, or 4%, as shown in Table 15. During each thermal-loading cycle, the current was ramped to a prescribed maximum at a rate of 15 mA/s. Then the current was maintained at the maximum for 10 s before being ramped down. The steps used to run this test are enumerated below. The pre-straining steps are labeled in Figure 157 and the experiment steps are labeled in Figure 158, with current shown in red, strain shown in black, and the measured stress in a clamped SMA wire in blue. The amplitude of the current on the first cycle was 150 mA, and the amplitude was increased by 30 mA per cycle until the adhesive bond failed. The tensile force and input current at failure was recorded.

- 1) Heat the wire with 250 mA under 0 stress (note Dynalloy lists the input current for transformation of a 100  $\mu\text{m}$  wire in 1 s as 200 mA [1]).
- 2) Pull and detect the wire using the load cell and record the wire austenitic reference length,  $L_{0,A}$ .
- 3) Turn off the current and give the wire 5 s to cool.
- 4) Pull the wire to the desired pre-strain value.
- 5) Relax the wire by extending the linear actuator until 0 stress is measured.

- 6) Apply the adhesive to the wire, which is under 0 stress adjacent to the removable insert.
- 7) Pull the wire again until the wire is detected by the load cell.
- 8) Cycle the input current with a trapezoidal step function of increasing amplitude, as shown in Figure 158.

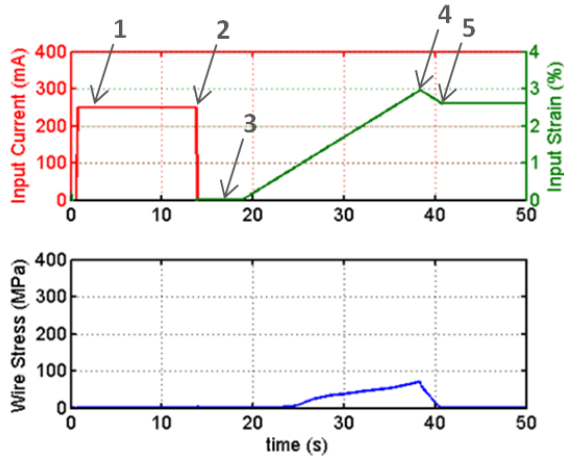


Figure 157: Constant Current Pre-straining Inputs and Wire Stress

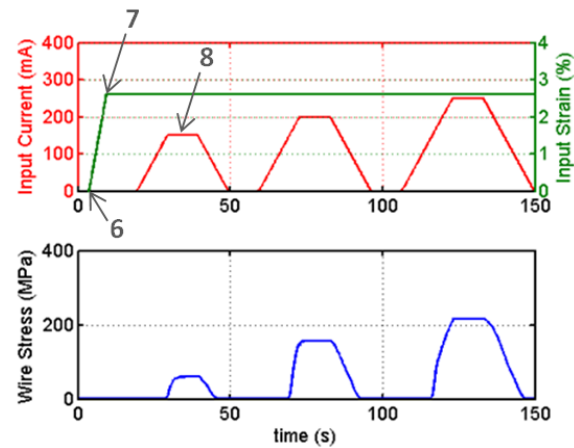


Figure 158: Constant Current Experiment Inputs and Measured Wire Stress

### A.3.4 Procedure for Constant Current Pullout Tests

In the constant current tests, the current was maintained at a fixed value while the strain was cycled to simulate a mechanical loading scenario. Once again, wire memory was cleared by heating the wire under 0 stress, then the reference strain was determined before the experiment cycles were run, as shown in Figure 159. In the experiment cycles, the wire end displacement was controlled so that the average wire strain would follow a trapezoid wave shown in with a trapezoid of increasing amplitude until failure. The trapezoid wave ramps up at a rate of 1%/s and the peak amplitude increases by 0.5% per cycle, as shown in Figure 160. The steps are once again enumerated below and labeled in the appropriate positions on Figure 159 and Figure 160.

- 1) Heat wire with 250 mA under 0 stress.
- 2) Pull and detect the wire using the load cell and record the austenitic reference length,  $L_{0,A}$ .
- 3) Turn off the current and give the wire 5 s to cool.
- 4) Attach the adhesive under 0 stress.
- 5) Turn on the current to the fixed value prescribed in Table 15.
- 6) Once again detect the wire at  $L_{0,A}$ .
- 7) Cycle the input strain with the waveform shown in Figure 160.

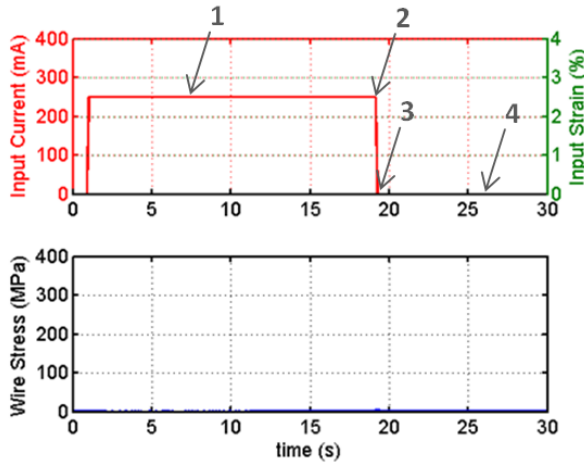


Figure 159: Test 2 pre-straining inputs and wire stress

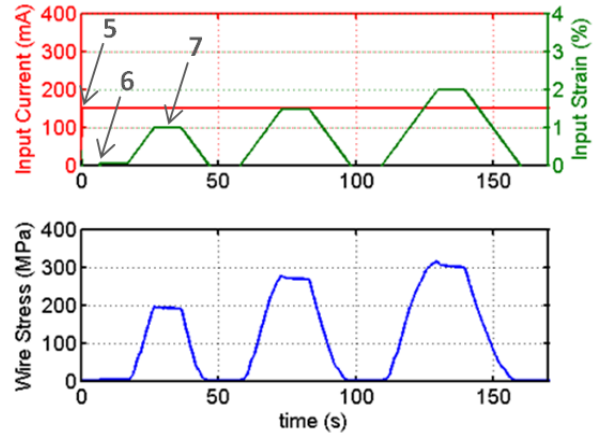


Figure 160: Test 2 inputs and measured wire stress

For each adhesive, 10 samples are prepared and tested. The force at failure is recorded and used to calculate the shear stress between the SMA wire and the adhesive,  $\tau_{adh}$ , that is calculated based on the force measured in the load cell via equation (1),

$$\tau_{adh} = \frac{F_{sma}}{\pi d_{sma} L_{adh}}, \quad (1)$$

where  $F_{sma}$  is the tensile force in the SMA wire,  $L_{adh}$  is the measured length of the SMA wire that is exposed to adhesive, and  $d_{sma}$  is the diameter of the SMA wire (100  $\mu\text{m}$ ).

## A.4 Results and Discussion

### A.4.1 Constant Displacement Test Time Histories

Figure 161 shows a typical time-history plot of the input signals and SMA wire stress for Loctite SuperGlue, E40-HT, and 1-Min Epoxy, as well as JB Weld and a steel clamp for the test run with a pre-strain of 3%. Transient responses for Nanotool and SEC1233 are not shown because they failed almost immediately. The top panel shows the inputs while the bottom panel shows the SMA wire stress, as calculated from the measured tensile force. The first 50 s show the inputs and measurements during the pre-heating and pre-straining procedure, while the remainder of the time shows the response of the SMA wire in series with each different adhesive. Note that the bottom plot shows wire stress, not the shear stress between the wire and the adhesive. Shear stress is dependent on the length of wire that is exposed to adhesive, as shown in equation (1), so samples exposed to a longer column of adhesive can often survive for many cycles without any sign of weakening. Since the goal of this work was to quantify failure shear stress, the exposed lengths were kept to a minimum to ensure the bond failed before the wire itself yielded under stress.

Figure 162 shows a close-up image of the time histories. First, note from Figure 162 that the wire does not see as much stress at the same strain in the adhesive tests as in the clamped test. This is because there was compliance in the removable insert of the test setup. In terms of the adhesive failure modes, the 1-Min Epoxy, SuperGlue, and JB Weld fail instantly, as indicated by the immediate

sharp drop in stress. The wire attached with Loctite E40-HT first experiences a slow reduction in stress (around 470 s) before the adhesive finally fails and stress drops considerably. This trend was observation in many of the tests, suggesting that the temperature-resistant epoxy has a tendency to soften before losing its grip.

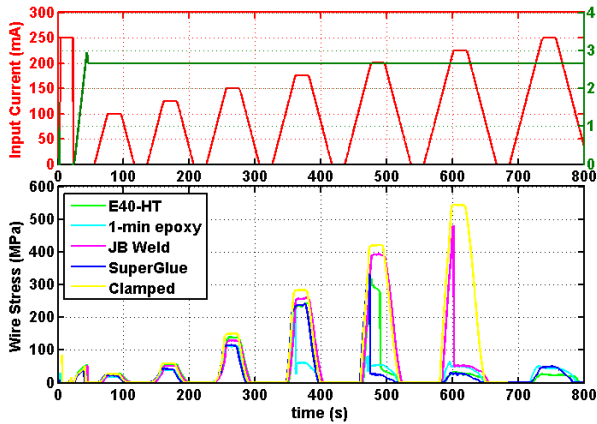


Figure 161: Transient Behavior of Constant Displacement Test

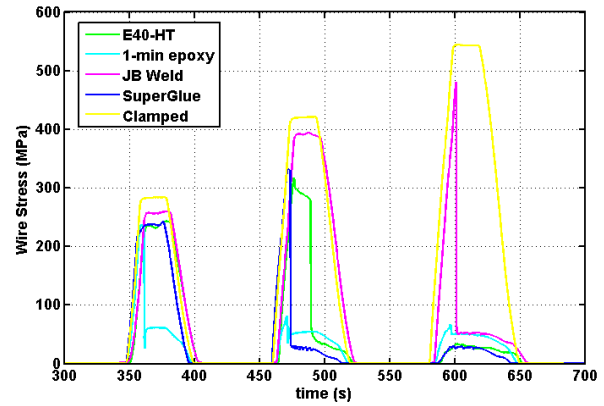


Figure 162: Close-up of Transient Behavior

Although it is possible to draw conclusions on failure modes from Figure 161 and Figure 162, it is not clear from just this one 3% pre-strain plot whether the failure is purely a result of the tension in the wire or whether the heat generated by the input current also plays a role. This information comes from compiling the results of tests with many different pre-strains as well as the results of the constant current tests, where the heating current is held at various fixed levels while the wire is strained.

#### A.4.2 Failure Shear Stress Results

Figure 163 through Figure 168 show the compiled failure shear stress for each adhesive. The failure points for the constant displacement tests (Test 1) vary in both current and stress, so an average cannot be taken and each point on the plots represents a single test. However, in many cases, the adhesive failed while the current was on its plateau, indicating that either the adhesive weakens slowly under a given set of harsh conditions before finally failing, or that the temperature of the wire-adhesive junction does not equilibrate until an input power is maintained for several seconds. The samples that were washed with acetone and handled with latex gloves are shown in red, and the unwashed samples are shown in blue. The square points from the constant current test (Test 2) represent the average failure shear stress for the 10 samples tested at each fixed current value. The error bars are two standard-deviations, representing a 95% confidence interval for normally distributed data. In general, the points from Test 1 fall within the confidence intervals from Test 2. However, the Test 1 samples that fall outside of the Test 2 confidence interval generally have a higher shear stress or current at failure. This is most likely due to a lag in the thermal equilibrium problem. The plots show applied current vs. shear stress, but it is actually the rise in temperature that is suspected to cause a weakening of the adhesive. Since temperature will inevitably lag input current slightly, it is expected that the Test 1 points will be skewed to the right, even though tests were intentionally run slowly so as to minimize this effect.

The data for both JB Weld and Loctite E40-HT epoxies plotted in Figure 164 and Figure 166, respectively, clearly show that treating the wire with an acetone wash actually reduced shear strain at failure by 10-70%. In other words, the extra steps taken to clean the wire samples led to a weakening of bond strength. This phenomenon was also observed by Jonnalagadda et. al. [77]. In general, oxide or other residues that may be left on the SMA wire surface increases bond strength; however, the acetone wash likely removes many of these materials. Also, if any residue of acetone remains on the wire surface, the curing of the epoxy would be effected, possibly resulting in a loss of bond strength.

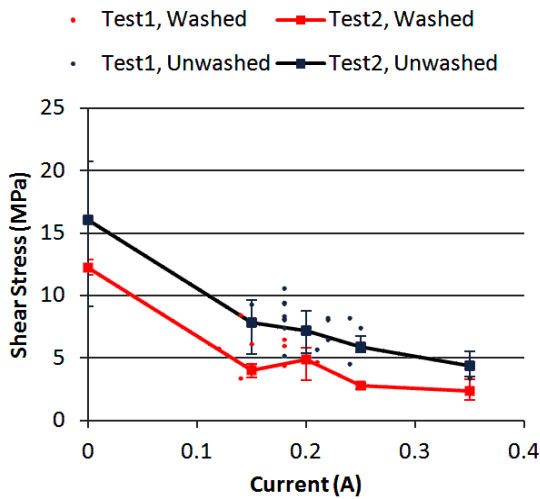


Figure 163: Nanotool UV-Cured Ceramic Resin

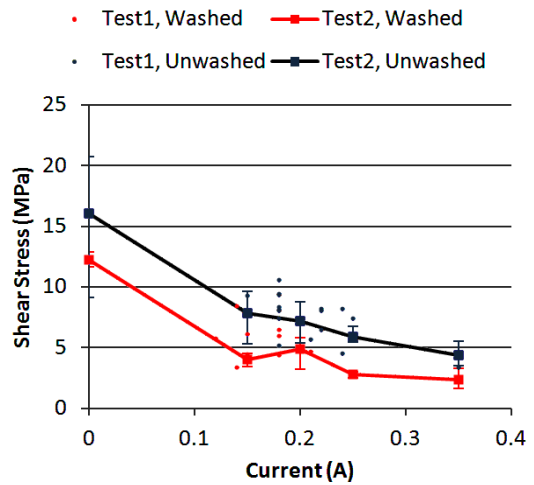


Figure 164: JB Weld Epoxy

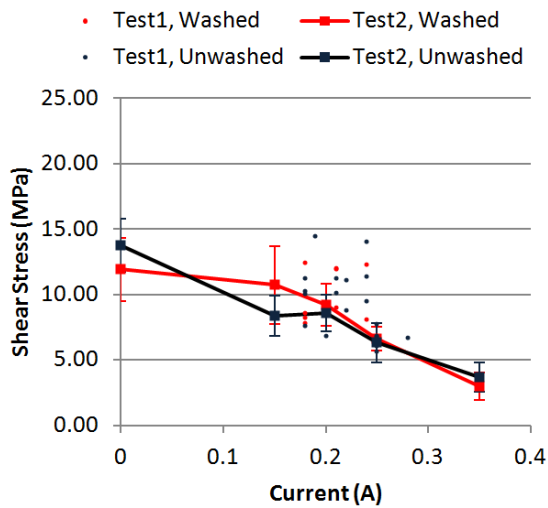


Figure 165: Loctite Superglue

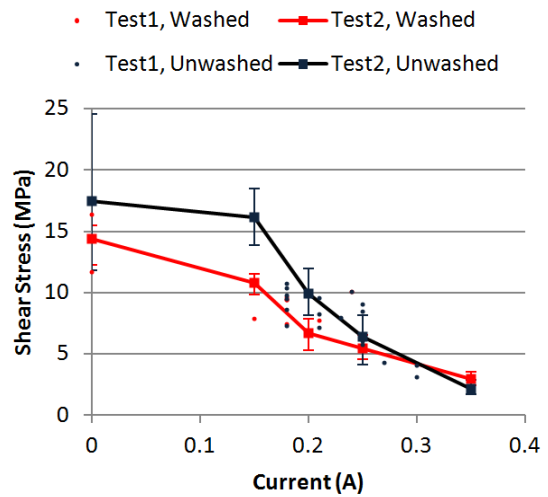


Figure 166: Loctite E40-HT High Temperature Epoxy

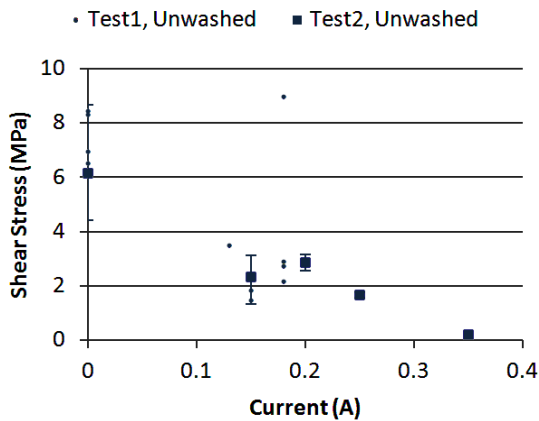


Figure 167: Loctite 1-Min Epoxy

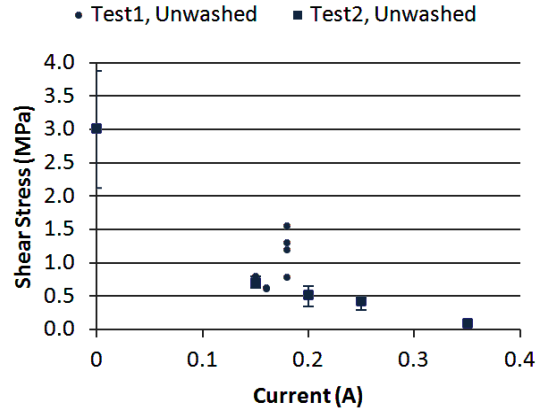


Figure 168: SEC-1233 Conductive Epoxy

The average failure stresses and currents from Test 2 for all of the adhesives are plotted together in Figure 169. The Loctite E40-HT shows the highest failure shear stress for heating currents below 200 mA; however, it required 5 days to fully cure, as prescribed by the product datasheet. The Loctite SuperGlue and JB Weld both behave similarly and show better bonding strength than the temperature resistant E40-HT at 350 mA. The JB Weld takes 24 hours to reach full cure, and the SuperGlue sets immediately on contact, but was given 30 minutes so that the areas that do not contact either the sample holder block or the SMA wire can harden. The conductive epoxy fails instantly when any heating current is applied, and the Nanotool and 1-Min Epoxy register very poor bonding at all temperatures.

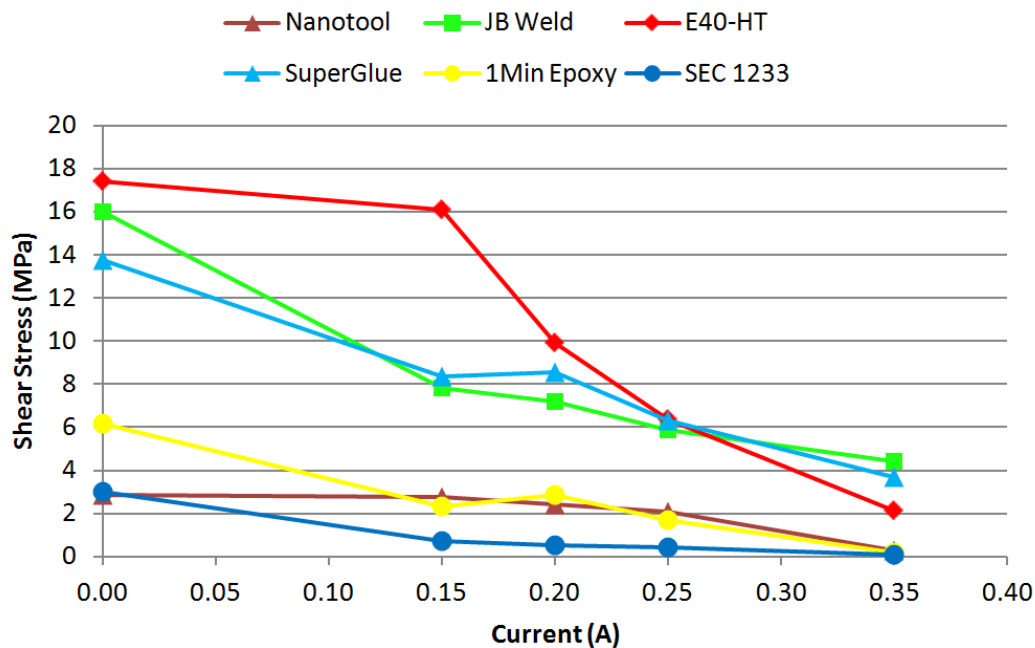


Figure 169: Comparison of Average Shear Stress at Failure of Unwashed, Test 2 Adhesive Samples

Figure 169 also clearly shows that the failure shear stress decreases as input current increases for all of the adhesives. This is entirely expected, as the input current raises wire temperature, in some cases above austenite finish temperature of the SMA wire (90 C). Product datasheets for all of the adhesives tested suggest it is typical for bond strength to weaken at higher temperatures. Also, the

adhesives themselves are generally insulating, so the temperature at the adhesive bond interface is likely substantially higher than in the center of the wire because the coating of insulating adhesive prevents heat from being transferred through the wire's surface and into the surrounding air.

## **A.5 Adhesive Test Conclusions**

The adhesive experiments successfully accomplished the stated objectives of quantifying the failure shear stress at the interface between various adhesives and SMA wires as a function of input current. Results show Loctite E40-HT, Loctite SuperGlue, and JB Weld hold relatively well. The epoxy that was designed for high temperatures, Loctite E40-HT, indeed has the highest bond strength at current inputs up to 250 mA. For this epoxy, when no acetone wash is used the bond can be expected to hold 10 MPa shear stress when the wire is heated with the recommended actuation current of 200 mA. For the case of a 2 mm exposure of the 100  $\mu\text{m}$  diameter wire to E40-HT adhesive, a 10 MPa shear stress will correlate to a 6.3 N tensile force and 800 MPa of wire stress. Since 800 MPa is approaching wire yield stress, and 200 mA will raise wire temperature to the austenite finish temperature, a 2 mm length of Loctite E40-HT can be expected to work for typical applications. Loctite SuperGlue offers only a slightly weaker bond than the E40-HT epoxy, and it cures much faster. However, the caustic nature of SuperGlue should be considered before it is applied to certain materials.

Also, results found that the extra effort associated with washing SMA wires with acetone actually has a negative effect on bond strength of epoxies. Although contamination of the wire surface by oils from human hands or dirt could be expected to weaken bond strength, washing with acetone is not recommended as a remedy. Clean, new wires should be used whenever possible. It is also likely that roughening the surface with sand paper or chemical etching would improve bonding strength, but these effects were not systematically tested.

Results show that JB Weld does a fair job at all temperatures, but in general it offers no advantage over Loctite E40-HT. Nanotool does a poor job holding in shear; however, it still offers advantages as a fast-curing thermal insulator. Loctite 1-Minute Epoxy was difficult to work with because of how quickly it cured, and it did not hold a strong bond. It should not be selected over the adhesives discussed above. The conductive epoxy, ResinLabs SEC1233, was also poor as an adhesive, but its conductive properties were observed to be excellent. It can be used in applications as a cold solder to make electrical connections, but it should not be relied on to hold substantial shear strain, particularly at high temperatures. Also, the electrical contact resistance does increase when the adhesive bond is broken by exposure to high temperatures.

The information learned during these tests can be used by designers to determine how much of what kind of adhesive can be used to make an adequate mechanical bond. Different adhesives can be used in many applications as an elegant means of embedding SMA-actuator wires within a structure. However, it should also be noted that adhesives hold very little shear stress under extremely high temperatures. Also, once an adhesive bond is broken, it cannot be easily repaired. Along the same lines, once an adhesive cured, it cannot be uncured, moved and re-cured. Therefore, if slack develops

in the SMA wire, it cannot be removed. As a result of these drawbacks, adhesives should be avoided in applications where extreme over-heating or SMA relaxation is possible.

# Appendix B: The Effects of Thermal Boundary Conditions on SMA Actuator Wires

## B.1 Introduction

### B.1.1 Motivation

Shape memory alloy (SMA) wires offer a unique solution to many applications requiring a small, embedded actuator or sensor with high power density. However, the behavior of SMA wires is often misunderstood, leading many to believe they are unpredictable and unsuitable for practical implementation. Oftentimes this is the result of an SMA wire exhibiting coupled thermo-mechanical behavior, whether it is embedded with an application or clamped into a controlled tensile test setup.

SMA wires contract and produce useable force when heated, typically by Joule heating. However, in most application settings the temperature of the wire cannot be directly controlled; only the power, voltage, or current input can. The wire temperature, which is responsible for its state of contraction and mechanical force output, depends not only on the controlled heat input, but also on the heat losses that occur through convection with the environment or conduction into the structure at the attachment points. In the case of a small SMA wire, the surface area through which convective cooling can occur is substantial, while the thermal mass that resists the conductive pull of large heat sinks at the connection points is extremely small. A thorough analysis of these coupled thermo-mechanical considerations adds to the understanding of SMA materials making them more attractive for new applications, even those requiring precise position or force control.

### B.1.2 Background

Substantial work has already been done to model the hysteretic stress-strain behavior of an SMA wire for a variety of applications. Researchers such as Muller, Smith, Boyd, Lagoudas, and Seelecke have developed models based on the free energy function of the material [41]-[51]. These models help motivate the physical mechanisms that instigate the change in material properties that make SMA's so attractive. They also give engineers a means to optimize designs for real-world applications by predicting the behavior of a segment of material [4]. Implementing a SMA model into finite element software gives a designer the opportunity to study the effects of inhomogeneities along the length of SMA material as well as the interaction between the SMA and another structural element [62]-[64].

### B.1.3 Objective

The objective of this study is to conduct simulated and experimental tensile tests on a Dynalloy Flexinol SMA actuator wire [1]. In the tensile tests, the power input to the wire and the displacement of the wire endpoint are controlled; then the force generated by the wire is measured. This results in an experimental measurement of the stress-strain hysteresis of an SMA wire at several different

temperatures. Since the stress and strain are only measured at the end points of the wire, the experiments represent the average of the local behavior that may vary along the length of the wire.

The tensile test is then simulated using COMSOL Multiphysics simulation software (COMSOL, Inc., Burlington, MA) that considers not only the SMA behavior, but also the thermal convection between the wire and environment and the conduction between the wire and clamps with a large thermal mass. This model allows for predictions to be made about inhomogeneities along the length of the wire and for the effects of such an inhomogeneities to be studied. For example, a model simulates the effects that conductive heat loss has on the behavior of the SMA wires of different lengths. For different length wires, the behavior at the thermal boundary contributes to the average behavior over the length of the wire with varying magnitude. Therefore, conducting simulations and experiments on different length wires validates the existence of many of these effects. The resistance across the wire is also measured and compared to modeled predictions.

## B.2 Numerical Simulation

A numerical simulation is used to model the coupled thermo-mechanical behavior of an SMA wire during a tensile test. The thermal and mechanical problems are derived from local internal energy and momentum balance laws. Since the temperature is not constant along the length of the SMA wire, the balance laws must be solved locally. Then bulk wire behavior is determined by integrating over the spatial domain. The constitutive equations governing the non-linear, hysteretic stress-strain behavior of SMA wire come from an implementation of the SMA model proposed by Muller, Achenbach, and Seelecke, [28]. The balance laws and SMA model equations are solved with COMSOL Multiphysics finite element software.

### B.2.1 Balance Laws

The momentum balance law dictates the state of stress in the wire, and the internal energy balance law can be used to predict the temperature field. The homogeneity of the temperature field depends on the boundary condition prescribed during the solution of the internal energy equation. In order to capture the coupled thermo-mechanical behavior of an SMA wire during a tensile test, the momentum and internal energy equations must be solved simultaneously with appropriate boundary conditions. Implementation into COMSOL requires that the governing equations be solved locally within the FEA structure, so the balance laws are derived as partial differential equations.

#### ***Momentum Balance***

The momentum balance is used to define the mechanical stress state in the SMA wire. The momentum balance in local form is

$$\frac{\partial}{\partial t}(\rho v_i) + \frac{\partial}{\partial x}(\rho v_i v_j - \sigma_{ij}) = \rho f_i \quad (1)$$

where  $\rho$  is density,  $v_i$  and  $v_j$  are velocity components,  $\sigma_{ij}$  is the stress tensor, and  $f_i$  is the sum of body forces.

Since loading is slow and the inertia of a small wire is negligibly small, the analysis is assumed to be quasi-static. Therefore, the velocity terms are eliminated from the momentum balance, which yields

$$\frac{\partial \sigma_{ij}}{\partial x} = \rho f_i. \quad (2)$$

For the case of a 1D wire, only the axial load is considered and body forces such as gravity are neglected. Therefore the momentum balance finally simplifies to

$$\frac{\partial \sigma_x(x,t)}{\partial x} = 0. \quad (3)$$

Equation (3) indicates that the tensile forces at all points along the wire are equal since there are no stress gradients.

### **Internal Energy Balance**

The internal energy balance law governs the heating and cooling of a simulated SMA wire due to physical processes such as thermal convection, conduction, and Joule heating. The internal energy balance in local form is

$$\frac{\partial}{\partial t}(\rho u) + \frac{\partial}{\partial x}(\rho u v_j + q_j) = \rho r + \sigma_{ij} \frac{\partial v_i}{\partial x_j}, \quad (4)$$

where  $u$  is the internal energy,  $q_j$  is the heat flux, and  $r$  is an energy source term.

Given the quasi-static simplification and inserting constitutive relationships, the internal energy balance reduces to equation (5).

$$\rho C_V \frac{\partial T(x,t)}{\partial t} - \kappa \frac{\partial^2 T(x,t)}{\partial x^2} = -\frac{2h(T(x,t) - T_{ext})}{R} + \rho H \left( \frac{\partial x^+(x,t)}{\partial t} + \frac{\partial x^-(x,t)}{\partial t} \right) + \frac{j}{\pi R^2} \quad (5)$$

In equation (5) the first term is derived from the relation for internal energy, where  $c_V$  is the specific heat of the Nitinol wire. The second term describes the heat flux along the length of the wire with conduction coefficient  $\kappa$ . On the right hand side, the convective cooling from the surface of the wire is inserted as a negative source term, where  $h$  is the convection coefficient in still air,  $R$  is the radius of the wire, and  $T_{ext}$  is the ambient temperature.

The contribution due to latent heating appears in the second term on the right hand side, where  $H$  is the latent heat and  $x^\pm$  are the phase fractions, introduced in the SMA model constitutive equations in Section B.2.2.

Finally, the increase in internal energy due to Joule heating is derived as another source term where  $j$  is the power input per unit length.

### B.2.2 SMA Model

The model used to simulate the hysteretic thermo-mechanical behavior of an SMA is based on the Gibbs free energy landscape and the probability of a constitutive grain of SMA material switching phase from the low temperature martensite phase to the high temperature austenite phase. The Gibbs free energy landscape is defined by the stress, strain, and temperature at each point in the wire. The derivation of the model is described in more detail in [28],[61].

In this implementation, the SMA model consists of 3 first order partial differential equations that are solved locally using COMSOL FEA software. The first two equations describe the change in the fraction of the wire in the martensite phases. The third is the internal energy balance in equation (5) that models the wire temperature. In this simulation the wire is assumed to be 1D, with the phase fractions and temperature varying only along the wire length  $x$ . The evolution of the martensite plus phase fraction is

$$\frac{\partial x^+(x,t)}{\partial t} = -x^+(x,t)p^{+A} + x^A(x,t)p^{A+}, \quad (6)$$

and the martensite minus phase fraction is

$$\frac{\partial x^-(x,t)}{\partial t} = -x^-(x,t)p^{-A} + x^A(x,t)p^{A-}, \quad (7)$$

where  $x^+$  is the phase fraction of tension-induced martensite (martensite plus or  $M^+$ ),  $x^-$  is the phase fraction of compression-induced martensite (martensite minus or  $M^-$ ). The austenitic phase fraction  $x^A$  comes from the conservation relation

$$x^A(x,t) = 1 - x^+(x,t) - x^-(x,t). \quad (8)$$

The probabilities of a constitutive grain of SMA material transforming from one phase to another are described by the  $p^{\alpha\beta}$  terms, where  $p^{+A}$  represents the probability of a grain transforming from the martensite plus phase to the austenite phase, and so-forth. Phase transition probabilities are described in detail in [61]. Stress and strain in the SMA are then related through

$$\sigma(x,t) = \frac{\varepsilon(x,t) - \varepsilon_T (x^+(x,t) - x^-(x,t))}{\left( \frac{x^A(x,t)}{E_A} + \frac{x^+(x,t) + x^-(x,t)}{E_M} \right)}. \quad (9)$$

The elastic moduli of austenite and martensite are  $E_A$  and  $E_M$ , respectively. The strain value  $\varepsilon_T$  represents the maximum recoverable strain of the SMA material. Note in equation (9) that stress  $\sigma(x,t)$  is written as a function of both space and time; however, the momentum balance in equation (3) inhibits stress gradients, so stress is in fact uniform over the length of the wire.

### **Resistance Model**

The resistance model is an extension of the model proposed by Furst and Seelecke [67]. The local resistivity of the material is the sum of the phase-dependent resistivities weighted by the local phase fractions,

$$\rho_{SMA}(x,t,T) = [x^A(x,t)\rho_A(T) + x^+(x,t)\rho_M(T) + x^-(x,t)\rho_M(T)]. \quad (10)$$

The resistivity of each phase is also temperature-dependent. The temperature dependence of the austenite resistivity value is given by

$$\rho_A(T) = \rho_{0A}(1 + \alpha^A \Delta T(x,t)), \quad (11)$$

and the martensite resistivity is given by

$$\rho_M(T) = \rho_{0M}(1 + \alpha^M \Delta T(x,t)). \quad (12)$$

Note that temperature  $T(x,t)$  is not homogenous over the length of the wire when an isothermal boundary condition is imposed on the internal energy balance.

Additionally, the resistance model presented in [67] is extended by accounting for the elastic deformation of the wire, since elastic strain causes the wire to stretch and the cross-sectional area to be reduced. The elastic component of the strain is resolved by removing the term for strain change due to phase transformation  $\varepsilon_T$  from equation (9) and solving for  $\varepsilon(x,t)$ , which gives

$$\varepsilon_e(x,t) = \sigma(x,t) \left( \frac{x^+(x,t) + x^-(x,t)}{E_m} + \frac{x^A(x,t)}{E_A} \right). \quad (13)$$

Elastic strain alters the differential length of the SMA via

$$dx(x,t) = (1 + \varepsilon_e(x,t)) dx_0, \quad (14)$$

and the SMA effective radius via

$$R(x, t) = R_0 (1 - \nu \varepsilon_e(x, t)), \quad (15)$$

where  $\nu$  is the Poisson's ratio and is taken as 0.3 [67]. Note that for the mechanical problem, the wire is assumed to be 1-D with uniform cross-sectional area – the changes to the radius due to elastic strain have a small impact on stress and are therefore ignored in this study. Nevertheless, future implementations of the model will also solve for the inhomogeneous stress field that results from radius change.

However, for the resistance model the change in radius is significant and easy to calculate in a post-processing step, so it is included. In general, the total resistance of a wire can be calculated as

$$\Omega = \frac{\rho L}{A}. \quad (16)$$

Therefore, the differential contribution to resistance is

$$d\Omega(x, t, T) = \frac{\rho_{SMA}(x, t, T)(1 + \varepsilon_e(x, t))dx_0}{\pi(R_0(1 - \nu \varepsilon_e(x, t)))^2}. \quad (17)$$

Then total resistance of the SMA wire is the differential contributions integrated over the reference length  $L_0$

$$\Omega(t, T) = \int_0^{L_0} \frac{\rho_{SMA}(x, t, T)(1 + \varepsilon_e(x, t))}{\pi(R_0(1 - \nu \varepsilon_e(x, t)))^2} dx_0, \quad (18)$$

where  $\rho_{SMA}$  and  $\varepsilon_e$  are space and time dependent, as shown in equations (10) and (13), respectively. The nominal and temperature dependent resistivity's of each phase are shown in Table 16

Table 16: SMA Wire Resistance Model Parameters

Parameter	Value	Unit	Description
$\rho_{0A}$	8.9e-7	$\Omega\text{m}$	Resistivity of austenite phase
$\rho_{0M}$	10.4e-7	$\Omega\text{m}$	Resistivity of martensite phase
$\alpha^A$	0.0002	K-1	Temperature dependence of austenite phase
$\alpha^M$	0.0003	K-1	Temperature dependence of martensite phase

### SMA Modeling Parameters

The SMA model parameters need to be set such that the model closely replicates the behavior of the SMA wire without causing numerical instability. Table 17 shows the material properties and model parameters that can be independently set to match published or experimental data. The parameters  $\tau_x$  and  $V_d$  affect the rate at which a constitutive element changes phase. All of the parameters in Table 17 and Table 18 are used to calculate the probability of a constitutive grain of material changing phase. These relations are omitted here but derived rigorously in [28],[61].

Table 17: SMA Model Material Parameters

Parameter	Value	Unit	Description
$E_A$	71.1e9	Pa	Modulus of austenite
$E_M$	30.9e9	Pa	Modulus of martensite
$\epsilon_T$	0.042		Maximum recoverable strain
$V_d$	5e-23	m <sup>3</sup>	Volume element size
$\tau_x$	5e-2	s	Scale factor on transition probability
$\rho$	6.4e3	kg/ m <sup>3</sup>	Density of Nitinol
H	24e3	J/kg	Latent heat of phase transformation
h	90	W/ m <sup>2</sup> /K	Heat convection coefficient
$\kappa$	40	W/m/K	Heat conduction coefficient
$c_v$	500	J/kg/K	Specific heat

The parameters in Table 18 are inter-related, and they need to be set such that they do not violate a physically realizable material state. Figure 61 shows the stress-strain hysteresis of an SMA wire at an elevated temperature, along with several modeling parameters.

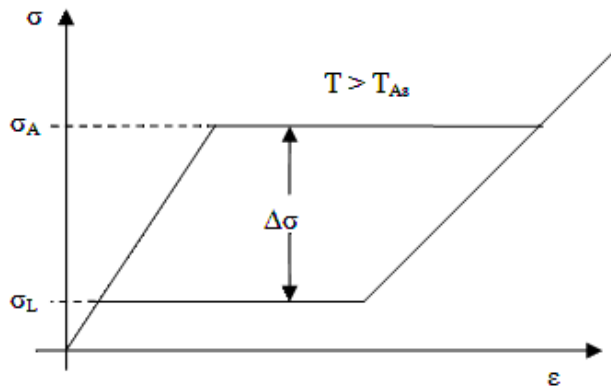


Fig. 1 Diagram of Model Parameters on Stress-Strain Hysteresis Loop

The transition stress from austenite to martensite  $\sigma_A$  is defined in the SMA model by

$$\sigma_A = \sigma_L + \Delta\sigma_T (T(x,t) - T_L) \quad (19)$$

where  $T_{As}$  is the temperature at which austenite first becomes stable under zero stress and can be found in the product specifications. In equation (19),  $\Delta\sigma_T$  describes how much the hysteresis loop in a stress-strain diagram will rise when the temperature of the material increases and should be set first based on experimental data showing the stress-strain behavior at two or more temperatures. The parameter  $\Delta\sigma$  can be found by looking at the width any stress-strain hysteresis plot.

Table 18: Interrelated SMA Model Parameters

Parameter	Value	Unit	Description
$\sigma_L$	100e6	Pa	Austenitic transformation stress
$\Delta\sigma_T$	4e6	Pa	Stress-strain plateau temperature dependence
$T_{As}$	343	K	Austenitic start temperature
$T_L$	311	K	Austenitic conversion temperature
$\Delta\sigma$	225e6	Pa	Width of stress-strain hysteresis

### B.2.3 COMSOL Implementation

The 1D local balance laws described in equations (3) and (5) along with the phase fraction evolution equations (6) and (7) are fit into the general form PDE, equation (20). COMSOL then uses the finite elements method to solve the coupled equations simultaneously at each point along the length of the wire.

$$\mathbf{e}_a \frac{\partial^2 \vec{u}(x,t)}{\partial t^2} + \mathbf{d}_a \frac{\partial \vec{u}(x,t)}{\partial t} + \nabla \cdot \Gamma = \vec{F} \quad (20)$$

#### ODE Solver Coefficients

The terms in equation (20) are as follows:

$$\vec{u}(x,t) = [\delta(x,t) \quad x^+(x,t) \quad x^-(x,t) \quad T(x,t)]^T \quad (21)$$

$$\mathbf{e}_a = [0] \quad (22)$$

$$\mathbf{d}_a = \begin{bmatrix} 0 & 0 & 0 & 0 \\ 0 & 1 & 0 & 0 \\ 0 & 0 & 1 & 0 \\ 0 & -\rho H & -\rho H & \rho c_v \end{bmatrix} \quad (23)$$

$$\mathbf{\Gamma} = \begin{bmatrix} \sigma & 0 & 0 & 0 \\ 0 & 0 & 0 & 0 \\ 0 & 0 & 0 & 0 \\ 0 & 0 & 0 & -\kappa \frac{\partial T(x,t)}{\partial x} \end{bmatrix} \quad (24)$$

$$\vec{F} = \begin{bmatrix} 0 \\ -x^+(x,t)p^{+A} + x^A(x,t)p^{A+} \\ -x^-(x,t)p^{-A} + x^A(x,t)p^{A-} \\ -\frac{2h(T(x,t) - T_{ext})}{R} + \frac{j}{\pi R^2} \end{bmatrix} \quad (25)$$

### **Boundary Conditions**

Appropriate initial and boundary conditions are needed to solve equation (20). The phase fraction evolution equations for the SMA model do not have a spatial derivative term, so they only require initial conditions.

The momentum balance equation requires boundary conditions on both ends of the wire. The displacement is  $\delta = 0$  on the left boundary at all times. To simulate a tensile test experiment, the right boundary condition can either be set as force controlled or displacement controlled depending on the stage of the experiment being simulated.

## **B.3 Experimental Tensile Test Setup and Procedure**

Tensile tests were run in a carefully controlled manner to experimentally characterize the force, displacement, and resistance behavior of an SMA wire. Since the ultimate goal of the simulations is to capture the intricacies of the wire behavior that result from the treatment of the wire during the tensile tests, it is important to discuss the experimental procedure before defining the boundary and initial conditions that are set at different stages of the simulation.

### **B.3.1 Tensile Test Setup**

The experimental setup used for the tensile tests is shown in Fig. 2 and Fig. 3. The force in the SMA wire is measured using a strain-gage-based load cell (Futek Model LSB200) with a 9 N load limit. A ball screw linear actuator (Zaber Model TNA08A25) is used to pull on the wire and report the position of the right end of the wire. A 100  $\mu\text{m}$  diameter Flexinol wire from Dynalloy [1] was used in all experiments. The clamps are machined from steel. Both of the clamps have a lead wire junction near the back of the clamp, and the mechanical load is carried by the front of the clamp, as noted in Fig. 2. Although the lead wire connects near the back of the clamp, the steel clamp itself is conductive so the electrical connection to the SMA wire is actually made at the same location as the mechanical connection.

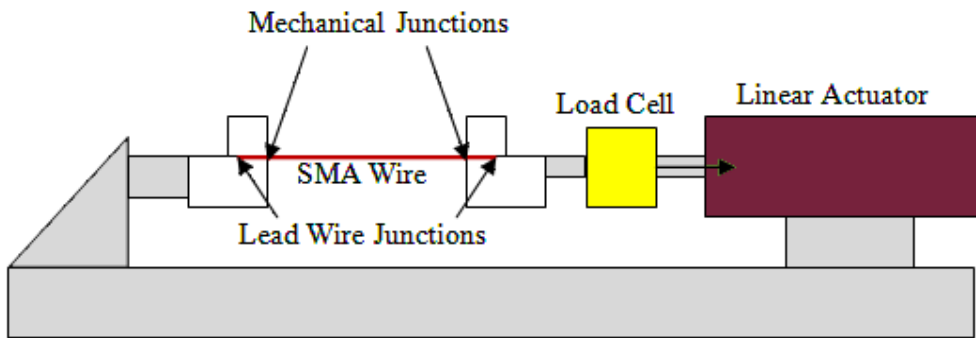


Fig. 2 Diagram of Tensile Test Experiment Setup

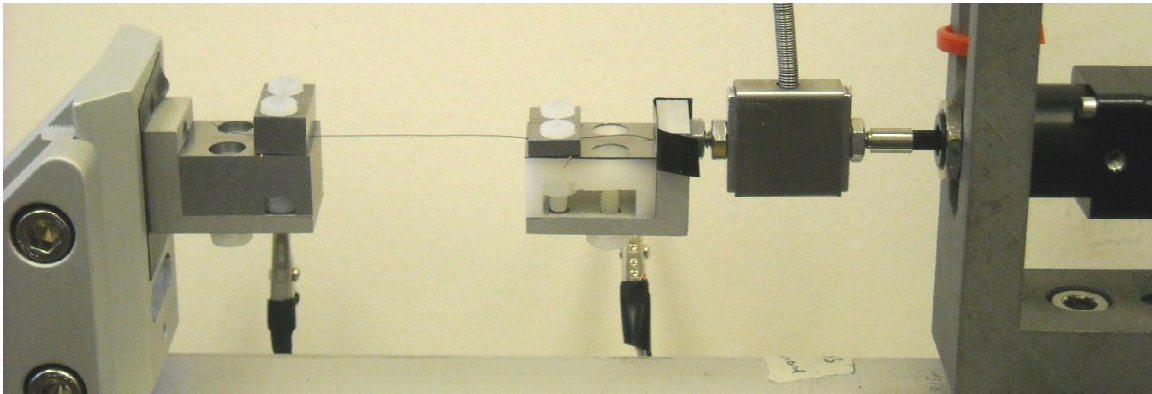


Fig. 3 Photograph of Tensile Test Setup

Fig. 4 shows a close-up photo of the SMA wire at its junction with the steel clamp. Note that three parallel lines have been etched into the clamp. These lines are used to ensure that the SMA wire enters and exits the clamping surface normal to its face. This will reduce unwanted torsion or bending stresses. Fig. 4 also shows how the lead wire is used to create a fulcrum at the back of the clamping surface. This helps to ensure that there is a firm mechanical junction between the clamp and the SMA wire right at the front of the clamp. It also ensures that there is enough pressure on the lead and SMA wires to reduce contact resistance.

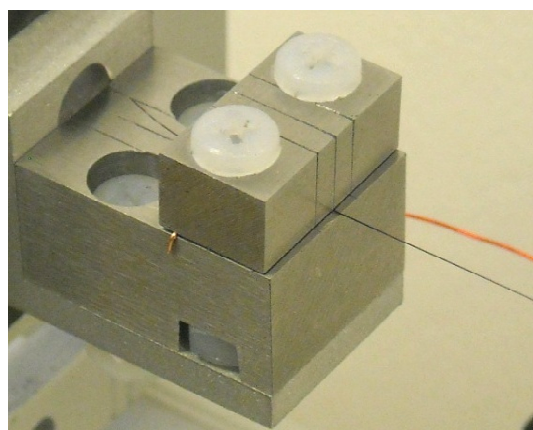


Fig. 4 Close-up Photo of SMA Wire in Steel Clamp

### B.3.2 PWM-Based Power Controller

The electrical power used to heat the wire through Joule heating is generated using a PWM-based power controller. The power controller ensures that the total power put into the wire remains

constant, even as the resistance of the SMA wire changes during a tensile test. It does this by pulsing a current wave with constant amplitude at high ( $\sim 1\text{kHz}$ ) frequency, while adjusting the duty cycle to adjust the total power going into the wire every millisecond. Since the heating and cooling process happens much more slowly than 1 ms, the temperature of the wire is not affected by the individual pulses, only the average of many pulses.

At the same time as the current is pulsed, the peak voltage across the SMA wire is measured. As the wire is strained during a tensile test its resistance changes, thus causing a voltage drop across the SMA wire to change. This feedback measurement is used to update the duty cycle of the constant current pulse for the next cycle. Since the increase in temperature is proportional to the power input, as was shown in equation (5), controlling power gives the best control over SMA temperature; a constant, continuous current source would cause more heating as the wire lengthens and its resistance increases, and a constant voltage input would have the opposite effect.

When using a constant power controller to heat a variable length wire, it is important to consider the effects of the parasite or loop resistance that exists between the actual SMA wire and the analog inputs of the power supply. The parasite resistance arises from the resistance of the lead wires and the contact resistance made at each electrical connection, especially the connection between the SMA and the clamp. In reality, the supply is providing power to both the SMA and these components, shown in Fig. 5.

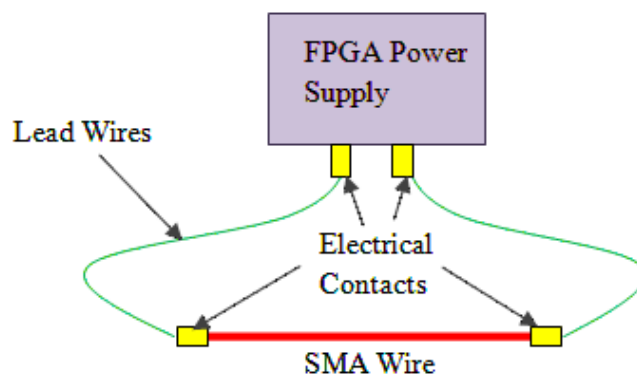


Fig. 5 Flow of Power from FPGA-Controlled Supply through SMA Wire

Parasite resistance was measured and compensated for in the power control algorithm. More information on the power controller development, calibration, and testing is presented in [69].

### B.3.3 Procedure

The exact treatment of the SMA wire before and during a tensile test is especially important because of the hysteretic nature of SMA wires. The treatment of the SMA wire is chronicled below:

1. Pre-cycle the SMA wire.
  - a. Cut a 200 mm length of SMA wire off the roll.
  - b. Secure about  $L = 150$  mm of the wire between the Steel clamps.
  - c. Pull the wire to a stress of 300 MPa.

- d. Relax the wire and heat with 0.006 W/mm under zero load for 10 s.
  - e. Pull the wire with the actuator until a load is detected and record the wire length at  $L_{0A}$ .
  - f. Turn off the power and wait for 10 s.
  - g. Pull the wire with the actuator until a load is detected and record the wire length at  $L_{0M}$ .
  - h. Return to  $L_{0A}$  and then heat the wire with  $P_{set} = 0.0045$  W/mm for 10 s.
  - i. Pull the wire between 0 and 6% strain at a rate of  $\pm 0.6\%/s$ . Repeat for 10 cycles.
2. Run the Tensile Test
- a. Using the  $L = 150$  mm wire in the clamps after pre-cycling (above), repeat steps 1c-1i.
  - b. Repeat step 2a with  $P_{set} = 0.004$  W/mm.
  - c. Repeat step 2a with  $P_{set} = 0.003$  W/mm.
  - d. Repeat step 2a with  $P_{set} = 0$  W/mm.
  - e. Release the left clamp and choke in on the wire until about 100 mm of wire ( $L$ ) is between the clamps.
  - f. Secure the left clamp and repeat steps 2a-2d for wire length  $L = 100$  mm.
  - g. Repeat steps 2e-2f with  $L = 75$  mm.
  - h. Repeat steps 2e-2f with  $L = 50$  mm.
  - i. Repeat steps 2e-2f with  $L = 25$  mm.

The two inputs, strain and power, are shown alongside the measured stress in the SMA wire for a representative tensile test in Fig. 6. For the test shown, preheat power per millimeter of SMA wire was set to 0.006 W/mm and the cycles were run at a constant input power of 0.0045 W/mm. The strain value on the y axis of the top panel is actually the engineering strain, the measured displacement divided by  $L_{0A}$ . The power plot shown in the middle panel is the total power put out by the FPGA-controlled power supply. The measured stress plot in the bottom panel shows the 300 MPa stress (11 s) that the wire is pulled to prior to each experiment as well as the small  $\sim 5$  MPa readings that result when the wire is detected at  $L_{0A}$  (34 s) and  $L_{0M}$  (62 s). The strain at  $L_{0M}$  is almost 4% for this particular experiment, as indicated by the strain value at 62-65 seconds in the top panel.

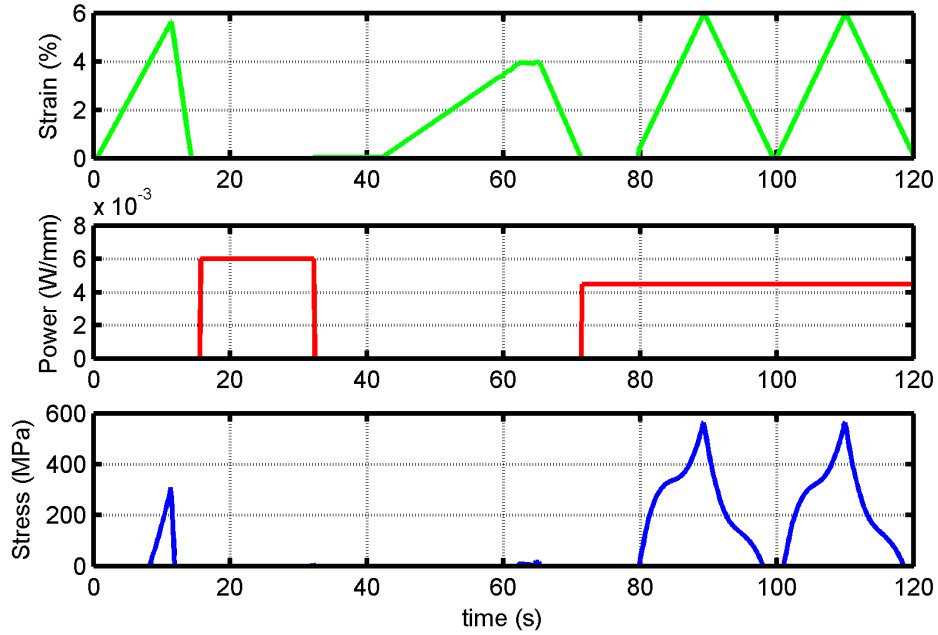


Fig. 6 Strain Input, Power Input, and Stress Measurement for Typical Tensile Test

## B.4 Results

### B.4.1 Effect of the Thermal Boundary Condition on Temperature Distribution

The temperature and phase fraction distributions across simulated 60 mm and 20 mm long SMA wires are shown in Fig. 7 and Fig. 8, respectively. The dash-dot lines represent the temperature and phase fractions that result from a 0.006 W/mm input power after thermal equilibrium has been reached. The dotted lines and the solid lines show the same for a 0.004 and 0.003 W/mm input power, respectively. The isothermal boundary condition ensures that the ends of the wire are kept at 295 K; however, Fig. 7 shows that the middle of the wire reaches substantially higher temperatures, and the larger input power results in a higher temperature in the middle of the wire.

Also, Fig. 7 and Fig. 8 show that the thermal inhomogeneity has an impact on the phase fractions near the boundaries. This is because austenite is only stable at temperatures above  $T_{As}$ , which cannot occur near the boundaries. When a high input power (0.006 W/mm) is used, the region that is above  $T_{As}$  extends closer to the boundary, resulting in a thin, 2 mm long boundary layer where the material remains in the  $M^+$  phase. Conversely, the lowest power input (0.003 W/mm) results in a larger, 6.5 mm boundary layer. When the wire cools under zero stress, the section of the wire that is in austenite will divide up evenly to create the  $M^+/M^-$  twin phase, while the wire within the boundary layer will remain  $M^+$ . Since the  $M^+$  phase has drastically different geometric properties from the  $M^+/M^-$  twin phase, the length of the boundary layer can have a significant impact on the bulk behavior and strain of a wire during a tensile test.

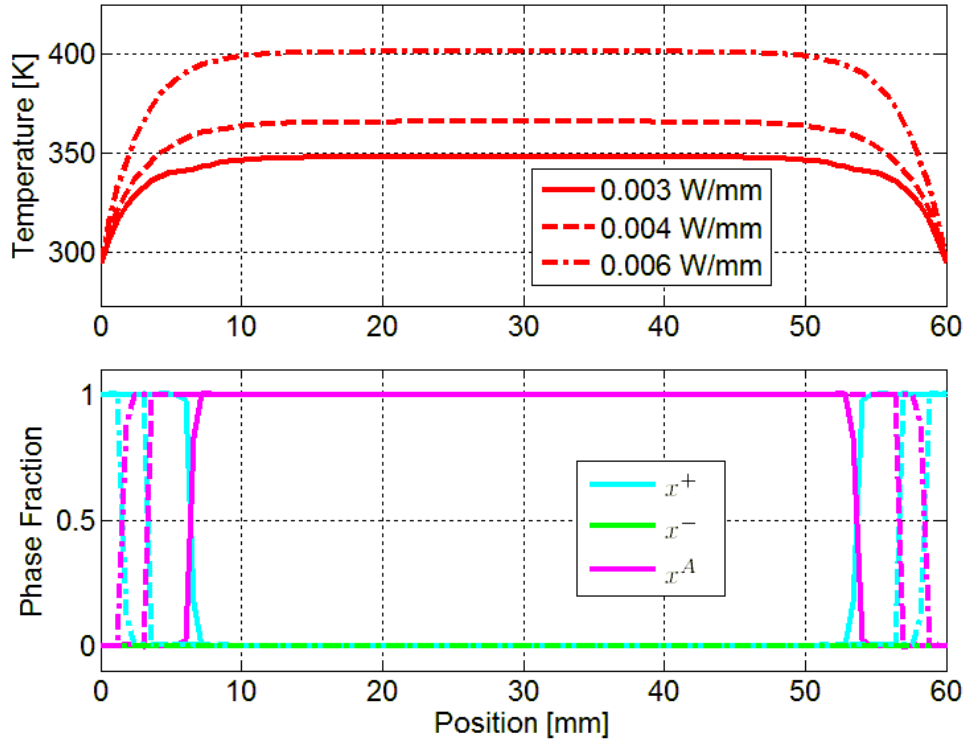


Fig. 7 Comparison of Temperature and Phase Fractions of a 60 mm Wire with 0.003, 0.004, and 0.006 W/mm input Power

Fig. 8 shows the same comparison for a 20 mm wire. The trends in Fig. 8 are the same, with the larger input power resulting in a greater temperature increase in the middle of the wire and a smaller boundary layer at the end. It is interesting to note that the peak temperature in the middle of the 20 mm wire is nearly the same as the 60 mm wire. Also, the boundary layers on the 20 mm wire are about 2 and 6 mm for the 0.006 and 0.003 W/mm power input cases, respectively. These are similar to the values noted for the 60 mm wire. The uniformity of the boundary layer length for different length wires is expected, since the temperature in the center of the wire is almost able to reach the same plateau values of 400 and 350 K for the 0.006 and 0.003 W/mm cases. However, it is important to note that in the case of the 20 mm wire, the boundary layer comprises a much larger percentage of the total wire length.

The bulk load-deformation behavior observed at the endpoints during a tensile test represents the average of the behavior at each individual point along the length of the wire. In the case of a 20 mm wire heated with 0.006 W/mm, only 80% of the wire transforms to austenite during heating, then  $M^+/M^-$  after cooling, while 20% remains in  $M^+$  throughout. In the case of the 60 mm wire, 93% of the wire ends up in  $M^+/M^-$  after cooling, while only 7% remains in  $M^+$ . Since the reference position for 0% strain is set after the heating stage, the two strain-controlled tensile will clearly have a different starting point in terms of both strain and phase fraction – the shorter the wire, the more  $M^+$  it will have at the start of the experiments.

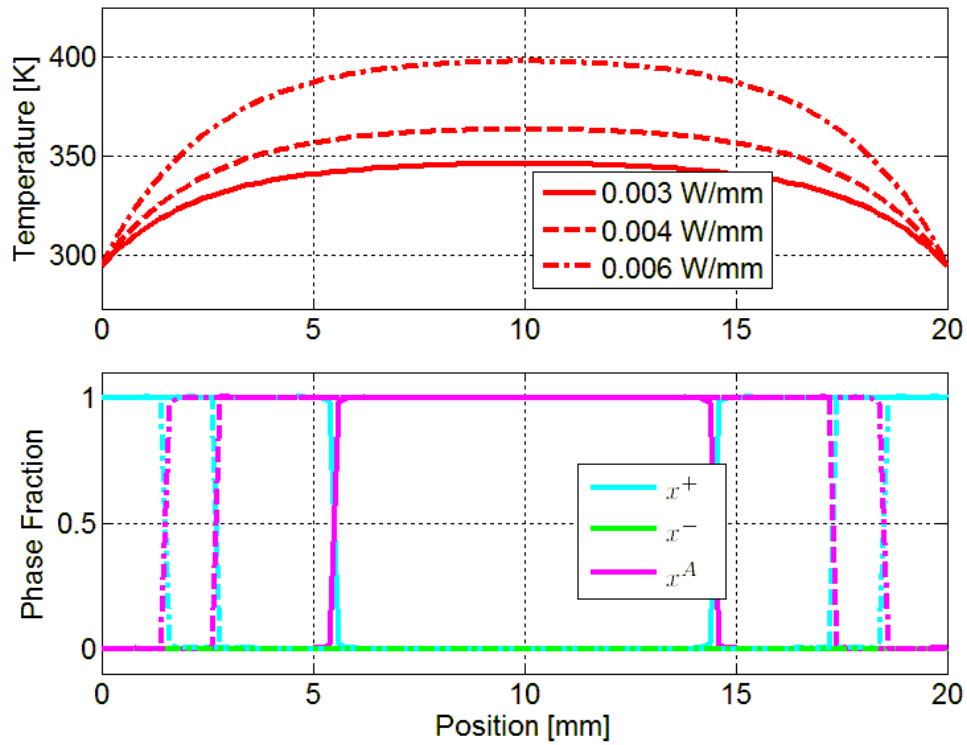


Fig. 8 Comparison of Temperature and Phase Fractions of a 20 mm Wire with 0.003, 0.004, and 0.006 W/mm input Power

When the simulation is run with adiabatic boundary conditions, as shown in Fig. 9, the temperature of the wire is homogenous, and the entire wire is able to transform to 100 % austenite during heating. As a result no boundary layer forms and the load-deformation behavior of the bulk wire will be independent of wire length.

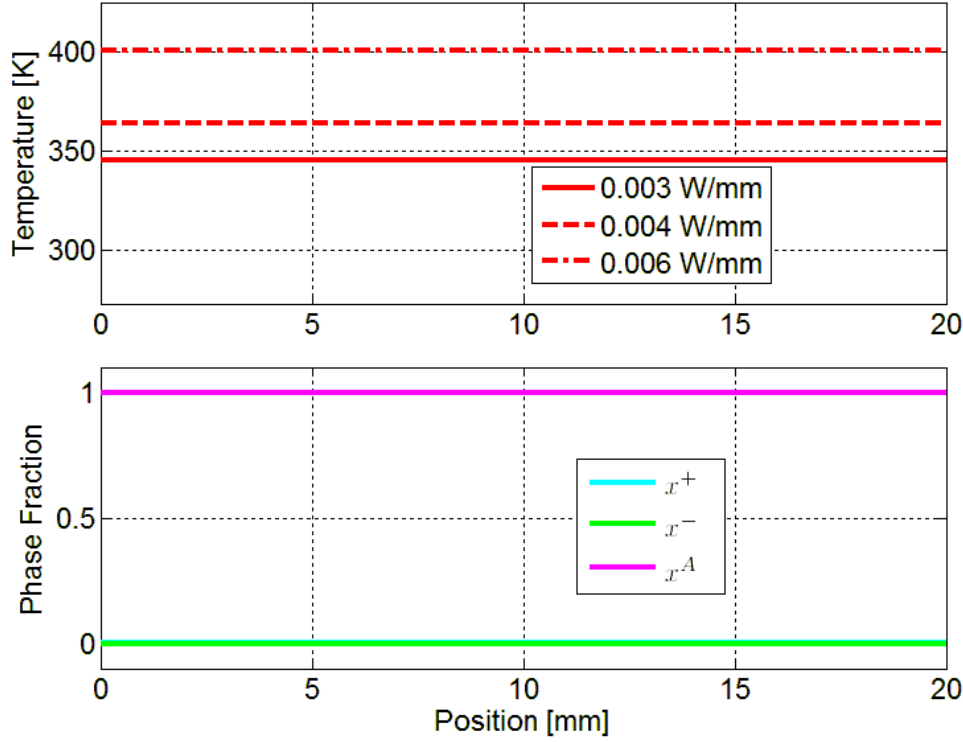


Fig. 9 Comparison of Temperature and Phase Fractions of a 20 mm Wire with Adiabatic Boundary Conditions for 0.003, 0.004, and 0.006 W/mm Input Power

#### B.4.2 Using Boundary Conditions to Simulate a Tensile Test

The initial conditions of the phase fractions, thermal boundary conditions on both ends of the wire, and mechanical boundary condition on the right end of the wire were used to simulate each stage of the experiment as outlined in Table 19. The first step of each experiment is to pull the wire to 300 MPa at low temperature; this step is simulated by simply setting the initial phase fraction to 100% martensite plus.

During the simulated heating step, the Joule heating term,  $j$  in Equation (5), is set to 0.006 W/mm, and the right end is free, simulating the zero stress condition. This step is important for establishing the reference length that serves as the zero strain ( $\delta = 0$ ) starting point during the tensile experiments. The isothermal boundary conditions prevent sections of the wire near the ends from heating and changing phase from  $M^+$  to austenite. During cooling, the right end is once again free as the austenite that developed away from the isothermal ends switches to the  $M^+/M^-$  twin phase. After the simulated heating/cooling step, the displacement of the right end is recorded as the reference length of the SMA. Finally, the displacement at the right end is controlled using a triangle wave displacement input,

$$\delta(t) = \frac{\delta_{\max} t}{t_{\text{seg}}} (t < t_{\text{seg}}) + \left( \delta_{\max} - \frac{\delta_{\max} (t - t_{\text{seg}})}{t_{\text{seg}}} \right) (t \geq t_{\text{seg}}) \quad (26)$$

Table 19: Boundary Conditions Used to Simulate Steps of a Tensile Test Experiment

Experiment Step	Thermal BC (both ends)	Mechanical BC (right end)	Phase Fractions
Pull the wire to 300 MPa at low temperature	NA	NA	100 % M <sup>+</sup>
Heat wire under 0 stress	$T = T_{external}$	$\sigma = 0$	Continue from above
Cool wire under 0 stress	$T = T_{external}$	$\sigma = 0$	Continue from above
Displacement $\delta(t)$	$T = T_{external}$	$\delta = \delta(t)$	Continue from above

In equation (26)  $\delta_{max}$  is the maximum displacement that the wire endpoint is pulled to during a cycle of the tensile test and  $t_{seg}$  is the time that it takes to go from 0 strain to  $\delta_{max}$  (10 s for all experiments). The end displacement  $\delta$  is centered such that  $\delta = 0$  when the SMA wire is in the austenite phase at zero stress. The maximum displacement is set such that the average strain in the SMA will be 6%, so  $\delta_{max} = L_0(0.06)$ . The Boolean operation terms are equal to 1 when the inequality is true and 0 when it is false. On unloading, a similar expression describes displacement as it slopes back to the starting point at the same rate. Two loading/unloading cycles are repeated, and the phase fractions at the conclusion of one step are passed on as the initial conditions for the step that follows.

### B.4.3 Effect of the Thermal Boundary Condition on Hysteresis

The difference in the load-deformation behavior of a tensile test simulated with adiabatic and isothermal boundary conditions is apparent in Fig. 10. The adiabatic case plotted in the left panel shows 5 coincident hysteresis lines for the 5 different wire lengths. However, in the isothermal case shown in the right panel, the difference in the percentage of the wire in the M<sup>+</sup> phase at 0% strain has a significant impact on the load-deformation behavior. The short 18.7 mm wire that contains a large percentage of M<sup>+</sup> requires over 600 MPa of stress to reach 6% strain, while the 148.8 mm wire requires only 400 MPa. This is not unexpected, because after the preheating step the shorter wire contains less austenite that can change phase to M<sup>+</sup>, and thus gets to the M<sup>+</sup> line at lower strain value of strain. The percentage of the wire that is encompassed by the constant length boundary layer  $x_{BL}$  is

$$\%BL(L_0) = \frac{x_{BL}}{L_0}. \quad (27)$$

As the wire gets longer, the impact of the boundary layer decreases until the load-deformation characteristic converges towards the adiabatic case. This is verified in the Fig. 10, which shows a lessening variation in load-deformation behavior as the wire length approaches 148.8 mm.

Fig. 10 also shows that the equilibrium state does not return directly to the austenite line and then the origin on unloading. This is because at the start of cycle 1 the wire was in a state created by heating at 0.006 W/mm, while during the tests, the wire is heated by a constant input power of only 0.004 W/mm. The large preheat power induces a small boundary layer at the start of cycle 1, but once the entire wire is pulled to M<sup>+</sup>, the lower 0.004 W/mm power allows for a larger boundary, as shown in

Fig. 7. As a result, the wire returns to zero stress on unloading in a state that still contains some of the  $M^+$  phase.

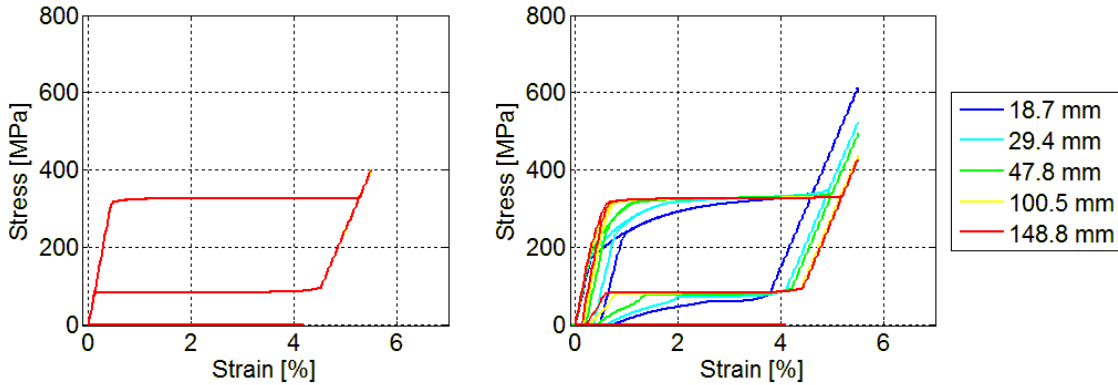


Fig. 10 Simulated Hysteresis for a SMA wire with Adiabatic (left) and Isothermal (right) Boundary Conditions

#### B.4.4 Comparison with Experimental Results

The simulated results are compared to experimental results in the sections below. The simulation uses the measured length of the SMA wire as the reference length for the model.

##### *Effect of Active SMA Wire Length*

The impact of the SMA wire length on the force-deformation curves at 0, 0.003, 0.004, and 0.0045 W/mm input powers are shown in Fig. 11 through Fig. 14, where the left panel shows experimental results and the right panel shows simulation. Starting with Fig. 11, the effect of the thermal inhomogeneity while establishing the reference austenitic (zero strain) length is apparent. Since the shorter wires contain a larger percentage of  $M^+$  when this reference length is set, less input strain is required to bring the wire to the 100%  $M^+$  line. This effect is well captured by the model that shows the shorter wires reaching the  $M^+$  line at a lower value of strain, then reaching a higher maximum stress at 5.5% strain. However, a known shortcoming with the SMA model is also apparent in Fig. 11. The experimental data shows that no force is generated until about 2.5% strain. This is the strain at  $L_{0M}$  mentioned in the procedure. This results from the wire being biased towards the  $M^+$  phase (instead of  $M^-$ ) when cooled under 0 load via the so-called two-way effect, which is not captured by the model. The two-way effect is a result of interstitial stresses and interactions between different grains within the material, and therefore cannot be captured by a single-crystal model.

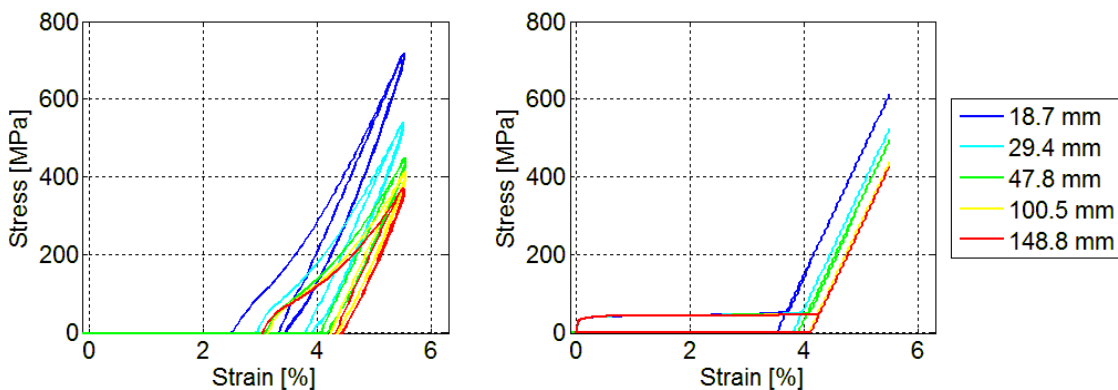


Fig. 11 Experimental (left) and Simulated (right) Hysteresis Loops for SMA Wires with 0 W/mm Input Power

When the input power increases, Fig. 12 through Fig. 14 show that the hysteresis loop begins to rise as expected. The impact of the two-way effect begins to diminish as more of the wire is transformed into the austenite phase. The effect of a higher percentage of  $M^+$  when reference length is established in the shorter wires is still apparent.

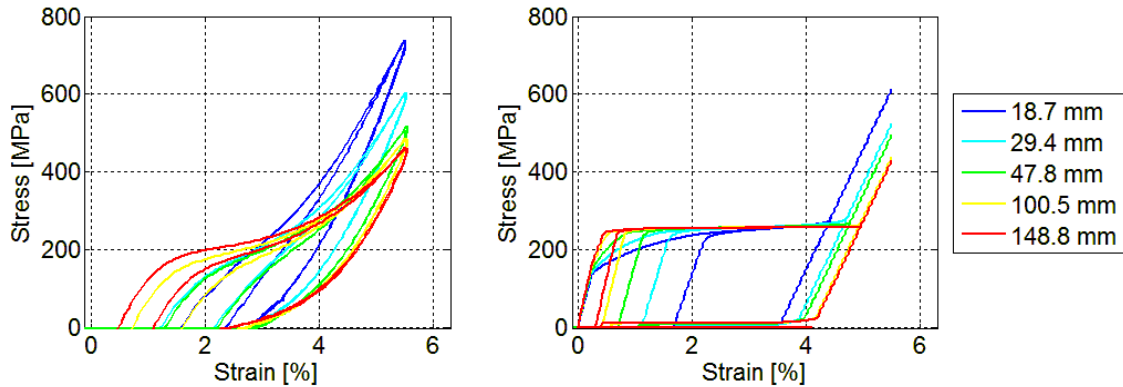


Fig. 12 Experimental (left) and Simulated (right) Hysteresis Loops for SMA Wires with 0.003 W/mm Input Power

As input power is increased further in Fig. 13 and Fig. 14, the effect of using a high input power during the preheating step and a constant, low input power during straining starts to become noticeable. As discussed above, the high (0.006 W/mm) input power used during preheating results in a fairly low percentage of  $M^+$ . However, when the cycling begins the input power is only 0.004 W/mm. Therefore, some of the sections that are pulled to  $M^+$  during straining cannot be returned to austenite when the wire is relaxed, because of the lower input power. The experimental results also show that the stress-strain curves return to the zero-stress axis at a non-zero value of strain, indicating that the wire contains more  $M^+$  than it did initially. This is exactly what is expected and is corroborated by the simulations.

Additionally, all of the experimental data shows that the longer wires have a boxier hysteresis loop with a nearly horizontal plateau on loading and unloading than do the shorter wires. This effect is also expected, because of the fact that the shorter wires contain a higher percentage of  $M^+$  phase near the attachment points and thermal heat sinks. The mixing of the soft (30.9 GPa modulus)  $M^+$  phase and the stiffer (71.1 GPa modulus) austenite phase has a softening effect on the hysteresis loops. Since both the experiments and simulations track behavior of the end points of the wire, the average behavior occurring between the clamp boundaries is represented by the plots. As a result, this softening effect is expected to appear in both experiments and simulations, as it does.

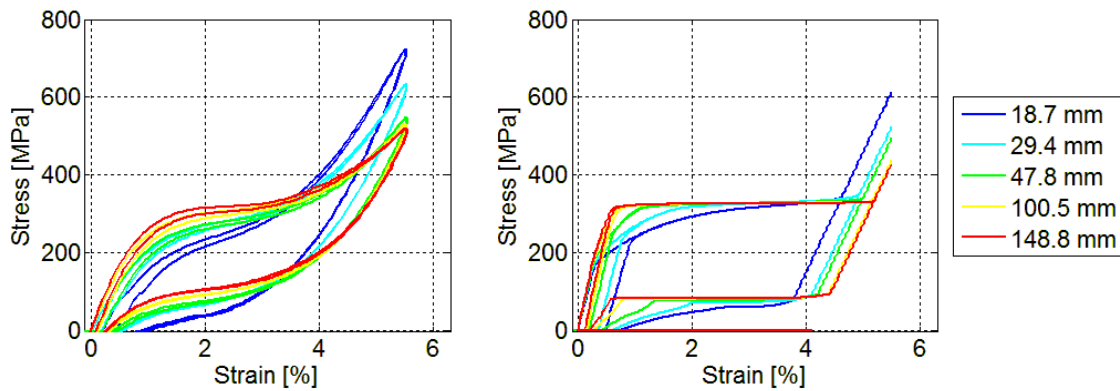


Fig. 13 Experimental (left) and Simulated (right) Hysteresis Loops for SMA Wires with 0.004 W/mm Input Power

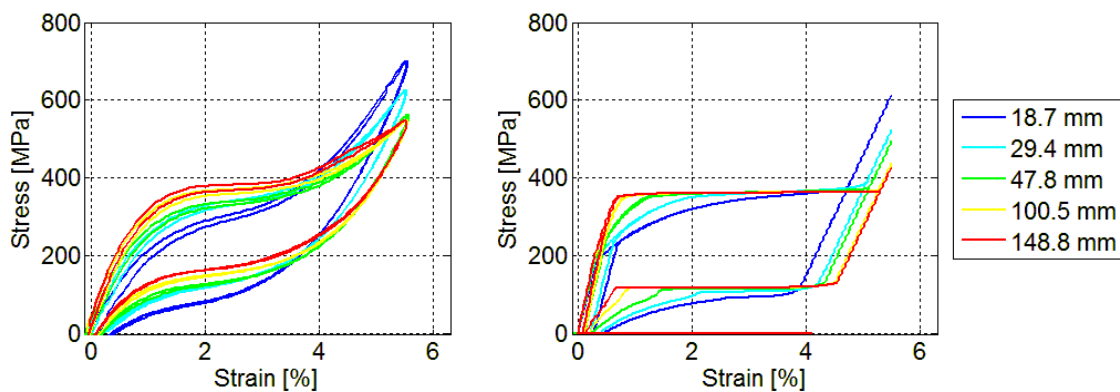


Fig. 14 Experimental (left) and Simulated (right) Hysteresis Loops for SMA Wires with 0.0045 W/mm Input Power

### ***Effect of Input Power***

Fig. 15 through Fig. 19 show the effect of different input powers on the different length wires. The simulated results show that input power should have no impact on the force level needed to generate 5.5% strain for wires of the same length. This is generally validated by the experimental data. The only significant disparity occurs for very long wires with low input power, where the impact of the un-modeled two-way effect dominates the wire behavior.

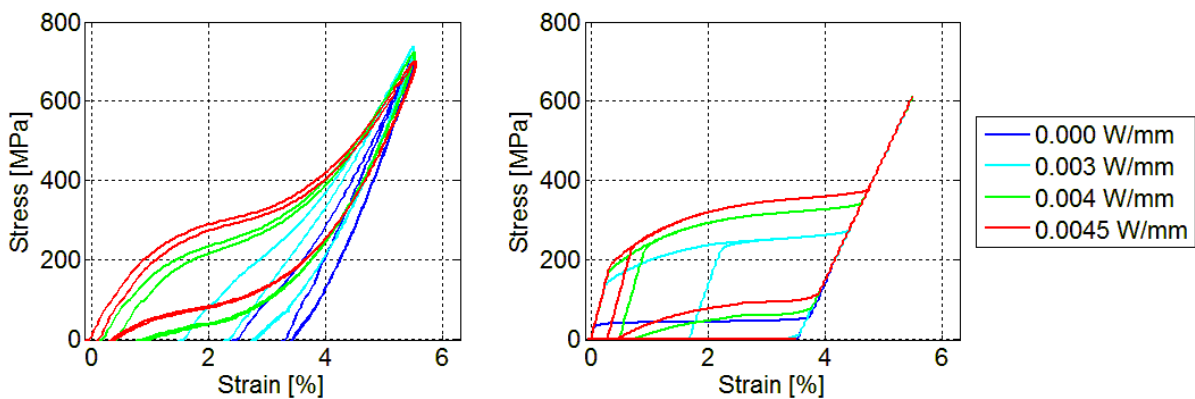


Fig. 15 Experimental (left) and Simulated (right) Hysteresis Loops for 18.7 mm SMA Wire

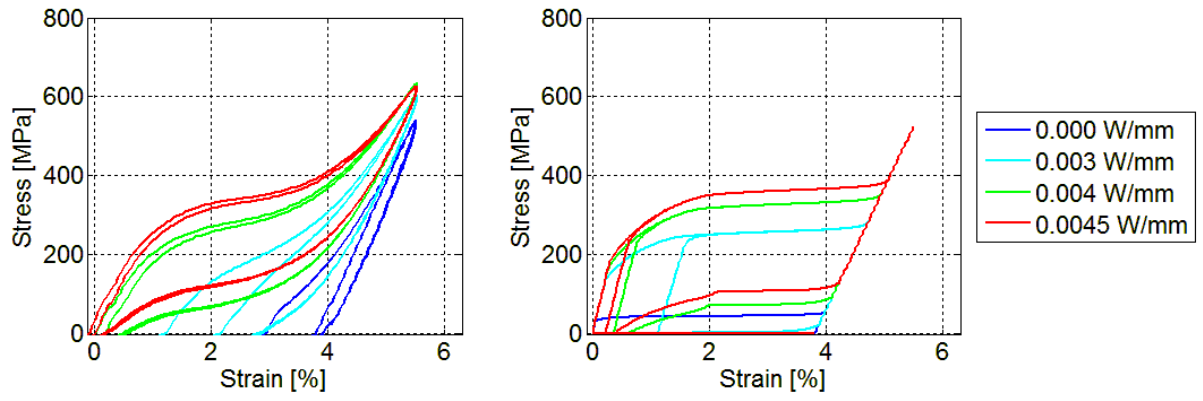


Fig. 16 Experimental (left) and Simulated (right) Hysteresis Loops for 29.4 mm SMA Wire

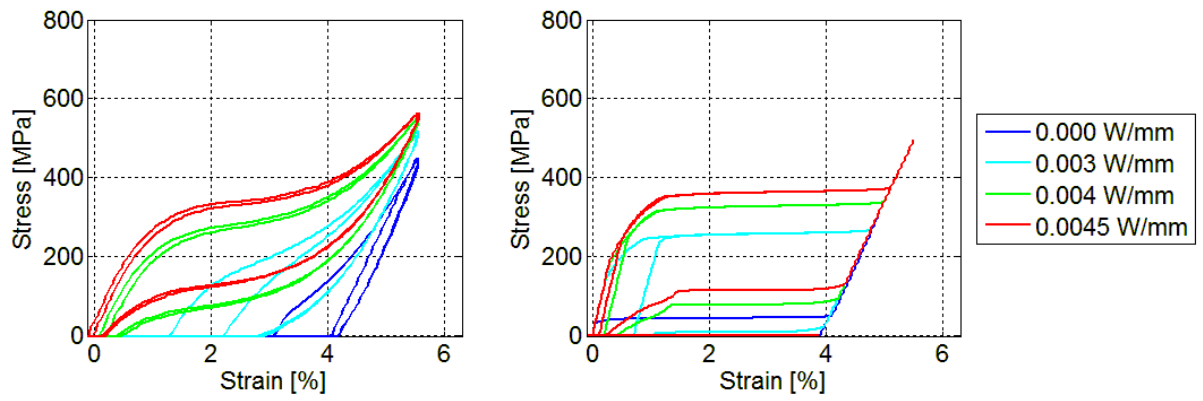


Fig. 17 Experimental (left) and Simulated (right) Hysteresis Loops for 47.8 mm SMA Wire

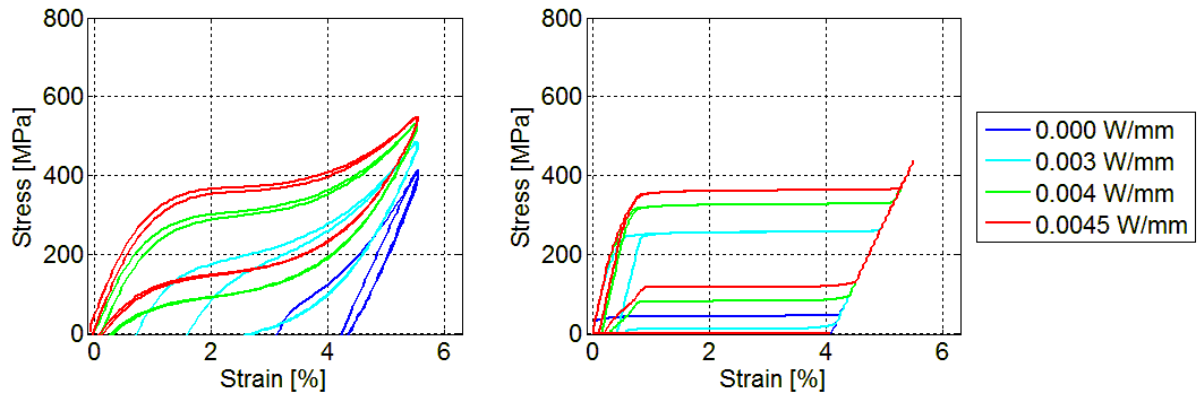


Fig. 18 Experimental (left) and Simulated (right) Hysteresis Loops for 100.5 mm SMA Wire

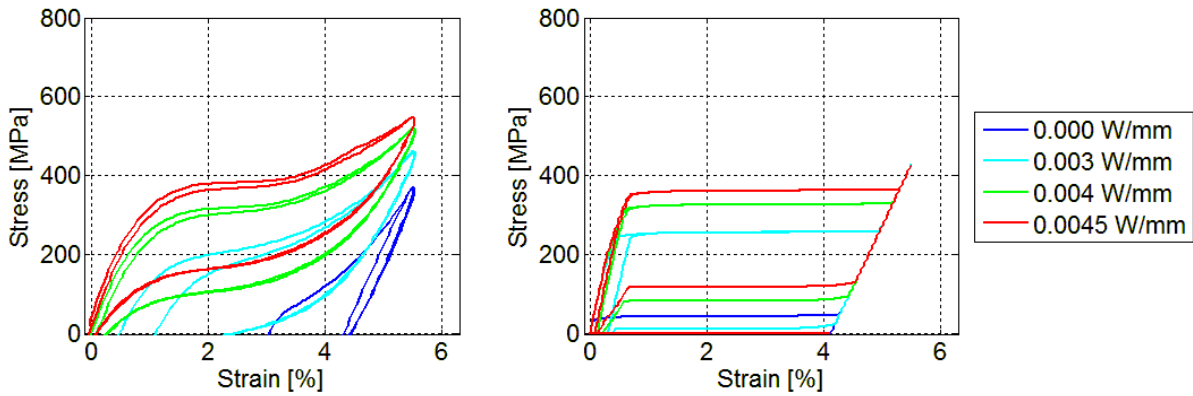


Fig. 19 Experimental (left) and Simulated (right) Hysteresis Loops for 148.8 mm SMA Wire

### ***Measured and Simulated Wire Resistance***

The resistance measured across different length SMA wires at different input powers is shown in Fig. 20 through Fig. 24. In these plots, the total resistance is normalized by the nominal length of the SMA wire to make comparisons easier to visualize on the same scale. The simulated resistance model, plotted in the right panel, suggests that the resistance should be slightly hysteretic due to the phase fraction dependence. However, the hysteresis is very narrow, because the elastic strain and thermal effects counter-act the effect of the phase fractions.

On mechanical loading, the fraction of austenite is high, and as a result the resistance is expected to be lower than on unloading. However, the stress is also higher on the loading, which leads to more elastic strain, and thus a longer, thinner wire with higher resistance.

A number of observations can be made from comparing the experimental and simulated results. First, the experimental results show almost no hysteresis while simulations show a narrow hysteresis. The hysteresis in the simulation could be eliminated completely by adjusting the thermal dependence coefficients. Also, the polycrystalline material generally has smoother behavior than the single crystal model will predict, which could contribute to the lack of hysteresis in the experimental results. Regardless, in both the experimental and simulated results, the plots for all length wires show a lower slope in austenite and martensite regimes (less than 1% and more than 4.5% strain) than in the phase transition regime. The lower slope of the martensite phase is particularly noticeable in the zero input power cases of Fig. 20 through Fig. 24. However, due to the polycrystalline nature of the real wire, the effects are smoothed and thus less noticeable than in the simulation.

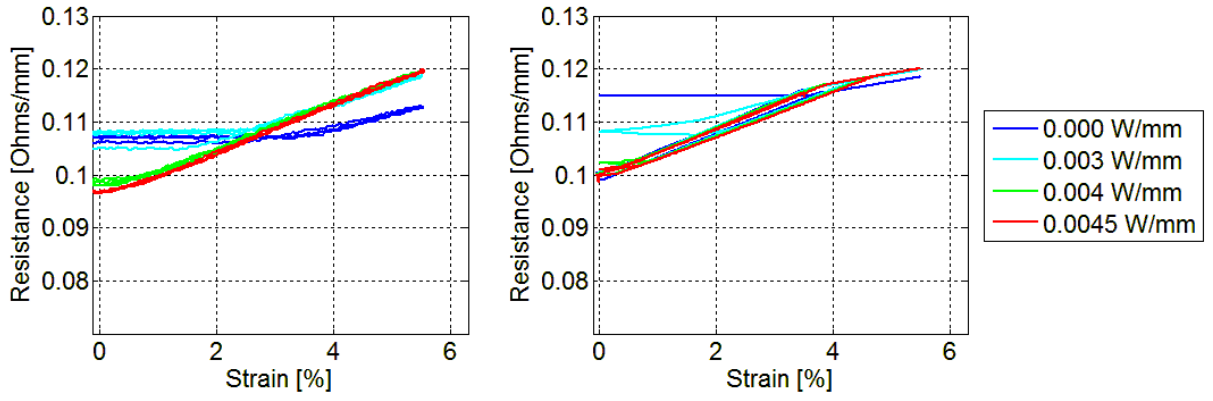


Fig. 20 Experimental (left) and Simulated (right) Resistance for a 18.7 mm SMA Wire

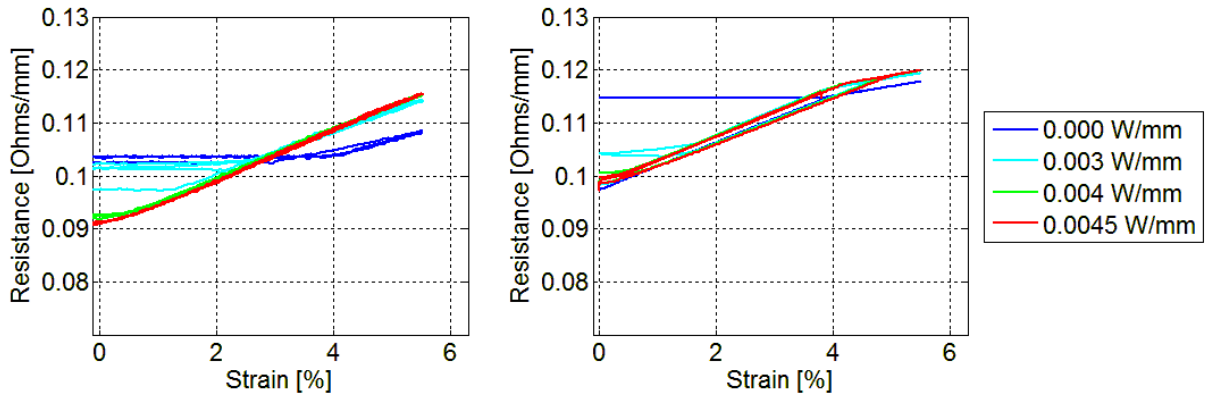


Fig. 21 Experimental (left) and Simulated (right) Resistance for a 29.4 mm SMA Wire

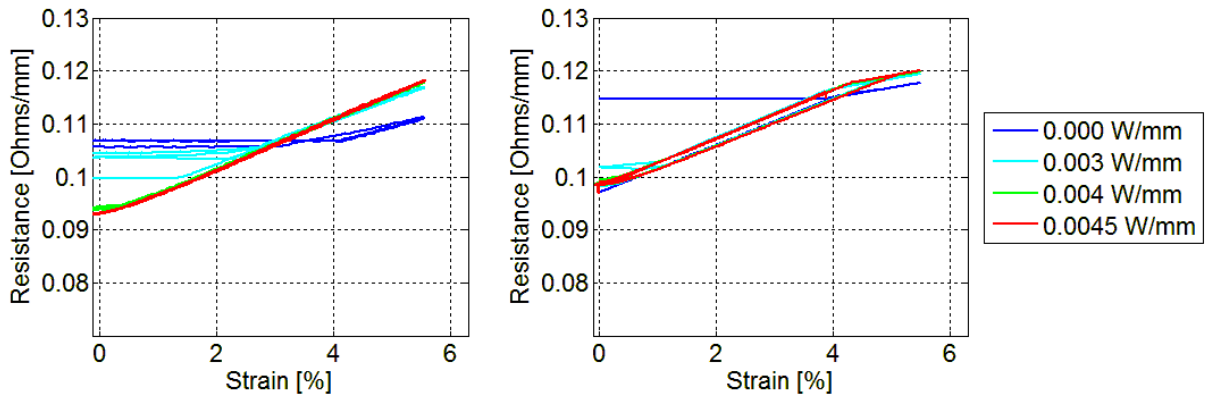


Fig. 22 Experimental (left) and Simulated (right) Resistance for a 47.8 mm SMA Wire

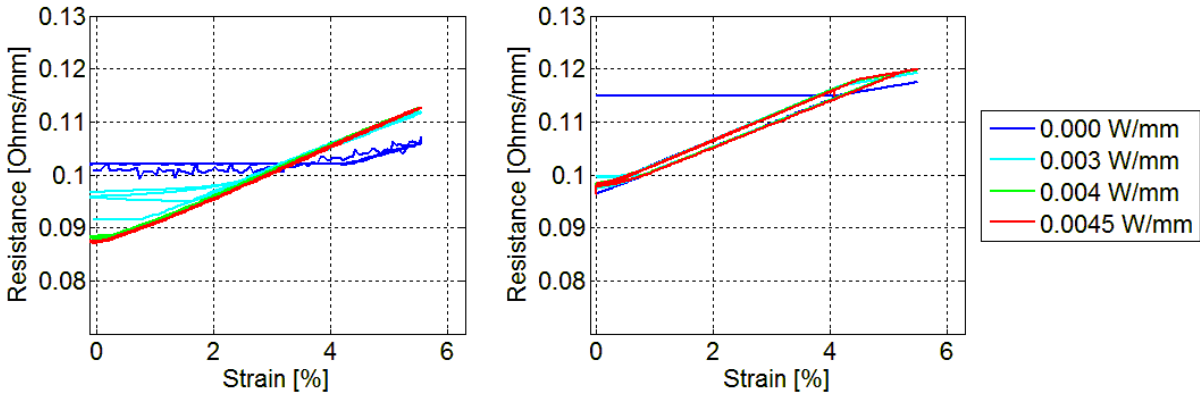


Fig. 23 Experimental (left) and Simulated (right) Resistance for a 100.5 mm SMA Wire

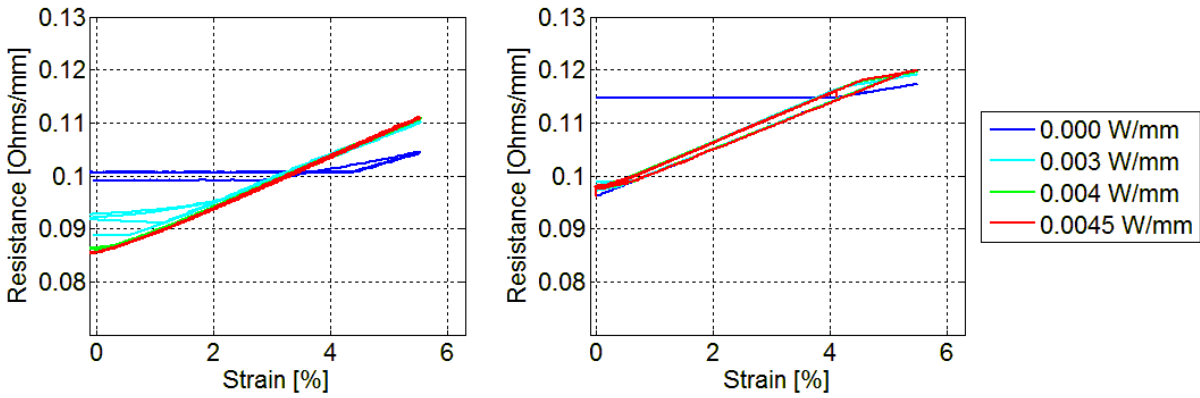


Fig. 24 Experimental (left) and Simulated (right) Resistance for a 148.8 mm SMA Wire

Fig. 25 clearly shows the comparison between the resistance curves of different length wires for a single power input level. Both the model and experimental results show that the normalized resistance per nominal length is expected to be higher in the shorter wires. This is expected from the thermal inhomogeneity, because shorter wires will contain more martensite near the thermal boundaries. Also, at high values of strain, the shorter wires achieve a higher stress and thus more elastic straining than the longer wires.

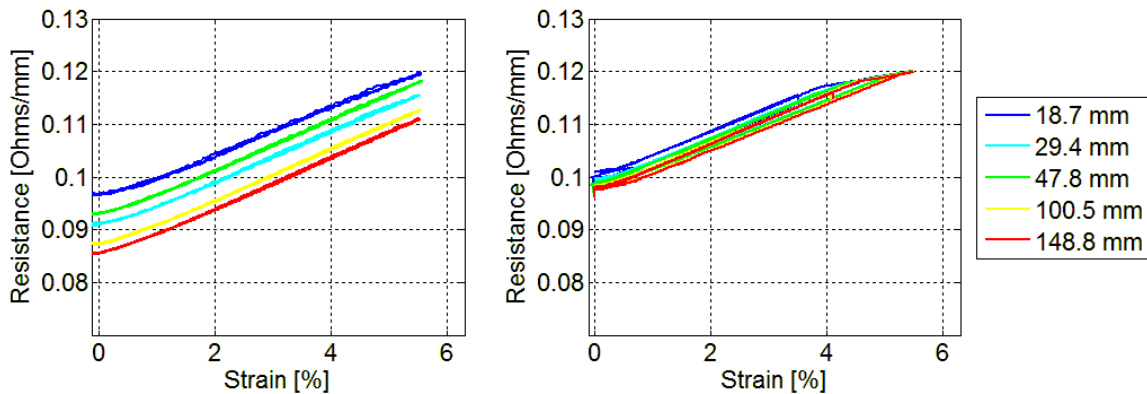


Fig. 25 Experimental (left) and Simulated (right) Resistance for a 4.5 W/mm Input Power

## **B.5 Conclusions on the Effects of Thermal BCs on SMA Actuator Wires**

Both the experimental and modeled results show that the behavior of an SMA wire can vary greatly due to thermal inhomogeneity. Large heat sinks at the wire attachment points lower the temperature near the end of the wire, resulting in a persistent region of martensite, even when large input power is applied. Since these end-effects are more significant in shorter wires than in longer wires, a shorter wire will behave more “martensitically” than a longer wire.

This inhomogeneity may lead to a loss of stroke, particularly for short wires. Additionally, short wires have a different average resistivity than long wires. This is important for applications that endeavor to employ the multi-functional capabilities of SMA wires by using the resistance as a strain measurement. Surprisingly, experimental results indicate very little hysteresis in the strain-resistance characteristic for a constant-temperature tensile test. This is critical for sensor applications and eliminates some of the challenges of using SMA wire resistance as a high stroke, low force displacement sensor. Regardless of the effect, understanding the impact of attaching a wire to a larger structure is critical to the design of embedded SMA applications.